N°d'ordre NNT : **2023ISAL0114**

THESE de DOCTORAT DE L'UNIVERSITE DE LYON
Opérée au sein de
L'Institut National des Sciences Appliquées de Lyon

Ecole Doctorale N° ED162 MEGA
MÉCANIQUE, ÉNERGÉTIQUE, GÉNIE CIVIL, ACOUSTIQUE

Spécialité/ discipline de doctorat : Acoustique

Soutenue publiquement

Le 18/ Décembre /2023, par :

Léopold DIATEZO

Multifunctional materials for intelligent textile: Toward automotive applications

---

Devant le jury composé de :

GUIFFARD Benoit	Professeur /Université de Nantes	Rapporteur
BELHORA Fouad	Professeur/ Université Chouaib Doukkali	Rapporteur
DEMOLY Frédéric	Professeur / Université de UTBM	Examinateur
CONSONNI Vincent	Directeur de Recherche CNRS/LMGP	Examinateur
KANDA Masae	Associate Professor, Chubu University	Examinatrice
COTTINET Pierre-Jean	HDR, Maître de Conférences /INSA-LYON	Directeur de thèse
CAPSAL Jean-Fabien	HDR, Maître de Conférences /INSA-LYON	Co-directeur de thèse
LE Minh-Quyen	Maître de Conférences /INSA-LYON	Co-encadrante de thèse
Christine TONELLATO	Manager TESCA-Group France	Invité

Thèse accessible à l'adresse : https://theses.insa-lyon.fr/publication/2023ISAL0114/these.pdf © [L. Diatezo], [2023], INSA Lyon, tous droits réservés

Thèse accessible à l'adresse : https://theses.insa-lyon.fr/publication/2023ISAL0114/these.pdf © [L. Diatezo], [2023], INSA Lyon, tous droits réservés

Département FEDORA – INSA Lyon - Ecoles Doctorales

IGLE	ECOLE DOCTORALE	NOM ET COORDONNEES DU RESPONSABLE
ED 206 CHIMIE	**CHIMIE DE LYON** https://www.edchimie-lyon.fr Sec. : Renée EL MELHEM Bât. Blaise PASCAL, 3e étage secretariat@edchimie-lyon.fr	**M. Stéphane DANIELE** C2P2-CPE LYON-UMR 5265 Bâtiment F308, BP 2077 43 Boulevard du 11 novembre 1918 69616 Villeurbanne directeur@edchimie-lyon.fr
ED 341 E2M2	**ÉVOLUTION, ÉCOSYSTÈME, MICROBIOLOGIE, MODÉLISATION** http://e2m2.universite-lyon.fr Sec. : Bénédicte LANZA Bât. Atrium, UCB Lyon 1 Tél : 04.72.44.83.62 secretariat.e2m2@univ-lyon1.fr	**Mme Sandrine CHARLES** Université Claude Bernard Lyon 1 UFR Biosciences Bâtiment Mendel 43, boulevard du 11 Novembre 1918 69622 Villeurbanne CEDEX e2m2.codir@listes.univ-lyon1.fr
ED 205 EDISS	**INTERDISCIPLINAIRE SCIENCES-SANTÉ** http://ediss.universite-lyon.fr Sec. : Bénédicte LANZA Bât. Atrium, UCB Lyon 1 Tél : 04.72.44.83.62 secretariat.ediss@univ-lyon1.fr	**Mme Sylvie RICARD-BLUM** Laboratoire ICBMS - UMR 5246 CNRS - Université Lyon 1 Bâtiment Raulin - 2ème étage Nord 43 Boulevard du 11 novembre 1918 69622 Villeurbanne Cedex Tél : +33(0)4 72 44 82 32 sylvie.ricard-blum@univ-lyon1.fr
ED 34 EDML	**MATÉRIAUX DE LYON** http://ed34.universite-lyon.fr Sec. : Yann DE ORDENANA Tél : 04.72.18.62.44 yann.de-ordenana@ec-lyon.fr	**M. Stéphane BENAYOUN** Ecole Centrale de Lyon Laboratoire LTDS 36 avenue Guy de Collongue 69134 Ecully CEDEX Tél : 04.72.18.64.37 stephane.benayoun@ec-lyon.fr
ED 160 EEA	**ÉLECTRONIQUE, ÉLECTROTECHNIQUE, AUTOMATIQUE** https://edeea.universite-lyon.fr Sec. : Philomène TRECOURT Bâtiment Direction INSA Lyon Tél : 04.72.43.71.70 secretariat.edeea@insa-lyon.fr	**M. Philippe DELACHARTRE** INSA LYON Laboratoire CREATIS Bâtiment Blaise Pascal, 7 avenue Jean Capelle 69621 Villeurbanne CEDEX Tél : 04.72.43.88.63 philippe.delachartre@insa-lyon.fr
ED 512 INFOMATHS	**INFORMATIQUE ET MATHÉMATIQUES** http://edinfomaths.universite-lyon.fr Sec. : Renée EL MELHEM Bât. Blaise PASCAL, 3e étage Tél : 04.72.43.80.46 infomaths@univ-lyon1.fr	**M. Hamamache KHEDDOUCI** Université Claude Bernard Lyon 1 Bât. Nautibus 43, Boulevard du 11 novembre 1918 69 622 Villeurbanne Cedex France Tél : 04.72.44.83.69 direction.infomaths@listes.univ-lyon1.fr
ED 162 MEGA	**MÉCANIQUE, ÉNERGÉTIQUE, GÉNIE CIVIL, ACOUSTIQUE** http://edmega.universite-lyon.fr Sec. : Philomène TRECOURT Tél : 04.72.43.71.70 Bâtiment Direction INSA Lyon mega@insa-lyon.fr	**M. Jocelyn BONJOUR** INSA Lyon Laboratoire CETHIL Bâtiment Sadi-Carnot 9, rue de la Physique 69621 Villeurbanne CEDEX jocelyn.bonjour@insa-lyon.fr
ED 483 ScSo	**ScSo**[1] https://edsciencessociales.universite-lyon.fr Sec. : Mélina FAVETON Tél : 04.78.69.77.79 melina.faveton@univ-lyon2.fr	**M. Bruno MILLY** (INSA : J.Y. TOUSSAINT) Univ. Lyon 2 Campus Berges du Rhône 18, quai Claude Bernard 69365 LYON CEDEX 07 Bureau BEL 319 bruno.milly@univ-lyon2.fr

[1] ScSo : Histoire, Géographie, Aménagement, Urbanisme, Archéologie, Science politique, Sociologie, Anthropologie

Thèse accessible à l'adresse : https://theses.insa-lyon.fr/publication/2023ISAL0114/these.pdf © [L. Diatezo], [2023], INSA Lyon, tous droits réservés

INSTITUT NATIONAL DES SCIENCES APPLIQUÉES LYON

Département de la Formation par la Recherche et des Études Doctorales (**FEDORA**)

Bâtiment INSA direction, 1er étage
37, av. J. Capelle
69621 Villeurbanne Cédex
fedora@insa-lyon.fr

Référence : TH1054_DIATTEZO Léopold

L'INSA Lyon a mis en place une procédure de contrôle systématique via un outil de détection de similitudes (logiciel Compilatio). Après le dépôt du manuscrit de thèse, celui-ci est analysé par l'outil. Pour tout taux de similarité supérieur à 10%, le manuscrit est vérifié par l'équipe de FEDORA. Il s'agit notamment d'exclure les auto-citations, à condition qu'elles soient correctement référencées avec citation expresse dans le manuscrit.

Par ce document, il est attesté que ce manuscrit, dans la forme communiquée par la personne doctorante à l'INSA Lyon, satisfait aux exigences de l'Etablissement concernant le taux maximal de similitude admissible.

INSA LYON
Campus LyonTech La Doua
20, avenue Albert Einstein - 69621 Villeurbanne cedex - France
Tél. +33 (0)4 72 43 83 83 - Fax +33 (0)4 72 43 85 00
www.insa-lyon.fr

membre de UNIVERSITÉ DE LYON

Thèse accessible à l'adresse : https://theses.insa-lyon.fr/publication/2023ISAL0114/these.pdf © [L. Diatezo], [2023], INSA Lyon, tous droits réservés

Acknowledgements

This thesis is the result of three years' research at the Laboratoire de Génie Électrique et Ferroélectricité, Institut National des Sciences Appliquées, Lyon, in collaboration with TESCA-Group, Spain. I would like to express my deep gratitude to all the people who provided their support and help, without whom this thesis would not have been possible.

First of all, I would like to express my deep admiration and gratitude to my supervisor, Dr. Pierre-Jean COTTINET, my thesis director, for his immense support and exceptional contributions to this research. He placed his trust in me and provided me with invaluable new knowledge. His kindness, commitment, rigor, patience, invaluable advice, and constructive criticism have been invaluable throughout this thesis. Exchanges with him have been constant learning experiences, offering a fresh perspective on my results. I am sincerely grateful to him for all the validation and encouragement he gave me, which eased my anxiety and motivated me to take new steps.

Secondly, I would like to express my deep gratitude to Dr. Jean-Fabien CAPSAL, my thesis co-director, for his constant availability. Thanks to him, I have had the opportunity to acquire new scientific skills and knowledge that will prove invaluable for the realization of my future projects. His human qualities make him an outstanding example of personality.

Thirdly, I would like to express my deepest gratitude to my Co-supervisor, Dr. Minh Quyen LE, whose availability has always been invaluable when I needed assistance. She guided me with infinite patience through learning experimental methodology, data analysis, presentation, and scientific writing, thus contributing to my formation as a qualified researcher. My warmest thanks to her for the invaluable advice she has given me, whether in technical, scientific, professional, or personal matters.

Fourthly, I would like to express my gratitude to the engineers at Tesca, as well as to the manager Mr. Lluis PUIG, Albert Serra and Mrs. Christine TONELLATO, for their invaluable help, generosity and availability throughout this thesis.

In addition to my supervisors, I would like to express my gratitude to the other members of the jury: Pr. GUIFFARD Benoit, Pr. BELHORA Fouad, Pr. DEMOLY Frédéric, Pr. CONSONNI Vincent, and Dr. KANDA Masea, for their detailed reviews, insightful comments, and presence at my defense.

I would like to express my sincere gratitude to the staff and colleagues at the LGEF laboratory. In particular, I would like to thank Dr. Laurence SEVEYRAT, an experienced technical engineer, for her teaching of the introductory chemical room course and her helpful guidance on the SEM. I am also grateful to Mme. Véronique Perrin, a trusted electronics engineer, for her invaluable support in the polarization process. My thanks also go to Mr. Frédéric DEFROMERIE, a skilled technician at LGEF, for his essential contribution to mask and connector fabrication. Finally, I would like to express my special gratitude to Mrs. Evelyne Dorieux for her invaluable help in managing the complex administrative aspects.

I would like to express my gratitude to my colleagues and friends, who have helped to create a multicultural atmosphere at the office, full of smiles, rather than just a place to work. I would especially like to thank Mr. Van-Cuong NGUYEN for his invaluable support throughout my doctoral training, Giulia D'Ambrogio for her invaluable help in fabricating the composite material, and Mr. Amaury Fimbel for his expertise in metallization. Many thanks to Dr. Kritsadi Thetpraphi for her reliability and excellence as a senior, always ready to help me, especially in the field of 3D printing and fabricating electroluminescent composite. I would also like to express my gratitude to Mr. Omar Zahaf for his invaluable assistance in high-voltage characterization. Finally, I am deeply grateful for the unforgettable and precious moments spent with all the other people in the LGEF laboratory.

Finally, I would like to express my deepest gratitude to my family for their unconditional love and care. Thank you so much for always being by my side.

Thèse accessible à l'adresse : https://theses.insa-lyon.fr/publication/2023ISAL0114/these.pdf © [L. Diatezo], [2023], INSA Lyon, tous droits réservés

Résumé

Les matériaux multifonctionnels jouent un rôle crucial dans le développement des matériaux intelligents. En effet, le progrès des matériaux définis comme multifonctionnels, sera probablement le principal moteur de cette évolution technologique. Il s'agit de concevoir, optimiser, développer et d'intégrer des fonctions pour rendre les produits plus intelligents, ainsi que d'améliorer leurs processus de fabrication additive. Ces matériaux sont utilisés comme composants fonctionnels dans diverses applications, notamment dans le domaine de la santé, de la défense, de l'automobile et de la sécurité au travail. Par exemple, ils sont utilisés dans des systèmes de localisation intégrés, le suivi des conditions physiologiques des travailleurs, des systèmes de chauffants et de refroidissant intégrés, des dispositifs de communication, la captation d'énergie, etc.

Les matériaux composites conducteurs et composites électroluminescents ont suscité un grand intérêt de recherche en raison de leur potentiel pour améliorer les performances de matériaux multifonctionnels. Ces composites se forment en incorporant des particules conductrices (pour les encres conductrice) ou des particules phosphorescentes (pour les composite électroluminescents) dans une matrice polymère, ce qui donne des propriétés d'électrique et optique améliorées. Grâce aux avancées de la fabrication additive, ces deux types de matériaux peuvent être imprimés par sérigraphie dans des géométries complexes et intégrés dans des substrats textiles pour créer des structures intelligentes. Cette combinaison de matériaux multifonctionnels et de la technologie d'impression par sérigraphie a permis le développement de divers dispositifs personnalisables et rapides à fabriquer, tels que des nappes chauffantes, des capteurs photo-capacitifs.

Les travaux de thèse se sont focalisés sur deux applications principales. La première consiste en la création d'une application thermique en utilisant le chauffage par effet Joule de ces matériaux conducteurs. L'objectif était de concevoir une nouvelle génération de tissus intelligents destinés aux sièges de voitures, avec des applications spécifiques dans le domaine automobile. La seconde application concerne l'utilisation de matériaux composites phosphorescents, qui jouent un rôle central dans le fonctionnement des capteurs photo-capacitifs ou électroluminescents. Des études préliminaires ont été menées sur les caractéristiques électriques de ces matériaux afin d'optimiser leurs propriétés, de les rendre compatibles avec la technique d'impression par sérigraphie, et de mieux comprendre leurs limites et règles d'intégration.

Première application porte sur la création d'une nappe chauffante destinée aux sièges de véhicules. Ce dispositif de chauffage est composé de deux électrodes principales en cuivre, communément appelées "bus d'alimentation", ainsi que de trois résistances chauffantes identiques en composites de carbone. Les connexions entre les bus d'alimentation en cuivre et les résistances en carbone sont réalisées sous forme d'électrodes subdivisées, jouant un rôle essentiel dans l'assurance du couplage électrique-thermique. Des modèles basés sur la méthode des éléments finis (FEM) ont été développés pour prédire comment ces sous-ensembles se comportent en termes de conversion par effet joule, en tenant compte de différentes configurations de motifs. Il est souligné que la conception la plus optimisée permet de résoudre les problèmes inhérents à la conception initiale, notamment en ce qui concerne la régularité de la température et d'effet de surchauffe. Une analyse complète des propriétés électriques et thermiques, ainsi que des études morphologiques à l'aide d'images (SEM), a été réalisée sur différents échantillons revêtus d'encre conducteur. Cela a permis d'identifier les paramètres physiques pertinents des matériaux et de confirmer la qualité de l'impression par sérigraphie. Une combinaison de méthode des Éléments Finis (FEM) et d'évaluation expérimentale a révélé que les motifs de revêtement imprimés jouent un rôle crucial dans la conversion d'énergie et les performances de chauffage. Les architectures proposées et implémentées ont satisfait aux normes exigées par l'industrie automobile. Par conséquent, l'utilisation de matériaux multifonctionnels associés à la technologie d'impression pourrait offrir une méthode de chauffage très efficace pour les textiles intelligents, avec un niveau de confort nettement amélioré, tant pour les concepteurs et les utilisateurs.

Thèse accessible à l'adresse : https://theses.insa-lyon.fr/publication/2023ISAL0114/these.pdf © [L. Diatezo], [2023], INSA Lyon, tous droits réservés

Pour pousser plus loin la compréhension et limites technologiques des encres développées, une étude de vieillissement a été entreprise en lien avec les contraintes applicatives (cyclage mécanique, thermique en en humidité). Les travaux de corrélation structure propriétés ont permis de mettre en avant une limite technologique dans la formulation des encres. Pour répondre à ce point de blocage, des travaux de formulations sur de nouvelles matrices avec de meilleurs stabilités en raison de leurs propriétés physico-chimiques et aussi en modifiant les charges conductrices. Les travaux ont ainsi débouché sur la formulation d'une encre pouvant tenir les contraintes applicatives.

La deuxième application implique la création d'un dispositif électroluminescent en utilisant un matériau composite électroluminescent. L'objectif est d'identifier les paramètres clés à optimiser. Nous avons réalisé des simulations à l'aide de la méthode des éléments finis (FEM) pour déterminer le meilleur couplage entre les particules de phosphore et la matrice polymère. Nous avons également examiné l'impact des permittivités des particules, de la matrice du matériau et des dimensions du design. Pour mener à bien cette étude, nous avons sélectionné trois types de particules de phosphore en raison de leurs propriétés électrique et optique distinctes, ainsi que différents types de matrices polymères aux caractéristiques variées. Une analyse a été effectuée sur l'influence des particules de phosphore et des matériaux diélectriques en termes de permittivité et de proportion idéales dans la fabrication de composite électroluminescence, ainsi que leur luminosité. Les résultats obtenus montrent l'importance d'ajuster les permittivités des particules de phosphore et de la matrice polymère. En conséquence, nous avons pu établir des proportions optimales de phosphore et de diélectrique pour obtenir une émission lumineuse améliorée.

Mots clés: revêtements électroniques imprimés ; textiles chauffants intelligents ; simulation par éléments finis ; optimisation conception ; caractérisations thermiques et électriques ; composites électroluminescent ; particules phosphorescentes, matrix diélectrique ; applications automobiles.

Thèse accessible à l'adresse : https://theses.insa-lyon.fr/publication/2023ISAL0114/these.pdf © [L. Diatezo], [2023], INSA Lyon, tous droits réservés

Abstract

Multifunctional materials play a crucial role in the development of smart materials. Indeed, progress in materials defined as multifunctional is likely to be the main driver of this technological evolution. The aim is to design, optimize, develop and integrate functions to make products more intelligent, as well as to improve their additive manufacturing (AM) processes. These materials are used as functional components in a variety of applications, including healthcare, defense, automotive and occupational safety. For example, they are used in integrated localization systems, monitoring of workers' physiological conditions, integrated heating and cooling systems, communication devices, energy capture, etc.

Conductive composites and electroluminescent composites have attracted a great deal of research interest due to their potential for enhancing the performance of multifunctional materials. These composites are formed by incorporating conductive particles (for conductive inks) or phosphorescent particles (for electroluminescent composites) into adequate polymer matrix, resulting in enhanced mechanical, electrical and optical properties. Thanks to advances in AM, both types of material can be screen-printed in complex geometries and integrated into textile substrates to create intelligent structures. This combination of multifunctional materials and screen-printing technology has enabled the development of a variety of customizable, fast-to-fabricate devices, such as heating tablecloths, photo-capacitive sensors, actuators and feedback systems.

The first objective of the thesis involves the creation of a heating tablecloth based on the Joule heating effect of these conductive materials. The aim was to design a new generation of smart fabrics for car seats, with specific applications in the automotive field. Preliminary studies have been carried out on the electrical characteristics of these materials in order to optimize their properties, make them compatible with the screen-printing technique, and better understand their limits. The developed heating device consists of two main copper electrodes, and three identical heating resistors made of carbon composites. The connections between the copper supply and the carbon resistors are made in the form of subdivided electrodes, playing an essential role in ensuring good performance of electrical-thermal coupling. Finite element method (FEM) has been developed to predict how the fabric substrate are heated by the carbon resistors, for each pattern configurations of the copper electrodes. It is emphasized that the most optimized design solves the problems inherent in the initial design, particularly with regard to temperature regularity and overheating effects. A comprehensive analysis of electrical and thermal properties, as well as morphological studies using SEM (scanning electron microscope) images of the conductive coatings has been carried out via practical characterizations. Relevant physical parameters of the materials are identified and the quality of screen printing for different composite inks are assessed. A combination of FEM and experimental evaluation revealed that printed coating patterns play a crucial role in energy conversion and heating performance. Our first prototype, thanks to significant optimization in the electrode patterns, fully meets the standards demanded by the automotive industry. Consequently, the use of multifunctional materials combined with printing technology could offer a highly efficient heating method for smart textiles, with a significantly improved level of comfort for both designers and users.

In order to create conductive materials more resistant to the aging effect in the long run, this study also investigated on a new formulation of the copper composite inks that are combined with different types of polymer binder. The ultimate reliability of the cooper electrodes is assumed to be limited by their electrical property that are evaluated under accelerated thermal cycling, mechanical solicitation, and moisture procedure. Experimental tests together with morphological analyses confirm a degradation in the electrical conductivity of the copper electrodes after a severe humidity/temperature procedure, which favors an apparition of the oxidation, or even corrosion of the copper. To overcome such issues, two protective layers are considered. The first one deposited on the textile substrate to reduce its porosity and improve the homogeneity of the conductive ink, limiting the ageing effect under humidity. The second one is applied to the electrode surface to protect it from damage caused by rust, oxidation, or corrosion. Eventually, we have

Thèse accessible à l'adresse : https://theses.insa-lyon.fr/publication/2023ISAL0114/these.pdf © [L. Diatezo], [2023], INSA Lyon, tous droits réservés

successfully solved the problems associated with ageing and corrosion of the composite coatings, making them more resistant during application.

Another objective of the thesis concerns the use of phosphorescent composite material, which plays a key role in the creation of light emitting. This function could be easily integrated into a car seat for a specific purpose. When such a material is subjected to an alternating current field, it can emit visible radiation whose intensity is a function of the applied voltage as well as the frequency. Numerical solution-based FEM models together with experimental characterizations are carried out to determine adequate combinations between the phosphor particles and the polymer matrix that leads to satisfactory luminance (or brightness). It is pointed out that the dielectric constant of both matrix and particle phases, which strongly affects the electric field internally attributed to the phosphor particles, clearly determines the light intensity of the electroluminescent (EL) device. The simulation results confirm that the P(VDF-TrFE-CFE) terpolymer matrix with its high dielectric constant, when combined with the copper-doped zinc sulfide (ZnS:Cu) microparticles, leads to improved concentration of the electric field applied on the phosphorus particles. As a matter of fact, these materials allow for the formation of a composite with the most appropriate EL response as opposed to the other tested samples. Also, an optimal proportion of the phosphor particles is also of primary importance to achieve enhanced light emission. Finally, empirical results enable to validate the reliability of the proposed approach, paving the way for a new generation of multifunctional materials in the application of smart textiles.

Keywords: printed electronic coatings; smart heating textiles; finite element simulation; design optimization; thermal and electrical characterizations; electroluminescent composites; phosphorescent particles, dielectric matrix; automotive applications.

Thèse accessible à l'adresse : https://theses.insa-lyon.fr/publication/2023ISAL0114/these.pdf © [L. Diatezo], [2023], INSA Lyon, tous droits réservés

Acronyms

%vol.	Volume fraction
3D	three-dimensional
AC	Alternating current
MOD	Metal -organic decomposition
ITO	Indium tin oxide
AgNP	Silver nanoparticles
SWCNT	Single-walled carbon nanotubes
LEDs	Electroluminescent devices
ACEL	Alternating current electroluminescent device
ZnS: Cu	Zinc sulfide doped with copper, aluminum, and manganese
FEM	Finite element method
SEM	Scanning electron microscopy
EDS	Energy dispersive X-ray spectroscopy
DC	Direct current
C	Capacitance
AM	Additive manufacturing
PU-AR	Archroma polyurethane binder
AC-AR	Archroma acrylic binder
AC-Rud	Archroma acrylic Rudolf binder
RH	Relative humidity
PDMS	Polydimethylsiloxane
CAD	Computer Aided Design
ESD	Electrostatic discharge
PMMA	Poly (methyl methacrylate)
PVDF	Polyvinylidene fluoride
UV	Ultraviolet
TPU	Thermoplastic polyurethane
PET	Polyethylene terephthalate
EL	Electroluminescent
SSA	Specific surface area
T_g	Glass transition temperature
WD	Working distance
Cu	Copper ink
Ag	Silver ink

Thèse accessible à l'adresse : https://theses.insa-lyon.fr/publication/2023ISAL0114/these.pdf © [L. Diatezo], [2023], INSA Lyon, tous droits réservés

General introduction

Textiles have been an integral part of our consumption patterns for thousands of years. They were primarily used as clothing for protection, but their use has gradually evolved with the arrival of sensors, actuators and aesthetic functions, broadening their role and taking on a considerable role in human daily life. The incorporation of multifunctional values into textile design dates back to the end of the 19th century and has become an important area of interest in recent years. The development of intelligent textiles really began in the mid-80s with the invention of wearable computers and machines for incorporating optical fibers into textiles. Intelligent textiles are structures capable of detecting, reacting and adapting to a wide range of stimuli: electrical, magnetic, thermal, optical, acoustic, mechanical, chemical and many others. Fabrics, fibers, yarns, conductive inks, and many other materials with additional functionalities have been developed for a wide range of applications. By way of example, one of the first uses of intelligent textiles in protection dates back to 1968, when New York's Museum of Contemporary Art exhibited a spacesuit that could inflate/deflate, light up and heat/cool itself. Indeed, the first commercial applications of smart textiles appeared in the 2000s, in particular for monitoring vital signs.

Multifunctional materials used in the manufacture of intelligent textiles and soft materials include polymer matrices and many others. Due to their light weight and mechanical flexibility, they are promising candidates for the creation of smart textile structures. However, polymers have inherently low thermal conductivity, which limits their practical use in applications such as heating and cooling elements in textiles. To remedy this problem, numerous studies have explored coatings of additives with high thermal conductivity, such as silver (Ag), copper (Cu), carbon nanotubes, aluminum (Al), graphite (GR) and graphene oxide. This incorporation has made it possible to create thermal conduction pathways, thus improving heat diffusion in composites. Such a technique remains crucial, as the combination of multifunctional materials, manufacturing strategies and optimized designs has revolutionized the field of smart garment systems in the future. Manufacturing methods are varied, using different textile technologies such as weaving, knitting, embroidery, etc., as well as other techniques such as microcapsule incorporations, the use of composites, surface deposition, which enables the integration and combination of electronic and photonic devices, etc. Indeed, the combination of conductive materials, such as composite inks containing copper, carbon and textiles, in conjunction with various techniques, is frequently used to manufacture multifunctional structures.

Despite the interesting application potential of intelligent textiles, the textile market remains confined to niche applications. Indeed, the current technological bottleneck concerns the lack of maturity of the various technology bricks linked to smart textiles, and the resulting difficulties. For instance, current systems for measuring vital signs have weaknesses in terms of durability (perspiration, washing, wear and tear, etc.) and lack robustness. In fact, research has shown how conductive wires made from metal-coated polymeric filaments can break under mechanical stress during manufacture [8]. Today, advances in the field of intelligent textiles are facilitating the incorporation of functionalities directly into surface structures. This field of research is closely linked to the process of direct printing on a variety of substrates (rigid or flexible), through the combined use of conventional printing processes (screen printing, inkjet, flexography, etc.) and one or more functional inks (conductive, dielectric, etc.). The main advantages of this approach are: the ability to print on flexible substrates, the promise of high levels of efficiency thanks to the large production areas addressed by printing processes, an additive approach that limits manufacturing steps and production costs, and the integration of new, innovative materials thanks to the formulation of functional inks.

Printed electronics can be found in many fields, including biomedical, energy, energy, display, metrology etc. To connect these various components, or simply to power them, it is essential to carry an electric current via the production of high-performance conductive tracks. In the near future, additive manufacturing (AM) of multifunctional materials and its advances will be increasingly used to realize hybrid mechatronic functions that merge mechanical structure, electronic components, conductive tracks, and

Thèse accessible à l'adresse : https://theses.insa-lyon.fr/publication/2023ISAL0114/these.pdf © [L. Diatezo], [2023], INSA Lyon, tous droits réservés

functional materials. Indeed, these materials are capable of converting or adapting to physical stimuli and are gradually demonstrating their potential for technological innovation in various application sectors. In addition to the potential replacement of traditional transduction processes (sensors and actuators) in certain cases, the new possibilities offered by these materials in terms of performance and multiphysics-coupling functionalities are a compelling motivation to tackle and resolve challenges arising from societal and technical issues.

Indeed, functional materials, which feature multiphysic couplings, are a vast and heterogeneous field positioned between concepts, materials, and industrial application markets. And yet, this sector is fueling developments and innovations in the world around us, whether in transport, medicine, energy, or the environment. Because of its "in-between" position, the functionalization of materials needs to innovate strongly if it is to continue to support its application sectors, which are currently undergoing radical change. This race to innovate is also a sine qua non for staying ahead in a sector where international competition is fierce. This theme has undeniable scientific strengths, with the development of the printing theme and the exploitation of numerous multiphysics couplings that will enable us to support the breakthroughs and mutations of these application sectors. Materials with new multifunctional properties are of particular importance for the future competitiveness and sustainable development of industry. Today, they form the basis for technical progress in many sectors of activity.

These multifunctional materials are clearly an example of "upstream" solutions that can meet the new demands and changes of downstream industries, such as lightening for transport, reducing energy consumption or diagnosing sensitive structures. The development of these materials is largely determined by demand, and therefore by new applications and markets. Our thesis focuses on the development and optimization of multifunctional printable materials, with particular emphasis on the balance between material characteristics and the specific requirements of their use. The idea behind this thesis stems from an integrated approach between multifunctional materials and their integration into textiles using screen-printing technology. Indeed, TESCA's ambition is to create its own intelligent textiles by integrating multifunctional materials into its products in order to add new functionalities such as heating mats, sensors for mechanical quantities, light emitting, and many others, while remaining competitive on the market. As part of the ultimate collaboration between LGEF and TESCA, the aim of this thesis involves the optimization design of the printed coatings based on flexible conductive inks and electroluminescent composite, which adapted to the specific needs of automobile sectors. The report is divided into five main chapters.

Chapter 1 reports on the current existing development of multifunctional materials, with a particular focus on printed electronics for the design of smart textiles. Within this framework, we start with the definition of these concepts, then the applications are realized using various conductive materials such as fibers, metallic wires and conductive inks. The chapter then explores the evolution of printed electronics and the multifunctional materials associated with it. Finally, potential applications of the printed composite inks in the field of structural condition monitoring are drawn at the end of this chapter.

Chapter 2 presents two main aspects: the electrical and thermal properties of conductive inks made of carbon and copper composites, as well as the heating behavior-based Joule effect of the fabrics commonly integrated in car seats. Another aspect involves the development of electroluminescent (EL) composites that are elaborated with metal-doped zinc sulfide (ZnS) particles randomly dispersed in different polymer matrices. Detailed descriptions of the experimental set-ups used to characterize the properties of these materials are then carried out. To verify the durability and stability of the coated fabrics with respect to the environmental changes, several aging tests relied on industrial protocols were performed. These tests must be consistent with the functional characteristics at the various phases of the product's life cycle. Finally, a full description of the finite element method (FEM) built for the conductive and EL composite models is investigated.

Thèse accessible à l'adresse : https://theses.insa-lyon.fr/publication/2023ISAL0114/these.pdf © [L. Diatezo], [2023], INSA Lyon, tous droits réservés

Chapter 3 reports on the design optimization of the screen-printed composite coatings, as well as the assessment on their morphological, electrical and thermal properties. The initial prototype of the printed heating structure was first developed in response to the needs of the automotive industry (Tesca Group) so as to validate the efficiency of the thermal heating system. Next, results and discussions regarding the device performance are carried out on different patterns of the copper electrodes, demonstrating that optimization of such designs is of primary importance to fulfil the specifications defined by Tesca. Indeed, the new design should lead to a homogenous temperature on the whole surface of the fabric, with a range from 40 °C to 43.5 °C. Also, hot spots must be limited at 45 °C and avoided at all costs to minimize the degradation of materials and to improve the comfort of users. Finally, numerical simulations together with empirical measurements are conducted to better understand the Joule heating mechanism of the composite coatings in both transient and steady state conditions. To highlight the new perspectives of the research, the most optimized prototype figured out in this study is compared to the REF.22 design previously developed by Tesca. Prior to this thesis, the REF.22 design was considered as the most efficient solution used by the company to heat car seats.

Chapter 4 focuses on the development of electroluminescent (EL) devices which can be integrated into car seats for light emission. The main purpose of this study is to find out, among several types of EL particles and polymer matrix, those that lead to a fabrication of composite with high EL performance. In order to obtain such a device with easy process, low energy consumption, and effective cost, a simple design involving in a single-layered architecture is carried out. The EL composites are manufactured by dispersing ZnS-based phosphor particles into the polymer matrix, then depositing a single 50 µm-thick layer of composites (matrix/phosphorus) directly onto a glass slide coated with ITO (indium tin oxide) or onto a textile substrate covered with copper composite ink. These layers are placed between two secondary conductive gold electrodes, obtained by sputtering, or the transparent PEDOT electrode (screen-printed PSS). The homogeneity of particle distribution in the polymer matrix, as well as the structure of composites made with different volume fractions of metal doped ZnS are confirmed by microscopic analysis (SEM).

The electrical behavior of the EL composites are obtained through the polarization loop composed of current density versus electric field (J-E) characteristic. This characteristic depends on several key factors such as filler concentration, frequency and magnitude of the field excitation, and the ultimate electrical properties of both matrix and particles. Based on the analyses, several key parameters of these materials (i.e., electric conductivity, dielectric constant) are figured out, leading to a better understanding on the EL response that is supposed to be dependent on the matrix-particles combinations. To assesses and compared the EL performance of those composites, we opted for a mini-spectrometer capable of measuring the intensity of the emitted light driven from the samples, which is an image of the brightness or luminance. Experimental results confirm that the P(VDF-TrFE-CFE) terpolymer matrix, when combined with the copper-doped zinc sulfide (ZnS:Cu) microparticles, leads to the highest brightness of the emitted light (high luminance value as well) compared to the other tested samples. To some extent, this behavior is corelate to the model predictions developed through FEM using COMSOL Multiphysics. Based on the simulation results, it is pointed out that the dielectric constant of both matrix and particle phases, which strongly affects the electric field internally attributed to the phosphor particles, clearly determines the light intensity of the electroluminescent (EL) device.

Chapter 5 is devoted to exploring a new formulation of copper-based composite inks, designed to guarantee their stability with respect to critical changes in the surrounding environment. The aim is to analyze different polymer binders that are combined with the copper powder to create composites with improved electrical conductivity, somehow stable after three accelerated aging procedures including:

- thermal cycles of 24 hours and 48 hours at 100 °C;
- hygrothermal cycles of 12 days at 85°C with a humidity of 85% RH/-40°C;
- mechanical endurance tests in line with the European SAE standard.

Thèse accessible à l'adresse : https://theses.insa-lyon.fr/publication/2023ISAL0114/these.pdf © [L. Diatezo], [2023], INSA Lyon, tous droits réservés

It has been pointed out that oxidation or even corrosion of the copper electrodes occurred after the aggressive hygrothermal tests, i.e., contrary to the carbon coating which remined stable. Thanks to the new ink formulation as well as integration of two protection-based polymer as anti-corrosion coating layers (one for the substrate while the other for the copper electrode), it is possible to overcome the problems of oxidation and corrosion resulting from humidity. The results obtained are very encouraging from a practical point of view, where the electrical conductivity of the optimized coating is revealed to be satisfied the specifications (i.e., beyond the limited threshold value). In conclusion, we have succeeded in improving the electrical properties of conductive inks, making them more resistant during application.

Thèse accessible à l'adresse : https://theses.insa-lyon.fr/publication/2023ISAL0114/these.pdf © [L. Diatezo], [2023], INSA Lyon, tous droits réservés

Table of Contents

CHAPTER 1 PRINTED ELECTRONICS FOR SMART TEXTILE: STATE OF THE ART . 18

1.1 Background on smart textiles 19

1.1.1 Basic definition of smart textile 19

1.1.2 Classification of smart textile 20

1.2 Potential applications of smart textiles 22

1.2.1 Temperature controlled textiles 22

1.2.2 Electronic information 25

1.3 Printed electronic materials 28

1.3.1 Metal nanoparticle ink 28

1.3.2 Metal-oxide nanoparticle ink 28

1.3.3 Molecular ink 29

1.3.4 UV-curable ink 29

1.4 Printing Technologies 29

1.4.1 Contact-printing techniques 31

1.4.2 Non-contact printing techniques 33

1.5 Potential applications of printed composite inks 35

1.5.1 Piezoresistive ink 36

1.5.2 Capacitive ink 36

1.5.3 Piezoelectric ink 37

1.5.4 Electroluminescent (EL) ink 38

1.5.5 Resistive heating-element ink 39

1.6 Summary 40

CHAPTER 2 MATERIALS – PROCESS AND CHARACTERIZATIONS 41

2.1 Materials' selection and composites' elaboration 42

2.1.1 Conductive coatings 42

2.1.2 Electroluminescent composite (EL) 44

2.2 Additive manufacturing (AM) based screen-printing technique 47

2.2.1 Conductive coating 47

2.2.2 Electroluminescent (EL) composites 49

Thèse accessible à l'adresse : https://theses.insa-lyon.fr/publication/2023ISAL0114/these.pdf © [L. Diatezo], [2023], INSA Lyon, tous droits réservés

2.3 Characterization methods based experimental measurements 49
2.3.1 Morphology characterization 50
2.3.2 Profilometry characterization 50
2.3.3 Electrical characterization of conductive inks 51
2.3.4 Thermal characterization of conductive inks 52
2.3.5 Heatmap characterization of conductive inks 54
2.3.6 Aging characterizations of conductive inks 55
2.3.7 Dielectric characterization of EL composites 56
2.3.8 Luminance characterization of EL composites 57
2.4 Characterization methods based finite element model (FEM) 59
2.4.1 Model of heating fabric 59
2.4.2 Model of electroluminescent composites 60
2.5 Summary 61
CHAPTER 3 FLEXIBLE CONDUCTIVE COATING FOR HEATING TEXTILE : FROM MATERIALS CHARACTERIZATIONS TO DESIGN OPTIMIZATIONS 62
3.1 Materials' characteristics 63
3.1.1 Morphology analysis 63
3.1.2 Profilometry analysis 64
3.1.3 Thermal analysis 66
3.1.4 Electrical analysis 67
3.2 Specifications and design rules 69
3.3 Design optimization based on FEM 71
3.3.1 Simulation Model Built in COMSOL 71
3.3.2 Heating behavior in a steady regime 72
3.3.3 A first-order response in a transient regime 78
3.4 Heatmap analysis 79
3.5 Summary 82
CHAPTER 4 OPTIMIZATION OF ELECTROLUMINESCENT COUPLING USING PHOSPHORUS COMPOSITE COATED WITH FLEXIBLE ELECTRODES 83
4.1 Comprehension of the electroluminescent (EL) device 84
4.1.1 EL phenomenon 84
4.1.2 Configuration of EL device 84

Thèse accessible à l'adresse : https://theses.insa-lyon.fr/publication/2023ISAL0114/these.pdf © [L. Diatezo], [2023], INSA Lyon, tous droits réservés

4.2 Morphological analyses of EL composites 87

4.3 Electrical behavior of EL materials 90

4.3.1 Doped phosphor composites with different polymer matrices 90

4.3.2 Compact blocks of doped-phosphor particles 92

4.4 Optimization of EL based on adequate combinations of particle and matrix 93

4.4.1 Influence of EL particles 93

4.4.2 Influence of polymer matrix 96

4.4.3 Comparison with simulation-based FEM 98

4.5 Integration of EL devices on a textile substrate 100

4.5.1 Dielectric property of polymer binders 100

4.5.2 Morphological analyses of polymer binders 102

4.5.3 Preliminary prototype of EL device coated on textile substrate 103

4.6 Summary 103

CHAPTER 5 AGING TESTS OF CONDUCTIVE COATING: TOWARDS A DEVELOPMENT OF HIGH-PERFORMANCE FLEXIBLE ELECTRODES 105

5.1 Aging effect with non-optimized configurations 106

5.1.1 Stability tests on heating tablecloth 106

5.1.2 Morphology characterization 109

5.1.3 Material's aging after stability tests 110

5.2 Aging effect with optimized materials 112

5.2.1 Material selection 112

5.2.2 Stability tests on a sample unit 113

5.2.3 Corrosion effect-based morphology characterization 117

5.3 Aging effect with optimized designs 119

5.3.1 Solution based on protective coatings 119

5.3.2 Stability tests on a sample unit 120

5.3.3 Stability tests on heating mats 124

5.4 Summary 127

Thèse accessible à l'adresse : https://theses.insa-lyon.fr/publication/2023ISAL0114/these.pdf © [L. Diatezo], [2023], INSA Lyon, tous droits réservés

Chapter 1 Printed electronics for smart textile: State of the art

The progress of materials qualified as multifunctional is probably the major drive of this evolution, where it is a question of exploring and integrating functions to make the products intelligent. Following the example of mechatronics combined of mechanical, computational, and electronic functions, smart fabrics have found their first applications in recent years by integrating multifunctional materials. In the context of this research, we particularly focus on the heating purpose of these materials, with the aim of developing a new generation of smart car-seat fabrics for automobile applications.

Printed electronics has been developing over a long period, providing innovative and complementary solutions to traditional electronics, particularly in the fields of lighting, photovoltaics, and electronic devices. For the manufacture of electronic components, printing processes from the graphics industry have been adapted to print functional inks, whether conductive, semiconductive, resistive or thermochromic. Therefore, 3D printed coating, which is expected to improve the conventional technique of heater fabric, is investigated in this research. Actually, standard car-seat heating technology relies on resistive elements carrying electrical current to generate heat. Though this process is quite effective, it needs bulky power cables that must be covered in insulating foam to stop the seat from becoming unpleasantly hot, and it can take an annoyingly long time for seats to heat up. Printed electronic coatings promise to overcome these challenges and are starting to be used for heating car interiors. Since the printed elements only heat the surfaces that are in close proximity to the body, energy consumption is significantly reduced. In addition, compared to traditional seat heating systems, printed coatings are thinner and lighter, meaning less padding and foam is required, giving raise to considerably faster heat-up time. Furthermore, these heating elements can be printed on flexible materials such as textiles, making them easy to incorporate into car designs, thus improving sustainability.

The main aim of this chapter is to gain an in-depth understanding of the context in which conductive materials are being developed, with particular emphasis on printed electronics, to realize the various objectives of this research on smart textiles. Initially, we introduce the basic concepts concerning smart materials, the different types of smart textiles, and explain the directions of our research as well as the applications realized with different materials, such as fibers, metallic wires, and conductive inks. Next, the evolution of printed electronics together with various techniques employed for conductive materials are presented. Finally, we summarize several existing research dedicated to printed composites as well as their potential applications.

Thèse accessible à l'adresse : https://theses.insa-lyon.fr/publication/2023ISAL0114/these.pdf © [L. Diatezo], [2023], INSA Lyon, tous droits réservés

1.1 Background on smart textiles

Smart textiles are textile materials with the ability to detect, record or react adaptively to signals or stimuli. The technology behind these textiles goes back a long way, to nearly 1,000 years ago, when yarns woven from conductive materials were already being explored. For many centuries, craftsmen used fine metal threads, mainly gold and silver, to embroider around fabric threads [1,2]. These were dedicated to the outfits of society's high-ranking individuals and were a sign of wealth. However, the term "intelligent textile" only came into its own later, in the early 19th century. Since the introduction of the first electronic components, people have been seeking to combine clothing and electronics. Clearly, the components of the time were not yet capable of creating products that were both functional and aesthetically pleasing [3,4].

The first prototypes were worn by the women of the Electric Girl Company (a troupe of ballet dancers who used luminescent outfits in the late 19th century) [5]. They wore jewelry and dresses adorned with lights to entertain guests at social events. Smart textiles then remained in the shadows, waiting for technology to catch up with the concept. With recent technological advances and ever finer technologies, smart textiles are making a comeback. One exhibition featured astronauts' spacesuits, as well as garments that could inflate and deflate, light up, heat up and cool down [6–17]. The work of Diana Dew, a designer who has created a line of electronic fashions, stood out in particular in this collection, with electroluminescent evening dresses and belts capable of triggering alarm sirens [18,19].

1.1.1 Basic definition of smart textile

The concept of "intelligent materials" was first proposed in 1989 by Professor Toshiyoshi Takagi of Japan. He merged the principles of information science with the structure and function of existing materials [20,21]. Intelligent materials are those capable of detecting external stimuli such as temperature, pressure and light, among others [22], and responding manually or pre-programmed to changes in these conditions, performing appropriate actions [23]. The first civilizations built their development using natural resources such as wood, stone, leather, bone, horn, flax, and hemp, etc. Later, we witnessed the emergence of plastics, glass, metals and more. Today, we are entering the era of "multifunctional materials" that are capable of adjusting to their environment [24]. Broadly speaking, smart materials are new functional materials with seven characteristics: sensing, feedback, recognition and accumulation of information, response, self-diagnosis, self-repair and adaptability [25,26].

Intelligent textile materials go beyond the appearance and portability of ordinary textiles. As a matter of fact, they react to their environment by adjusting their performance, creating a new class of textile materials specially adapted to changing conditions [27]. They can be designed to offer functionalities such as temperature regulation, motion detection, health monitoring, information gathering, among others. These textiles can be made from conductive fibers or high-performance materials (e.g., conductive inks) to achieve enhanced functional properties. They can be found in a variety of fields, including.

- fashion: for the manufacture of health-monitoring and temperature-regulating garments);
- sport: to optimize athlete performance;
- medicine: for the creation of wearable medical devices;
- defense: to offer practical benefits and enhance textile performance [28].

Smart textile materials offer many advantages, such as flexibility, durability, lightness and ease of use, making them a popular choice for many applications [29,30]. They can act differently from an ordinary fabric and are above all capable of fulfilling particular specifications [31,32] by combining with glass, ceramics, conductive fibers, nanocomposites, conductive polymers, conductive metal or carbon inks, and electronic micro-components to produce lightweight hybrids with incredible properties [33]. Smart textiles are designed for a variety of applications, including heating, lighting, interactivity and more. The addition of sensors to textiles multiplies the possible uses of textile materials and makes it possible to imagine a world of novel products: sportswear capable of measuring heart rate, backpacks equipped with solar sensors that can recharge a smartphone, flexible textile-based display panels, tents that warm campers in cold

Thèse accessible à l'adresse : https://theses.insa-lyon.fr/publication/2023ISAL0114/these.pdf © [L. Diatezo], [2023], INSA Lyon, tous droits réservés

weather [31]. The future of smart textile development could include advances in biotechnology, nanotechnology and artificial intelligence to create more advanced and functional textiles [34–36]. In the following paragraph, we will classify the different smart textiles.

1.1.2 Classification of smart textile

1.1.2.1 Passive smart fabric textile

Passive smart textiles can only perceive changes or stimuli in the external environment, but cannot adjust to external changes [37]. This is the first generation of smart fabric textiles that have superior functionality to standard fabrics. However, it should be noted that passive materials include antibacterial textiles, anti-ultraviolet clothing, ceramic-coated and light-guiding fabrics, but are not considered part of smart fabric textiles in the strict sense and should instead be called functional textiles [37,38]. For example as shown in Figure 1.1, antistatic fabrics developed by companies such as Sophitex Ltd. are designed so that their electrostatic discharge (ESD) properties are not influenced by the environment to which they are exposed [39,40].

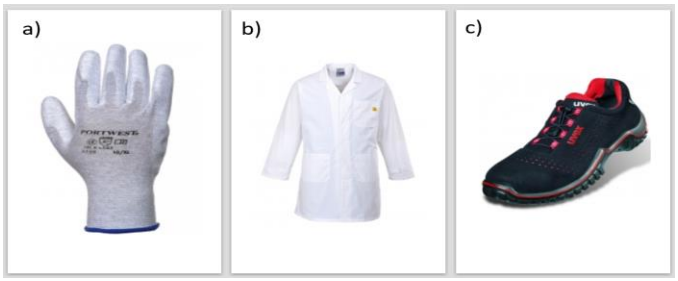

Figure 1.1. Passive smart textile :(a) Protective gloves, Antistatic ESD, (b) Smock Anti-static ESD White, and (c) Shoe safety UVEX S1P black-red-ESD antistatic [39].

1.1.2.2 Active smart fabric textile

Active smart textiles are capable of detecting variations in their external environment and reacting appropriately [41,42]. This is the second generation, comprising both actuators and sensors. The actuators act on the detected signal, either directly or from a central control unit. Active smart textiles are shape-memory, chameleon-like, water-resistant and those that are both vapor-tight (hydrophilic/non-porous) and breathable, heat-storing, thermoregulated, vapor-absorbing, heat-changing and electrically heated suits, as well as lightweight thermochromic textiles. In addition, intelligent textiles incorporating electronics are often referred to as e-textiles [28,43]. Figure 1.2 shows an example of an active smart textile.



Figure 1.2. Active smart textile materials [41].

Thèse accessible à l'adresse : https://theses.insa-lyon.fr/publication/2023ISAL0114/these.pdf © [L. Diatezo], [2023], INSA Lyon, tous droits réservés

1.1.2.3 Advance smart textile

Highly intelligent textiles represent the third generation of so-called smart textiles. They are capable of detecting, reacting and adapting to environmental conditions or external stimuli thanks to a self-regulating system. This system can be compared to that of the chameleon animal, which changes the color of its skin to blend into its environment, and the chameleon, whose nature is to adapt to blend into its environment, then react by changing the color of its skin, thus adapting to protect itself from predators [44,45].

A highly intelligent textile is essentially an entity that functions like the brain, with cognition, reasoning and activation capabilities. Thanks to the blending of traditional textile and fashion (clothing) technologies with other branches of science such as materials science, structural mechanics, sensor and actuator technology, advanced processing technologies, communication, artificial intelligence, biology, etc., the production of highly intelligent textiles is now a reality. These textiles are sensitive to their environment and are capable of automatically adjusting some of their functional parameters accordingly [46].

New conductive materials, such as metallic wires, conductive threads, polymer or nano-composite fibers, as well as conductive inks and new fabric materials, along with miniaturized electronic components (textile screens, vibrating micro-devices, LEDs, OLEDs...), now make it possible to produce intelligent textiles, creating truly usable and comfortable garments. These intelligent garments look like ordinary clothes, but can be useful in a variety of situations, depending on the applications envisaged [47]. After conducting several research projects as part of this thesis, it has been pointed out that active smart textiles could be perfectly involved in the area of automobile. Indeed, these textiles are equipped with additional functionalities that enable them to adapt, detect and react to changes in their environment. High-performance textile devices require a multidisciplinary approach to circuit design and development of smart textiles, as knowledge of materials, microelectronics and chemistry is integrated with a thorough understanding of textile production to achieve optimum results. Thanks to innovations in nanotechnology and materials science, it is now possible to print or incorporate new conductive materials and integrate them seamlessly or non-transparently into the fabric, paving the way for ergonomic, flexible and lightweight textiles. Figure.1.3 summarizes the main applications of smart textiles.

The main applications related to smart textiles are: color-changing smart textiles [48–50], temperature-controlled textile [48], Textile Memory Fabrics [51–54] waterproof and breathable textiles [55], as well as intelligent textile computer fabrics. However, among the various application areas for smart textiles, those of interest to my thesis project are smart textiles from different angles. In particular, we focus on smart thermal regulation textiles, which adapt to temperature variations to ensure optimum comfort. Therefore, integration of electronic components into fabrics is one of our main objective, opening up new perspectives for interactive and functional applications, ranging from smart clothing to wearable interfaces for data collection and interaction with electronic devices.

The aim is to find a printing function that combines the two key functions of electronics and transducers. Both functions are necessary to ensure efficient information transmission and physical transformation of materials, enabling remarkable physical effects to be achieved. The following paragraphs will be devoted to a detailed description of smart textiles with electronic information and temperature-controlled textiles, as well as the various applications in health monitoring, sportswear, temperature control and comfort enhancement, in addition to other functionalities in many other ends uses. For example, in medicine, these textiles can be used to monitor biological functions such as breathing and ECG (Electrocardiogram). In addition, these textiles can also be used to create structures that respond to various stimuli such as electrical, mechanical, optical, chemical, thermal, or magnetic signals. Research has been carried out to design, integrate, and develop techniques for printing materials on a textile substrate. Figure 1.3 illustrates several applications associated with smart textiles.

Thèse accessible à l'adresse : https://theses.insa-lyon.fr/publication/2023ISAL0114/these.pdf © [L. Diatezo], [2023], INSA Lyon, tous droits réservés



Figure 1.3. Several applications associated with smart textiles [53,56–60].

1.2 Potential applications of smart textiles

1.2.1 Temperature controlled textiles

Advanced temperature-regulated fabrics aim primarily to guarantee temperature comfort for those who wear or use them, regardless of external conditions or environment [61]. They fall into three categories: thermally insulating textiles, those with a *cooling* effect and those with automatic temperature regulation [62]. Among the most common thermal insulation materials used in these textiles are solar thermal storage fibers and far-infrared fibers. Solar thermal storage fibers are exploited to provide effective thermal insulation [63]. The principle is based on their ability to diffuse visible light and near infrared rays from sunlight absorption towards the human body, thus generating heat and promoting heat conservation [62]. As a result, far-infrared fibers offer superior heat conservation performance for thermal insulation. Indeed, these fibers have the ability to convert the heat emitted by the human body into a specific range of wavelengths corresponding to far-infrared rays. These rays are then reflected back to the human body, reducing heat loss, stimulating blood circulation and generating a beneficial heat conservation effect [20,64].

Cooling materials are made from special materials that offer a variety of functionalities. They include ultraviolet and heat protection fabrics, cool fabrics and heat dissipation fabrics. In fabrics designed to protect against ultraviolet rays and heat, a fine ceramic powder is blended and integrated into the fibers to fully exploit the reflective effect of ultraviolet rays. This feature creates a sensation of freshness for the wearer. Cooling textiles generally incorporate metal oxides into polyester fibers or fabrics. These metallic oxides are used to minimize discoloration from ultraviolet rays and light, while maintaining the feeling of freshness inside the garment. For textiles that promote heat dissipation, metallic powder coatings are added to the fibers. This process effectively dissipates the heat emitted by the body to the outside, thanks to the high thermal conductivity of metals such as silver (Ag), copper (Cu), aluminum (Al), and zinc (Zn) [65,66]. Materials featuring a phase change resulting from heating/cooling began to be developed in the 1980s by NASA, which developed materials capable of absorbing/releasing large amounts of energy accompanied by a phase change from solid to liquid. Some technologies contain pores whose size varies according to body temperature, and which can open or close depending on weather conditions. In this sense, the pores can open if it is hot and dry, while close if it is cold and wet, increasing the textile's ability to be waterproof and breathable [67–70]. Examples of textile-based heating systems can be grouped into two categories: polymer-based heaters and metal-based heaters [71]. Metal wires and sometimes metal foils are used to heat metal-based textiles. Examples of textile-based car seat heaters include the sleeping seat heating pad (see Figure

Thèse accessible à l'adresse : https://theses.insa-lyon.fr/publication/2023ISAL0114/these.pdf © [L. Diatezo], [2023], INSA Lyon, tous droits réservés

1.4a) where metal wires are implemented inside the car seat (Figure 1.4b). In Figure 1.4c, a pair of 12V universal is employed to power the car-seat heating pads, allowing to generate 30–38 W with adjustable temperature between 45 and 65 °C.

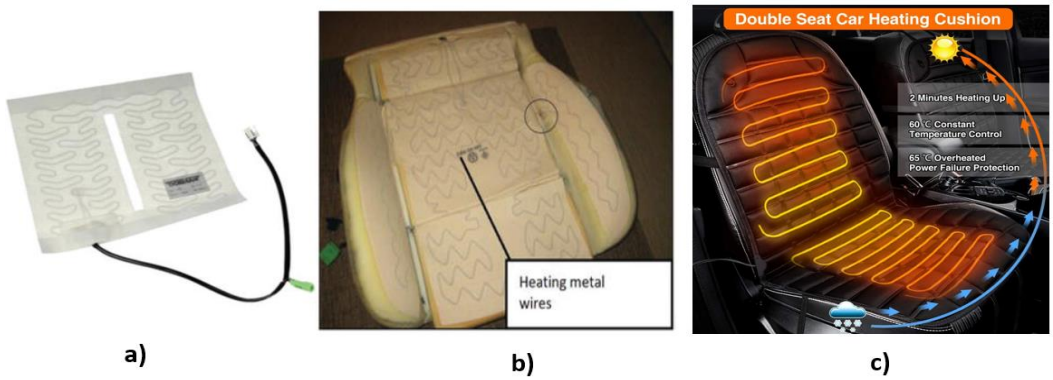

Figure 1.4. Temperature-controlling textiles: Textile-based car seat heaters (a) [72], (b) [73] and (c) [74].

At a time of increasing global warming and rising average temperatures, research is looking for alternatives to air conditioning and other cooling systems to combat ambient heat. To this end, several researchers [61,62,75] have developed a meta-fabric that reflects UV/visible light and re-emits absorbed infrared to lower the temperature of the wearer, whether a person or an object (such as a car). This meta-fabric could be used in commercial clothing within the next few years. Clothes and blankets made from an intelligent fabric that emits heat and reflects light could help people and objects exposed to the sun to stay cool, as illustrated in Figure 1.5 (a). The blue, green and red dotted boxes highlight, the three-level hierarchical structure responding to the ultraviolet (UV), visible–near–infrared (VIS–NIR), and mid infrared (MIR) bands. The boxes display the calculated scattering fields of 300 nm and 550 nm light from a 500 nm PTFE particle and a 400 nm TiO_2 particle, respectively. As indicated in Figure 1.5 (b)-(c), the PTFE and particles, together with the PLA fibers show strong scattering/absorption of all the three spectra [62].

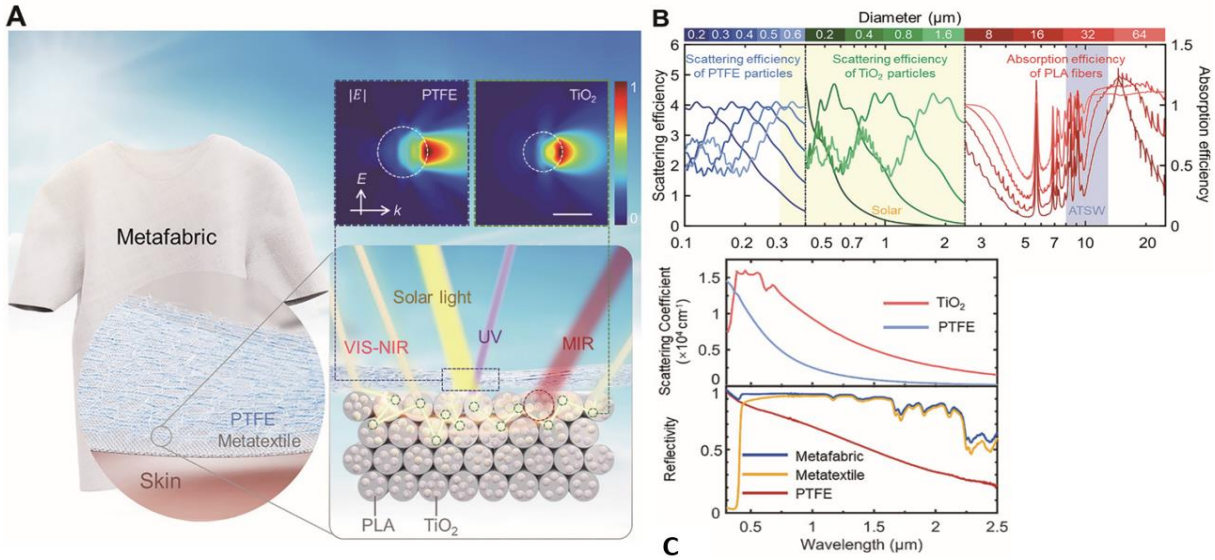

Figure 1.5 Proposed structure and simulated properties of the meta-fabric [76] : (a) Schematic of a meta fabric for daytime radiative cooling (scale bar: 400 nm); (b) Scattering and absorption efficiencies calculated for particles of different sizes encapsulated in the meta-fabric, (c) Top: scattering coefficients of PTFE and TiO_2 nanoparticles with optimized size distributions and 15% volume fractions. Bottom: solar radiation band reflectivity curves measured for meta-fabrics, meta-textiles and PTFE clothing films [62].

Thèse accessible à l'adresse : https://theses.insa-lyon.fr/publication/2023ISAL0114/these.pdf © [L. Diatezo], [2023], INSA Lyon, tous droits réservés

Meta-tissue is supposed to be effective when in contact with the skin. If someone wears a garment made of meta-tissue over a thick layer of normal clothing, much of the cooling effect would be lost as less body heat would be conducted to the meta-tissue and then radiated [62,77,78]. Intelligent textiles have a wide range of applications and offer outstanding prospects in almost every sphere of human activity. Numerous research projects are dedicated to the exploration and development of smart textiles for the fields of medicine [79] and healthcare [79], automotive [80], etc. The uses of these smart textile materials range from *in vitro* applications to *in vivo* use as an asset in everyday activities, performing functions such as physiological monitoring and communication with the environment.

Other researchers have developed active cooling or heating textiles to provide an additional source of coolness or warmth to the human body [77]. Joule effect heating, which uses electrothermal conversion, is widely used for active heating textiles. It is often achieved by modifying or incorporating electrically conductive materials on the surface of the textile or its fibers. Carbon-based materials (such as carbon nanotubes and graphene), [81,82] metallic (nano)materials [83–85] and conductive polymers [86] have all been reported as feasible solutions for Joule heating textiles. When voltage is applied, the reduction in electrical resistance achieved by the introduced materials enables textiles to generate Joule heating power suitable for heating the human body. For example, the percolation network of nanowires embedded in a polymer can produce a robust electrothermal effect in the event of mechanical deformation [85]. As far as metallic materials are concerned, they are generally known not only for their ability to heat by Joule effect, but also for their good reflectance to thermal radiation [84,87–89].

Mbises *et al.* [71] has developed an innovative polymer-based heating system. When direct current is applied, conductive polymer yarns carry the current and generate heat at the same time. The wire used is FabRoc®, a carbon-filled silicone wire made by combining silicone and carbon polymers. This wire is extruded using a patented process, which can be involved in a variety of product applications requiring flexibility. Unlike solid wires and panels, there is no risk of wire breakage or overheating build-up. Figure 1.6a-c shows flexible commercial based-polymer products (EXO2 use FabRocTM technology) that automatically reduces energy consumption as the temperature rises.



Figure 1.6. Flexible polymer-based heated back support (a) by EXO2 [80], (b) Storm Walker jacket by EXO2 [90], and (c) 5-zone heated jacket by DelphyneWomens [90].

Currently, polymer-based textile heating systems are mainly used in clothing and accessories, such as vests, jackets, gloves, insoles, slippers, heated socks, as well as in therapeutic products such as body warmers. In heated gloves (Figure 1.7a), extreme flexibility is required compared to jackets and vests, as the arms and fingers bend excessively. For that reason, flexible conductive wires, such as stainless-steel or silver-plated polyamide wires, can be a good option for the heating element in these structures. The production technique used can be knitting, but it is important to study the conductive wire's compatibility and tolerance in terms of conductivity level for processing with a knitting machine before starting production. In a heated sock system (Figure 1.7b), polymer-based conductive threads are knitted under the foot, through the heel and toes, to provide heat. Heated slippers (Figure 1.7c) have a heating system consisting of a woven

Thèse accessible à l'adresse : https://theses.insa-lyon.fr/publication/2023ISAL0114/these.pdf © [L. Diatezo], [2023], INSA Lyon, tous droits réservés

structure with conductive fibers in the insole, placed between the foam and the footbed lining. Rechargeable lithium-ion batteries provide the energy to heat the slipper, and a controller adjusts the level of heat [80]. Temperature-controlled textiles based on polymers, metal wire, fiber or conductive ink are especially advantageous because of their phase change resulting from efficient heating/cooling and their flexible structure for the human body, and they require less electrical energy thanks to small rechargeable batteries. They can be folded and compacted when not in use. Also, they can be found in various product ranges that can be worn between two layers of clothing and provide a controllable heating effect when needed.

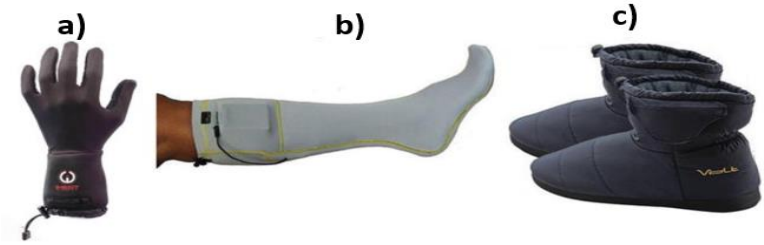

Figure 1.7. Heated gloves, socks and slippers based on flexible polymers [80].

1.2.2 Electronic information

Intelligent textiles with electronic information result from the combination of flexible microelectronic components with textiles. This combination enables the sensor to detect changes in the external environment, the information processor to treat the data, and the driver to modify the initial state of the material. These functionalities enable the intelligent textile to perform self-diagnosis, self-regulation, self-repair, and other purposes. The main technologies used to combine microelectronic components with fabric textiles are modular technology, embedded technology and other based on conductive fibers or inks, each of which is employed in a different way for this combination [64]. Modular technology involves the direct integration of electronic components as functional modules in fabric textiles. For example, various sensors can be added directly to the fabric to monitor human body temperature, heart rate and other data. Embedded technology, on the other hand, involves the direct integration of electronic components into parts of the fabric, such as the connection of printed circuit boards via conductive wires, flexible fabric-based sensors, integrated circuits, and so on. Fiber-based technology uses fibers or fabrics to directly create electronic components and sensors, such as flexible textile screens, flexible pressure-sensitive materials, etc. [20,91].

Medical applications for wearable smart textiles include monitoring patients' vital signs and temperature. Humidity and temperature sensors can be integrated into smart garments for more accurate analysis of a patient's condition. The humidity sensor can recognize excessive sweating or abnormal humidity [92]. In line with recent work [77,84] focusing on intelligent heat regulation systems, Joule-effect heated active textiles stand out as increasingly intelligent personal management devices. A recent study [84] presented a notable innovation in the form of a sandwich-structure textile. This is composed of silver nanofibers, silk fabric and platinum nanofibers, integrating both Joule heating elements and temperature sensors. The Ag nanofiber array film attached to the fabric functioned as a wearable heater, and the Pt nanofiber array served as wearable temperature sensors (Figure 1.8a). Figure 1.8b illustrates the schematic of a textile-based thermal control system, comprising a heater, a temperature sensor, a microcontroller unit (MCU) and a Bluetooth module. The desired temperature can be set by a mobile app, and then the digital output signal sent by the smartphone via Bluetooth can control the output of the energy module, which can modify the energy input for the Ag nanofibers to adjust their temperature [77,84]. Although the full application of the textile with the smart temperature controller has not been fully demonstrated, this work provides useful inspiration for the future direction of development of advanced integrated and interactive textiles.

Thèse accessible à l'adresse : https://theses.insa-lyon.fr/publication/2023ISAL0114/these.pdf © [L. Diatezo], [2023], INSA Lyon, tous droits réservés

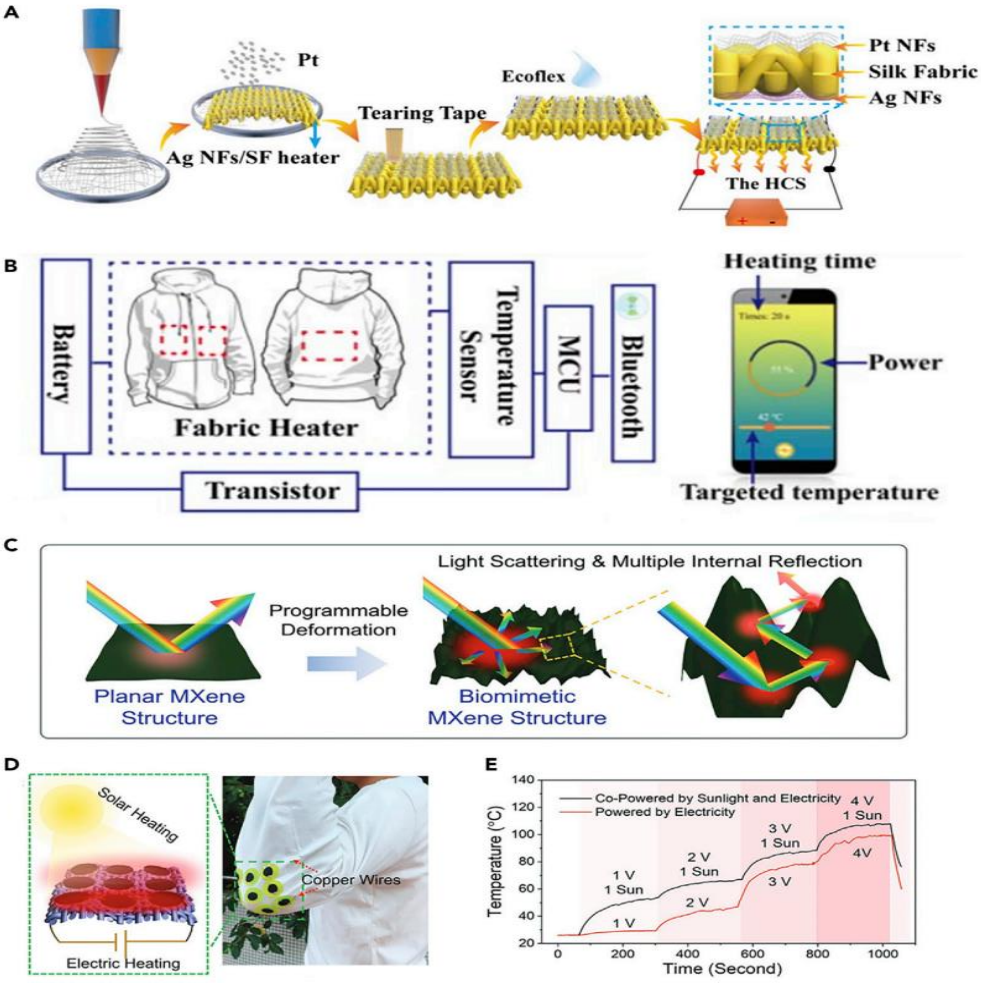

Figure 1.8. Active heating textiles based on Joule heat and light-to-heat conversion [77,84,93].

In addition to using the Joule heating mechanism for active heating, Li *et al.* presented an interesting innovation: a scalable heating system using both solar and electrical energy, integrated into textiles inspired by biomimetic textures the black scales of the Bitis rhinoceros [93]. As illustrated in Figure 1.8(c), this hierarchical structure not only increased light absorption over a wide band (reaching up to 93 %), but also improved the efficiency of light-to-heat conversion using mechanically deformed MXene structures. The conversion of light into heat was a significant complement to electric heating, as illustrated in Figure 1.8 (d)-(e) [93]. Advances in scientific research have had a significant impact on healthcare, mainly thanks to the creation of portable monitoring devices that have given rise to "telemedicine". These wearable devices enable continuous monitoring of physiological signals during daily activities, solving the problem of infrequent medical visits that provide only limited insight into a patient's state of health. A concrete example of this technology is a wireless garment equipped with integrated textile sensors, capable of continuously measuring and monitoring electrocardiogram (ECG), respiration, electromyogram (EMG) and physical activity [3,94,95]. A concrete example of this technology is a vest featuring fully woven textile sensors for ECG and respiratory rate detection, together with a wearable electronic board for motion evaluation, signal pre-processing and a Bluetooth connection for data transmission [3,96].

Another area of application for smart textiles is dedicated to monitor structural health in various engineering industries such as automotive, civil engineering, geotechnics and so on. In addition to their high performance, some smart textiles also have remarkable aesthetic value, making them suitable for use in the fashion and design industries [97]. Figure 1.9. illustrates an example of the use of optical fibers in various

Thèse accessible à l'adresse : https://theses.insa-lyon.fr/publication/2023ISAL0114/these.pdf © [L. Diatezo], [2023], INSA Lyon, tous droits réservés

engineering fields. It has been proposed that smart textiles can be characterized by their functionality, which often refers to the field of application and the level of integration of the "smart compound [98–101]. When exploring advances in the field of smart textiles in the literature, two main approaches can be identified: on the one hand, the addition of smart fibers or metallic wires to confer the textile its smart properties (i.e., by incorporating these elements directly into the textile), and on the other hand, the modification of the textile surface macroscopically by printing conductive materials onto a textile substrate (i.e., the main subject of this thesis). To achieve this, the use of conductive materials is necessary, but their characteristics call for a review of design and integration rules, as well as the establishment of aging laws. Figure 1.10. illustrates design principles.

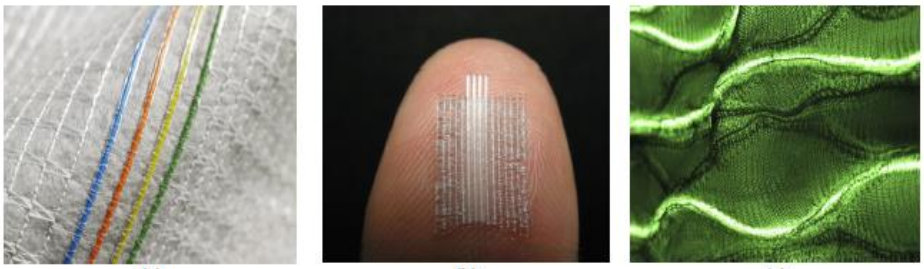

Figure 1.9. Optical fiber applications in smart textiles for environmental engineering [102] : (a) medicine [103], (b) design [104–106], and (c) decorative purposes [105].

To implement a printing function on textiles and make them smart, we need two overlapping functions such as electronics and transducers. These functions must include sensors, actuators and the whole electronic system integrated into the textiles (heating mat, electroluminescent devices, dielectric among others) which enable the recording and transmission of data, as well as wireless communication between the wearer and the operator, for example between a patient and medical personnel [107,108]. Today, the performance of printed circuits on large fabric surfaces is still limited due to several factors such as the performance of conductive materials, the porosity of textiles, the viscosity of ink, as well as problems related to ink printing. For example, gold and silver electrodes are expensive and have very low electrical resistance or conductivity for large-area printed circuits, which delays the development of large-scale applications. Textiles are highly flexible but have lower electrical conductivity.

In this study we focus on the development of flexible conductive composites that are used to be printed on the fabric surface of a car seat. Different functionalities of such materials are thoroughly investigated to effectively exploit their potentials in the development of both heating and electroluminescent devices. To achieve this objective, a study on flexible electrodes, highly electrical conductive and suitable to 3D printing, is carried out, followed by analyses of their aging effect in case of severe conditions.

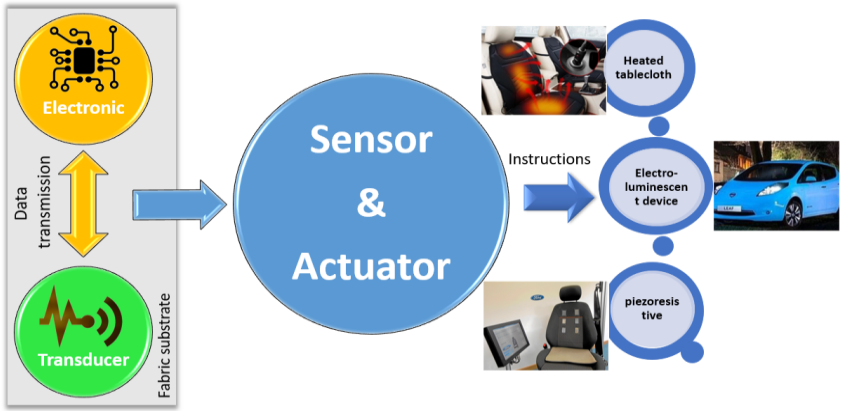

Figure 1.10. Design requirements [109–111].

Thèse accessible à l'adresse : https://theses.insa-lyon.fr/publication/2023ISAL0114/these.pdf © [L. Diatezo], [2023], INSA Lyon, tous droits réservés

1.3 Printed electronic materials

In the field of printed electronics, inks are frequently used to create structures with specific functions, such as sensors, radio-frequency devices, flexible displays and energy storage devices [112]. This complex electronic printing process requires different types of inks, including conductive, semiconductive and dielectric (or insulating) inks. In special situations, electroluminescent or photovoltaic inks can also be used [113]. Functional inks used in printed electronics must be carefully matched to form homogeneous layers that are compatible with other inks applied simultaneously [114].

Functional inks are generally composed of solvents, resins and/or polymers. They can contain both organic and inorganic components. However, it is often necessary for some materials to be in the micro- or nanoscale in order to minimize printer fouling problems [115]. Consequently, metallic particles are commonly used instead of pigments. In addition, additives such as dispersants are used to adjust the ink properties to the needs of the application. The polymer or resin present in the ink acts as a support for the metal particles on the substrate. Finally, solvents are used to regulate viscosity, improve the drying process and dissolve the polymer or resin, while preserving the integrity of the particles of interest [116]. Printable inks can be classified into several categories, including metal nanoparticle inks, metal oxide nanoparticle inks, molecular inks and resin-based inks.

1.3.1 Metal nanoparticle ink

Conductive inks can be developed in a variety of ways, including the creation of dispersed nanoparticles, the dissolution of organometallic compounds, or the dispersion of conductive polymers [117]. Metals are the materials most frequently used in the manufacture of conductive inks, often in the form of nanoparticle suspensions or via the metal-organic decomposition (MOD) process [118].

Inks containing metallic nanoparticles are made up of these particles, organic solvents and stabilizers. When the metal nanoparticle ink is heated, the organic solvents evaporate, leaving behind a highly conductive layer of the metal nanoparticles. This layer is particularly sought-after for the creation of conductive metal lines and electrodes [119]. Inks based on metal nanoparticles offer various advantages, including high conductivity, magnetic properties, oxidation resistance, and moderate cost. In addition, it is possible to customize the metal nanoparticle ink to adjust its electrical or magnetic properties to suit the targeted application [120]. To guarantee the quality of an electrode, it is generally recommended to use a highly conductive ink. This can be achieved by opting for conductive metal nanoparticles such as gold [121], silver [122], copper [123], aluminum [124], cobalt [125], nickel [126], platinum [127], zinc [128], palladium [129] and tin [130]. Paradoxically, inks based on metal nanoparticles are not suitable for devices subjected to high temperatures, as they tend to oxidize on contact with air. Thus, for electronic applications, it is recommended to use inks based on oxidized metal nanoparticles.

1.3.2 Metal-oxide nanoparticle ink

Nanoparticle-based inks are developed from highly stable metal oxide nanoparticles based on nanoparticles of copper oxide [131], indium tin oxide [132], zinc oxide (ZnO) [133] and iron oxide [134]. In general, inks based on metal-oxide nanoparticles are more environmentally friendly than those based on pure metal nanoparticles, and they are also easy to manufacture without the risk of oxidation [135]. Copper oxide nanoparticle-based ink is commonly used to create highly conductive metal lines. To achieve high conductivity, the surface oxide is removed by a reduction process [136,137]. The nanoparticle ink is protected by a coating on the sintered pattern to prevent post-deposition oxidation. Indium tin oxide-based conductive ink is commonly used for transparent electronic applications, with an impressive optical transmission of 98% [138]. To achieve the desired electrical conductivity, ITO-based conductive ink requires a high-temperature sintering process, reaching 300 °C [138]. ZnO is recognized as an ecological and sustainable material, with no impact on the ecosystem. It is a nanoparticle-based semiconductor ink, offering an economical alternative to ITO-based ink, thanks to its low-temperature manufacturing process

Thèse accessible à l'adresse : https://theses.insa-lyon.fr/publication/2023ISAL0114/these.pdf © [L. Diatezo], [2023], INSA Lyon, tous droits réservés

and because of its low cost [139]. ZnO nanoparticles exhibit unique properties suitable for optoelectronics, photovoltaics, electronics and various sensing applications [140]. IZO ink has a semiconducting nature that makes it desirable as a thin-film transistor [141]. Iron oxide metallic ink is a highly magnetic ink with good electrical properties [142]. Iron oxide metallic inks are suitable for the manufacture of printable patch antennas, inductors and other radio frequency devices [120].

1.3.3 Molecular ink

The essential elements in the development of molecular ink are metal and organic composition, generally based on the metal-organic decomposition (MOD) process to produce high-quality conductive thin films by thermal sintering [112,120]. Ink based on the MOD method offers several advantages over other inks: it is particle-free, inexpensive and can be easily adapted to a variety of printing techniques. Bhavana Deore *et al.* [143] developed a screen-printable cubic molecular ink, offering higher resolution, mechanical durability and excellent conductivity when applied to flexible substrates such as Kapton and PET. The copper MOD ink is a low-cost alternative to nanoparticle-based conductive inks. It is ideally suited to electronic applications, including printable antennas, encapsulated electroluminescent devices (LEDs) and printable electrodes for transistors, with excellent electrode stability after exposure to ambient air for 6 months [112,120].

Similarly, in a separate study, Arnold Jason Kell *et al.* [120,144] have developed a silver-based conductive molecular ink. This ink enables the printing of flexible electronic components with low surface resistance (< 10 mΩ/sq/mil) and high metallic conductivity, even under conditions of extreme bending and flexible environments. Thanks to its flexibility, this conductive ink is compatible with several printing methods, including inkjet printing, 3D printing and screen printing among others, opening up new prospects in the development of next-generation printable electronic devices.

1.3.4 UV-curable ink

Textile industries are showing increasing interest in UV-curable inks due to their characteristics, including mechanical strength and durability. In general, the formulation of UV-curable conductive inks involves combining UV-curable chemicals with metal nanoparticles, creating a uniform dispersion of the latter in a UV-curable base [145]. UV-curable inks need to be cured at low temperatures and have shorter curing times to be used in a wide range of applications.

In a recent study by Hong et al [145], a UV-curable conductive ink was presented. This screen-printed ink, composed of silver nanoflakes, is to act as an antenna for ultra-high-frequency RFID tags coated on textile substrate. Stretchable conductive textiles offer great potential for revolutionizing the field of wearable electronic devices. This is illustrated by recent advances exploiting a UV-curable silver-based ink combined with Polypyrrole (PPy), offering advantages of improved structural strength and high conductivity, particularly when applied to cotton fabrics [146]. Another study explored silver nanoparticles' ink screen-printed on various nylon fabrics, achieving superior electrical conductivity, a feature particularly sought-after for applications related to wearable electronic devices [147].

1.4 Printing Technologies

Accurate printing of complex structures requires design tools capable of creating models with the exact dimensions of the device. Typically, the design of the print model is carried out using commercial tools such as computer-aided design (CAD) software and computer-aided manufacturing (CAM) applications. This creates the three-dimensional (3D) representation of the complex structure, an essential step in preparing the printing machine. Conductive layer printing can be achieved using a variety of printing techniques, including gravure, flexography, offset, screen and inkjet printing, as illustrated in Figure 1.11 [120,140]. These technologies are often grouped into contact printing processes, which use a printing substrate [148], non-contact (non-impact) printing processes, which do not require a substrate [149], and hybrid printing

Thèse accessible à l'adresse : https://theses.insa-lyon.fr/publication/2023ISAL0114/these.pdf © [L. Diatezo], [2023], INSA Lyon, tous droits réservés

processes, which combine different printing and deposition techniques. In brief, all these processes are used to deposit stacked layer structures, such as electrodes, conductive layers, insulating layers for electronic components [150]. After deposition, the ink changes phase at the desired site [151–154].

The initial properties, flow and phase transitions of the ink on the substrate are mainly influenced by factors such as viscosity, density, surface tension, solvent evaporation rate, solubility, as well as the curing characteristics of the ink. In addition, the way in which the ink interacts with the substrate is also determined by factors such as its ability to wet the surface and the permeability of the substrate used [155,156]. Furthermore, printed final devices, due to their complexity in terms of multiple layers and materials, require compatibility between these layers to ensure their proper functioning. This means, for example, minimizing the electrical resistance of the foil in a short space of time, without causing damage to the layers already deposited. As mentioned above, current applications for printed devices encompass a diverse range of products, such as sensors, batteries, capacitors, transistors, solar cells, memories, electroluminescent devices, large displays and light panels [112,157].

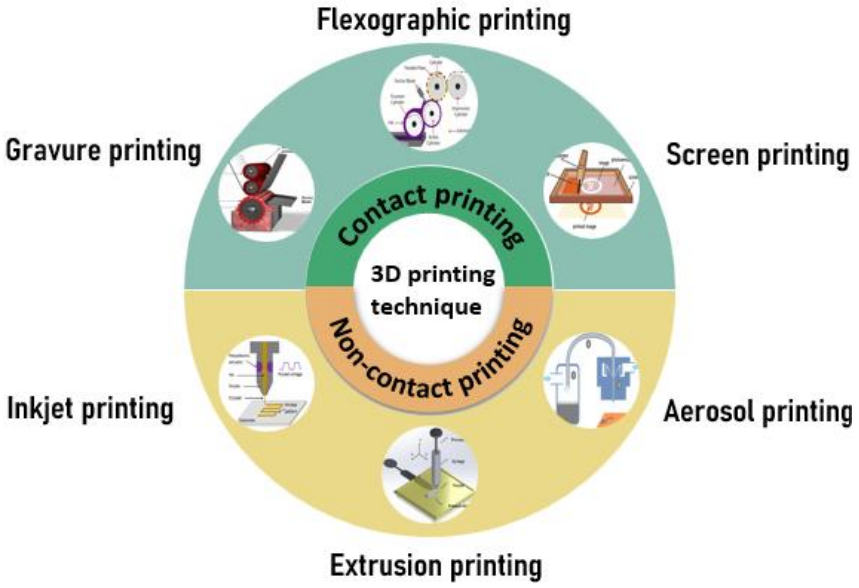

Figure 1.11. Classification of printing techniques to manufacture electronic components and circuits.

The key properties and parameters of the various printing techniques are summarized in Table 1.1. Inkjet printing is traditionally best suited to R&D or special applications, screen printing is excellent for stacking several thick prints, while gravure and flexography offer more possibilities for mass production of printed electronics [158]. Flexographic printing creates a thin printed layer with a line size of 80 µm and a throughput of 3 to 30 m^2/s. Offset and gravure printing offer similar characteristics, the latter being the fastest printing technology in terms of printing press speed. Screen printing and inkjet printing enable greater layer thickness: up to 20 µm for inkjet printing and up to 100 µm for screen printing, even at lower throughputs of 2 to 3 m^2/s for screen printing and 0.01 to 0.5 m^2/s for inkjet printing.

Table 1.1. Key properties and parameters of different printing methods [159,160]

	Gravure	Flexography	Screen	Inkjet	Extrusion	Aerosol
Throughput (m^2/s)	3-60	3-30	2-3	0.01-0.5	0.2-50	0.01-0.5
Resolution (lines/cm)	20-400	60	60	60-250	≈ 100	5-30
Printing speed (m/min)	100-1000	100-700	10-15	15-500	10-1000	Up to 200

Thèse accessible à l'adresse : https://theses.insa-lyon.fr/publication/2023ISAL0114/these.pdf © [L. Diatezo], [2023], INSA Lyon, tous droits réservés

1.4.1 Contact-printing techniques

In contact printing techniques, ink is transferred directly to the substrate by means of physical contact. Typically, these processes use an embossed or engraved roller to accomplish this ink transfer. Initial costs are high, and these methods require relatively long preparation periods [153]. However, their low production costs, their ability to operate at high manufacturing speeds, and their ability to guarantee reproducibility, make them particularly suitable for mass production [161].

1.4.1.1 Gravure printing

Rotogravure is renowned for its excellent print quality and speed. For example, it offers resolutions ranging from 20 to 400 lines/cm and print speeds from 1.13 to 16 m/s. Other advantages include simplicity of the printing process, precision of ink application and flexibility of press design.

In this printing process, image elements are etched onto the surface of a printing cylinder, while unprinted areas remain at their initial level. As shown in Figure 1.12, the engraved printing cylinder rotates in a partially filled ink trough. The entire surface of the cylinder captures the ink from the pan, and excess ink is then removed from the unprinted areas with a doctor blade, leaving the ink in the engraved recesses. Subsequently, the ink is transferred directly from the cylinder to the substrate via a pressurized printing device. Often, this ink transfer is enhanced by the use of an electrostatic assist system (ESA), which creates an electric field across the printing device. This electric field facilitates the lifting of ink from the recesses onto the substrate. Finally, the ink layer is dried by evaporating the ink solvent using a stream of hot air [120,153].

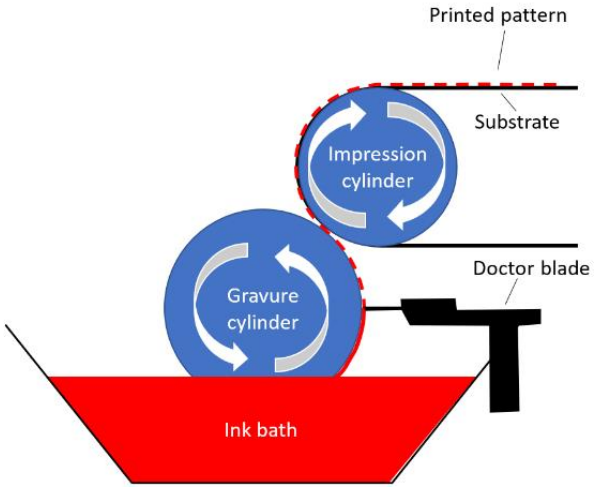

Figure 1.12. Schematics of gravure printing [153].

1.4.1.2 Flexographic printing

Flexographic printing is renowned for its ability to deposit a wide variety of thicknesses while maintaining constant resolution. In this printing method, an indirect process is used with the same nominal plate resolution, but with anilox rollers of different cell volumes. The main components of flexographic printing include the impression cylinder, plate cylinder, anilox roller, doctor blade and inking unit, as shown in Figure 1.14 [162]. The doctor blades and anilox rollers are generally made of stainless steel. The flexible plate is usually made of photopolymer or rubber. The image areas of the plate are raised relative to the plate surface. The anilox roller transfers ink from the reservoirs to the image areas of the plate cylinder, while the impression cylinder facilitates ink transfer from the image areas to the substrate.

Resolution is typically 60 lines/cm and print speed 3 to 12 m/s. The greatest challenge is to maintain color saturation and density in fixed areas. Flexography is suitable for a wide range of printing substrates. For example, non-porous and porous substrates can be printed without difficulty [163].

Thèse accessible à l'adresse : https://theses.insa-lyon.fr/publication/2023ISAL0114/these.pdf © [L. Diatezo], [2023], INSA Lyon, tous droits réservés

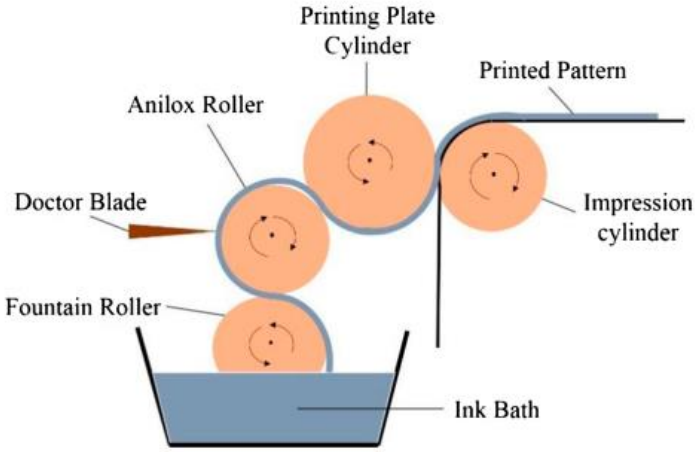

Figure 1.13. Schematic drawing of flexographic printing technique [112,163].

1.4.1.3 Screen Printing

Screen printing uses the so-called blocking stencil method, in which ink is pushed through a thin fabric (screen) made of plastic or metal fibers or threads. The unprinted areas of the screen are covered with a stencil that defines the printed image and serves as a printing plate, as shown in Figure 1.14. The screen is filled with ink, which is pushed through the image areas of the screen using a squeegee. The achievable print thickness is greater than with other printing methods. The ink layer is generally dried by evaporation, oxidation or ultraviolet (UV) curing. Drying can be accelerated by blowing hot air over its surface [145,153,163]. Print quality is determined by the material, screen thinness and thickness, the distance between the top and bottom of the screen, and the open area of the screen. Screen fineness is generally between 90 and 200 fibers/cm.

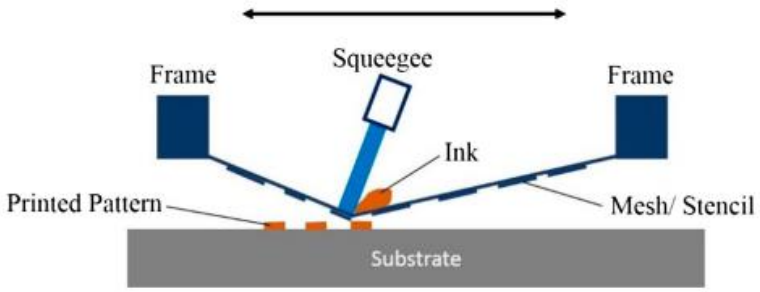

Figure 1.14. Schematic drawing of flatbed screen-printing [164].

Screen printing is a simple, versatile process for transferring ink onto a variety of substrates. The technique is compatible with a wide range of materials, from paper and ceramics to foils and continuous webs. It can also print on curved surfaces. The applications of screen printing are manifold, ranging from art to large-scale industrial applications, covering objects as small as electronic components to advertisements measuring several square meters, and enabling mass production, whether of a single piece or massive runs. However, screen printing has certain limitations, which are relatively modest. Despite this, it remains a common choice due to its ability to economically produce large-scale patterns with high precision and reproducibility, particularly for electronic components [165]. Nevertheless, it is essential to control various parameters, such as printing conditions, ink condition and screen condition. In some cases, post-processing, such as heat treatment, may be necessary, depending on the ink composition and its interaction with the substrate [153,166,167].

Thèse accessible à l'adresse : https://theses.insa-lyon.fr/publication/2023ISAL0114/these.pdf © [L. Diatezo], [2023], INSA Lyon, tous droits réservés

1.4.2 Non-contact printing techniques

In the field of non-contact printing, also known as direct-write printing, one technique stands out. It enables high precision when projecting the materials to be printed through a nozzle, while avoiding direct contact with the substrate. The main aim of this approach is to minimize nozzle contamination. Although non-contact printing technologies are significantly slower than R2R (roll-to-roll) contact printing methods, they are distinguished by their ability to print digital patterns. Thanks to their flexibility, these techniques are also used for on-demand production, enabling efficient use of materials. However, they do have some notable drawbacks, such as frequent nozzle clogging and the risk of unwanted spreading of the printed ink. Achieving a precise pattern depends on careful deposition, making the process relatively time-consuming [153].

1.4.2.1 Inkjet printing

The main advantage of inkjet printing technology lies in its lack of need for physical masks or traditional image carriers. Instead, inkjet printing relies on a direct deposition method using a virtual digital image carrier. This technique is renowned for its ability to produce very fine ink deposits and can be divided into two main categories: continuous inkjet printing and on-demand inkjet printing, depending on how the ink is transferred. On-demand inkjet printing, for its part, is subdivided into two sub-categories: thermal inkjet printing and piezoelectric inkjet printing. High-resolution printing is achieved by applying layers of ink that dry to form an extremely thin layer, followed by successive deposits of these layers. You can see the principle of inkjet printing technology in Figure 1.15, as illustrated in [43].

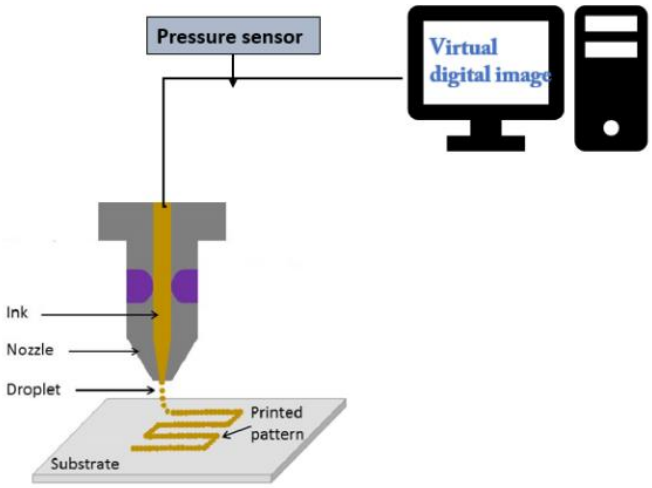

Figure 1.15. Principal schema of inkjet printing [168].

Inkjets are flexible and versatile, but their flow rate is low, at around 100 m^2/hr. They are therefore well suited to low-viscosity products. It is therefore well suited to low-viscosity soluble materials, such as organic semiconductors [169]. With high-viscosity materials, such as organic dielectrics, and dispersed particles, such as inorganic metallic inks, difficulties due to nozzle clogging arise. As the ink is deposited in droplet form, the thickness and homogeneity of the dispersion can be reduced. The simultaneous use of numerous nozzles and substrate pre-structuring can improve productivity and resolution, respectively. However, in the latter case, methods other than printing must be employed for the actual structuring step [168].

1.4.2.2 Extrusion printing

Three-dimensional (3D) printing, also known as additive manufacturing (AM), represents an emerging technology for printing customizable objects in three dimensions, opening up new prospects for the generation of a new class of multifunctional materials such as conductive inks, nano-composites and many

Thèse accessible à l'adresse : https://theses.insa-lyon.fr/publication/2023ISAL0114/these.pdf © [L. Diatezo], [2023], INSA Lyon, tous droits réservés

others [170]. This method enables reconfigurable objects to be manufactured using computer-aided design (CAD) software, allowing the design and three-dimensional structure to be optimized by following a sequence of layers (see Figure 1.16) [168].

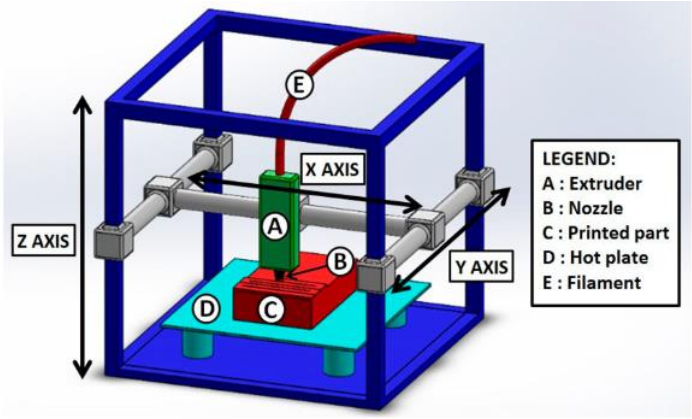

Figure 1.16. Schematic diagram of a representative fused deposition modeling (FDM) installation. FDM consists of an extruder (A), which directs the ink to the nozzle (B) for fluid ejection to form the printed object (C). The process involves forming the printed object on a heating plate (D) to control the temperature and fluidity of the resulting ink. The ink is usually a highly viscous fluid obtained by heating a thermoplastic material, and is deposited through the extruder/nozzle system in the form of a continuous filament of well-defined dimensions (E) [140,171].

3D printing is based on the extrusion of continuous filaments (or inks) layer by layer, using CAD tools. This technique enables the creation of structures with typical characteristics at microscopic (0.1 to 100 µm) and mesoscopic (>100 µm) scales, depending on the nozzle diameter. It is essential to emphasize that the ability to manufacture a diversity of structures requires precise control of the formulation and rheological behavior of inks, as well as management of key printing parameters such as print speed and extrusion pressure [170,172–174]. In addition to its current use for polymers and biomolecular systems, this technology has also been applied to ceramics, thanks to adaptations in the manufacturing process, subsequent treatments and control of interactions between the energy source and the material [168,170].

1.4.2.3 Aerosol-jet printing

In the aerosol jet printing technique, also known as Maskless Mesoscale Materials Deposition (M3D), relies on the atomization of an ink, creating very small aerosol droplets ranging from 1 to 5 µm in diameter [175]. As illustrated in Figure 1.17, ink atomization can be achieved by either a pneumatic or ultrasonic method [112,176]. These droplets are fed to the ceramic nozzle attached to the printhead with a vacuum generated by means of a nitrogen sheath gas stream, and are projected as a high-velocity jet onto the substrate surface [177]. This technique enables printing on flat, conformal surfaces. For the production of complex 3D patterns, precise control of the beam is essential. To achieve this, a shutter is placed in front of the nozzle to selectively interrupt the droplet flow. In addition, it is necessary to maintain an appropriate distance between the nozzle and the substrate, not exceeding 10 mm and not falling below 1 mm, in order to guarantee precision. Any deviation from these values usually results in defects in the printed pattern [120,153]. Like inkjet printing, aerosol printing is capable of reproducing designs based on digital models. The major advantage lies in the fact that this technique is not subject to nozzle clogging. It can produce features as small as 10 µm, enabling high-resolution printing [178]. However, the main disadvantage of aerosol jet printing is speed, which does not exceed 12 m/min; it is therefore not suitable for the mass production of printed electronics [112,153].

Thèse accessible à l'adresse : https://theses.insa-lyon.fr/publication/2023ISAL0114/these.pdf © [L. Diatezo], [2023], INSA Lyon, tous droits réservés

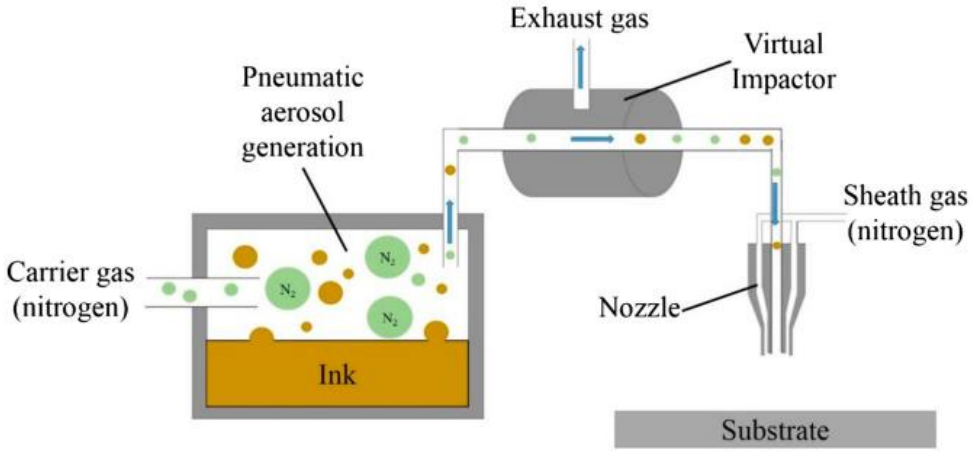

Figure 1.17. Schematic of the aerosol jet printing process [179].

1.5 Potential applications of printed composite inks

Multifunctional materials have recently attracted a great deal of interest in the technological field for the development of sensors, actuators, electrodes, heating elements, antennas, and energy collectors in the form of thin, flexible and potentially extended films. This class of materials combines the excellent properties of metallic or phosphorescent particles with those of the polymer matrix, enabling dielectric constants to be obtained and the electrical conductivity of inks to be evaluated. In addition, they offer excellent thermal, mechanical and electrical properties, which are being successfully applied in fields such as consumer electronics, aerospace, automotive and biomedicine.

The use of 3D printing is spreading widely across different sectors, from construction to prototyping. Similarly, 3D printing is gaining in importance in the manufacture of electronic products for a variety of applications. In addition, conductive ink has been booming worldwide in recent years, due to growing needs in a variety of application areas, including flexible and silicon-based electronic products. The emergence of printable electronics on flexible substrates opens up a wide range of applications such as biomedical devices, biosensors, thin-film transistors, solar cells, sensors, actuators, photodetectors, energy devices including supercapacitors and fuel cells, as shown in Figure 1.18.

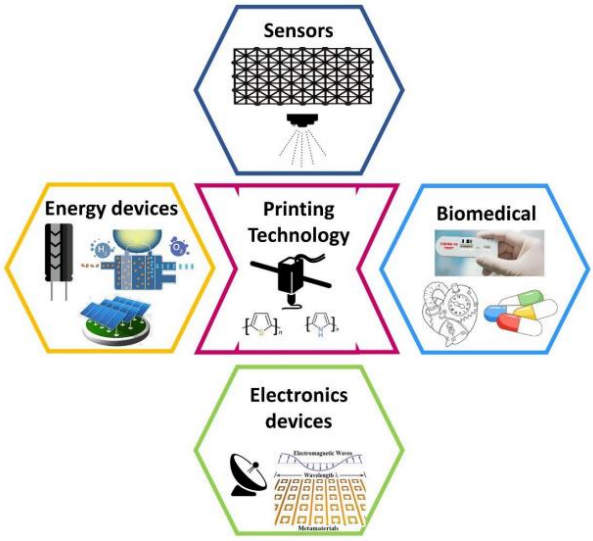

Figure 1.18. Printed electronics applications: sensors, biomedical devices, energy devices and other electronic communication devices such as antennas [120].

Thèse accessible à l'adresse : https://theses.insa-lyon.fr/publication/2023ISAL0114/these.pdf © [L. Diatezo], [2023], INSA Lyon, tous droits réservés

Aerosol jet printing, ideally suited to semiconductor packaging, interconnects and metallization [135,180,181], is widely used in solar cell metallization applications [120,180]. For inkjet or screen-printed tactile sensors, there are three types of transduction technology: piezoresistive, capacitive and piezoelectric, depending on the application. Thanks to inkjet printing technology, screen printing, silver, single-walled carbon nanotubes (SwCNTs) and graphene are conductive materials used in many works [182–186]. The contribution of inkjet and screen printing to the manufacture of this type of sensor is to introduce a lower-cost alternative aimed at minimizing complexity without compromising sensing quality and performance for the target application. The significant advantages and related studies of these aspects are discussed in the following subsections. In addition, we presented current developments of inks based on electroluminescent materials as well as heating resistance, which are ultimately related to the purpose of this research.

1.5.1 Piezoresistive ink

Piezoresistive inks shows a strong variation of the electrical resistance upon mechanical deformation, allowing the implementation of force, pressure and stretchable sensors on different types of substrates. Lo *et al.* [184] reported on an inkjet-printed piezoresistive pressure sensor that offers high sensitivity and can be fabricated using a very simple process. The device comprises a conductive layer of silver nanoparticles (AgNP) directly printed onto a polydimethylsiloxane (PDMS) substrate and encapsulated by a very high adhesion (VHB) tape. Pressure is measured by the change in electrical resistance caused by pressure-induced deformation in the printed AgNP thin film. In terms of geometry, Li *et al.* [182] have proposed a novel ring-shaped piezoresistive pressure. Nanocomposites-based carbon nanotubes (CNTs) and polyimide (PI) with different CNT concentrations are prepared in a liquid mixture as the fabrication material. The ring-shaped nanocomposite thin-film device is deposited on a circular polyimide diaphragm by an inkjet printing manufacturing method. The inkjet printers on-demand manufacturing process enables nanocomposite thin films of different geometries and shapes to be produced, for improved structural compatibility with the sensor port and overall measurement accuracy. Thanks to these latter features, the sensors offer advantages such as an easy manufacturing process, excellent flexibility and high sensitivity. Figure 1.19 shows the piezoresistive touch sensors manufactured in several researches [119,182,184].

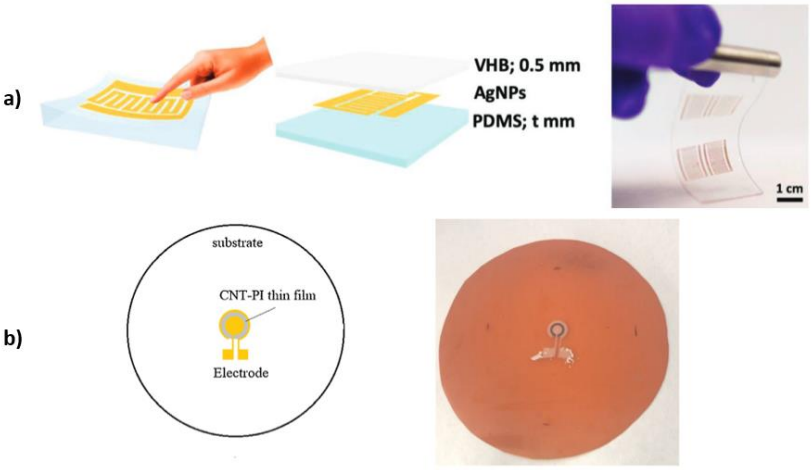

Figure 1.19. Illustrations of printed piezoresistive sensor: (a) [184] and (b) [182].

1.5.2 Capacitive ink

Inkjet printing technology facilitates the use of a variety of flexible substrates for diverse designs [187]. Polyethylene terephthalate (PET) is widely used as a flexible substrate for inkjet-printed capacitive sensors

Thèse accessible à l'adresse : https://theses.insa-lyon.fr/publication/2023ISAL0114/these.pdf © [L. Diatezo], [2023], INSA Lyon, tous droits réservés

[188–191]. In addition, printed electronics on paper enables the implementation of flexible sensors and has been used to fabricate printed capacitive sensors in [192–194]. The paper substrate has many advantages like inexpensive, environmentally friendly, lightweight, stretchable, foldable in three dimensions, and commercially available [195–197]. Zhang *et al.* [198] have developed their capacitive sensors printed on thermoplastic polyurethane (TPU) and aluminum substrates. Mikkonen *et al.* [199] proposed a new approach using a water-soluble polyvinyl alcohol (PVA) layer as substrate. In this study, a simple method has been outlined for the fabrication of fully printed elastomeric capacitive sensors, characterized by high flexibility and sensitivity covering a wide pressure range. One of the major benefits of this research lies in the development of an easy inkjet printing technique for PDMS. The researchers fabricated conductive electrodes using inkjet printing of silver nanoparticles on PVA. They then placed a dielectric layer between these electrodes, consisting of a PVA mesh structure embedded in an inkjet-printed PDMS layer, to create a capacitive touch sensor [199]. Figure 1.20 shows different capacitive sensors printed on different substrates.

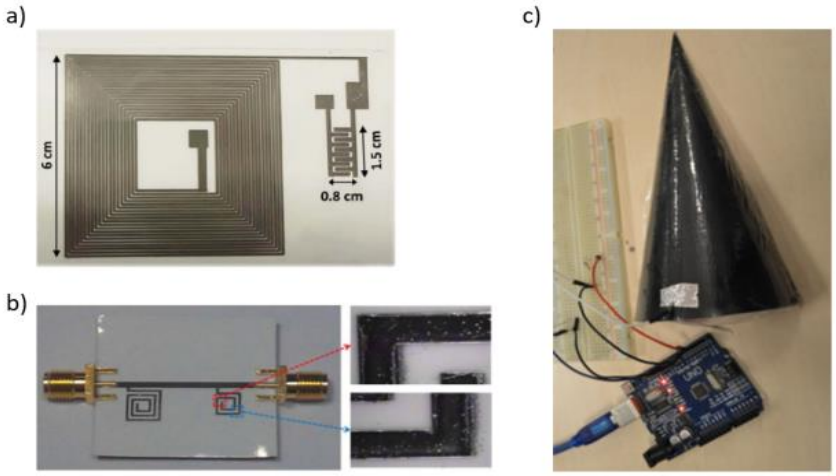

Figure 1.20. Layout of an inkjet-printed capacitive sensor on (a) PET substrate [189]. (b) Photo paper [193] and (c) TPU substrate [200].

1.5.3 Piezoelectric ink

Among existing piezoelectric materials, piezoelectric polymers are the most suitable for printing tactile sensors, due to their superior flexibility and high transparency. These materials are the subject of much research due to their high mechanical stability and compatibility with solution printing technologies [201]. Of particular interest is polyvinylidene fluoridetriflouroethylje, also known as P(VDF-TrFE), a piezoelectric material commonly used to fabricate 3D-printed tactile sensors [202,203] and inkjet [204,205]. Two of its applications in inkjet printing are shown in Figure 1.21.

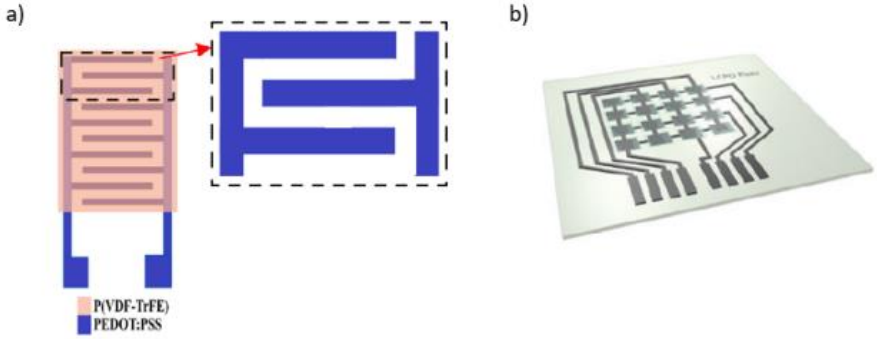

Figure 1.21. Illustration of printed piezoelectric sensor coatings : (a) [204] and (b) [205].

Thèse accessible à l'adresse : https://theses.insa-lyon.fr/publication/2023ISAL0114/these.pdf © [L. Diatezo], [2023], INSA Lyon, tous droits réservés

1.5.4 Electroluminescent (EL) ink

AC-powered EL devices have been integrated into polyester, cotton or polyester-only fabrics to create an intelligent lamp. Tao et al. has developed innovative methods to produce electroluminescent lamps using the technique of screen printing directly onto fabric, specifically for wearable electronic applications [206,207]. Woven fabrics are already widely used in clothing, as they are comfortable, flexible and washable [208]. Several researchers have already explored methods for printing conductor tracks directly onto fabric using screen printing [209–213]. Screen printing enables any pattern to be printed in any orientation relative to the fabric's warp and weft directions. Moreover, the paste can be placed directly on the fabric, preserving its properties close to the skin [207]. The lamps printed on the fabric have been designed using a blend of 65% polyester and 35% cotton. These lamps can produce the following colors: light blue, dark blue and orange, as illustrated in Figure 1.22 (a)-(c). Color variations are controlled by varying the phosphor particles incorporated in the printing process developed at the University of Southampton. This process relies on an interface layer, which smoothes the surface of the fabric when necessary, ensuring a more uniform surface than the base fabric [210]. The flexible properties of the fabric are maintained, as shown in Figure 1.22 (e), allowing for a large range of wearable applications without restriction of movement. The printed lamps are fabricated in a capacitor structure using six individually printed layers [207], as illustrated in Figure 1.23.

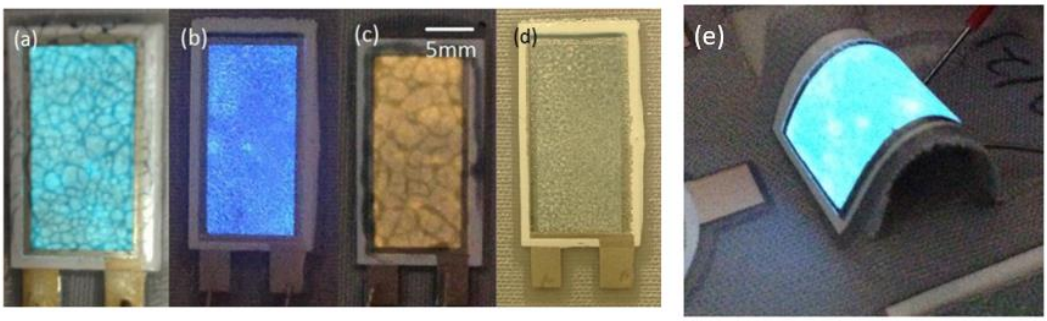

Figure 1.22. Screen-printed EL samples on fabrics (a) Light blue powered, (b) Dark blue powered, (c) Orange powered, (d) Dark blue unpowered, and (e) Light blue EL lamp on flexibility fabric [207].

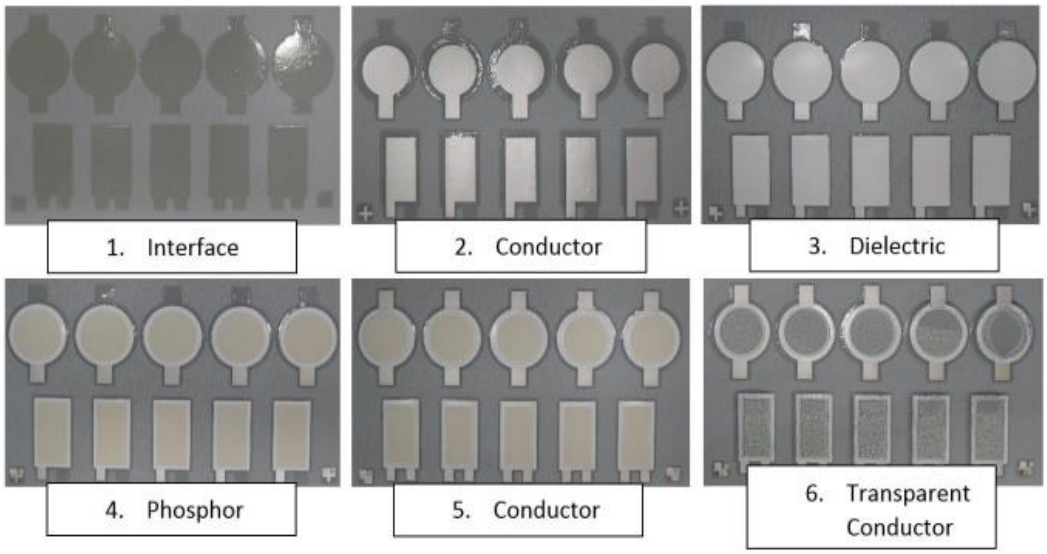

Figure 1.23. Six individually printed layers built up to produce EL display [207].

Thèse accessible à l'adresse : https://theses.insa-lyon.fr/publication/2023ISAL0114/these.pdf © [L. Diatezo], [2023], INSA Lyon, tous droits réservés

1.5.5 Resistive heating-element ink

Several authors have developed stretchable heating elements using resistive inks that are screen-printed onto a stretchable film. This breakthrough was achieved with the aim of creating a passive heat-retaining device for use as a portable heating system for elite athletes. The uniformity of heat distribution and thermal performance of these large-area, lightweight electrothermal heaters were assessed by varying the applied voltage via thermal imaging [214–216]. The printed heaters consist of a $15 \times 4\ cm^2$ resistive-carbon coating that generates heat by the Joule effect. Silver busbars are positioned parallel to each end of the heaters to ensure a constant current flow through them (see Figure 1.24a) [215]. The resistance of a foil resulting from monolayer printing of carbon- and silver-based inks was found to be $230 \pm 12\ \Omega/m$ and $0.078 \pm 0.001\ \Omega/m$, respectively. This occurred at thicknesses of 8.0 ± 0.8 µm for carbon and 8.7 ± 0.5 µm for silver. At a 0% nominal strain and a 15 V power supply, the heaters showed excellent heat uniformity (Figure 1.24b) for the whole heated surface of ~ 59 °C.

The electrical resistance of the coating and the applied voltage determine the heater power and output temperature. Indeed, the resistance of the heating elements depends on the ink properties and the print quality, while the temperature of the heating elements varies as a function of the applied voltage (see Figure 1.24c). In accordance with the Joule's law, increasing the supply voltage to the heating elements increased both the target temperature and the heating rate (Figure 1.24c). In the three cases where the input voltage equals 10, 15 and 20 V, the heaters reached equilibrium temperatures of 39, 54, and 72 °C within 90 s, respectively. This plateau corresponds to the point at which the power absorbed by the heater is in equilibrium with the heat loss to the environment due to conduction and convection. When the power supply is switched off (at 180 s), the heaters return to a temperature below 30 °C within 30 s [215].

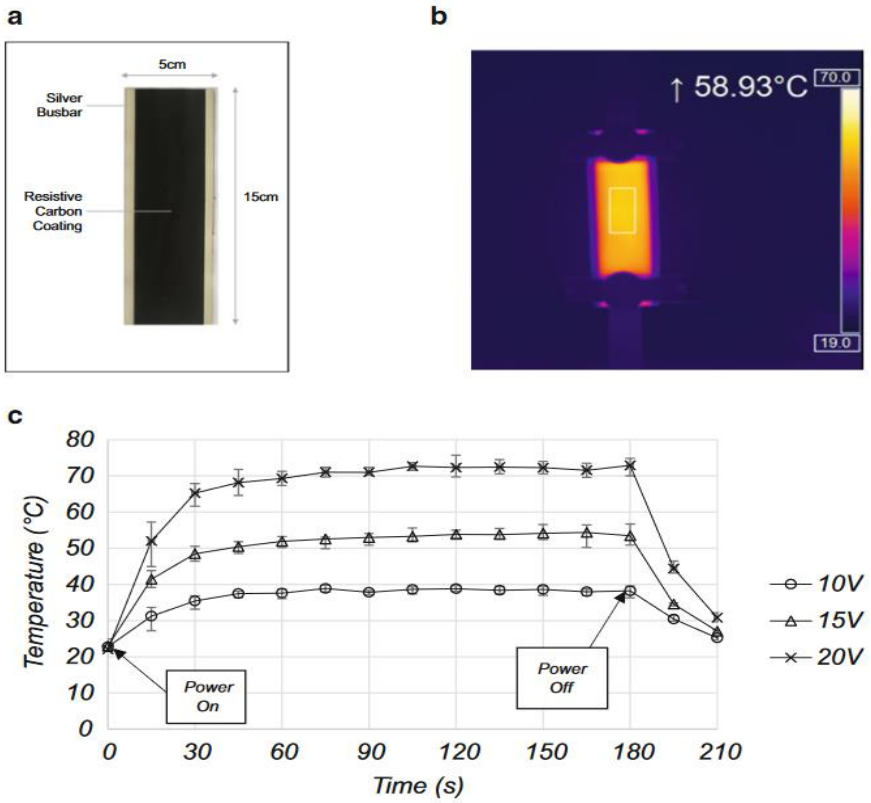

Figure 1.24. (a) Photograph of the printed carbon heater (b) thermal image of the heater at 15 V at 0% nominal strain clamped in the Hounsfield tensile tester (c) the effect of the applied voltage on the heating response of the printed carbon heaters [215].

Thèse accessible à l'adresse : https://theses.insa-lyon.fr/publication/2023ISAL0114/these.pdf © [L. Diatezo], [2023], INSA Lyon, tous droits réservés

The above research work demonstrated a reliability of involving resistive heating element in a 3D printing additive manufacturing. Good homogenous temperature was attained on the entire heated surface. However, such a surface is too small to be able to generate enough energy to heat a car seat. Printing resistive heaters with a larger surface is more challenging, which needs a development of more complex coating design. Current existing prototype of the heaters integrated in car seats developed by Tesca still have several critical issues in terms of temperature homogeneity as well as important hotspots. Therefore, one of the main objectives of my thesis is to figure out such a technological block so as to achieve a better performance of the heating device.

1.6 Summary

The target of this thesis aims to develop printed heater fabric integrated in a car seat that matches specifications imposed by automobile industry (Tesca group). In this chapter, we first explained the benefits of printed electronics that are currently in full development particularly in the area of smart textiles. One of the key challenges in this project is to achieve homogeneous conductor tracks to connect and power the various components of the printed circuit. According to the standards defined by Tesca, the proposed system must fulfil several criteria such as high heating efficiency, good temperature homogeneity for the whole fabric surface, fast time response while avoiding overheating effect. Among several printing methods available for this purpose, screen-printing-based industrial process is chosen. Currently, inks based on silver or copper nanoparticles are the most commonly used due to their excellent ability to conduct electricity, thus a small concentration of these fillers into polymers may result in high electrical conductivity of the composites. A careful choice of polymer matrix and incorporated conductive particles can lead to the creation of composite coatings with enhanced mechanical, thermal and electrical properties. The developed composite coatings aim to convert the fabric substrates into electrically and thermally conductive materials, without greatly altering the fabric substrate properties.

It is obvious that textile-based printed electronics open new opportunities for next-generation smart heating devices. Nonetheless, essential understandings on the characteristics of material's coatings are still uncovered to accelerate their large-scale production. Therefore, the next two chapters involve design optimization of the printed composite coatings, together with their characterizations on morphological, electrical, and thermal properties.

Thèse accessible à l'adresse : https://theses.insa-lyon.fr/publication/2023ISAL0114/these.pdf © [L. Diatezo], [2023], INSA Lyon, tous droits réservés

Chapter 2 Materials – Process and Characterizations

In this chapter, we focus on the electrical properties of conductive inks based on carbon, copper, and silver composites as well as the thermal properties of the heating fabric commonly used in a car seat. Another aspect of this study involves the development of electroluminescent (EL) polymer-based composites containing metal-doped ZnS particles. To carry out these studies, it is important to determine the methods to approach tasks or problems, and it is necessary to draw the process of the actions required. Here we start with the choice of particles and polymer matrix for the composite formulations to get high-performance ink. The manufacturing steps of screen printing for both coated heating fabric and EL-based composite are then presented. Experimental set-ups used to characterize the properties of these materials combined with their aging effect will be described in detail, covering microstructural analysis, mechanical, electrical, thermal and moisture properties, providing precise information on experimental set-ups and measurement conditions. Finally, a full description of finite element setup built for both conductive and EL composite models are investigated.

Thèse accessible à l'adresse : https://theses.insa-lyon.fr/publication/2023ISAL0114/these.pdf © [L. Diatezo], [2023], INSA Lyon, tous droits réservés

2.1 Materials' selection and composites' elaboration

2.1.1 Conductive coatings

2.1.1.1 Conductive inks

Conductive ink is the most important component in the printing of metallic structures. Several conductive materials can be considered for this purpose, such as conductive polymers [217], carbon [218,219], organic/metallic compounds [219], metal precursors [220] and metal nanoparticles/microparticles [221]. Conductive polymers are inexpensive and can be used on large surfaces requiring high flexibility, but their performance is lower due to their low electrical conductivity compared with pure metal precursors [222,223]. On the other hand, the use of metallic precursors requires additional thermal treatment (> 250 °C) to reduce the precursors to metallic species, which is not suitable for printing into flexible structures. Organic/metallic compounds appear to be an alternative solution for achieving the best compromise between mechanical and electrical performance. Most commercially available conductive inks are therefore based on compounds of silver, gold, carbon particles or other metals such as copper, which is cheap and easy to disperse in water. As gold ink is rather expensive, it was not considered in this study.

Three conductive inks, all of which are commercially available, have been selected accordingly: one is a silver solvent-based ink (i.e., the Ag/BGA composite), while the other two are copper-carbon water-based inks (i.e., the Cu/PU and C/PU composites). Recently, these conductive materials have been widely used for functional printed electronics applications. In addition, they are adaptable to various types of flexible substrates such as polyamide, polyester, polyethylene terephthalate (PET), photographic paper and so on. Table 2.1 summarizes the basic properties of the three selected inks as listed in the manufacturers' technical literature.

Table 2.1. General properties of commercially available conductive inks.

	C/PU ink	**Cu/PU ink**	**Ag/BGA ink**
Polymer matrix	Polyurethane (PU)	Polyurethane (PU)	Butyl Glycol Acetate (BGA)
Particles	Carbon (C)	Cooper (Cu)	Silver (Ag)
Particle size	≤ 2.5 μm	30–40 μm	≤ 10 μm
Viscosity ($\boldsymbol{Pa.s}$)	$6.0 - 7.0$	$6.5 - 7.0$	0.15
Curing time at 120 °C ($\boldsymbol{min}$)	2	3	15
Particle's content (**wt.** %)	30	40	62
Mass density ($\boldsymbol{g/cm^3}$)	1.33	1.74	2.16
Particle's content (**vol.** %)	17.6	7.8	12.9

As can be seen from this table, the Ag/BGA composite has an extremely low viscosity, suggesting that it would penetrate a textile substrate more easily than the other two inks. As a result, the continuity of the printed track could be interrupted, particularly with a very thin layer of silver. In fact, viscosity turns out to be a critical parameter that can have a significant impact on the fidelity of the printed form during the AM procedure. As mentioned in our previous work [224,225], the ideal viscosity range was around 0.5-50 Pa.s for the screen printing process, and a similar criterion was found for the extrusion-based 3D printing technique [226]. Consequently, the Ag/BGA coating, whose viscosity is particularly low (i.e., outside the ideal range), needs to be printed in multilayers to avoid discontinuity of electrical contact. Finally, to effectively render the printed track conductive, post-processing by thermal annealing is carried out for all inks. This step may limit the type of substrates that can be used or compromise the conductivity of the printed line.

The three composite inks are then printed on flexible, foam-lined fabrics supplied by the Tesca Group. The most optimized coated fabric is then integrated into a polyester web. In fact, over 90% of all car seat

Thèse accessible à l'adresse : https://theses.insa-lyon.fr/publication/2023ISAL0114/these.pdf © [L. Diatezo], [2023], INSA Lyon, tous droits réservés

fabrics worldwide are coated with polyester, as only this fiber combines the required characteristics of high strength, reasonable cost, low mass density, high abrasion and UV resistance [227,228].

2.1.1.2 Polymer binders used to improve electrodes' properties

In order to solve the accelerated ageing issues associated with the electrode properties, a new conductive ink formulation was optimized using polymer binders with different glass transition temperatures. Three commercially available polymer binders were selected as shown in Table 2.2: the acrylic polymer Rudolf (AC-RUD) supplied by Rudolf Group Better Chemistry, while the polyurethane polymers Achroma (PU-AR) and the acrylic Archroma (AC-AR) supplied by Archroma Life Enhanced. These materials were expected to weaken the ageing effect related to changes in temperature, humidity and mechanics.

Other products were also used to optimally formulate the ink. For example, Verdicker 41 N supplied by Schill + Seilacher Struktol was used to control the viscosity and homogeneity of the formulated ink. HEPrint Antimousse XLP silicone supplied by Sarl Hexdis France allowed to eliminate air bubbles in the solution. Tubiprint BL supplied by CHT Smart Chemistry was supposed to prevent the formulated ink from drying too quickly and sticking to the printing screen mesh. Tubicoat Fix H26 supplied by the same company was useful for cross-linking of the polymer, making the ink more resistant with respect to variations in temperature, humidity, and mechanical stress, among other factors.

Table 2.2. General properties of commercially available binders and percentage of copper particles used.

		Supplier	**Binder**	**T_G**	**% Particles**	**Viscosity (Pa.s)**	**Mass density (g/cm^3)**
Cooper Ink	Initial Ink	Bozzetto	PU	Unknown	Unknown	$6.5 - 7.0$	1.74
	Improved formulation	Archroma	AC-AR	**+ 10 °C**	30	Unknown	1.05
		Archroma	PU-AR	**Ca –47 °C**	30	$0.01 - 0.1$	1.042
		Archroma	AC-RUD	**+ 26 °C**	30	3.0	1.06
Carbon Ink	Initial ink	CHT	PU	Unknown	Unknown	$6.0 - 7.0$	1.33
	Enhanced ink	Dycotec	Unknown	Unknown	Unknown	$3.5 - 5.5$	1.2

2.1.1.3 Elaboration of conductive composite

Polymer composites were prepared prior to the addition of copper particles, in order to produce a conductive ink used in screen printing. The characteristics of the conductive ink are influenced by various factors, such as the choice of copper particle content, solvents, the composite used and the addition of other additives to the formulation. Figure 2.1 illustrates the conductive ink formulation process [229–236]. The conductive ink was prepared in an aqueous-based solvent.

- First, Verdicker 41 N, followed by Binder (Ac/Pu) L'appretan N92121 liquid M1000 was added into the water-based solvent as shown in Figure 2.1(a). The solution was then agitated by a Stirring Mixer at 2000 rpm for 5 minutes as illustrated in Figure 2.1(b).
- Second, Silicon Heprint XLP was added to eliminate air bubbles in the solution, together with Tubiprint BL to prevent the ink from drying and sticking quickly. Then, Tubicoat Fix H26 was introduced to crosslink the polymer and improve the ink's resistance. The whole solution was then stirred for 30 minutes (Figure 2.1(c)).
- Last, 30 wt.% of the copper powder (econduct 314000 particles, supplied by Eckart) was added to the solution and mixed using a Stirring Mixer at 2000 rpm to isolate large non-dispersed aggregates. Verdicker 41N was then added and the mixture was stirred again for 10 minutes to obtain an optimum viscosity of 6.5 –7.0 Pa s. The formulated copper inks were then printed on fabric substrates using a screen-printing technique.

Thèse accessible à l'adresse : https://theses.insa-lyon.fr/publication/2023ISAL0114/these.pdf © [L. Diatezo], [2023], INSA Lyon, tous droits réservés

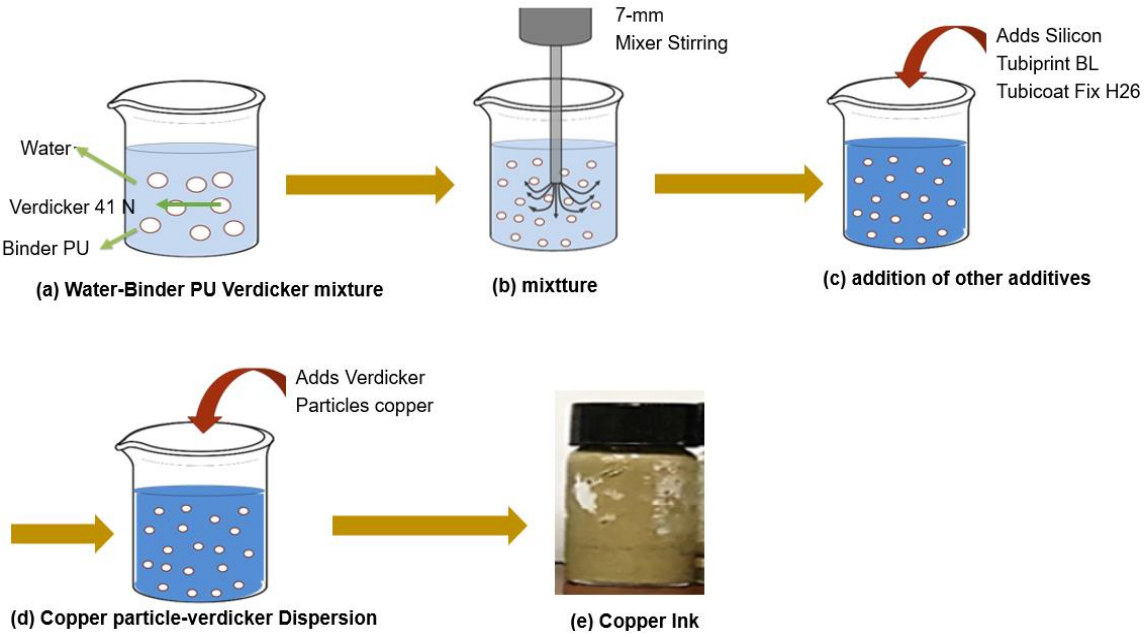

Figure 2.1. Formulation process with copper conductive ink.

2.1.2 Electroluminescent composite (EL)

2.1.2.1 Phosphorus particles

The effect of the permittivity of phosphor particles and the charging rate were studied to produce an electroluminescent composite. Initially, three types of metal-doped zinc sulfide phosphorescent materials (such as Cu, Cu, Al and Cu, Mn) were selected. Micrometric ZnS powders, with an average size of 3-9 µm respectively, were purchased from (Shanghai Dongzhou Industrial CO.LTD, China). Some properties of the metal doped ZnS powders are listed in Table 2.3. The powders were stored at room temperature and directly used to prepare the composite without any chemical modification. The substrates are 25x75 mm clear indium tin oxide (ITO) coated glass (100) 578274-25PAK. They were supplied by the company (Sigma-Aldrich). These materials were selected for the development of ACEL devices because of their customizable optical properties, their responsiveness to multiple electrical stimuli (electric field *E*), low optical contribution in the visible range, easy processing, compatibility with printing systems and the absence of curing agents during the manufacturing process.

Table 2.3. General properties of commercially available electroluminescent phosphors.

Description	Lighting color	Chemical Components
EL Phosphor D502S	Bleu-green	ZnS: Cu
EL Phosphor D417S	Dark Bleu	ZnS: Cu, Al
EL Phosphor D611S	Orange - white	ZnS: Cu, Mn

2.1.2.2 Polymer matrix

Also, three types of polymer matrices were selected including (descriptions shown in Table 2.4**)**:

1) polycarbonate purchased from (Sigma Aldrich 65553598-1EA, France);

2) poly(vinylidene-fluoride-trifluoroethylene) (P(VDF-TrFE) 70-30 mol.%), the so-called *copolymer*;

3) poly(vinylidene-fluoride-trifluoroethylene-chlorofluoroethylene) (P(VDF-TrFE-CFE) 56.2-36.3-7.5 mol.%), the so-called *terpolymer*. Both copolymer and terpolymer were purchased from Piezotech S.A.S, Arkema Group, Lyon, France.

Thèse accessible à l'adresse : https://theses.insa-lyon.fr/publication/2023ISAL0114/these.pdf © [L. Diatezo], [2023], INSA Lyon, tous droits réservés

Polycarbonate, a thermoplastic resin, possesses a number of attractive properties such as high impact strength, excellent elastic modulus, and broad temperature resistance [237,238]. These features, coupled with the fact that the polycarbonate is ease of colorability and compounding, almost unaffected by water and many inorganic and organic solvents, permit its use in a variety of applications. A very large, diverse, and important market has been developed for such a material, ranging from medical [239–241] to automotive [242], electronics[239], and so on [243].

Since the discovery of the piezoelectric behavior of poly(vinylidene-fluoride) — PVDF by Kawai [244] and the understanding of the molecular origin of this electroactivity [245–247], organic ferroelectric materials have attracted the interest of researchers for their potential use in specific applications such as low weight and flexible sensors [248], electromechanical devices [249,250], and high-K capacitors [251,252]. For electroactive applications, P(VDF-TrFE) copolymer is the most widely used thank to its low input poling field and high dielectric permittivity compared to other ferroelectric polymers [253–256]. Also, this copolymer does not need any mechanical stretching before the poling process [257]. It has been demonstrated that an electron irradiation of the P(VDF-TrFE) and the random incorporation of the CFE unit in P(VDF-TrFE-CFE) terpolymer can achieve an electrostrictive strain greater than 5% with respect to the copolymer [258,259]. As indicated in Table 2.4, the terpolymer, with its extremely high dielectric constant, gives rise to excellent electrostrictive response, especially when combined with plasticizers [260–262]. Furthermore, this material has been demonstrated to be biocompatible [263], flexible and adaptable to 3D printing technology [264,265], making it as one of the most appropriate candidates for various applications in sensor and actuator devices based on additive manufacturing [266–268].

The main purpose of this study is to find out, among several types of electroluminescent (EL) particles and polymer matrix, those that lead to a fabrication of composite with high performance EL response. In order to obtain EL device with easy process, low energy consumption, and effective cost, a simple design involving in a single-layered architecture is carried out. Regarding recent progress in the flexible ACEL devices, multilayered composites with stacking patterns have been revealed to achieve more compact and luminous systems [269–273]. This issue is considered as one of priorities in our future development where 3D printing is getting involved to improve precision and simplify the procedure in an automatic manner.

Table 2.4. General properties of commercially available dielectric matrices

Dielectric matric	ε_r between 500 Hz-1kHz	Module Young (MPa)	Matrix density (g.cm3)
Polyurethane	3	2200	1.2
Copolymer P(VDF-TrFE)	10	2000	1.8
Terpolymer P(VDF-TrFE-CFE)	35	100	1.8

2.1.2.3 Elaboration of EL composites-based casting method

For a sake of simplicity, the electroluminescent (EL) composites were firstly prepared using solution casting method that has been employed in our previous works [274,275]. The next subsection 2.2.2 will describe the additive manufacturing (AM) process of those materials based on the screen-printing technique.

Different volume fractions of composites, the contents of metal-doped ZnS microparticles and polymer matrix were calculated based on the volume mixing law given by:

$$\Phi_m = \frac{M_p}{M_p + M_m} \tag{2.1}$$

$$\Phi_{vol} = \frac{\rho_c - \rho_m}{\rho_p - \rho_m} \tag{2.2}$$

Thèse accessible à l'adresse : https://theses.insa-lyon.fr/publication/2023ISAL0114/these.pdf © [L. Diatezo], [2023], INSA Lyon, tous droits réservés

where Φ_m and Φ_{vol} are respectively the mass fraction and volume fraction; and M and ρ denote the mass and mass density, respectively. The subscripts c, p and m correspondingly denote the composite, the particles, and the polymer matrix. The mass density of the composite (ρ_c) can be calculated as following:

$$\frac{1}{\rho_c} = \frac{1-\Phi_m}{\rho_m} + \frac{\Phi_m}{\rho_p} \tag{2.3}$$

As illustrated in Figure 2.2, the elaboration of the ZnS consists of several stages.

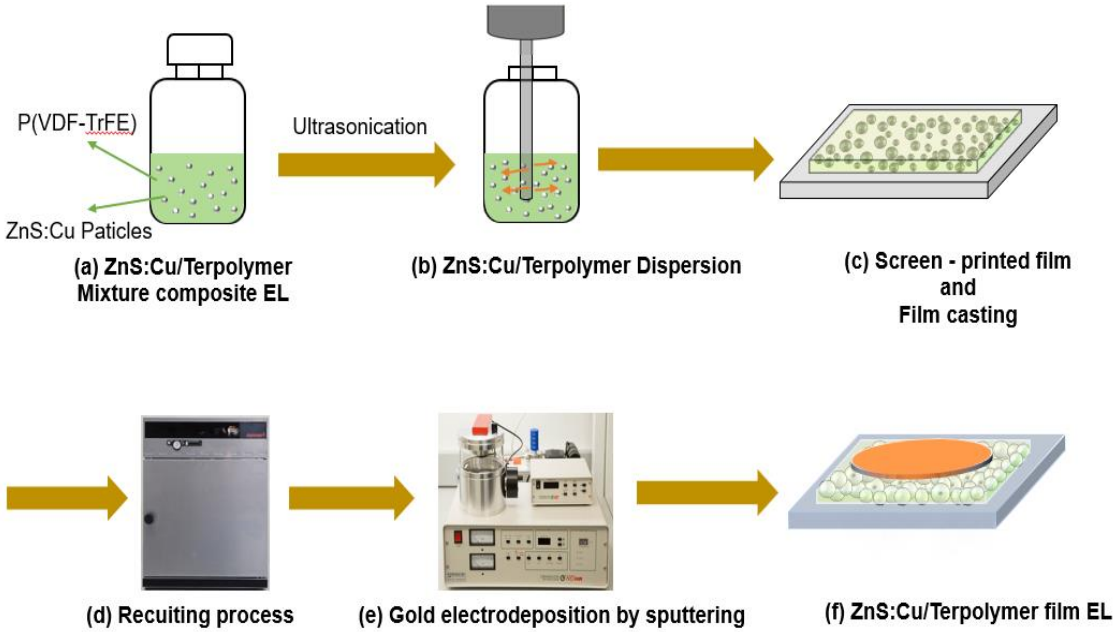

Figure 2.2. Elaboration of phosphorus composites based using a casting and screen-printing method, consisting of several stages: (a) mixing the metal-doped ZnS microparticles with a polymer solution at a specific ratio; (b) dispersing the ZnS particles by ultrasound to obtain homogeneous suspensions; (c) implementing the composite mixture onto ITO coated glass substrate and textile, and (d) thermal treating the film thank to annealing process; (e) depositing gold electrodes by sputtering technique, and (f) illustrating the whole electroluminescent sample with electrode deposition.

First, the polymer powder was dissolved in a specific solvent with a fraction of 14 wt% for 30 minutes. For the terpolymer and fluorinated copolymer, butanone (also known as methyl ethyl ketone or MEK) was chosen as solvent while in the case of the polycarbonate polymer, 1M dichloromethane was employed instead. The doped phosphorus microparticles were then introduced into the polymer solutions (Figure 2.2 (a)) with a volume fraction of 20 vol%, which was determined based on Equations (1)– (3). Second, a 2-minute ultrasonication (Hielscher Ultrasound Technology, UP400S) was performed for the whole solution under a ventilated table (I Type Cabinet B - ADS air Dusted), allowing a perfectly uniform dispersion of phosphorus particles in the polymer matrices (Figure 2.2 (b)). To be cast as a thin film, the mixture was poured on a glass substrate covered with indium tin oxide (ITO), as indicated in Figure 2.2 (c). The thickness of the film can be controlled by a specific slide, with a thickness of 50 µm, the size required in the experiment set. After that, the films were left to dry at room temperature of 20°C for 30 minutes. The drying process allows the volatile solvent to be removed, and then crystallized, as the three polymers are thermoplastic and semi-crystalline materials [276]. The casted films were then placed into the oven to be thermal treated through annealing process (Figure 2.2 (d)). This treatment allows the composites to grow and rearrange the crystal systems, homogenize the matrix as well as promote particles' distribution. At the beginning of the process, the temperature was gradually increased up to 115 °C for 2 h; then held at a steady state of 115 °C for 2h more; and slowly cooled down to the room temperature for 20h. Last, all annealed thin films,

Thèse accessible à l'adresse : https://theses.insa-lyon.fr/publication/2023ISAL0114/these.pdf © [L. Diatezo], [2023], INSA Lyon, tous droits réservés

corresponding to nine combinations of particle (phosphor with three different dopants) and matrix (among terpolymer, copolymer, and polycarbonate), were successfully made with the same volume fraction (20 vol%) and thickness (50 µm). A 20-mm diameter circular gold electrode were sputtered on the top with using a Cressington Sputter Coater (208 HR) that helps to deposit a very thin layer (25-30 nm). On the other hand, for the bottom electrode, the ITO conductive substrate was used with an area of 25×75 mm² and a thickness of 100 µm, leading to the total thickness of the whole sample of around 150 µm.

The aim is to manufacture composites containing increasingly higher fillers, up to the maximum concentration by volume, while improving their properties. However, above a certain concentration, metal doped ZnS microparticles tend to agglomerate and precipitate out of solution, resulting in high viscosity and non-uniform dispersion. These characteristics make them unsuitable for the manufacture of EL composite films. Microparticles can reach a higher maximum volume fraction, of the order of 40%, but this leads to poor dielectric and luminous responses.

2.1.2.4 Casting method

Electroluminescent devices are manufactured using the tape casting method. First, viscous solutions with the required composition are prepared. Next, we produce composite films by applying this solution to ITO-coated glass plates using an Elcometer 3700 doctor blade film applicator to control their thickness. Due to the concentration of the solution and the evaporation of solvents, an initial thickness of 500 µm, obtained with the Elcometer, turns into a final composite film thickness of around 50 µm. Annealing processes are then carried out as per section 2.1.2.3 in an oven to remove solvents. The dried films are removed from the oven, then a 20 mm diameter circular gold electrode is deposited on the top surface using a Cressington sprayer (208 HR), resulting in a very thin layer of around 25-30 nm. This is how we obtain our composite electroluminescent devices, as shown in Figure 2.3 above.

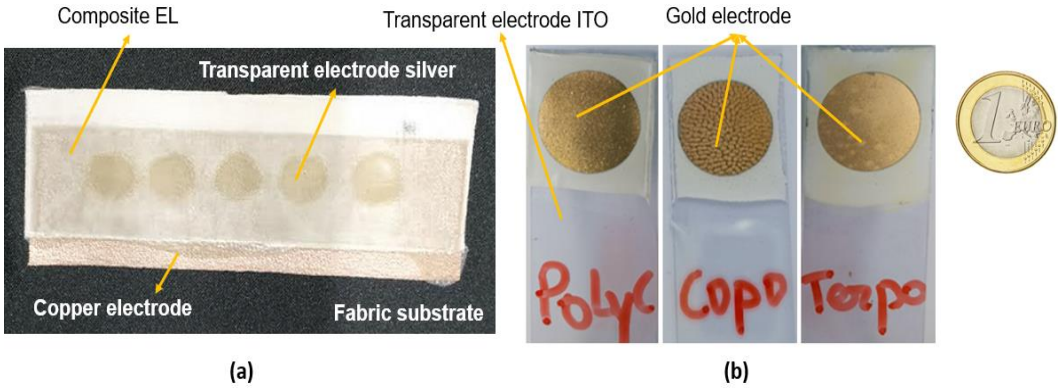

Figure 2.3. 50 µm-thick ZnS:Cu/matrix composite films with volume fractions of 20%: (a) EL device deposited on a textile substrate with a transparent silver electrode by screen printing technique and (b) EL device deposited on ITO-coated glass substrates with a gold electrode deposited by sputtering technique.

2.2 Additive manufacturing (AM) based screen-printing technique

2.2.1 Conductive coating

Various manufacturing processes have been investigated for the realization of stretchable interconnects. For example, thin sheets of copper have been laminated onto a TPU substrate, then etched to produce the desired in-plane stretchable shape [277]. Others have used one graphite-based, one polymer-based and two silver-based conductive inks, which were screen-printed onto four primer-coated metal substrates [278]. Inkjet printing has also been investigated as a manufacturing method for stretchable interconnects [229,279,280]. One of the most used methods is screen-printing, which is also employed in this thesis. The

Thèse accessible à l'adresse : https://theses.insa-lyon.fr/publication/2023ISAL0114/these.pdf © [L. Diatezo], [2023], INSA Lyon, tous droits réservés

choice of this method is mainly based on the fact that it is recommended by the ink manufacturer, as the screen-printing parameters allow precise control of ink deposition.

At the start of the process, the substrate is placed under the screen and the ink is applied evenly to the top of the screen. Next, the squeegee is pressed against the screen with such pressure that the screen stretches slightly and, at the same time, the squeegee moves towards the other end of the screen. The squeegee then pushes the ink through the screen and the ink is deposited on the substrate, resulting in a pattern defined by the screen. Screen printing is a technique that can be used to print on a wide variety of textile substrates.

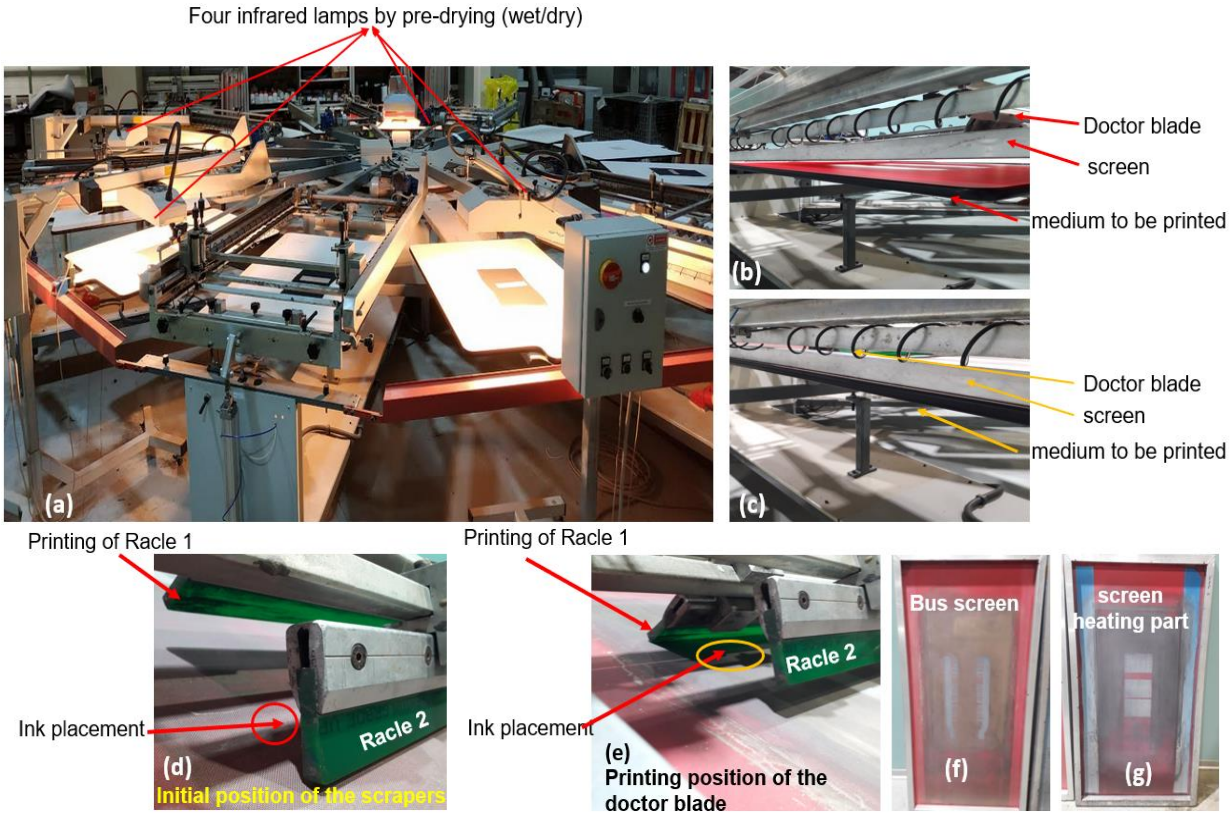

Figure 2.4. Silk-screen printing process used by Tesca.

As shown in Figure 2.4 (a) above, the rotary screen-printing machine used at Tesca is equipped with 15 tables and 6 positions, offering the possibility of printing up to 6 layers. Four dryers are positioned between the positions to pre-dry the ink applied to the textile. Dryers are particularly important when printing multiple layers (e.g., including carbon composite and copper electrodes) with significant thickness of app. 100 µm for each layer. As depicted in Figure 2.4 (b)-(c), the initial position of the machine acts as a separation between the screen and the table where the fabric substrate to be printed is located. Figure 2.4 (d)-(e) show the alternative rotational position of the two doctor blades with respect to the screen, which allow for an adequate distribution of ink regarding the desired pattern. Such a rotary machine possesses a 15 wires/cm mesh that is adapted to the copper patterns, as shown in Figure 2.4(f). Figure 2.4(g) illustrates a screen for a heating section of the carbon zone, as well as the two doctor blades with the same characteristics together with a lamp dryer.

As soon as being printed, the copper electrodes were put into a pre-drying system. The carbon ink was then printed above the dried copper layer. Subsequently, the whole sample were passed through an infrared oven at around 100–120 °C for 2 minutes, and crosslinking at 160-170°C for the same duration. It is important to note that there is no oven passage between the copper and carbon layers. Accordingly, the 3D

Thèse accessible à l'adresse : https://theses.insa-lyon.fr/publication/2023ISAL0114/these.pdf © [L. Diatezo], [2023], INSA Lyon, tous droits réservés

printing AM opted for this study allows to achieve high-quality prototype with complex patterns combined with multilayers, easy process, and less time consuming.

2.2.2 Electroluminescent (EL) composites

To screen printing the EL composites, we opted for a mesh size of 43 threads/cm and a thickness of 100 µm. The fabric substrate was cut into a dimension of 10 cm width and 20 cm length, then heated via an infrared oven at 160-170°C for 4 minutes to prevent wrinkling during the printing process. Figure 2.5 illustrated the printing setup, which is similar to the one described above on Subsection 2.2.1. Crosslinking of the printed coating (composed of the EL composite and the transparent electrodes) was carried out with the infrared oven at 160-170ºC for 10 minutes. The annealing process described in subsection 2.1.2.3 (Figure 2.2 (d)) was then performed, allowing to favor the crystalline growth and rearrangement, as well as to homogenize the matrix and the particle distribution.

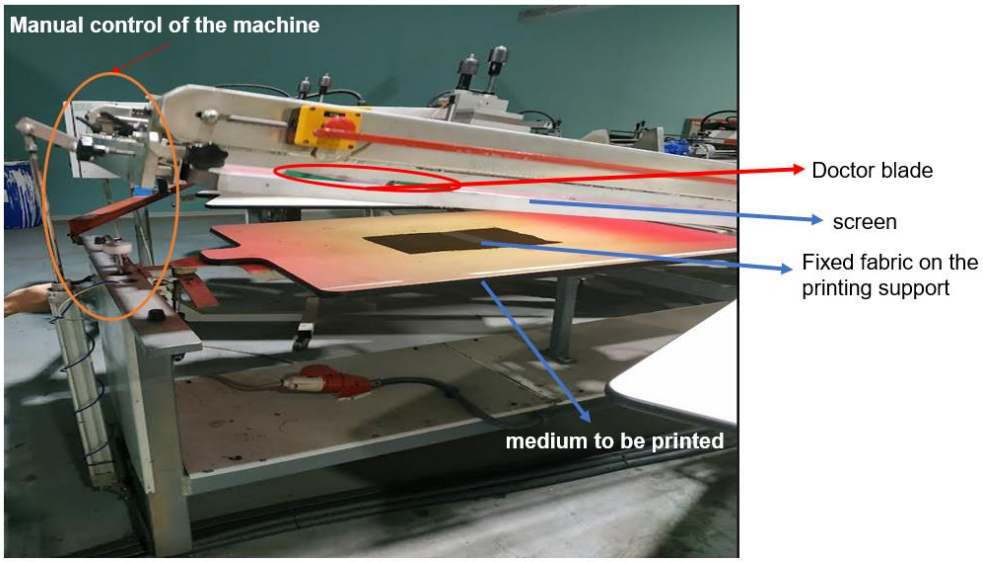

Figure 2.5. Screen-printing process for electroluminescent composites

2.3 Characterization methods based experimental measurements

Thermal and electrical characterizations of the composite ink were carried out using experimental measurements that can be adapted to a theoretical model based on mixing rules. Table 2.5. shows the various properties of the polymer matrices (PU and BGA) and conductive particles (Cu, Ag and C), such as thermal conductivity (λ), specific heat (Cp) and electrical conductivity (σ). These parameters are assumed to be constant over an operating temperature range from 0 to 50°C. The mass density (ρ) of the polymer matrix and particles, shown in the last column of Table 2.5, were used to determine the mass density (ρ_{comp}) of the polymer matrix and particles. The mass density (ρ_{comp}) and particle volume fraction (v) of the ink (shown in the last two rows of Table 2.1), using the following procedure rows of Table 2.1), following the mixing rules:

$$\frac{1}{\rho_{comp}} = \frac{1-w}{\rho_m} + \frac{w}{\rho_p} \tag{2.4}$$

$$v = \frac{\rho_{comp} - \rho_m}{\rho_p - \rho_m} \tag{2.5}$$

Thèse accessible à l'adresse : https://theses.insa-lyon.fr/publication/2023ISAL0114/these.pdf © [L. Diatezo], [2023], INSA Lyon, tous droits réservés

where *w* is the particle weight fraction of the various conductive inks, the values of which are given in Table 2.1. The indices *comp*, *m* and *p* refer to the composite, matrix and particles, respectively.

According to the literature [281], the electrical conductivities (σ) of polymer matrices (e.g. PU and BGA) are of the order of 10^{-12} – $10^{-8}\ S.m^{-1}$. This value, which is extremely low compared to that of conductive particles, should not significantly influence the σ value of the composite. It is therefore reasonable to take an average value of σ (~ $10^{-10}\ S.m^{-1}$) for the PU and BGA matrices.

Table 2.5. General properties of matrix and particles used in the composite inks.

	λ $(W.m^{-1}.K^{-1})$	C_p $(J.kg^{-1}.K^{-1})$	σ $(S.m^{-1})$	ρ $(g.cm^{-3})$
Polymer matrix	[282,283]	[284,285]	[286]	
Polyurethane (PU)	0.23	1500	~ 10–10	1.13
Butyl Glycol Acetate (BGA)	0.19	2000	~ 10–10	0.94
Conductive particles	[287,288]	[289,290]	[291–293]	
Cooper particles (C)	138	720	$\sim 1.0 \times 10^5$	2.26
Carbon particles (Cu)	380	380	5.98×10^7	8.96
Silver particles (Ag)	420	240	6.30×10^7	10.4

2.3.1 Morphology characterization

In order to visualize the surface condition and edge effect of the conductive coatings, morphological characterization by scanning electron microscopy (SEM) was carried out. Observational tests were carried out on the top surface and cross-section of the samples using compact SEM equipment (FlexSEM 1000II, Hitachi High-tech, Tokyo, Japan). These observations provide a better understanding of the interaction between the ink/tissue interfaces, which justifies the choice of materials, essential in the design developed. The quality of the conductive tracks on a textile substrate was also assessed, in order to improve the absorption of the inks inside the substrates, which can lead to a wide variation in the thickness of the conductive layers. Next, an analysis was carried out on the three electroluminescent composites using a microscope to evaluate and compare the dispersion of phosphor particles and the cohesion between fillers and matrices. The analysis was carried out under vacuum at 30 Pa, with a working distance (WD) of between 5 and 6 mm and an acceleration voltage (Vacc) of between 10 and 20 kV. Energy dispersive X-ray spectroscopy (EDS) was performed to obtain information on these inks.

2.3.2 Profilometry characterization

An MDL FP10 laser profilometer was used to measure the thickness of each deposited layer. Some key parameters were defined, including scan length (5000 µm), scan speed (60 um/s), sampling frequency (100 Hz) and stylus force (3 mg). Conductive layer thicknesses were measured using a profile on cross-sections of printed ink samples. The straight line (B) indicates the base of the fabric, while the straight line (A) corresponds to the gap between the fabric and the printed ink. The difference in straightness determines the thickness of the printed ink on the fabric substrate, as shown in Figure 2.6 as below.

Thèse accessible à l'adresse : https://theses.insa-lyon.fr/publication/2023ISAL0114/these.pdf © [L. Diatezo], [2023], INSA Lyon, tous droits réservés



Figure 2.6. Principle of thickness measurement by laser profilometer.

2.3.3 Electrical characterization of conductive inks

The electrical characterization of composite inks is carried out by determining their resistance (noted R). This enables us to estimate the material's conductivity (σ) using the following expression:

$$\sigma = \frac{l}{R \times S} \tag{2.6}$$

where *S* and *l* represent the surface area and length of the sample, respectively.

There are many methods for determining the resistivity of a material, but the technique can vary depending on the type of material, the magnitude of the resistance, and the shape and thickness of the material. One of the most common methods for measuring the resistivity of thin, flat materials, such as semiconductors or conductive coatings, is to use the two-point probe method. In this technique, two probes are brought into contact with a material of unknown resistance. A direct current is applied between the two probes, and a voltmeter measures the voltage difference between them. Resistivity is calculated from geometric factors, source current and voltage measurement. For direct resistance measurement, the ohmmeter (RM_804) used for this test comprises a DC current source, a sensitive voltmeter and a two-point probe (see Figure 2.7). To improve measurement accuracy, several resistance values are recorded with different distances between the two probes.

The simple mixing rule, used in practice, is an alternative phenomenological approach for estimating the electrical conductivity of composite inks (σ_{comp}). The most appropriate form of the mixing rule, which agrees with effective medium models and satisfactorily represents experimental data, can be written as follows [227,294]:

$$\sigma_{comp}^{\alpha} = (1-v)\,\sigma_{m}^{\alpha} + v\,\sigma_{p}^{\alpha} \tag{2.7}$$

where α_m and α_p are respectively the electrical conductivity of the polymer matrix and the particles, the values of which are available in Table 2.5. α is a power factor that can be determined by fitting equation (2.5) to the experimental conductivity values (detailed later in subsection IV.3). In the case of an ideal parallel arrangement of the particles, where the composite has a columnar structure oriented parallel to the direction of the electric field, the factor $\alpha = 1$. On the other hand, when the particles are connected in series and the aligned columns are perpendicular to the direction of the electric field, the factor $\alpha = -1$. In fact, the α value in real composites is determined by the composite morphology and lies in the interval $-1 < \alpha < 1$. In the case α→0, the power function described in equation (2.5) can be simplified as Lichtenecker's linear formula [227,295]:

$$\log(\sigma_{comp}) = (1-v)\log(\sigma_{m}) + v\log(\sigma_{p}) \tag{2.8}$$

As pointed out in [227,296], the electrical conductivity of plastic foams can be represented by Lichtenecker's formula.

Thèse accessible à l'adresse : https://theses.insa-lyon.fr/publication/2023ISAL0114/these.pdf © [L. Diatezo], [2023], INSA Lyon, tous droits réservés

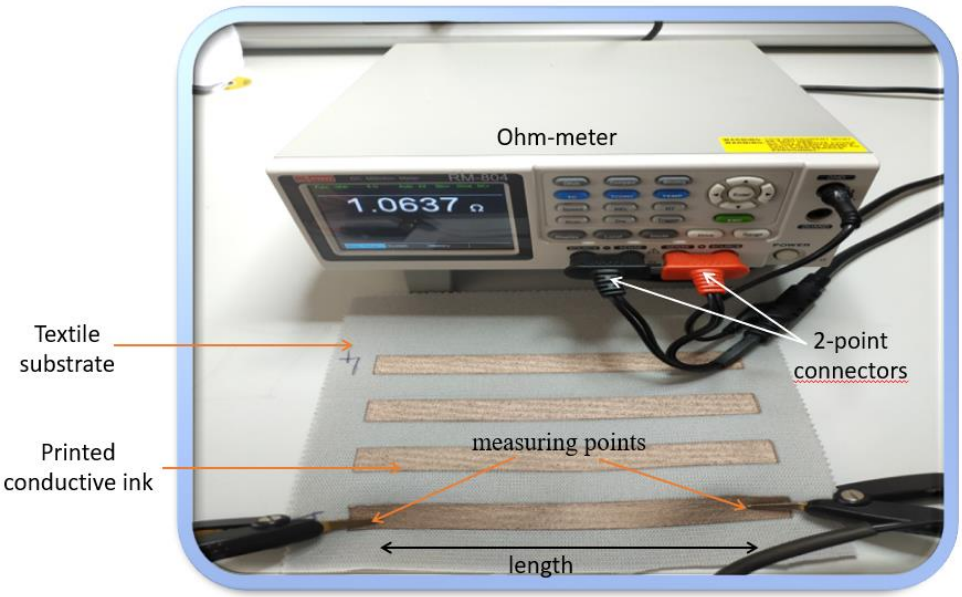

Figure 2.7. Experimental setup used for measurement of the electrical resistance.

2.3.4 Thermal characterization of conductive inks

A specific device (Jeulin, Ref. 253118, CS 21900, Evreux Cedex, France) was used to determine the thermal conductivity of samples (with or without coating), which were cut with the specific square shape with a length of 40 mm and a thickness of 2 mm. The sample was then inserted between two metal blocks whose height could be adjusted to eliminate the air gap appearing on the sample surface (see Figure 2.8.a). The lower block was set at room temperature, while the upper block was controlled by a heat source so that the temperature difference between these two blocks (ΔT) was perfectly regulated at 24°C. The thermal resistance (R_{th}) of the sample can thus be determined in steady state, i.e., defined as the ratio between ΔT and the heat flux induced (Q) through the thickness of the sample. Knowing the thickness (e) and surface area (S) of the sample under test, it is possible to deduce its thermal conductivity (λ) according to the following relationship:

$$\lambda = \frac{e}{R_{th} \times S} \tag{2.9}$$

After 10 minutes, when steady state had certainly been reached, λ and R_{th} values were recorded. All measurements were carried out at room temperature ($T_{amb} = 25°C$). To reduce uncertainty, each measurement was carried out on two samples assumed to be identical in terms of dimensions and physical properties, since they were cut from the same initial fabric [227].

On the basis of the thermal resistance measurements of the bare fabric (noted R_{th_nf}) and the coated fabric (noted R_{th_cf}), we can determine the thermal conductivity of the coating itself. A simple equivalent diagram of bare and coated samples is shown in Figure 2.8(b). If we consider the fabric and coating layers to be thermally connected in series, R_{th_cf} turns out to be the sum of R_{th_f} and the resistance of the conductive coating layer (R_{th_cond}):

$$R_{th_cf} = R_{th_nf} + R_{cond} \tag{2.10}$$

Finally, R_{cond} can be deduced from measurements of R_{th_f} and R_{th_c}. Consequently, the thermal conductivity of the conductive material (λ_{comp}) is estimated using the expression in equation (2.8).

Thèse accessible à l'adresse : https://theses.insa-lyon.fr/publication/2023ISAL0114/these.pdf © [L. Diatezo], [2023], INSA Lyon, tous droits réservés

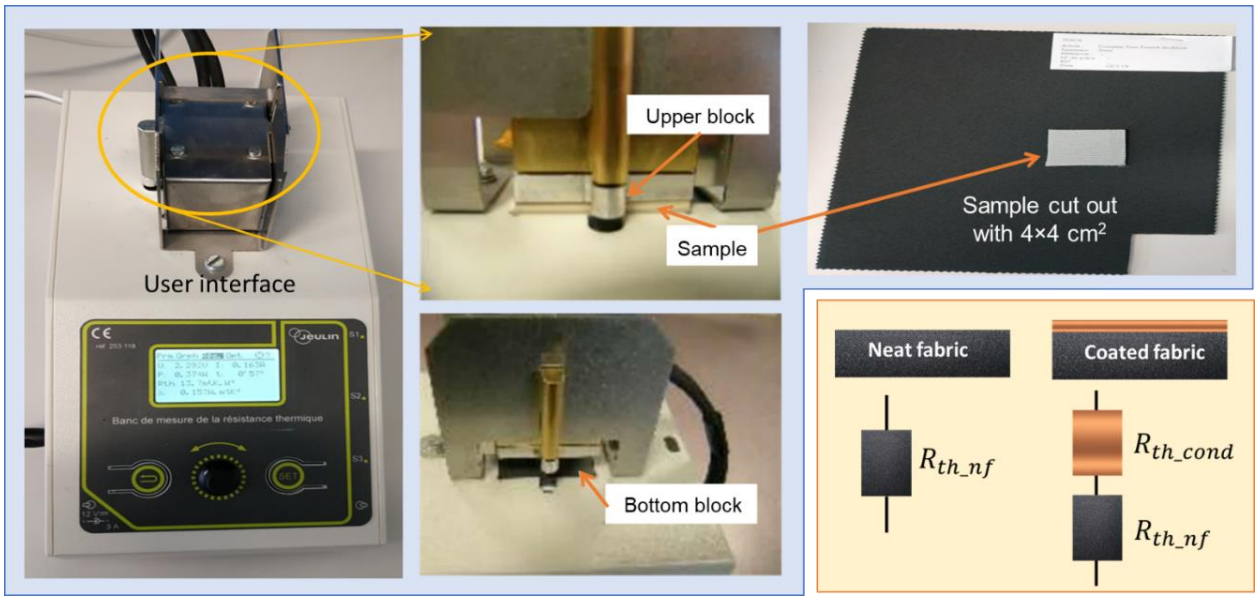

(a) (b)

Figure 2.8. Thermal characterization of fabrics with and without printed coatings: a) Thermal resistance measurement using a Jeulin device; b) Equivalent scheme of a simple thermal model.

Another approach is to predict λ_{comp}, which tends to increase with increasing particle volume fraction (v), based on an analytical mixing law. Maxwell's model, considered one of the most commonly used, is adapted to composites made up of a dispersed phase and a continuous phase. This model used for thermal conductivity is given by the following expression, particularly in the case of particles randomly dispersed in a polymer matrix [227,297,298] :

$$\lambda_{comp} = \lambda_m \frac{\lambda_p + 2\lambda_m + 2v(\lambda_p - \lambda_m)}{\lambda_p + 2\lambda_m - v(\lambda_p - \lambda_m)} \tag{2.11}$$

where λ_m , λ_pet λ_{comp} comprepresent the thermal conductivity of the matrix, particles and composite. The values of λ_m and λ_p are shown in Table 2.5, from which λ_{comp} can be deduced as shown in Table 2.6. It should be noted that the thermal conductivity of the composite inks is close to that of the matrix, given that the volume fraction of the particles is relatively low.

Table 2.6. Thermal properties the composite inks based on the mixing laws.

	$\boldsymbol{\lambda}$ $(\boldsymbol{W.m^{-1}.K^{-1}})$	$\boldsymbol{C_p}$ $(\boldsymbol{J.kg^{-1}.K^{-1}})$
C/PU composite	0.377	1266
Cu/PU composite	0.289	1052
Ag/BGA composite	0.274	908

As shown in [299], the specific heat capacity of a composite ($C_{p,comp}$) can be predicted by equation (2.12). In fact, ($C_{p,comp}$) is modeled as the weighted average of each constitutive heat capacity in the case of an isotropic material at constant pressure and volume (negligible thermal expansion) with no local deformation or stress [227,300].

$$C_{p,\,comp} = (1-w)\,C_{p,m} + w\,C_{p,\,p} \tag{2.12}$$

Thèse accessible à l'adresse : https://theses.insa-lyon.fr/publication/2023ISAL0114/these.pdf © [L. Diatezo], [2023], INSA Lyon, tous droits réservés

where *w* represents the concentration by weight of the particles dispersed in the inks (Table 1). $C_{p,m}$ and $C_{p,p}$ are are respectively the specific heat capacity of the polymer matrix and the particles, the values of which are given in Table 2.5. Finally, $C_{p,comp}$ of the three inks can be estimated (see Table 2.6) using equation (2.12). Due to its higher specific heat, the carbon composite can minimize temperature changes compared to its copper and silver counterparts. In fact, carbon takes slightly longer to heat up once it's energized. Conversely, copper and silver cool down faster than carbon.

2.3.5 Heatmap characterization of conductive inks

Figure 2.9. illustrates the experimental setup used to characterize the heating profile of a tablecloth (similar to a car seat, supplied by Tesca), which is implemented with the coated fabric developed in this study. The mat is electrically supplied with a 12 V DC voltage (Rohde & Schwarz HMP 2020 amplifier) via the connection with two main copper electrodes. The resulting current is then conducted to the carbon plates, which naturally generate heat by the Joule effect. This effect is well known as Joule's law, which states that the heating power (P) generated by an electrical conductor is equal to the product of its resistance (R) and the square of the current (I). I is measured using a current probe (Fluke 80 Meter Clamp). For an estimate of electrical-thermal conversion, voltage and current are recorded in real time using a DEWE-Soft SIRIUS card. To get a more intuitive picture of the web temperature (on the back side as opposed to the coating surface), an infrared thermal camera (Optris Xi400) was used during the experiment. Thermal imaging involves transforming infrared radiation measurements into a radiometric image, reflecting the thermal characterization of the web. Each pixel of the radiometric image is converted into a temperature value using complex numerical algorithms.

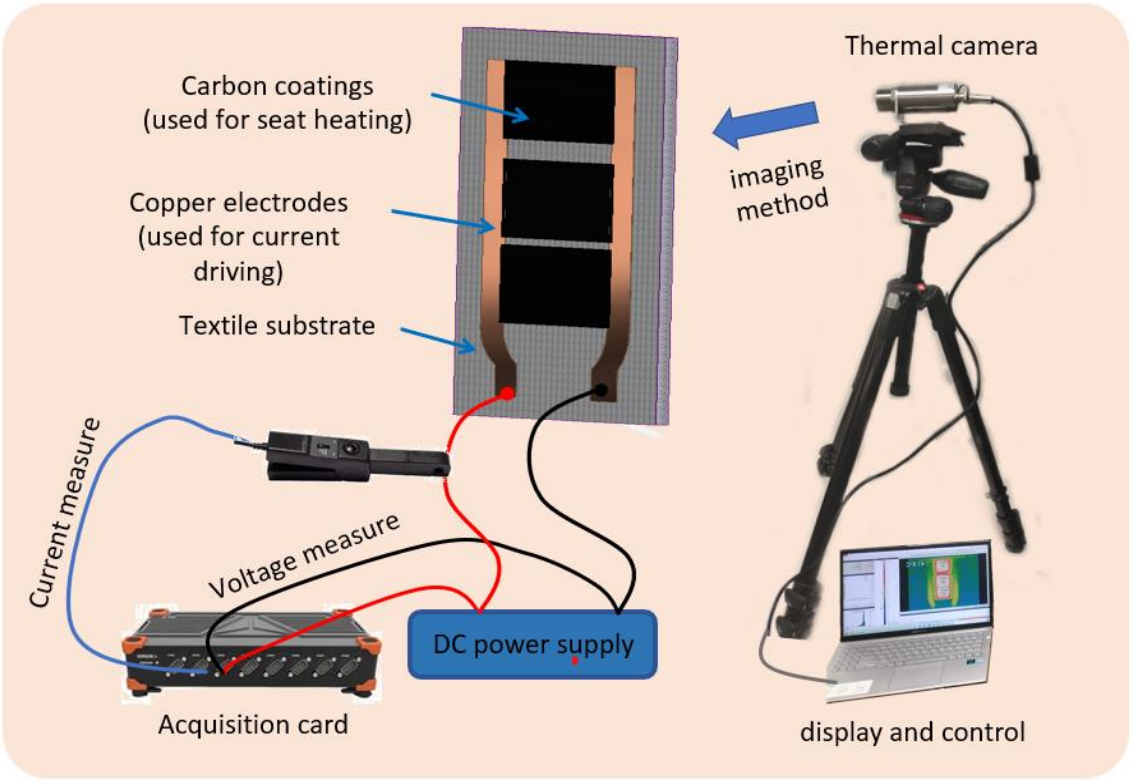

Figure 2.9. Schematic illustration of the measuring bench used for the thermal characterization of heated tablecloth.

Thèse accessible à l'adresse : https://theses.insa-lyon.fr/publication/2023ISAL0114/these.pdf © [L. Diatezo], [2023], INSA Lyon, tous droits réservés

2.3.6 Aging characterizations of conductive inks

To verify the durability and stability of the coated fabrics vis-à-vis the environmental changes, several aging tests were carried out including (1) a heating test, (2) a humidity test in a climatic chamber, and (3) a mechanical test. These tests must be consistent with the functional characteristics at the various phases of the product's life cycle. The specifications for assemblies, sub-assemblies or individual parts are values which must be validated in the final configuration of the vehicle.

2.3.6.1 Thermal cycle stability

The convection oven (Memmert 2-UFE400) is preheated to 100°C for 1 h, in accordance with the procedure described in Renaultt specifications. Afterwards, the sample is put into the 100°C oven for 24 h, and then cooled down at room temperature for 30 mn. Similar procedure can be repeated to create the samples undergone two-cycle treatment of 48 h. The treated samples (either with 24 h or 48 h), after 30 mn cooling down, are performed resistivity measurement as a function of the temperature variation.

2.3.6.2 Humidity cycle stability

The CTS Type C-70 climatic chamber (see Figure 2.10**)**, also known as a temperature test cabinet, is used to assess the material properties of a sample as a function of temperature and humidity. It is adequately ventilated with plenty of air circulation, ensuring efficient transmission to the sample. The air handling space is located at the rear of the inner chamber and the components, easily accessible from all sides. The control unit is integrated into the rear of the cabinet, while the operating unit is conveniently integrated into the test chamber door. The climatic/thermal stability chamber offers a working temperature range from – 70 °C to 180 °C. With a 2000-liter water capacity to control humidity inside the chamber, it can perform climatic aging cycles with an accuracy of ± 2 °C and ± 5 % relative humidity. The humidity range extends from 10 % to 98% between 10°C and 95 °C, with a dew point range from 7 °C to 94 °C. Temperature variation speed can be set between + 3.5 °C/min and – 2.5 °C/min.

Temperature and humidity aging studies, including 4AF+6BF cycles in accordance with PSA PEUGEOT - CITROËN specifications (as per D47 1309 [301]), was carried out over a 12-day period. The aim of this study was to evaluate the morphological and/or physical characteristics of the samples so as to check whether they had undergone any degradation. Concretely, the characteristics of the samples were determined by measuring their electrical resistance before and after the thermal and moisture (humidity) stability tests. This enables us to better highlight their impact on the electrical performance of the printed coating.



Figure 2.10. Thermal/climatic stability enclosures.

2.3.6.3 Mechanical stability

Monotonic tensile and compression tests were carried out with the Shimadzu TCE-N300 to evaluate the mechanical properties of the conductive ink coated on textile substrates, together with the evolution of strength as a function of displacement. Unit specimen samples were cut to a dimension of 15 mm wide and

Thèse accessible à l'adresse : https://theses.insa-lyon.fr/publication/2023ISAL0114/these.pdf © [L. Diatezo], [2023], INSA Lyon, tous droits réservés

150 mm long. Rectangular specimens with a size of approx. $15 \times 150\ mm^2$ were used for the tensile testing, as shown in Figure 2.11 (a). The thickness of all samples was accurately measured using a laser profilometer, and the dimensions were measured using a caliper. In the tensile mode, two sample's limits were set in the upper and lower clamps at a distance of 25 mm without displacement (model MWG-20kNA), and an increasing tensile load at a rate of 0.1 mm.s^{-1} was applied to obtain a stress-strain model. The coated fabric was subjected to increasing force until failure occurred. This experiment was used to determine the ultimate tensile strength (T_{max}), i.e., the maximum force with which the material can withstand before breaking when stretched. Compressive behavior was also studied in the context of a complete mechanical cycle. This involved loading the specimen until it reached maximum deformation, then unloading it until it returned to its initial position. Hundreds of compressive strain cycles (0.1 to 3%) were performed at strain levels of 0.1% and 3% on the substrate coated with conductive copper ink. The maximum stress reached at maximum strain was measured for each strain level. During both tests, axial force (F) and strain data (ΔL) were recorded at a sampling frequency of 100 Hz using TRAPEZIUM software. Stress-strain curves were then plotted by calculating the stress (i.e., $T = F/A$ where A denotes the surface perpendicular to the force F), and the strain (i.e., $\varepsilon = \Delta L/L_0$, L_0 is the initial length). The elastic modulus of the materials was derived from the slope of the stress-strain curve in the linear regime, based on elastic deformation behavior [227,302–305].

Finally, a mechanical endurance test was performed on the knee pads as shown in Figure 2.11(b), and a seating test was performed as shown in Figure 2.11 (c) on a car seat fitted with an integrated heating system. These tests were carried out in accordance with the SAE European standard using the J826 H-point dummy [306] from ETD Technical Trading based in D-21218 Seeveta, Germany. A load of 890 N was applied for 200,000 cycles at a speed of 100 cycles per minute [307]. During the test, temperature measurements were taken on all three areas of the carbon surfaces, for both sewn and unsewn samples.



Figure 2.11. Load frames for (a) tensile test as a function of sample size; (b) mechanical compression endurance test of knee strike on heating tablecloth, (c) sitting endurance test European SAE Standard using J826 H-point manikin.

2.3.7 Dielectric characterization of EL composites

A frequency response analyzer (Solartron, 1255) and a dielectric interface (Solartron, 1296A) at room temperature were used to measure the broadband dielectric spectroscopy, as shown in Figure 2.12. Each composite was placed in a sample holder (AMETEK, 12962a). To obtain accurate measurements, an AC voltage with an RMS value of 200 mV was applied at a frequency ranging from 0.1 Hz to 1 MHz [308].

Thèse accessible à l'adresse : https://theses.insa-lyon.fr/publication/2023ISAL0114/these.pdf © [L. Diatezo], [2023], INSA Lyon, tous droits réservés



Figure 2.12. Experimental setup for dielectric characterization

The principle of the dielectric spectrometer is to measure the magnitude and phase relationship between output and input signals as a function of frequency. Specifically, an AC voltage alternative $u(\mathrm{t}) = Ucos(\omega t)$ is applied to the sample, and the current density $i(t) = I\cos(\omega t + \phi)$ is measured, where ϕ is the phase shift, I and U are the current and voltage amplitudes respectively. For a parallel-plate capacitor, the capacitance C can be calculated as follows [308]:

$$C = \frac{A\varepsilon_0\varepsilon_r}{d} \tag{2.13}$$

where A is the area, d is the thickness, $\varepsilon_0 = 8.854 \cdot 10^{-12}$ F/m is the permittivity of vacuum, $\varepsilon_r = \varepsilon_r' - i\varepsilon_r''$ is the relative complex permittivity of the material, where ε_r' is the real part and ε_r'' is the imaginary part of the permittivity. Consequently, given the known parameters, the complex impedance Z of a capacitive medium can be calculated as follows.

$$\underline{Z} = \frac{u(t)}{i(t)} = \frac{U}{I}(cos\phi - j\sin\phi) = \frac{1}{jC\omega} \tag{2.14}$$

Combining equations (2.12) and (2.13), we can deduce that.

$$\varepsilon_r' = \frac{Id}{UA\varepsilon_0\omega}\cos(\frac{\pi}{2} - \phi) \tag{2.15}$$

$$\varepsilon_r'' = \frac{Id}{UA\varepsilon_0\omega}\sin(\frac{\pi}{2} - \phi) \tag{2.16}$$

and the electrical loss tangent is defined as follows.

$$\tan\delta = \frac{\varepsilon_r''}{\varepsilon_r'} = \tan(\frac{\pi}{2} - \phi) \tag{2.17}$$

Different experimental conditions are applied to dielectric spectroscopy measurements for various purposes: Characterization of frequency-dependent behavior over a wide frequency range from 0.1 Hz to 1 MHz in an ambient environment.

2.3.8 Luminance characterization of EL composites

The intensity of the emission light driven by the EL composite is quantified by a Mini-Spectroradiometer (SpectriLight ILT 560, InternationalLight), i.e., a measurement tool capable of determining both the wavelength and amplitude of the light. Spectrometer discriminates the wavelength based on the position the light hits at the detector array, allowing the full spectrum to be obtained with a single acquisition. Most spectrometers have a base measurement of counts which is the un-calibrated reading

Thèse accessible à l'adresse : https://theses.insa-lyon.fr/publication/2023ISAL0114/these.pdf © [L. Diatezo], [2023], INSA Lyon, tous droits réservés

and is thus impacted by the sensitivity of the detector to each wavelength. By applying a calibration, the spectrometer is then able to provide measurements of spectral irradiance/radiance, and/or spectral flux. This data is then treated with built-in or software based on numerous algorithms to provide equivalent readings of irradiance (W/m²), luminance (cd/m²), flux (lumens or Watts), etc. In order to assess the EL performance of the composite developed in this study, the luminance (denoted L) is chosen, which depends on several factors regarding the following expression:

$$L = \alpha . \varepsilon_o . \varepsilon_r . f . E \tag{2.18}$$

where α is the coefficient of EL conversion; f denotes the frequency corresponding to the emitted wavelength; E is the input electric field; ε_0 and ε_r denote the vacuum permittivity and the relative dielectric constant of the material. It is worth noting that for a given value of E, materials with higher ε_r leads to an improvement in the luminance, which in turn inversely proportional to its own emitted wavelength. This behavior is somehow corelate to the findings explored on our previous work where the EL composite is more sensitive with the blue ray (lower wavelength) than the red one [309].

Figure 2.13 shows the experimental bench for a characterization of the EL device. The light detector, spaced from the sample's holder by a distance of around 3 cm, was placed on the top of the sample to entirely capture light generated by the source. To properly evaluate the luminous efficiency that might be disturbed by the ambient light, both spectroradiometer and sample were implemented inside a protective enclosure to make sure particle tests being conducted under the absolute dark.

An alternative voltage was applied to the electrodes of the composite using a sinus waveform generator (Agilent, 33210A) coupled to a high voltage amplifier (Trek, model 10/10B). The resulting current was detected by a low-noise current preamplifier (Stanford Research Systems, SR570) with a tunable gain set from 10 to 500 mA/V. Both voltage and current signals were monitored and recorded in a digital storage oscilloscope (KEYSIGHT, DSOX1102G). An electrical polarization loop based on the current-voltage curve (or current density-electric field curve) was then obtained, allowing to determine with precision the electrical conductivity and the dielectric constant [310].

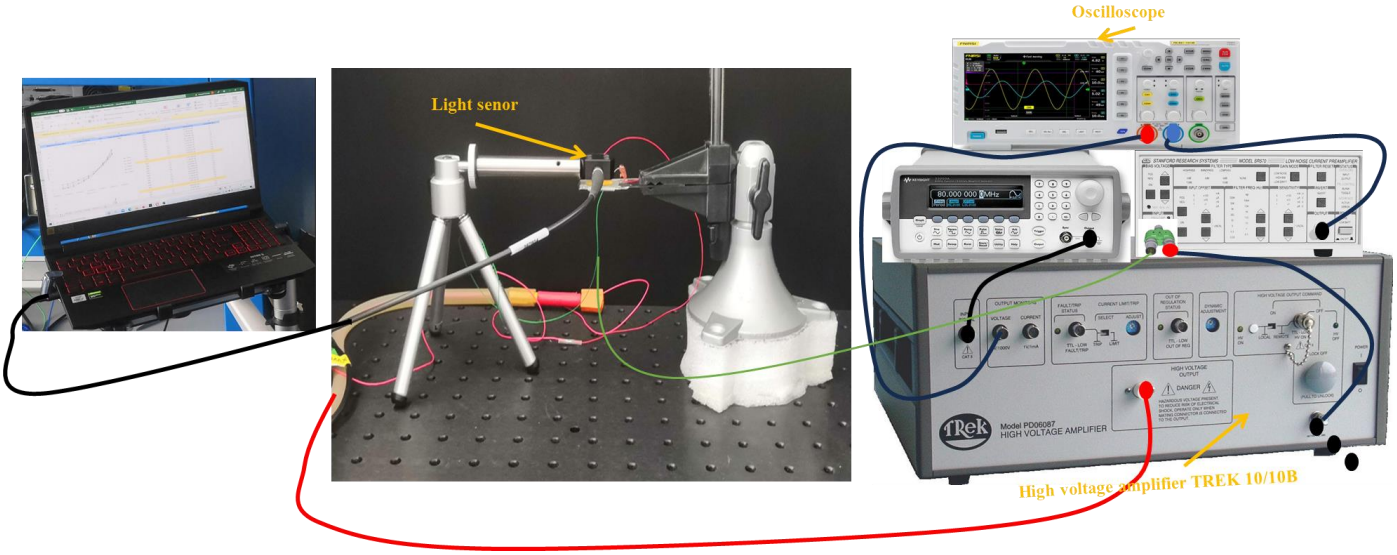

Figure 2.13. Electrical characterization bench for the electroluminescent (EL) device.

Thèse accessible à l'adresse : https://theses.insa-lyon.fr/publication/2023ISAL0114/these.pdf © [L. Diatezo], [2023], INSA Lyon, tous droits réservés

2.4 Characterization methods based finite element method (FEM)

2.4.1 Model of heating fabric

The finite element method is used to model and numerically simulate physical phenomena in electrical and thermal physics. This method is implemented using COMSOL Multiphysics software. The study consists in coupling these two physics to obtain a predictive 3D model in steady state and transient conditions. The equations required to build the finite element model are described in the following paragraphs.

In order to estimate the time required to reach the target temperature, a study based on a transient regime was carried out. The time evolution of the heating temperature profile (T) of the web (comprising a fabric covered with three layers of carbon plates and two layers of copper electrodes) can be estimated by the following first-order heat transfer problem [227,311,312]:

$$\rho_{tab} V C_{p_tab} \frac{\partial T}{\partial t} + \frac{1}{R_{th_tab}} (T - T_0) + h_c S (T - T_0) = \Phi_J \tag{2.19}$$

The system is modeled as a linear RC thermal circuit in which R_{th_tab} and C_{th_tab} are respectively the thermal resistance and specific capacity of the mat; ρ_{tab} represents its mass density; S is the exchange surface between the structure and the ambient air (corresponding to the three carbon patches); V is the heated volume ($V = S \times e$, where e is the thickness of the mat); h_c is the natural convection heat transfer coefficient; T_0 is the ambient temperature; and Φ_J is the injected electrical power. Note that $R_{th,tab}$ is taken as the sum of the three thermal resistances corresponding to a multi-layer structure (fabric/copper/carbon). On the basis of the geometric parameters and thermal conductivities of these three materials (Table 3.5 over chapiter 3), $R_{th,tab}$ was estimated to be equal to 1,34 W^{-1}. K. Since the volume of the fabric is much greater than that of the coating inks, while their mass densities are comparable, the weight fraction of the fabric proves to be the most important. Consequently, ρ_{tab} and C_{th_tab} are close to the mass density and specific capacity of the fabric, respectively. In other words, the copper and carbon coatings, due to their negligible mass, do not significantly alter ρ and C_{th} of the fabric substrate.

For the model in equation (2.19), the input power (Φ_J) is assumed to be made up of three terms. The first term (from left to right) is time-dependent and expresses the heat required to reach the limit temperature (T_l). When $T \to T_l$, there is no longer any temperature variation, and this term tends towards 0. The second term corresponds to the heat circulating within and through the materials themselves, from a hot surface to a cold one. The last term refers to heat transfer by free or natural convection due to air movement in the presence of a temperature gradient ($T - T_0$).

For initial and boundary conditions, where $T(t = 0) = T_0$ and $T(t \to \infty) = T_l$, the transient temperature follows the form of an exponential function, given by

$$T(t) = (T_0 - T_l)\, e^{-t/\tau} + T_l \tag{2.20}$$

where T_l corresponds to the temperature limit (steady state), which depends on Φ_J and other material parameters, and τ denotes the time constant, expressed as follows:

$$\tau = \frac{\rho_{tab} V C_{p_tab}}{h_c S + 1/R_{th_tab}} \tag{2.21}$$

Experimental and theoretical temperatures were compared using two data sets on the carbon plate (zone 2). The first data set was obtained using the optimized model (D2), which corresponds to the final design of the optimized, printed heating tablecloth. The second data set was obtained using the Tesca REF.22 tablecloth, which is considered to be the best-performing solution from an experimental point of view.

Thèse accessible à l'adresse : https://theses.insa-lyon.fr/publication/2023ISAL0114/these.pdf © [L. Diatezo], [2023], INSA Lyon, tous droits réservés

2.4.2 Model of electroluminescent composites

In this work, the finite element method (FEM) was applied to better understand the effect of the local field distribution seen by the phosphorus particles and its environment. A 3D anisotropic model of the composite ZnS:Cu/ P(VDF-TrFE-CFE) was built using the COMSOL Multiphysics tool, as described in the following 3 steps.

a) Geometry creation

As shown in Figure 2.14, the 3D composites are composed of a rectangular P(VDF-TrFE-CFE) polymer measuring 20 µm². In this polymer, spherical copper-doped phosphorus particles (ZnS:Cu) with a radius of 6.66 µm are incorporated. The proportion of these phosphorus particles is 3 particles to a volume of 20%. The particles are randomly dispersed in the polymer. To avoid undesirable effects at the edges, the 3 particles are brought closer together towards the center of the matrix. Different volume fractions from 10% to 40% were respectively designed by increasing the ZnS:Cu phosphorus concentration, but with different polymer matrix volume. In this study, an electric field of 5.5 V/µm is applied. The aim of this electric field is to understand the overall impact of permittivity gradients between the phosphor particles, the polymer matrix, as well as their light emission and environment.

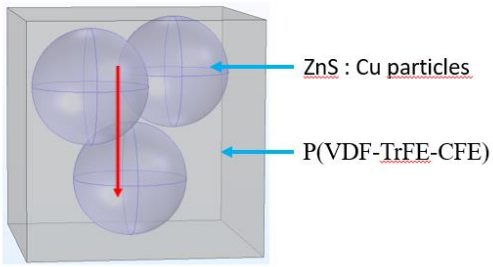

Figure 2.14. Geometric design of the ZnS:Cu/ P(VDF-TrFE-CFE) composite.

b) Model setting

The electrostatic module was used to simulate the effective permittivity of the ZnS:Cu/ P(VDF-TrFE-CFE) composite. The local electric field seen by the particles was evaluated by coupling the electric potential module with the electric circuit under the appropriate final conditions. Besides the physical parameters provided by COMSOL library, the dielectric constant and dielectric losses of the materials obtained from the empirical characterization were used to feed to the simulation model. Figure 2.2. shows the boundary conditions of the electrostatic modulus. The lower part of the matrix is grounded, while a potential is applied to the upper part, creating an electric field of 5.5 V/µm throughout the composite. Periodic electrical conditions were applied to the side walls of the matrix to form a tangential DC electric field across the periodic boundary. This simple 3D geometry can therefore be considered as the repeating unit representing the entire composite material.

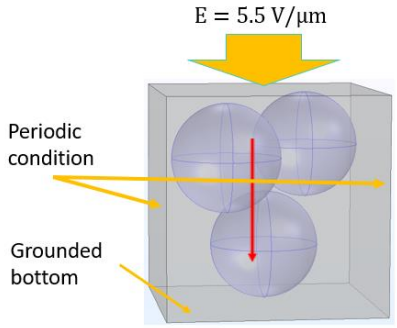

Figure 2.15. Boundary conditions of the electrostatic modulus

Thèse accessible à l'adresse : https://theses.insa-lyon.fr/publication/2023ISAL0114/these.pdf © [L. Diatezo], [2023], INSA Lyon, tous droits réservés

c) Model solving

The accuracy of the solution is influenced by the size and the number of the mesh elements. In our model, a physics-controlled fine mesh was chosen to improve the model precision. The dielectric prediction study was carried out in the frequency domain. The effective permittivity (ε_{eff}) of the composite can be calculated using the following formula [313]:

$$\varepsilon_{eff} = \frac{D}{\varepsilon_0 E} \tag{2.22}$$

where *D* is the charge displacement response of the material when subjected to a given electric field *E*.

2.5 Summary

This chapter revealed that the conductive inks including carbon and copper composites were successfully screen printed on a textile substrate. To solve the problem of electrode ageing with respect to the environment changes, optimization in the formulation of the copper solution was investigated. Regarding the electroluminescent (EL) materials, two approaches of fabrications were performed, comprising the conventional casting method as well as the 3D printing additive manufacturing (AM).

Electrical property measurements were then carried out to characterize the electrical conduction, thermal, moisture, mechanical and morphological behavior of the various components of a heating fabric (including carbon and copper inks coated on textile substrates), as well as the EL composites. The experimental set-ups developed during this study enabled to observe the evolution of the thermal and electrical conductivities of the fabrics printed with smart coating, also their aging effect.

In addition, a simple 3D model was built using the COMSOL Multiphysics tool to simulate and estimate the local field distributions observed by the EL particles and the complex simulation of a heating fabric. To achieve the best fitting between simulation and measurements, relevant physical parameters used in the simulation software of materials are carefully adjusted. Discussions regarding numerical solution together with empirical data will be thoroughly investigated in the next two chapters.

Thèse accessible à l'adresse : https://theses.insa-lyon.fr/publication/2023ISAL0114/these.pdf © [L. Diatezo], [2023], INSA Lyon, tous droits réservés

Chapter 3 Flexible conductive coating for heating textile : from materials characterizations to design optimizations

The aim of this chapter is to examine the design optimization of screen-printed composite coatings, as well as the characterization of their morphological, electrical and thermal properties, and the thickness of conductive coatings. The first prototype of a printed heating system combined with smart material design successfully meets the specifications of the automotive industry (Tesca Group). Thanks to significant optimization of the conductive patterns, it is possible to obtain a system with excellent performance, such as high heating efficiency, good temperature homogeneity and fast response, while avoiding overheating. Numerical solutions and empirical measurements are carried out to better understand the heating mechanism relating to the Joules effect of the composite coatings, in both transient and steady states. To highlight the new insights of our research, the most optimized prototype reported in this study is compared to the REF.22 design previously developed by Tesca. Before my thesis, the REF.22 patten has been considered as a best-performing solution used by the company to heat a car seat.

Thèse accessible à l'adresse : https://theses.insa-lyon.fr/publication/2023ISAL0114/these.pdf © [L. Diatezo], [2023], INSA Lyon, tous droits réservés

3.1 Materials' characteristics

3.1.1 Morphology analysis

Figure 3.1. shows SEM images in top view (a-c) and cross-section (d-e) for carbon, copper and silver inks. The aim of this study is to assess ink quality, including the homogeneity of particle dispersion and the level of ink penetration into the tissue substrate (which is related to fluid viscosity) [227].

As shown in Figure 3.1.(a), carbon ink produces a homogeneous printed surface, despite some tiny defects appearing on the coating layer. Copper ink produces a rougher surface, which may be due to the inhomogeneity of the particle dispersion. The light areas are rich in copper particles, while the dark areas represent the onset of atmospheric oxidation of the copper ink (Figure 3.1.b). Note that the particle size (median value) of the copper composite is around 10 to 20 times larger than that of the carbon composite. This explains why more detail is observed for copper particles, particularly when the images in Figure 3.1.(a) and (b) are manipulated under the same magnification. As shown in Figure 3.1.(c), the silver surface, on which large defects appear (in black), is not homogeneous compared to the others. This is because the silver ink, with its low viscosity unsuitable for 3D printing, is too liquid not to penetrate the pores of the fabric [314]. As a result, the fabric would not be completely covered by the printed silver surface, especially in the case of a thin coating layer. The presence of significant defects or large holes on the printed fabric using SEM analysis has also been mentioned in previous work [315]. Such a phenomenon could arise from solvent evaporation during the polymerization process, as well as from bubbles introduced in the 3D printing process.

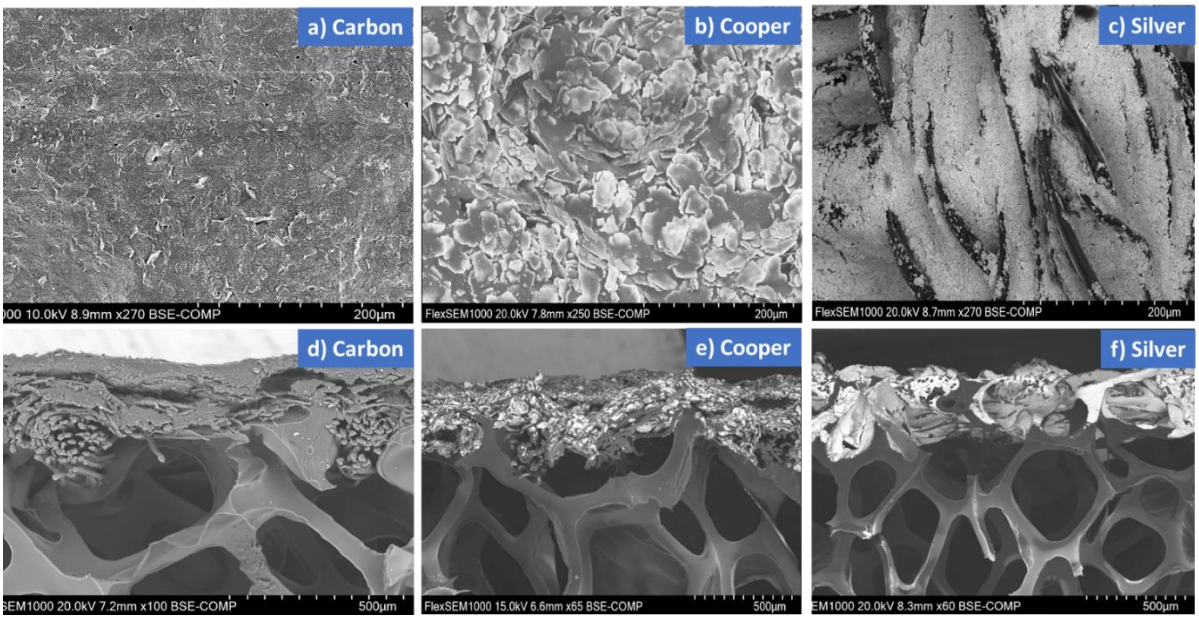

Figure 3.1. Micrographs of carbon, copper, and silver coatings respectively for a-b-c) the top view (Performed on the top surface); and d-e-f) for the edge view (performed on the cross-section) [227].

Further details on morphological properties can be found on cross-sectional micrographs. As shown in Figure 3.1.(d-e), carbon and copper inks are present on the surface of the fabric, confirming that their binding strength and viscosity are sufficient to maintain them in a good state of sharpness. Several unavoidable minor defects such as zigzag burrs and small catches are observed, but from a macroscopic point of view, they should not affect the electrical properties of the device. Finally, the SEM results demonstrate satisfactory print quality of the carbon-copper composites, which is essential for reliable heating

Thèse accessible à l'adresse : https://theses.insa-lyon.fr/publication/2023ISAL0114/these.pdf © [L. Diatezo], [2023], INSA Lyon, tous droits réservés

performance [316]. On the contrary, the silver ink in Figure 3.1 (f) shows excessive and irregular spreading on the edges of the fabric, on which zigzag burrs of the conductive lines form. The reasons for this effect are probably due to the rheological properties of the inks to some extent [317]. In addition, the fabric substrate is a regular multiscale porous structure as well as a rough surface so that its surface energy shows a regular variation. This results in different ink propagation in the inter-thread space compared to the fabric surface [318].

Finally, there is always a gap between the pressurized syringe and the porous substrate during the printing process. On the one hand, the periodic ink spills through the pressurized syringe onto the fabric substrate, resulting in the penetration of suspended ink, as well as the formation of zigzag burrs on the edges of 3D printed lines. On the other hand, surface roughness is one of many factors affecting the electrical properties of printed conductor lines. A smooth, uniform surface could enable the formation of continuous conductive lines and prevent short circuits [319,320]. For this reason, copper and carbon inks are considered the most suitable solutions for our final design [227].

3.1.2 Profilometry analysis

As illustrated in Figure 3.2 (a, c), the raw signal issued from the profilometer exhibited typical coffee-ring effect [322,323] when extracting topological data point from a surface of the printed coatings. Such an undesired effect could be post-treated via a percentile filtering method with 100-point smoothing in Origin software. After the treatment, the smoothy curves for both copper and carbon inks were obtained as demonstrated in Figure 3.2 (a, c). Figure 3.2 (b, d) showed the treated data corresponding to the layers' number of the coating whose thickness could be easily deduced based on those results. As seen in Figure 3.2(c, d), the carbon composite pattern is coarser at the two edges (in a symmetrical manner) and becomes progressively more refined towards the center. As a matter of fact, when dried at a low temperature (~ 30°C slow evaporation), almost 90% of suspended particles accumulate at the edge of the conductive line and form a spherical cap. In the case of the copper ink (see Figure 3.2(a, b)) where higher dried temperature is used, more particles settle in the center of a spherical cap (rapid evaporation), making the surface fraction of the annular region stable. Consequently, the thickness profile of the copper inks, whatever the number of the layers, is revealed to be more constant with respect to the one of the carbon.

Figure 3.2(e) shows the variation in thickness between two transverse lines as a function of the number of carbon and copper composite layers. Obviously, the thickness increases with the number of the layers, but not perfectly linear. Such a behavior can be supposed due to the fact that as the inks have not completely dried, there is a penetration of copper and carbon ink into the fabric pores. This observation is somehow consistent to the morphology analyses previously described in Subsection 3.1.1. Table 3.1 summarizes the average values of the thickness obtained from at least 15 samples for each type of ink.

Table 3.1. Average thickness measured by laser profilometer.

Textile substrate	Number of printed layers	Thickness of copper layer (µm)	Thickness of carbon layer (µm)
DOUBLURE FOAME	1	109	123
	2	131	120
	3	218	167
	4	326	204
	5	421	374

Thèse accessible à l'adresse : https://theses.insa-lyon.fr/publication/2023ISAL0114/these.pdf © [L. Diatezo], [2023], INSA Lyon, tous droits réservés

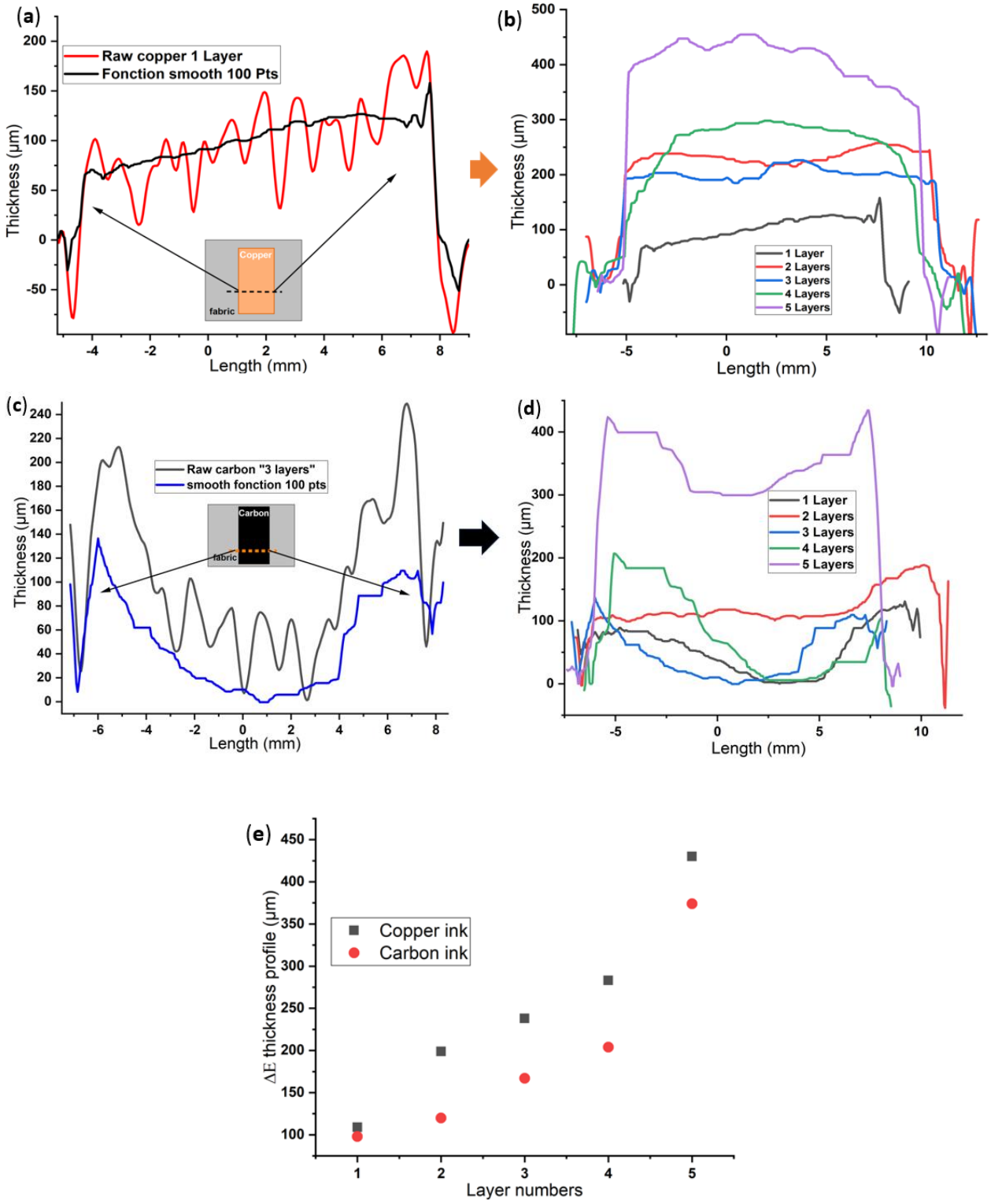

Figure 3.2. Thickness variation profiles observed on the textile substrates: (a) and (c) comparison between the raw and treated data for the copper and carbon inks respectively; (b) and (d) treated data with different layers of copper and carbon inks respectively; (e) evolution of the thickness variation versus the layers number of these two inks.

Thèse accessible à l'adresse : https://theses.insa-lyon.fr/publication/2023ISAL0114/these.pdf © [L. Diatezo], [2023], INSA Lyon, tous droits réservés

3.1.3 Thermal analysis

Table 3.2 shows the measured values for thermal resistance (R_{th}) and thermal conductivity (λ) of the raw fabric as well as the other coated fabrics printed with composite inks composed of C/PU, Cu/PU and Ag/BGA. As observed, the thermal resistance of the coated fabric (R_{th_cf}) is slightly higher than that of the pure sample (R_{th_nf}). Subtracting these values, we obtain the resistance of the conductive coating R_{th_cond}, according to the model in (Equation 2.9 cf. chapter 2). Coatings are stacked with different numbers of layers, resulting in a slight modification of (R_{th_cf}) (see Table 3.2). Logically, the higher the number of layers, the greater the (R_{th_cf}) value, which translates into an increase in R_{th_cond} (i.e., proportional to the coating thickness). Table 3.2 shows the value of R_{th_cond} calculated with 1 layer, enabling the thermal conductivity (λ_{comp}) of the corresponding composite to be determined. These values are consistent with those (cf. Table 3.1) estimated using the mixing law (Equation 2.10, cf. Chapter 2).

Table 3.2. Measured thermal conductivity of coated and neat fabric samples. The resistance and the conductivity of the conductive coatings were deduced from Equations (2.8) and (2.9) of Chapter 2.

	$\boldsymbol{R_{th}}$ $(\boldsymbol{W^{-1}.K})$	$\boldsymbol{\lambda}$ $(\boldsymbol{W.m^{-1}.K^{-1}})$
Fabric sample <u>without</u> conductive coating	20.16	0.062
Fabric samples <u>with</u> conductive coating of :		
3-layer C/PU	21.18	0.065
4-layer C/PU	21.55	0.064
2-layer Cu/PU	21.02	0.066
3-layer Cu/PU	21.45	0.064
3-layer Ag/BGA	21.52	0.064
Conductive inks (1 layer)		
C/PU	0.34	0.367
Cu/PU	0.42	0.296
Ag/BGA	0.45	0.280

The thermal resistance of the coated fabric is similar to that of pure samples, regardless of the composite ink chosen. In fact, the thickness of the coated layer is much lower than that of virgin fabrics, while its thermal conductivity (λ_{nf}) is in turn lower than that of (λ_{comp}) (Table 3.2). Consequently, R_{th_cond} is negligible compared to R_{th_nf}, which explains why the coating ink does not affect the thermal conductivity of the fabric (i.e., $\lambda_{cf} \sim \lambda_{nf}$). This hypothesis is validated in a design condition where the coating is sufficiently thin compared to that of the pure fabric[227].

Table 3.2. shows the results of measurements carried out on samples with different numbers of coating layers (two, three or four layers), demonstrating that the number of coating layers does not significantly alter the fabric's thermal resistance. However, it does affect the flexibility of the textile, which becomes stiffer with a greater number of conductive coating layers. Consequently, the number of layers has been chosen to be less than four. On the other hand, as the fabric is quite porous and a small amount of ink can penetrate the fabric (see SEM image in section 3.1.1), more than one coating layer is preferable. Based on the best compromise between fabric mechanical flexibility and print quality, the number of coating layers was chosen to be equal to two or three, which is considered the most optimized design configuration [227].

Considering that the entire system is supplied with the same heat flux (Q) throughout its entire thickness, the temperature variation (ΔT) of the fabric itself turns out to be much higher than that obtained by coating.

Thèse accessible à l'adresse : https://theses.insa-lyon.fr/publication/2023ISAL0114/these.pdf © [L. Diatezo], [2023], INSA Lyon, tous droits réservés

In other words, the ratio (ΔT) between the fabric and the coating is equal to the corresponding resistance ratio, as expressed in the following Equation 3.1 [227]:

$$\frac{\Delta T_{fabric}}{\Delta T_{coating}} = \frac{R_{th_fabric}}{R_{th_coating}} \tag{3.1}$$

On the basis of the thermal resistance given in Table 3.2, it appears that the above ratio is equal to around 20 with the three-layer coating or 60 with the single-layer coating. This means that almost all the heat flux energy is transmitted to the fabric, while a very small amount of heat loss is due to the conductive coating. The above results confirm the high efficiency of the system developed to heat a car seat.

3.1.4 Electrical analysis

Figure 3.3(a) shows the evolution of the electrical resistance of the three coatings as a function of sample length, which is defined by the distance between the probes at two fixed points on the samples. Figure 3.3(b) shows the conductivity of all coatings, i.e., deduced from the expression of Equation 2.5 (cf. Chapter 2).

Copper and especially silver composites show extremely low resistance values, reflecting the high electrical conductivity of the corresponding particles (see Table 2.5 of Chapter 2). Such low values could lead to high measurement uncertainty, explaining why resistance is not perfectly linear with length. As shown in Figure 3.3(a), carbon composite has a significantly higher resistance than the other two inks, making it effective in producing the Joule heating effect. For a given moderate current, higher material resistance results in higher heating power. It should be noted that the resistance value of the carbon composite is sufficiently high compared to that of the copper and silver inks, resulting in a lower uncertainty measurement. As a result, the carbon sample shows a better linear trend in resistance, making the estimation of its electrical conductivity (σ) more accurate. As shown in Figure 3.3(b), σ of the carbon composite is almost constant with different lengths, while that of the copper and silver composites fluctuates slightly. In addition to uncertainty, this behavior could be affected by sample homogeneity, depending on how the particles disperse in the polymer matrix.

Figure 3.3 shows the conductivity of the three composites, calculated as the average of the four values shown in Figure 3.2(b), then fitted to the model of Equation 2.8 (cf. chapter 2), allowing the power factor α to be determined. All samples lead to a similar value of α, which correlates with results found in the literature. Landau et al [102,103] derived with $\alpha = 1/3$ for any isotropic two-phase mixture, which is similar to our case. It should be noted that the mixing rule of (Equation 2.8) with constant α is in agreement with effective medium models or percolation theory only in a narrow concentration range. In other words, α must be different within the dilution limits. For example, at $v \to 0$ (particle-free composite) and $v \to 1$ (composite with 100% particles) for spherical particles, $\alpha = 2/3$ and $\alpha = -1/3$, respectively. Consequently, the theoretical value $\alpha = 1/3$ is the arithmetic mean between the two limit values [324,325]. As the composite inks used in this study were manufactured with a low particle concentration (less than 20%), the α factor can be considered constant. Finally, these results may help to better understand the combined structure of fillers in the polymer matrix, which will broaden the field of application of these materials [227].

As a result, electrical analysis leads to the conclusion that copper and silver composites have interesting properties that can be used as electrical electrodes with good electrical conductivity. The carbon composite, however, is more suitable for use as a heating resistor, thanks to its reasonable resistance value (i.e. not too high to conduct electricity, and not too low either to dissipate sufficient Joule heat). Thermal analysis reveals that all composites have the ability to enhance thermal conductivity without radically altering the fabric's thermal properties. Finally, SEM morphological analysis shows poor printing quality of silver ink, justifying its absence in the design of a real prototype.

Thèse accessible à l'adresse : https://theses.insa-lyon.fr/publication/2023ISAL0114/these.pdf © [L. Diatezo], [2023], INSA Lyon, tous droits réservés

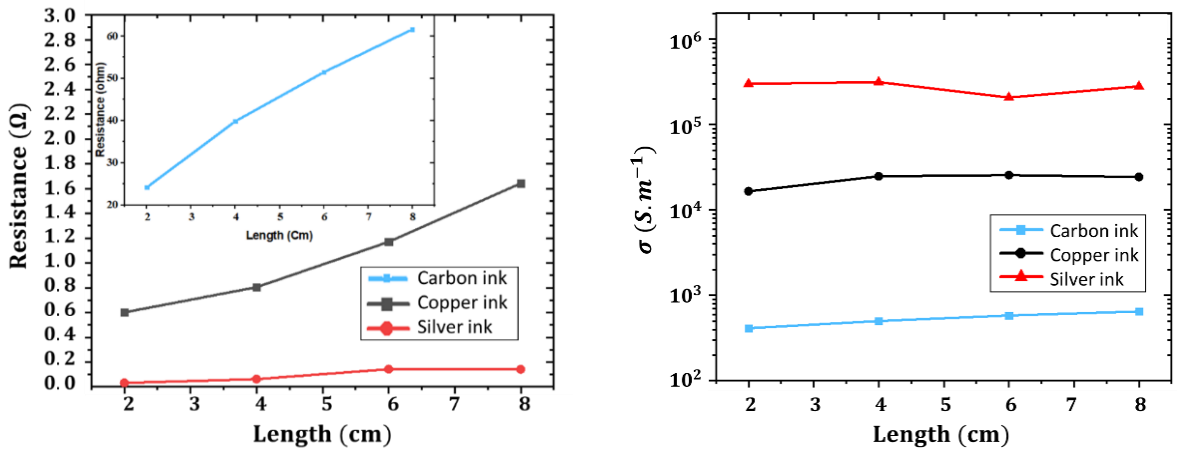

(a) (b)

Figure 3.3. Evolution of the electrical property as a function of the length of different conductive inks: (a) electrical resistance; (b) electrical conductivity [227].

Table 3.3. Measured electrical conductivity (σ) and fitting factor (α) [227].

.	$\boldsymbol{\sigma}$ $(\boldsymbol{S.m^{-1}})$	$\boldsymbol{\alpha}$ **(fitting factor)**
C/PU composite (17.6 vol%)	$4.23E+2$	0.317
Cu/PU composite (7.8 vol%)	$1.43E+4$	0.307
Ag/BGA composite (12.8 vol%)	$1.88E+5$	0.323

To assess the dispersion of conductive inks, electrical resistance was measured on seventy identical samples printed with either a carbon or copper layer. The box plot in Figure 3.4. gives a statistical overview of the results obtained on these 17 samples, including the locality, dispersion and asymmetry of the data acquired. Numerical values including mean value, coefficient of variation (noted *VR*, which is equal to the ratio between standard deviation (SD) and mean), maximum and minimum values are shown in Figure 3.4. The three quartiles are also indicated, Q_1 being the 25th percentile (also called the lower quartile), Q_2 the 50th percentile (i.e., the median of the data set), Q_2 the 75th percentile (also called the upper quartile), and *IQR* the interquartile range. To better assess the variability of the data, we provide here an estimate of the quartile dispersion coefficient (*QCD*), given by Equation 3.2. The higher the *QCD* value, the more dispersed the data set [227].

$$QCD = \frac{Q_3 - Q_1}{Q_3 + Q_1} = \frac{IQR}{Q_3 + Q_1} \tag{3.2}$$

As in the discussion above, the copper coating results in a high dispersion of the data, with electrical conductivity (σ) ranging from $0.5\text{–}2 \times 10^4\ S.m^{-1}$. On the other hand, carbon coating shows a lower dispersion, with a range of $3.3 - 4.6 \times 10^2\ S.m^{-1}$. The detailed box plot data in Figure 3.3. leads to the following conclusion [227]:

- In terms of mean and median electrical conductivity values, it's clear that the copper composite has better electrical performance than the carbon composite.
- In all cases, the data distributions are asymmetrical, with the median (horizontal lines inside the whisker box) higher than the mean (the cross). Consequently, the distributions obtained for the

Thèse accessible à l'adresse : https://theses.insa-lyon.fr/publication/2023ISAL0114/these.pdf © [L. Diatezo], [2023], INSA Lyon, tous droits réservés

copper and carbon samples are asymmetrical to the left (or negative asymmetry). to the left (or negative asymmetry), appearing as curves inclined to the right.

- None of the measurements showed outliers or extreme values (i.e., below $Q_1 - 1.5\,IQR$ or above $Q_3 + 1.5\,IQR$), meaning that the highest and lowest values were within this range.
- A more detailed analysis of data dispersion using two relative coefficients, *VR* and *QCD*:
- The *VR* and *QCD* coefficients were calculated in different ways, but have similar values, whatever the composite studied. Both coefficients are considered relevant indicators for effective analysis of data variability.
- Electrical measurements of copper cladding show a significantly higher dispersion than those of carbon cladding, which is ultimately linked to measurement accuracy.
- In the carbon coating, the *QCD* and *VR* values are relatively low, confirming good data repeatability (< 7%). This is in contrast to the copper cladding, where these coefficients exceed 20 %. This is due to the low resistance values of copper, which considerably increases measurement uncertainties [227].

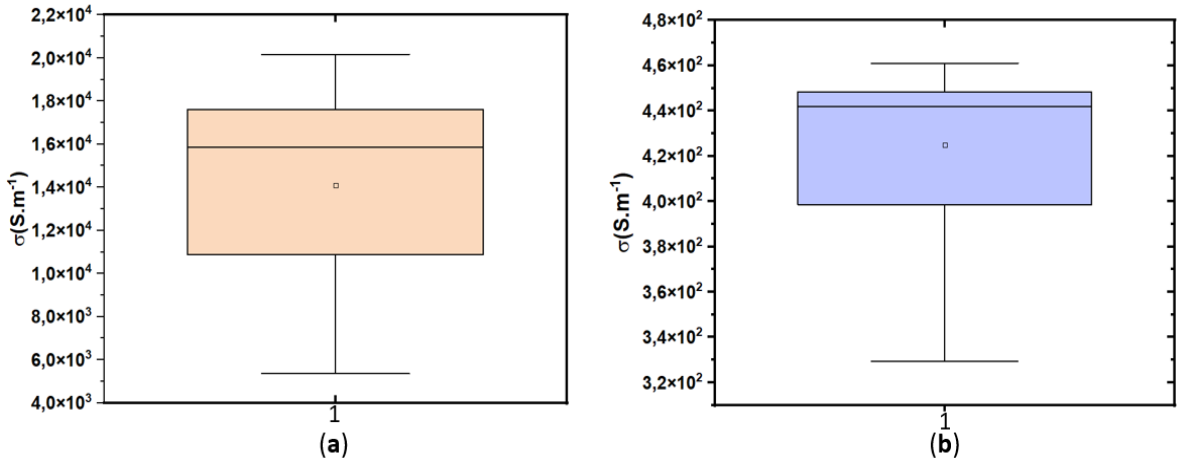

Figure 3.4. Whisker-box plots calculated from 17 samples coated with (a) copper or (b) carbon composites [227].

Table 3.4. Statistical data relating to the electrical properties of conductive coatings. All parameters have the same unit of electrical conductivity $\sigma\ (S.m^{-1})$, with the exception of the two relative coefficients *VR* and *QCD* in % [227].

$\sigma\ (S.m^{-1})$	*Mean*	*VR*	*Min*	*Max*	Q_1	Q_2	Q_3	*IQR*	*QCD*
Cu/PU composite	4.3×10^2	28.7%	3.3×10^2	4.6×10^2	4.0×10^2	4.4×10^2	4.5×10^2	50	23.7%
Cu/PU composite	1.4×10^4	6.9%	5×10^2	2.0×10^4	1.1×10^4	1.6×10^4	1.8×10^4	7×10^3	5.9%

3.2 Specifications and design rules

The system modelled here is based on the Tesca's top-performing REF.22 solution. The heating fabric is designed to be integrated into a web (i.e., assimilated to a car seat), which must meet the following specifications defined by Tesca-group [227]:

- Temperatures generated range from 40 °C to 43.5 °C at the rear of the heating surface;

Thèse accessible à l'adresse : https://theses.insa-lyon.fr/publication/2023ISAL0114/these.pdf © [L. Diatezo], [2023], INSA Lyon, tous droits réservés

- Good homogeneity of the different heating zones, with a maximum deviation of 0.5°C;
- The transient response time (i.e., the time required to reach the target temperature) must not exceed 2 minutes;
- Hot spots should be avoided at all costs ($peak < 45°C$).

In addition, the printed coatings (copper and carbon) need to be flexible and as thin as possible so as not to alter the properties of the fabric substrate. As shown in Figure 3.5(a), a 3D system consists of a rectangular fabric substrate on which a flexible electrical heating circuit is printed. The circuit consists of two main copper electrodes directly connected to a 12 V DC supply voltage, and three heating resistors made of carbon composites. The two copper supply buses are divided into three segments containing several sub-electrodes of identical cross-section, enabling the same current to be transmitted to the three resistors across the connection points [227].

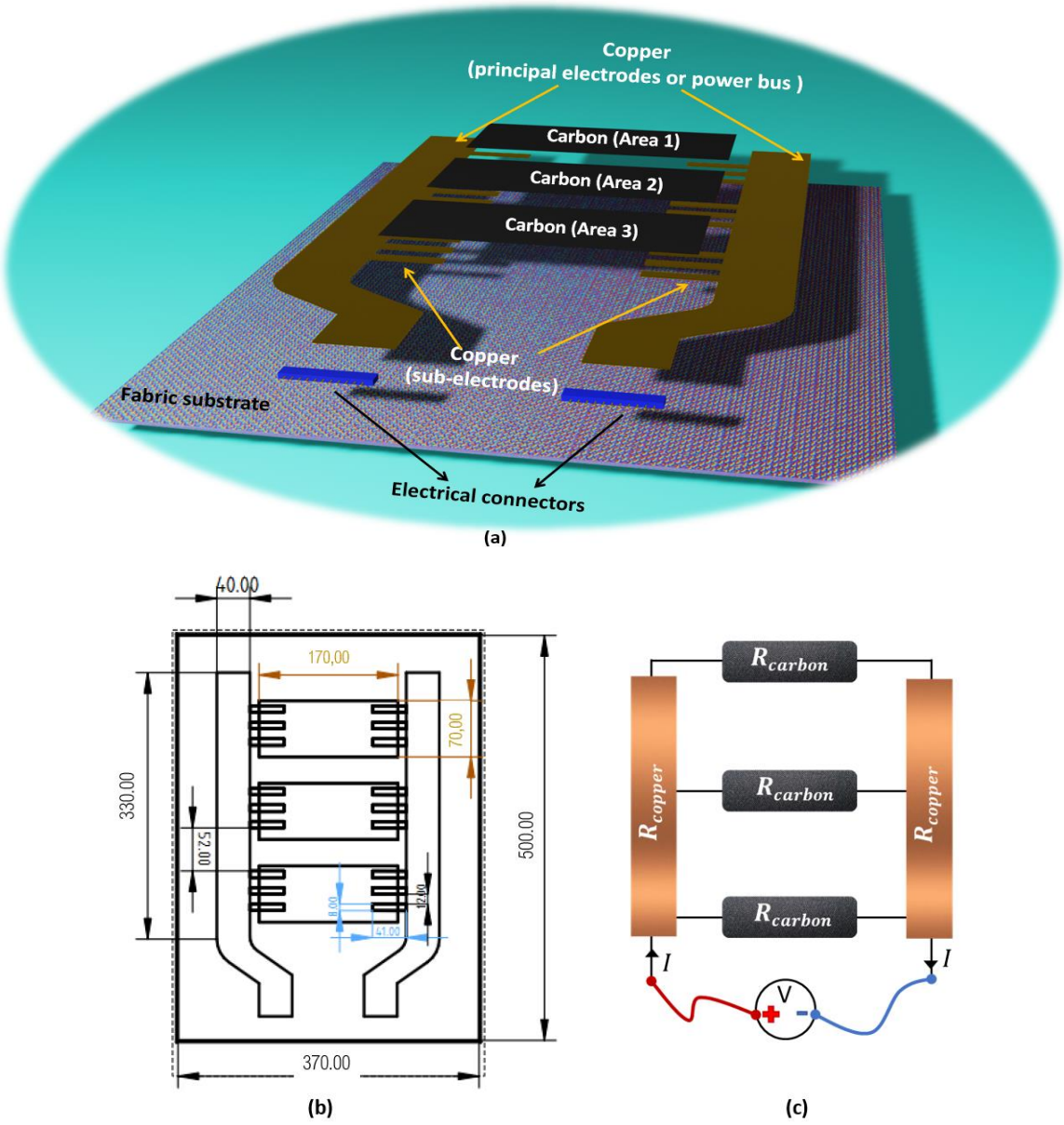

Figure 3.5. a) Heating system composed of copper tracks and carbon patches built on a fabric substrate; b) 2D dimension of the heater design; c) Equivalent electrical scheme [227].

Thèse accessible à l'adresse : https://theses.insa-lyon.fr/publication/2023ISAL0114/these.pdf © [L. Diatezo], [2023], INSA Lyon, tous droits réservés

The analyses lead to an initial heating system design with a good compromise between the dimensions of the copper supply bus and the carbon resistors (Figure 3.9). As demonstrated later in section 3.3.1.2, two fundamental problems persist in this design: the presence of significant lateral hot spots (overheating) and temperature inhomogeneity between the three carbon zones. Since zone 3 is closer to the energy source, it is expected to attain higher temperature than the other zones.

The geometrical characteristics of the carbon plates have been adapted to obtain a reasonable resistance at room temperature (around 5 to 10 Ω for each heating zone) and to minimize the energy consumption of the mat [326]. In order to improve temperature distribution, the three carbon elements have the same dimensions with maximum heating surface, which should make it possible to obtain a homogeneous temperature for all zones. The width of the copper feed bus must be sufficiently large (~40 mm) to facilitate current flow, which in turn is hampered by the thin conductive coating (a few hundred µm). The resistances of the main electrodes have been designed to be equal to around 2 to 3 Ω, which is small enough to minimize Joule effect losses. The subdivided electrodes, on the other hand, were built with a narrow width, as they receive a much lower current intensity. Due to their short length, the resistances of the sub-electrodes were considered negligible, resulting in a simplification of the equivalent electrical model of the fabric (Figure 3.5 (c). As can be seen, the copper power bus plays a key role in conducting the electric current, while the carbon patches contribute to the electrical-thermal conversion, with the aim of efficiently heating the fabric to the target temperature [227].

3.3 Design optimization based on FEM

This study focuses on the optimization of heat transfer in a sheet, based on the numerical solutions of a finite element model (FEM). Generally faster and less costly than physical experimentation, this is a powerful method of great interest in many fields of application. The results of numerical simulations can be used to select the optimum operating parameters, while complying with the imposed specifications [227].

3.3.1 Simulation Model Built in COMSOL

The FEM used in this study involves both electrical and thermal behaviors, which are suitably coupled to obtain a predictive 3D model of a heating tablecloth. The main geometric and physical characteristics of the three materials used in the model are summarized in Table 3.5. The parameters of the conductive inks were deduced from experimental characterizations and analytical mixing rules, which will be detailed in Sections 3.1 and 2.3 of Chapter 2. Some properties of the fabric substrate were found in the COMSOL library [227].

The thermal radiation effect of the materials is considered: emissivity (ε) is equivalent to 0.9 for the carbon ink and substrate, while it is only 0.5 for the copper electrode. To assess the effect of dissipation induced by natural convection from free air, the heat transfer coefficient (h_c) was kept equal to 5 ($W.m^{-2}.K^{-1}$) [327,328]. The theory on thermal conduction and convection patterns used in FEM has already been developed in the literature [329–331].

Table 3.5. Measured thermal conductivity of coated and neat fabric samples [227].

	Dimension $W \times L \times H$ (mm^3)	Thermal conductivity $\lambda\ (W.m^{-1}.K^{-1})$	Heat capacity $C_p\ (J.kg^{-1}.K^{-1})$	Electrical conductivity $\sigma\ (S.m^{-1})$	Density $\rho\ (g.cm^{-3})$	Surface emissivity ε
Fabric	370×500×2	0.062	1200	$1E-9$	0.8	0.9
Cooper	40×440×0.6	0.367	1052	$1.43E+4$	1.74	0.5
Carbon	100×170×0.4	0.296	1266	$4.23E+2$	1.33	0.9

The system was powered by a 12 V DC voltage source connected to the copper electrodes, one fixed at 12 V and the other grounded. As shown in Figure 3.6, the mesh constructed for the slick model was

Thèse accessible à l'adresse : https://theses.insa-lyon.fr/publication/2023ISAL0114/these.pdf © [L. Diatezo], [2023], INSA Lyon, tous droits réservés

triangular and heterogeneous in shape, with a finer mesh at the electrode-tissue interface where the highest electrical gradients were expected. To obtain a high discretization quality of the modeled system, the mesh must be as fine as possible [332,333]. The problems encountered when refining the mesh are mainly related to the connection of the structure, but also to the limits imposed by the software or the computer. Consequently, a compromise between numerical resolution accuracy and computation time must be considered [227].

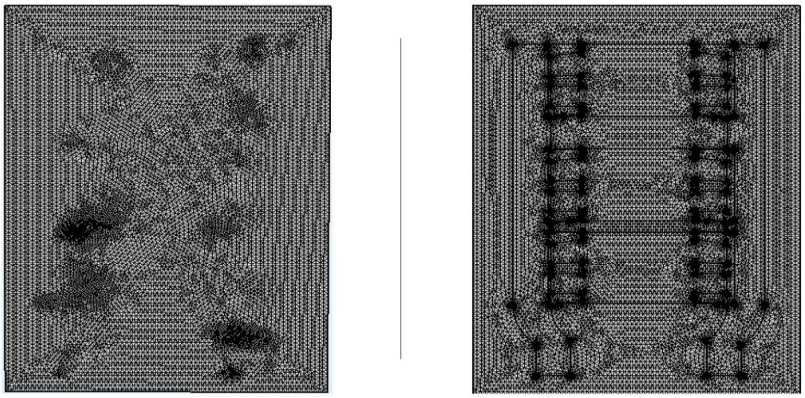

(a) (b)

Figure 3.6. Mesh build in COMSOL Multiphysics for model geometry of the tablecloth. a) face of fabric substrate (back side), and b) coating face (front side) [227].

3.3.2 Heating behavior in a steady regime

In steady-state operation, the design is optimized so that the temperature is homogeneous for all three carbon zones (i.e., the deviation is ≤ 0.5 °C), and the opposite surface of the mat can be heated up to 43°C. Another objective is to minimize the number of hot spots between the carbon zones and the copper electrodes, in order to avoid burns. We will now compare the first result of the non-optimized tablecloth modeled in COMSOL with the experimental results conducted with the Tesca REF.22 tablecloth [227].

For easier and more accurate comparison, the numerical values are presented in Table 3.6. The mean value (T_{mean})and standard deviation (SD) of temperature are calculated from 40 data points acquired on each surface. The relative variation (*RV*, Equation 3.3. is then deduced as follows [227]:

$$RV = \frac{SD}{T_{mean}} \times 100\% \tag{3.3}$$

The relative deviation from the temperature of zone 3 (denoted *DT3* in Equation 3.4) is another indicator of how evenly the three surfaces are heated.

$$DT3 = \frac{T_3 - T_i}{T_3} \times 100\% \tag{3.4}$$

where T_i represents the temperature of zone *i* (with $i = 1, \text{or } 2, \text{or } 3$).

Figure 3.7 reveals the preliminary result obtained with our initial design (D0), which is supposed to be compared with the measurement of the reference design-based Tesca REF. 22. Numerical values calculated from Equations (3.3) – (3.4) are resumed in Table 3.6. It is pointed out that D0 leads to significant discrepancy in the temperature for the three zones. The model also reveals the appearance of the hot spots, particularly in the zone 3 with a peak of 48°C. In the Tesca REF. 22 prototype, the temperatures are found to be more dispersed across the three zones, with an excessive value of hot spots up to 55°C in zone 3 and 50°C in zone 2, largely beyond the authorized temperature limits. Both designs demonstrated that the most

Thèse accessible à l'adresse : https://theses.insa-lyon.fr/publication/2023ISAL0114/these.pdf © [L. Diatezo], [2023], INSA Lyon, tous droits réservés

critical issues are relied in the area 3. In the following studies, different designs are investigated to achieve homogeneous thermal diffusion for all the areas while minimizing the overheating.

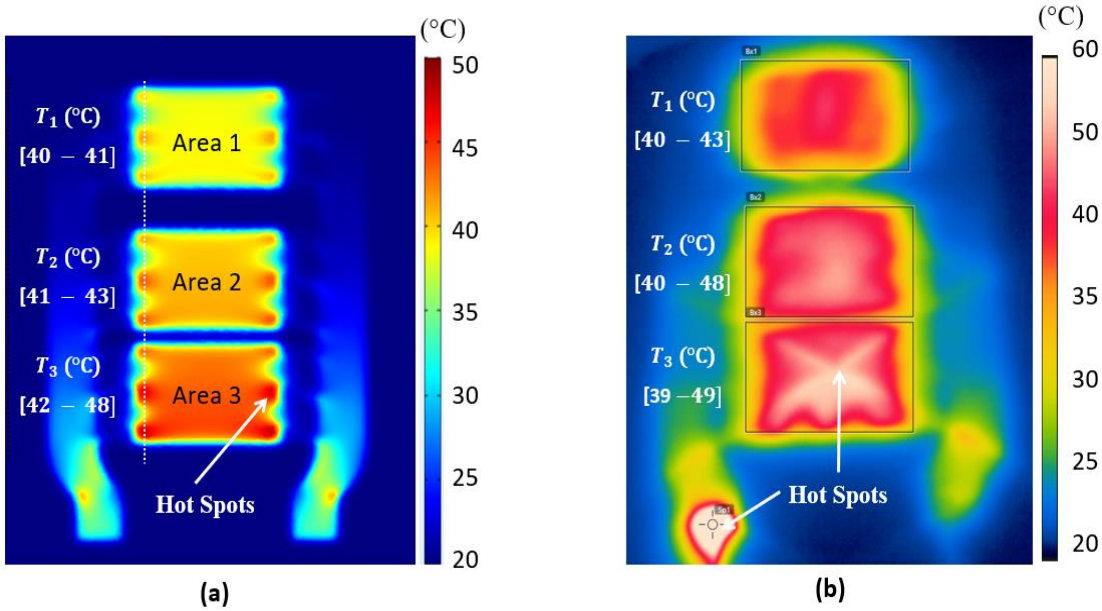

Figure 3.7. Comparison of the three temperature zones of (a) the initial theoretical design (denoted D0) and (b) the practical model Tesca REF. 22 (denoted D).

Table 3.6. Measured thermal conductivity of coated and neat fabric samples.

Area	T_{mean} (°C)		DT3 (%)		RV (%)	
	D	D0	D	D0	D	D0
1	43.3	38.8	12.3	11.2	7.4	6.5
2	48.3	40.8	3.2	6.5	12.4	6.3
3	49.4	43.6	0	0	15.7	9.0

3.3.2.1 Influence of materials' characteristics

The first idea is to modify one of the main physical parameters of composite inks, namely thermal conductivity (λ). Simulation tests are carried out on the same initial model Figure 3.8(a) but with two configurations of λ_{carbon} and λ_{copper}: one uses the actual values found from experimental material characterizations (Figure 3.8(a)) while the other uses the modified values, with the aim of reducing hot spots (Figure 3.8(b)). In terms of color scale, Figure 3.8(a) clearly shows a wide disparity in temperatures for the three zones, with zone 3 having the highest temperature. In this model, too, there are noticeable hot spots on the lateral carbon plates. Zone 3, in particular, produces a significant peak of 48°C, i.e., well above the permitted temperature limit. Increasing and equalizing the thermal conductivity of the copper and carbon inks $\lambda_{carbon} = \lambda_{copper} = 10\ W.\mathrm{m}^{-1}.\mathrm{K}^{-1}$ may solve the hot-spot problem, as suggested in Figure 3.8(b). However, the gap between the three zones is still not perfect (with a deviation of 2°C to 5°C), reflecting the inhomogeneity of the thermal zone of the entire slick surface. Furthermore, the temperature of all zones decreases considerably, which is logical since increasing the thermal conductivity of materials leads to a decrease in the temperature gradient, for a given rate of heat source [227].

Thèse accessible à l'adresse : https://theses.insa-lyon.fr/publication/2023ISAL0114/these.pdf © [L. Diatezo], [2023], INSA Lyon, tous droits réservés

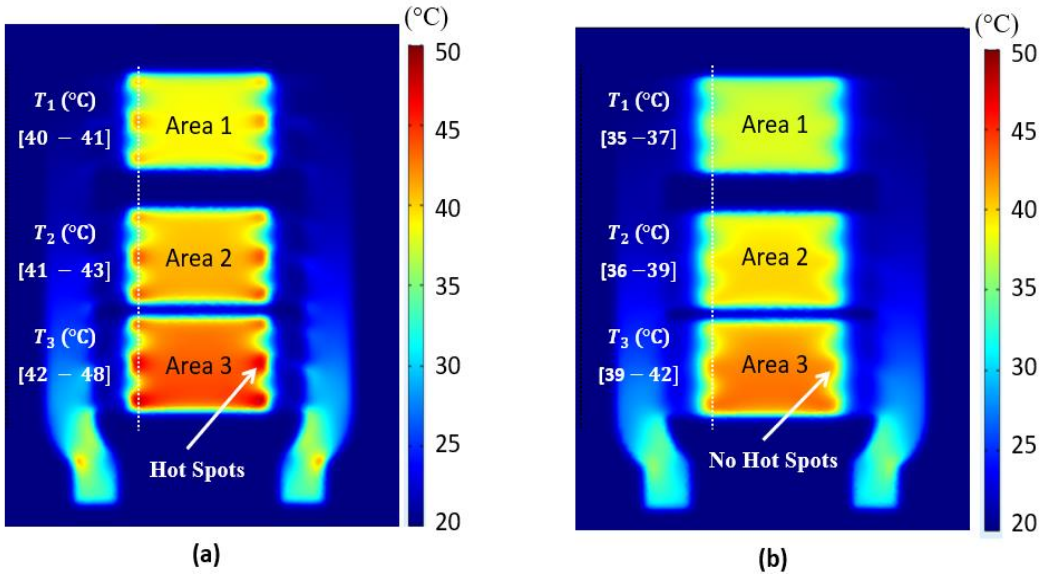

Figure 3.8. Influence of the on the numerical heatmap of tablecloth set with different thermal conductivity of inks (λ): (a) λ_{carbon} and λ_{copper} are shown on Table 3.5; and (b) $\lambda_{carbon} = \lambda_{copper} = 10\ W.\mathrm{m}^{-1}.\mathrm{K}^{-1}$ [227].

The above example revealed that optimization based on modifying coating parameters can be an effective approach, but several problems can be encountered in practice. The fact is that modifying one material parameter can influence other properties in one way or another, and trade-offs usually have to be considered. For example, increasing the thermal conductivity of coatings requires composites with a higher particle concentration, which would considerably affect their mechanical flexibility and fluid viscosity. This could be critical in certain approaches, particularly in screen printing. In addition, composite inks with the desired characteristics are not always commercially available. Customizing materials to obtain a new adequate formulation of ink is thus necessary. This matter is, however, costly and time-consuming that requires extensive research in future work. Further experiments were carried out to modify the dimensions of the carbonaceous zones to increase the temperature of each zone, thereby reducing their length and width, in order to assess their impact on heat generation. The results showed uneven heat diffusion, with hot spots appearing in all three zones. Zone 1 showed less heat diffusion than the other two zones. In addition, it was observed that the larger the size of the carbon patch, the more the temperature decreased, with a drop of around 2°C. In the following Subsection, a study will be carried out to assess the impact of the copper ink electrode on the three zones of the design.

3.3.2.2 Influence of copper electrodes' design

The objective here is to modify the size of the copper electrodes using CAD software (Solide Edge). The aim is to reduce the temperature in the last two zones, which have a higher diffusion temperature gradient than zone 1. We also want to increase the copper electrode cross-sections in the first zone, in order to increase current density, without modifying the geometry of the carbon zones. This modification is intended to improve the heat diffusion in zone 1 as well. Indeed, zone 3 tends to heat up more than the other two zones, as illustrated in Figure 3.9(a), while zone 1 does not receive sufficient current density, resulting in insufficient heat generation. According to our analysis, there is a quasi-homogeneous distribution of heat diffusion temperatures over the three carbonaceous zones, with a difference of at least 3°C between zone 1 and the last two zones. However, hot spots are present in the last two zones, with a temperature of 47.4°C in zone 2 and 49.7 in zone 3, i.e., well above the permitted temperature limit. Although the results show an improvement on the initial designs (see Figure 3.8 (a)), the problem of hot spots persists. So our question is: how can we limit the presence of these hot spots on the sheet surface? It's important to take measures to avoid damaging the circuit [227].

Thèse accessible à l'adresse : https://theses.insa-lyon.fr/publication/2023ISAL0114/these.pdf © [L. Diatezo], [2023], INSA Lyon, tous droits réservés

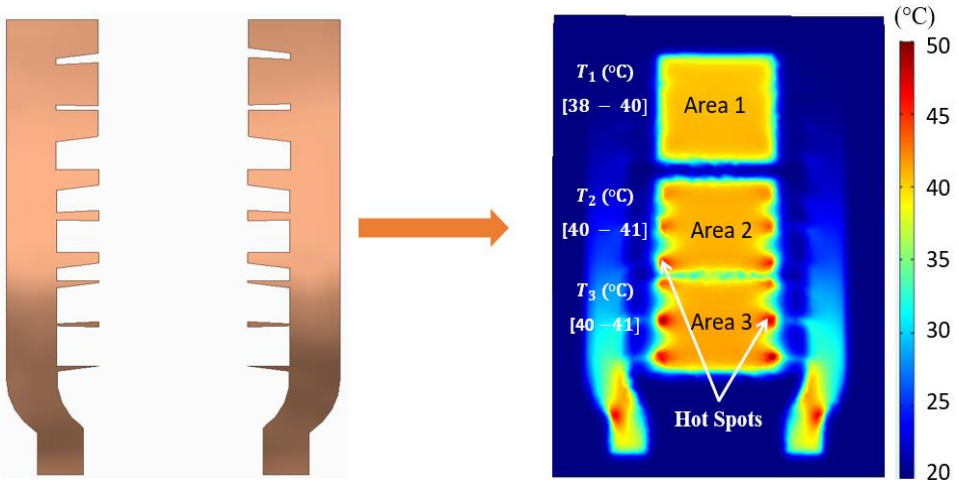

Figure 3.9. Influence of changing the size of the copper electrode in the design [227].

In order to solve the hotspot problem, two hypotheses are involved. The first is to increase the number of connection points. This is equivalent to subdividing a supply arm while keeping the same cross-section and surface area (creating a comb) and assuming that the electrical resistances of the carbon zones are identical. The second hypothesis consists in increasing the exchange surface (or the contact-point surface), by modifying the copper electrode tips to avoid the appearance of hot spots. The analyses result in an improved system design with a good compromise between the dimensions of the copper supply bus and the carbon resistors (Figure 3.10). As previously demonstrated in Subsection 3.3.1, two fundamental problems persist in this design: the presence of significant lateral hot spots (overheating) and temperature inhomogeneity between the three carbon zones. As zone 3 is closer to the power source, it is expected to receive a higher current intensity, resulting in a higher temperature than the other zones. The connections between the two materials of different resistances (copper and carbon, as shown in Figure 3.10 (b) lead to the creation of hot spots, which are even more contrasted in the case of a high resistance gap. This is due to the accumulation of charges when moving from a low-resistance conductor (copper) to a higher-resistance conductor (carbon), as shown in Figure 3.10 (a). To solve these problems, we have proposed two innovative designs focused on improving the architecture of subdivided electrodes, i.e., considered as key elements for the conversion between electrical energy and thermal heating.

The first model features a larger number of sub-electrodes (noted N), with the aim of limiting the presence of hot spots that would damage the circuit and textile substrate in the long term. The current flowing through each sub-electrode (inversely proportional to N) is considerably reduced, as is charge build-up at contact points between the copper and carbon coatings. To achieve the same current density in each zone (in order to induce the desired temperature), the surface areas of all sub-electrodes are equal to that of the initial design (see Figure 3.10 (b)-(c)) [227].

In addition to the issue of hot spots, resolved by design 1 (D1), another solution to the problem of heating homogeneity is considered in the second design (D2). The aim of this design is to improve the exchange surface of the subdivided electrodes (particularly for zones 1 and 2), while retaining the advantages of D1 (Figure 3.10.c). Consequently, certain modifications have been made to design 1 by increasing the size of the contact points as well as the number of sub-electrodes (N). In fact, it is not necessary for N to be identical in all three carbon zones to compensate for the different distance between these zones and the electrical source (since Joule losses depend on conductor length) [227].

Thèse accessible à l'adresse : https://theses.insa-lyon.fr/publication/2023ISAL0114/these.pdf © [L. Diatezo], [2023], INSA Lyon, tous droits réservés

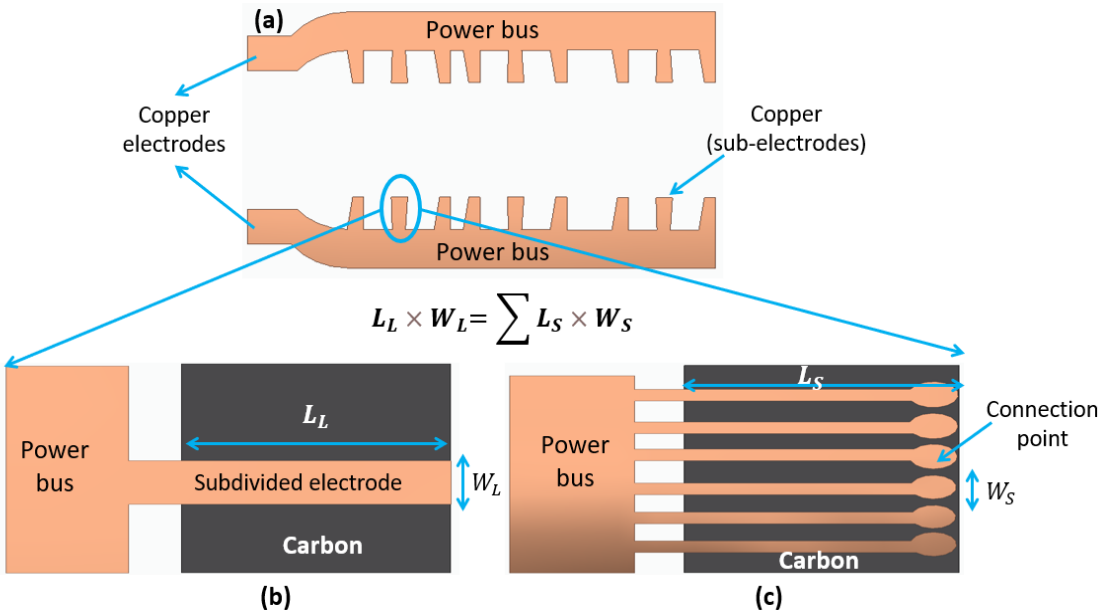

Figure 3.10. Optimization of the printed coatings: a) Initial design; b) Zoom-in on the connection between copper electrode and carbon patch; c) Optimizations performed in designs 1 and 2 [227].

In the following subsection, the three designs mentioned above (Figure 3.11) will be implemented in Solid Edge and COMSOL Multiphysics. Their thermal performance will then be analyzed and compared, enabling us to check whether they are suitable for the intended purpose [227].

Another solution is to optimize the design of the coatings, as described in section 3.2 above. In reality, over 300 models were produced to find the most suitable candidate corresponding to our specifications. For the sake of simplicity, only 3 representative models were shown and compared, as illustrated in figure 3.11. Here, D0, D1 and D2 correspond to the initial design (Figure 3.11.a and also Figure 3.10.a), design 1 (Figure 3.11.b) and design 2 (Figure 3.11.c). Unlike D0, D1 achieves a significant reduction in hot spots, but temperatures between the three zones are still not homogeneous. Exceptionally, D2 (the most optimized design) definitively resolves these two criticisms and will therefore be used for the development of a real prototype (see Sections 3.4) [227].

The results in Table 3.7 lead to the following comments:

- Zone 3 has the highest mean temperature and data dispersion, whatever the model chosen.
- T_{mean} increases from zone 1 to zone 3, which explains why DT3 in zone 1 is higher than in the other zones.
- A lower value of RV compared to D0 leads to an improvement in the thermal regularity of each zone of D1, which explains the reduction in hot spots. However, the lack of change in DT3 indicates that, as with D0, heat transfer in D1 is not homogeneous across the three zones.
- For all surfaces, D2 gives the smallest DT3 and RV compared with other designs. This shows that only D2 meets expectations, as it is able to dissipate heat evenly over all zones (maximum deviation of 0.6°C) and has a low dispersion of the data collected on each surface (~ 2%) [227].

Thèse accessible à l'adresse : https://theses.insa-lyon.fr/publication/2023ISAL0114/these.pdf © [L. Diatezo], [2023], INSA Lyon, tous droits réservés

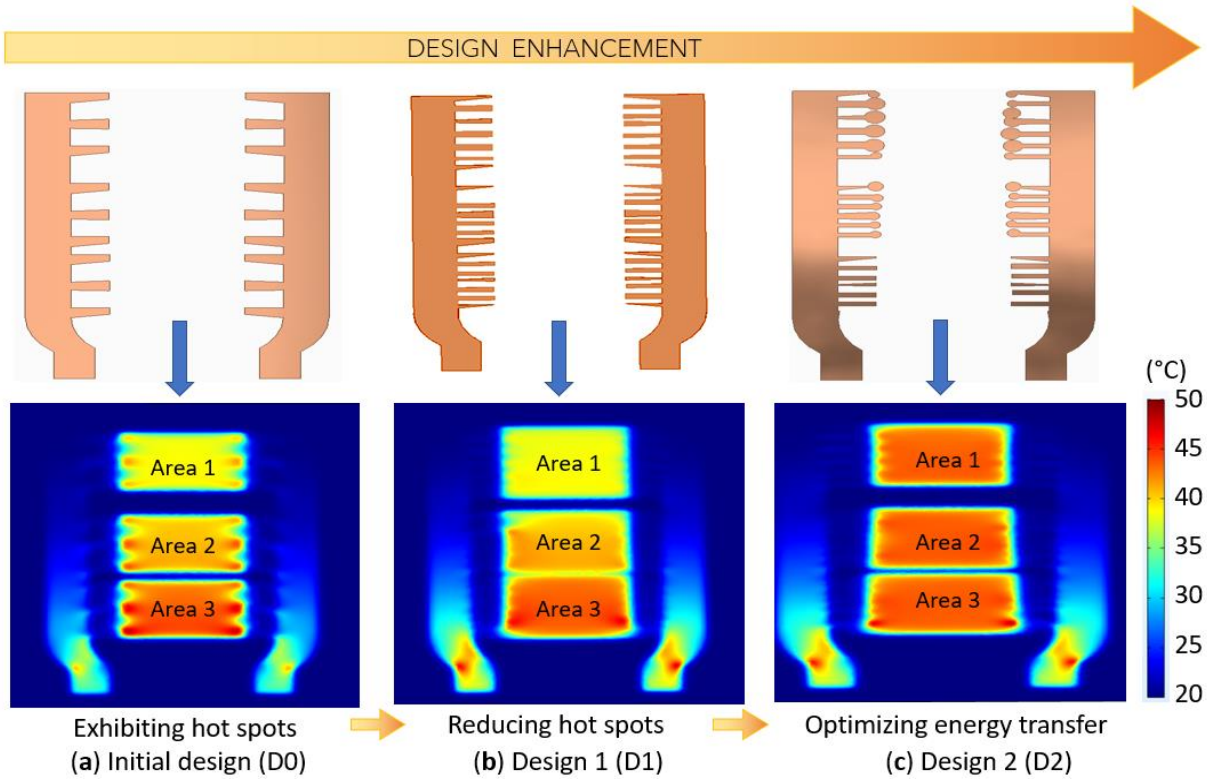

Figure 3.11. Design enhancement for reducing hot spots and reaching uniform heating surface [227].

Table 3.7. Comparison of the heating performance for the three designs.

Area	T_{mean} (°C)			DT3 (%)			RV (%)		
	D0	D1	D2	D0	D1	D2	D0	D1	D2
1	38.8	38.6	42.5	11.2	12.2	1.2	6.5	3.4	1.9
2	40.8	41.4	42.8	6.5	5.9	0.7	6.3	5.1	1.8
3	43.6	43.0	43.1	0	0	0	9.0	2.9	2.2

Figure 3.12(a) and (b) examine the lateral and central temperature profiles along the x axis (the direction of the slick length) for the three models, respectively. It can be seen that [227]:

- The central profile appears more stable and homogeneous than the lateral profile, on which hot spots caused by the connection of subdivided copper electrodes appear.
- D1 and D0 show significant hot spots in zone 3, in excess of 45 ◦C (i.e., above the permitted limit).
- In zone 3, D1 and D0 give rise to higher lateral and central temperatures than D2. This is in contrast to the other zones.
- The lateral and central profiles of D1 and D0 show a clear decrease along the length of the slick, while those of D2 are almost constant.
- Only the D2 manages to homogenize the temperature of all three heating surfaces, and avoid the presence of major hot spots.

Thèse accessible à l'adresse : https://theses.insa-lyon.fr/publication/2023ISAL0114/these.pdf © [L. Diatezo], [2023], INSA Lyon, tous droits réservés

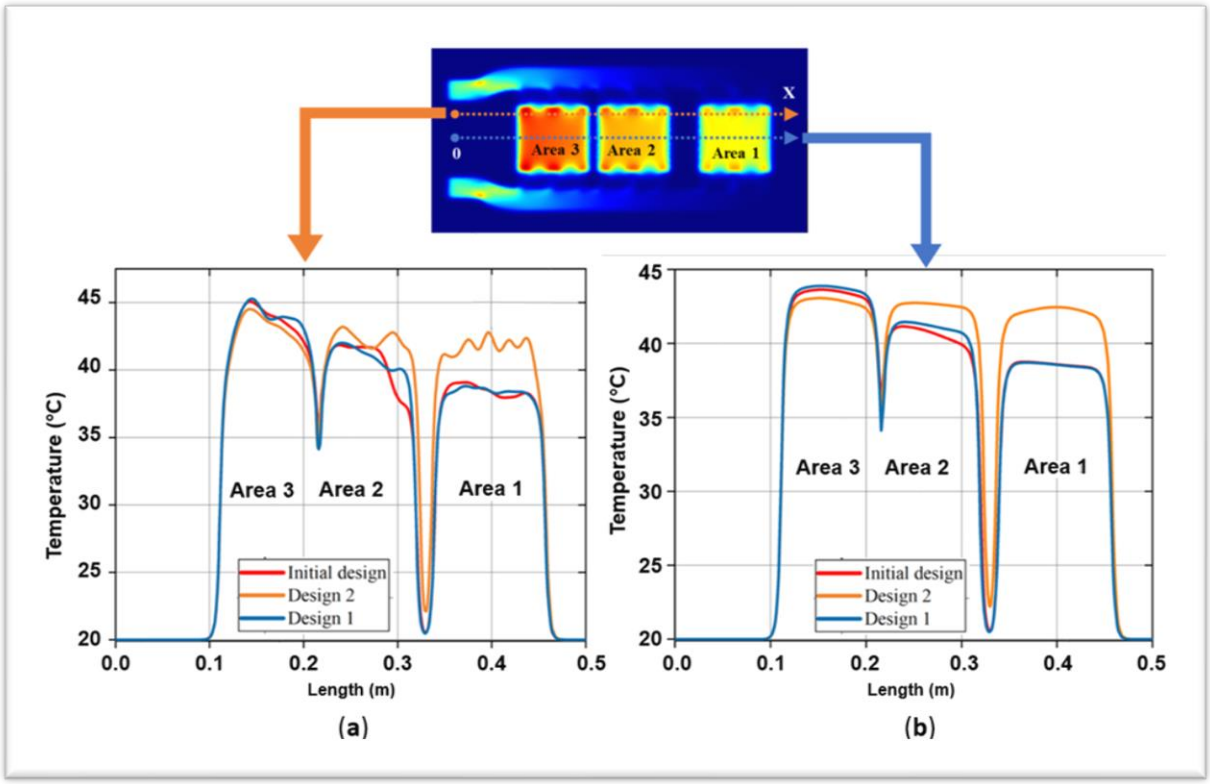

Figure 3.12. Temperature evolution along the x axis: (a) lateral temperature, and (b) central temperature.

In the next study, we take a closer analysis on the transient regime relating to the thermal transfer and the Joule effect behaviors. The discussion particularly focuses on discrepancies between the empirical data and the theoretical results of the new designs.

3.3.3 A first-order response in a transient regime

We will examine the transient regime to represent the heating system used in the experiments. The aim is to determine the time required to reach heating temperatures as a function of time, focusing on the new design optimized both practically and theoretically .

In order to compare experimental and theoretical temperatures, we collected data on zone 2 of the carbon patch using the optimized model (D2). As shown in Figure 3.13, the time response of both temperatures during the transient state shows a typical first-order trend, which is consistent with the model in Equation (2.18) of Chapter 2 and the results reported by Xiang et al [334]. Empirical measurements show that the system reaches 95% of the temperature limit after about 112 s (the so-called response time), which corresponds to three times the time constant (τ). This finding perfectly meets the requirements imposed by the Tesca Group, according to which the time needed to reach the target temperature must not exceed 2 minutes. Reducing material parameters such as thermal resistance and/or specific heat leads to a smaller value of τ, and therefore to a faster response to temperature. Substituting the parameters from Table 3 into Equation (2.19) of chapter 2 gives an estimated theoretical value of τ (~ 330 s, i.e., three times greater than the actual value), reflecting a discrepancy between experiment and numerical model. It has therefore been pointed out that the FEM is fairly reliable in the steady state, where a good prediction of the static temperature is given. Conversely, the estimate of the time response in the transient regime does not match the real system to some extent .

Thèse accessible à l'adresse : https://theses.insa-lyon.fr/publication/2023ISAL0114/these.pdf © [L. Diatezo], [2023], INSA Lyon, tous droits réservés

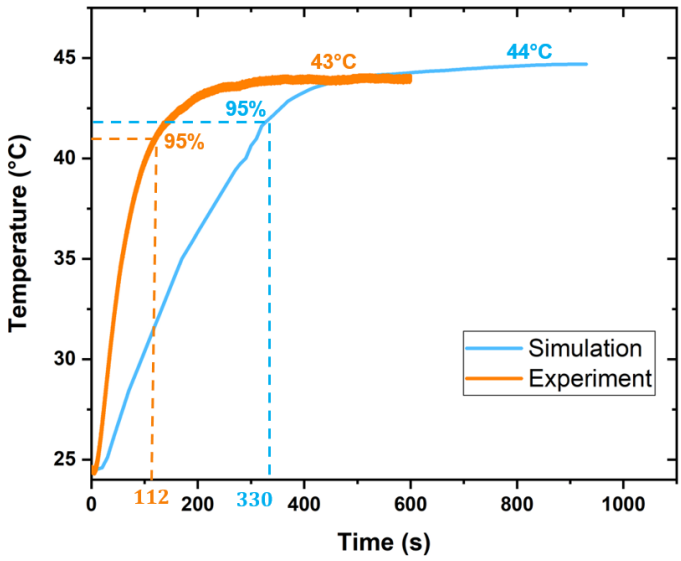

Figure 3.13. Time evolution of the measured and simulation temperatures performed on the tablecloth with optimized design.

The following section presents a comparison of thermal performance between a real screen-printed prototype and the corresponding digital model created by COMSOL Multiphysics software. The aim is to determine whether these two approaches are suitable for achieving the thermal performance objective.

3.4 Heatmap analysis

In this study, the optimized coating (D2) is selected to be printed on a fabric and implemented in a real web. An analysis of the thermal map on the reverse side of the tablecloth was carried out using the experimental setup described in Subsection 2.3.5 of Chapter 2. The real prototype consisted of conductive coatings comprising three-layer carbon plates and two-layer copper electrodes, similar to the model built in the FEM. Thanks to the optimized design and suitable materials of the smart coating, the heating tablecloth successfully met the specifications defined by Tesca.

As shown in Figure 3.14(a), the sheet surface temperature was almost homogeneous for all three zones, with no significant hot spots. This finding is in agreement with the results obtained from the numerical simulation shown in Figure 3.14(b). For a better comparison between the FEM method and the empirical data, Table 3.8 summarizes the mean temperature value and the coefficient of deviation (DT3) for the three zones. It is remarkable that the empirical measurement indicates the same temperature for all these zones, with very low DT3 values of 0.2 to 0.5%. For zones 1 and 2, this deviation is slightly higher in the finite element method, at around 0.7-1.2%. In both experiment and simulation, zone 1 gives a higher value of DT3 than Zone 2. This is evident from the fact that the temperature of zone 2 is closer to that of zone 3, which in turn is closest to the electrical source. Consequently, the temperature gradually decreases from zone 3 to zone 1 as shown in Figure 3.14.

Table 3.8. Comparison between measured and theoretical temperatures of three heating areas.

Area	T_{mean} (°C)		DT3 (%)		D_{e-s} (%)
	Experiment	Simulation	Experiment	Simulation	
1	43.6	42.5	0.5	1.2	2.5
2	43.7	42.8	0.2	0.7	2.1
3	43.8	43.1	0	0	1.6

Thèse accessible à l'adresse : https://theses.insa-lyon.fr/publication/2023ISAL0114/these.pdf © [L. Diatezo], [2023], INSA Lyon, tous droits réservés

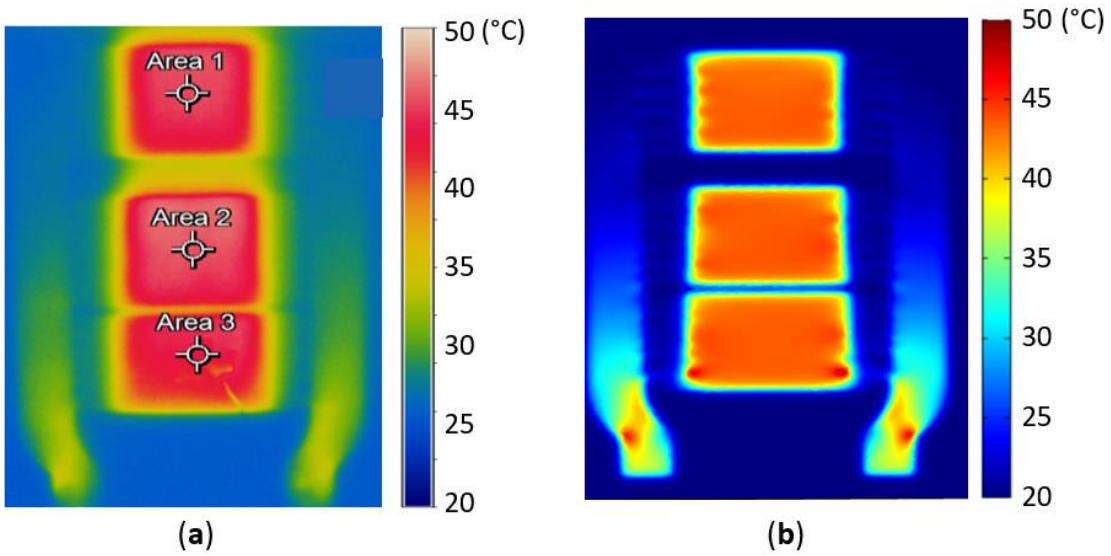

Figure 3.14. Heat map of (a) a real prototype screen-printed with a thermal camera and (b) a digital model using COMSOL software.

The deviation between experiment and simulation can be evaluated by means of another relative deviation coefficient (denoted D_{e-s}), i.e., given by [227]:

$$D_{e-s} = \frac{T_e - T_s}{T_e} \times 100\% \tag{3.5}$$

where T_e and T_s are the temperatures of a given zone obtained from experiment and simulation, respectively. For all three zones, D_{e-s} is relatively low, reflecting a good correlation between the numerical model and practical data. Like the DT3 coefficient trend, D_{e-s} decreases (from 2.5% to 1.6%) from zone 3 to zone 1.

In the following, the heating behavior of the coated fabric was studied under different voltage levels (denoted *U*), from 3 V to 18 V. Current measurements were also taken (denoted *I*), enabling electrical power to be determined (i.e., $P = U \times I$). Figure 3.15 (a) illustrates the temporal evolution of temperature, which is used to determine the response time. All raw and estimated data obtained during the experiment are summarized in Table 3.9. At 12V, the temperature reaches 43°C after a response time of 112 s. With a higher applied voltage (e.g. 15V and 18V), the resulting temperature increases, but the response time remains unchanged. Logically, a lower voltage leads to a faster heating process, but the temperature is not sufficient to ensure user comfort, given the criteria imposed by the automotive partner. As shown in Figure 3.15 (b), the electrical power (denoted P) is the square of the input voltage U^2. Based on the Joules effect of a conductor, the ratio U^2/P gives an estimate of the electrical resistance of the two copper power buses, which turns out to be equal to around 5.5 Ω. This is consistent since each copper electrode has been designed to have a resistance value of 2-3 Ω. Figure 3.15 (b) also confirms a square behavior between temperature change and applied voltage. In fact, the temperature change is assumed to be linear with respect to the heat flux (*Q*), which is ultimately related to the electrical power as far as the Joule heating effect is concerned.

Based on the specifications defined by Tesca, the applied voltage was chosen equal to 12 V, leading to an electrical power consumption (Φ_J) of approximately 25.5 W (see Table 3.9). The thermal resistance (R_{th_tab}) of the mat being equal to 1,34 $W^{-1}.K$ (found in section 3.3), the rate of conductive heat transfer (P_{cond}, en W) to reach the limit temperature ($T_l \rightarrow 43°C$) is equal to :

$$P_{cond} = \frac{T_l - T_f}{R_{th_tab}};\ 14.2\,\text{W} \tag{3.6}$$

Thèse accessible à l'adresse : https://theses.insa-lyon.fr/publication/2023ISAL0114/these.pdf © [L. Diatezo], [2023], INSA Lyon, tous droits réservés

On the other hand, the convective heat transfer rate (P_{cond}, in W) is calculated as follows:

$$P_{conv} = h_c S(T_l - T_0); \quad 4.8\,\mathrm{W} \tag{3.7}$$

Therefore, $P_{cond} + P_{conv} \sim 19W$. The efficiency of the heating tablecloth is therefore estimated at around 75%. Energy losses (~ 25%, i.e., not taken into account in equation (2.17 cf. chapter 2)) are probably due to Joule heat dissipated by the two main copper electrodes and to heat leakage through the materials caused by the connection between the fabric and the coating layers . In reality, the fabric of a car seat is in contact with a human body, so there is no convection. Instead, thermal conduction between the heated seat and the body is used. This issue should be considered in the next stages of this work.

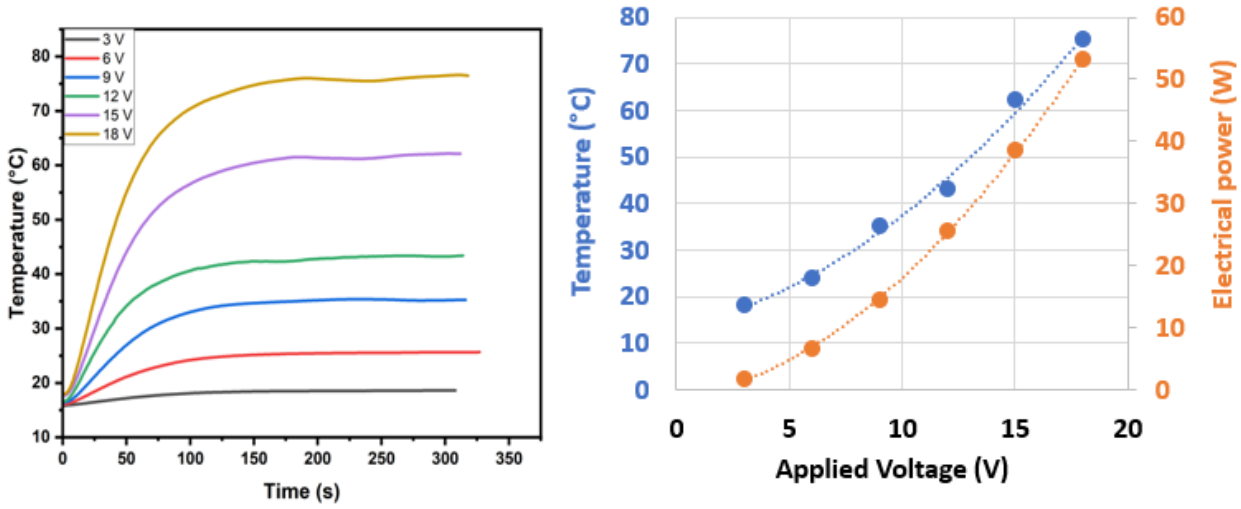

a) b)

Figure 3.15. Thermal behavior under different applied input voltages: (a) Time evolution of temperature behavior; (b) Temperature (blue curve) and electrical power (orange curve) versus the input voltage. Dotted lines represent the quadratic models.

Table 3.9. Electrical power and temperature at steady state were obtained with different input voltage levels. The response time during which the system reaches 95% of the steady temperature were also provided.

Voltage (V)	Current (A)	Power (W)	Temperature (°C)	Response time 95% (s)
3	0,7	1,7	18	65
6	1,105	6,6	24	70
9	1,62	14,5	35	100
12	2,129	25,5	43	112
15	2,56	38,5	62	115
18	2,95	53,1	75	115

Thèse accessible à l'adresse : https://theses.insa-lyon.fr/publication/2023ISAL0114/these.pdf © [L. Diatezo], [2023], INSA Lyon, tous droits réservés

3.5 Summary

The aim of this study was to develop Tesca's product range by proposing a new generation of car seat heaters based on an innovative flexible electronic design combined with an additive manufacturing (AM) screen-printing technique. The heating fabric surface covered with several layers of conductive materials must maintain an even temperature up to 40–43 °C, with rapid response and no risk of overheating. Scanning electron microscopy (SEM) was opted to analyze the morphological structure, allowing to confirm the quality of the printing and determine whether the composite inks chosen were suitable for the AM. Conductive layers were measured using a laser profilometer to determine the optimum number of layers to deposit in order to improve the ink's conductivity properties. In addition, the porosity of the ink on the fabrics was measured as a function of the layers number. Electrical and thermal characterizations were carried out using experimental set-ups and analytical mixing rules, with the aim of identifying relevant material parameters. These results were not only necessary for the implementation of FEM via COMSOL software, but also enabled a better understanding of the design strategy. It was highlighted that the copper composite ink, thanks to its excellent electrical conductivity, was chosen to design the electrodes, while the carbon composite was more appropriate for use as a heating resistor. Silver ink, due to its high cost and unsuitable viscosity, was not considered for the practical prototype. Characterization of the heat map was carried out using COMSOL simulation, which was then run on a real tablecloth. Good agreement between numerical results and empirical measurements was observed. By optimizing the critical connections between the copper and carbon coatings, a perfectly homogeneous temperature was achieved across the entire surface of the fabric, definitively resolving the problem of hot spots.

Following the successful development and integration of the heating device in its planned configuration, further studies are carried out, chiefly focusing on the ageing analyses of the conductive coatings under various external conditions, including temperature, humidity and mechanical loading (dynamic and static regimes). It is believed that optimizing the design structure and material properties, as well as improving print quality, will definitely promote the development of heated textiles for the future.

Thèse accessible à l'adresse : https://theses.insa-lyon.fr/publication/2023ISAL0114/these.pdf © [L. Diatezo], [2023], INSA Lyon, tous droits réservés

Chapter 4 Optimization of electroluminescent coupling using phosphorus composite coated with flexible electrodes

This chapter involves the development of electroluminescent (EL) composite designed to be integrated into car seats for aesthetic purposes. The main aim here is to analyze the influence of the polymer matrix and the phosphor particles on the light emission, which is demonstrated to be significantly impacted by the permittivity gradient between these two materials as well as the phosphor concentration of the composite. In order to fulfil the specifications defined by Tesca, the developed device should be easy in process/integration, good light intensity, and low energy consumption. To determine the best combination of matrix and particles for an optimization of EL response, three types of polymer matrix are selected including terpolymer, copolymer and polycarbonate. Also, phosphorescence doped with different metallic elements like copper (Cu), copper-aluminum (Cu-Al), and copper-manganese (Cu-Mn) are chosen thanks to their interesting optical characteristics.

The electrical behavior of EL composites is obtained based on the polarization hysteresis-loop composed of current-density versus electric-field (J-E) curve. This characteristics depends on several key factors such as charge concentration, frequency and magnitude of the field excitation, as well as the ultimate electrical properties of the matrix and particles. Analyses allow for the determination of several key parameters of these materials (electrical conductivity, dielectric constant), leading to a better understanding of the EL response. Experimental results confirm that the P(VDF-TrFE-CFE) terpolymer matrix, when combined with copper-doped zinc sulfide microparticles (ZnS:Cu), leads to the highest brightness of the light emitted (as well as a high luminance value) compared to the other tested samples. To a certain extent, this behavior matches the numerical predictions of the model developed by finite element method (FEM) that enables to evaluate the local field distribution seen by the phosphor particles. Based on the simulation results, it is emphasized that the dielectric constant of the matrix and particle phases, which strongly affects the electric field attributed internally to the particles, clearly determines the luminous intensity of the electroluminescent (EL) device. Evaluation of the electrical power of the composites were also carried out in practice, which helps find an ideal compromise between the brightness intensity and the electrical consumption. The first EL device is integrated into a real textile substrates, followed by experimental tests and validation.

Thèse accessible à l'adresse : https://theses.insa-lyon.fr/publication/2023ISAL0114/these.pdf © [L. Diatezo], [2023], INSA Lyon, tous droits réservés

4.1 Comprehension of the electroluminescent (EL) device

4.1.1 EL phenomenon

Electroluminescent (EL) devices generate light from electrical excitation, which is necessary for the electrons to absorb sufficient energy to reach a higher energy level so that, on returning to its ground state, it emits a photon. The EL properties of conjugated organic compounds were observed as early as 1963 [335] on molecules like anthracene. Renewed interest arose in 1987 when Tang and Van Slyke of Eastman Kodak demonstrated that it was possible to obtain intense light emission at low voltages within a bilayer diode (one hole-injecting layer, one emitting layer) made by evaporation of small organic molecules [336]. In 1990, R. Friend *et al.* discovered the EL properties of poly(p-phenylene vinylene) (PPV) in its undoped (semiconducting) state [337]. In recent years, this phenomenon has been successfully found from several conjugated polymers. The use of these polymers is very promising, as they possess sufficient electroluminescence properties to compete with inorganic materials, whether for applications such as organic light-emitting diodes (OLEDs), solar cells or photovoltaics, ultra-thin and flexible displays, or lasers. Figure 4.1 shows the Jablonski diagram, which details the different electronic states of a molecule and the transitions between them. The vertical axis is an energy axis, while the states are grouped horizontally according to their spin multiplicity. Radiation transitions are symbolized by straight arrows, while non-radiation transitions are symbolized by red arrows. The fundamental vibrational state of each electronic state is represented by a thick line, and the other vibrational states by a thin line [338].

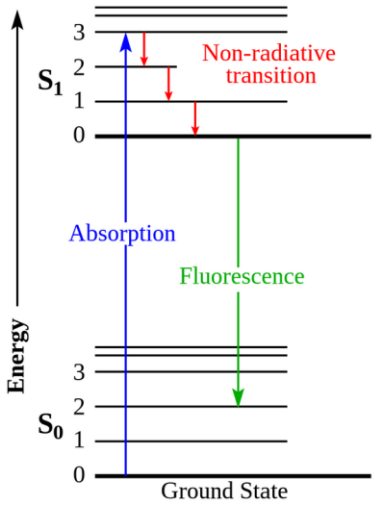

Figure 4.1. Jablonski diagram, extracted from [338].

A radiative transition involves the absorption or, on the contrary, the emission of a photon to pass from one state to another. This is the case of fluorescence and phosphorescence. Consequently, the condition of the electric field is that it must be alternating, so that the electrons of the phosphor can reach a higher energy level when the field is high, then fall back to lower levels when the field decreases. In fact, direct current does not allow the phosphor particles to reach lower levels, and therefore prevents them from emitting light.

4.1.2 Configuration of EL device

Since it was first discovered by Destriau in an oil dispersion containing ZnS:Cu phosphorus, alternating current electroluminescence (ACEL) has found many significant applications in lighting, color displays and optoelectronics [269]. Electroluminescence (EL) is the phenomenon whereby a material emits light when subjected to an alternating current or electric field. Several researchers have developed electroluminescent

Thèse accessible à l'adresse : https://theses.insa-lyon.fr/publication/2023ISAL0114/these.pdf © [L. Diatezo], [2023], INSA Lyon, tous droits réservés

(EL) devices composed of superpositions of 4, 5 or even 6 layers, which are individually fabricated using various techniques [269,270] . For example, in the case of a 4-layer device, it consists of two conductive layers, a dielectric layer and a phosphor layer, as shown in Figure 4.2 (a), which represents the classical configuration and the research focus. The two conductive layers and the dielectric layer are used to create a capacitor that generates an electric field inside the phosphor layer, enabling light emission. It is important to note that one of the electrodes' conductive layers must be transparent to allow light to pass through the phosphor layer [271].

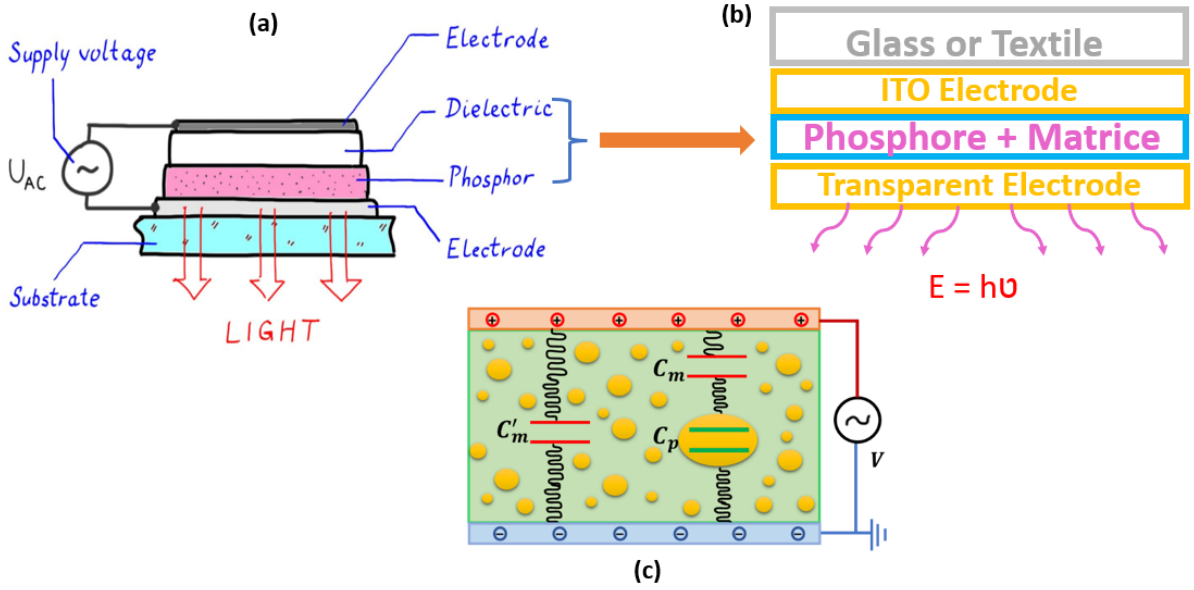

Figure 4.2. (a) classic configuration and research axis [271], (b) Schematic principal and structure of the EL device and (c) Equivalent electrical circuit of a 0-3 particle-polymer composite based on the mixed model.

As shown in Figure 4.2(b), the electroluminescent (EL) system designed in this research is a multi-layer configuration consisting of a composite layer sandwiched between two thin conductive electrodes. When an adequate electric field is applied to the electrodes, the EL device is supposed to emit visible light through the transparent glass substrate, thanks to the electrical-light conversion mechanisms. This phenomenon is strongly affected by the dielectric constant (denoted ε) of the phases involving polymer matrix and EL particles. Considering these two phases interact as a series of capacitors excited by an input voltage V (see Figure 4.2(b)), the electric field (denoted E) is revealed to be internally redistributed, which, to some extent, depends on the ε value of each phase [339,340]. Assuming the electric displacement (denoted D) between the particle and the matrix interface being continuous, the values of the internal electric field in each phase could be estimated by [341]:

$$D = \varepsilon_m E_m = \varepsilon_p E_p \tag{4.1}$$

where the subscripts *p* and *m* correspond to the particle and matrix, respectively.

Under a frequency range of 100–1000 Hz, the dielectric constant layer of different polymer matrices is supposed to be smaller than that of the doped ZnS particles (i. e., $\varepsilon_m < \varepsilon_p$), indicating that the electric field distribution should be more concentrated on the matrix (i. e., $E_m > E_p$) [310,342]. This concentration is even more obvious, particularly with high discrepancy between the permittivity values of the two phases (i. e., $\varepsilon_m \ll \varepsilon_p$). Among the three selected matrices, terpolymer possesses the highest permittivity, which is thus closer to the one of the doped ZnS particles. Consequently, the internal electric field seen by the particle phase is revealed to be higher in the ZnS/terpolymer composite than in the others made of copolymer and

Thèse accessible à l'adresse : https://theses.insa-lyon.fr/publication/2023ISAL0114/these.pdf © [L. Diatezo], [2023], INSA Lyon, tous droits réservés

polycarbonate. This result will be confirmed by numerical finite element (FE) models via COMSOL software.

To explain the electromechanical properties of the composites, Tunkasiri *et al.* proposed an equivalent electrical circuit for a typical 0-3 connectivity [343], where the particles are randomly dispersed within the matrix as indicated in Figure 4.2(c). In this theory, two conduction paths are supposed be created inside the composite: one can pass through the polymer phase (i.e., modeled as a simple branch containing of only one capacitor C'_m); and the other pass through both polymer and particle phases (i.e., modeled as a serial branch of two capacitors C_m and C_p). These two branches are considered to be parallel, creating the mixed connectivity that is inspired from the model developed by Pauer [344]. The Pauer's model describes the 0–3 composites based on a unit cube representing the volume of the composite material containing within it a smaller cube of length *a* representing the particle's dimension. The relative dielectric constant of the composite using the mixed model ($\varepsilon_{r_{mixed}}$), in which both parallel and serial connectivity exist, can be computed as:

$$\varepsilon_{r_{mixed}} = \varepsilon_{r_{\mathrm{m}}} \left[(1-a^2) + \frac{\varepsilon_{r_{\mathrm{p}}}.a^2}{\varepsilon_{r_{\mathrm{m}}}.a+\varepsilon_{r_{\mathrm{p}}}(1-a)}\right] \tag{4.2}$$

Besides the mixed model, some other ones prosed in literature only consist of either serial or parallel model. For instance, according to the serial spring model developed by Reuss [345,346], the relative dielectric constant of the serial branch ($\varepsilon_{r_{serial}}$) can be given by:

$$\varepsilon_{r_{serial}} = \frac{\varepsilon_{r_{\mathrm{m}}} * \varepsilon_{r_{\mathrm{p}}}}{\emptyset_{vol}\, \varepsilon_{r_{\mathrm{m}}} + (1-\emptyset_{vol})\, \varepsilon_{r_{\mathrm{p}}}} \tag{4.3}$$

where $\emptyset_{vol}$ is the volume fractions of the particles in the composite.

Based on the parallel spring model of Kelvin-Voigt [347,348], the relative dielectric constant ($\varepsilon_{r_{parallel}}$) is deduced as:

$$\varepsilon_{r_{parallel}} = \varepsilon_{r_p}.\emptyset_{vol} + \varepsilon_{r_{\mathrm{m}}}.(1-\emptyset_{vol}) \tag{4.4}$$

In addition to the above models, Maxwell-Garnett developed another one that is adapted to a two-phase composite with spherical particles in a continuous medium. The relative dielectric constant of the composite (ε_{r_c}) can be expressed by [349]:

$$\varepsilon_{r_{\mathrm{c}}} = \varepsilon_{r_{\mathrm{m}}} \frac{2\varepsilon_{r_{\mathrm{m}}} + \varepsilon_{r_{\mathrm{p}}} + 2\emptyset_{vol}\,(\varepsilon_{r_{\mathrm{p}}} - \varepsilon_{r_{\mathrm{m}}})}{2\varepsilon_{r_{\mathrm{m}}} + \varepsilon_{r_{\mathrm{p}}} - \emptyset_{vol}(\varepsilon_{r_{\mathrm{p}}} - \varepsilon_{r_{\mathrm{m}}})} \tag{4.5}$$

In conclusion, the dielectric constant of both matrix and particle phases, which strongly affects the electric field internally attributed to the phosphor particles, clearly determines the luminescent intensity of the electroluminescent device [350]. The emitted light results from the recombination of excitons within the intrinsic heterojunction of the ZnS phosphor powders when subjected to an alternating electric field. The wavelength of the light is tuned by the dopants in the ZnS lattice while the voltage-induced luminance emitted by the conductor does not require electrons injected into the ZnS phosphor particles [351,352]. Furthermore, the electronic structure of the dielectric layer as a host matrix would not affect the excitation mechanism of the ZnS particles, while the higher permittivity of the dielectric layer would lead to improved concentration of the electric field applied on the phosphorus particles [353]. Based on these analyses, it seems that the terpolymer, with its extremely high permittivity compared to the other selected polymers, has further advantage in the development of high performance EL composite device. In the next section, we will analyze the distribution of phosphorus particles on the surface of the polymer matrix using scanning electron microscopy.

Thèse accessible à l'adresse : https://theses.insa-lyon.fr/publication/2023ISAL0114/these.pdf © [L. Diatezo], [2023], INSA Lyon, tous droits réservés

4.2 Morphological analyses of EL composites

This study aims to observe the dispersion state of the zinc sulfide (ZnS) phosphor particles doped with metals (such as Cu, Cu-Al and Cu-Al) randomly distributed into a dielectric matrix (terpolymer, copolymer, or polycarbonate).

Figure 4.3 shows scanning electron microscopy (SEM) images of different metal-doped phosphor particles. It can be revealed that the diameter of these particles is very heterogenous, with the average value is in the range of 3-12 µm. On a one hand, the ZnS doped with copper (Cu) and copper-aluminum (Cu-Al) principally present small particle size, with quasi-spherical shape. On the other hand ZnS doped copper-manganese (Cu-Mn) is abundant with larger microparticle size. These particles are not spherical shape but hexagonal shape. Phosphors doped with copper (Cu) and copper-aluminum (Cu-Al) will have a higher stacking density. This is explained by the occupation of interstitial sites by small particles, thus reducing surface vacancies and significantly improving their distribution, as opposed to copper-manganese doped phosphorus (Cu-Mn), where the abundance of large particles of phosphorus leads to lower density and more surface vacancies

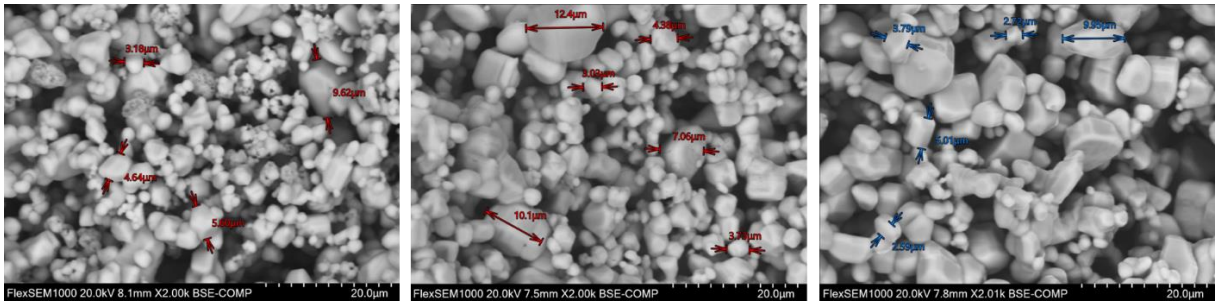

a) b) c)

Figure 4.3. SEM images (magnification × 2000 with the scale bar of 200 µm) of phosphorus particles with different doppants : a) ZnS:Cu-Al; b) ZnS:Cu; and c) ZnS:Cu-Mn.

Figure 4.4 shows the SEM images of composites made of three distinct types of polymer matrices (i.e., terpolymer, polymer, and polycarbonate) doped with 20 vol.% (Zn:Cu) or (Zn:Cu-Mn) fillers. As observed, the phosphorus particles were well randomly distributed within most of polymer matrices. However, there are also agglomerates of particles on the surface, which could be attributed to a quasi-homogeneous dispersion. It is worth noting that for the composite consisting of polycarbonate, a presence of small cracks appeared as a result of poor solvent evaporation during the annealing process. The gaps seems to be somewhat larger with the bigger size as in the case of (Zn:Cu-Mn) particles, provoking a formation of tiny cracks on the sample's surface. Regarding the other composites made of (Zn:Cu-Al) fillers, similar observation were obtained as shown in the SEM images of those elaborated with (Zn:Cu). These particles, with their smaller micro-size, were revealed to be easily dispersed into the three polymer matrices.

Figure 4.5 (a) and (b) shows the SEM images of the terpolymer/(ZnS:Cu) composites with the volume fraction increasing from 10% to 40%, performed under two different magnifications comprising × 100 and × 750, respectively. It is noted that at 10 and 20 vol.%, the fillers seems to be well dispersed within the polymer matrix. Increasing the fillers' content up to 30 and 40 vol.% could provoke particles' agglomeration, or even percolate that degrades the electroluminescent (EL) effect of the device. Indeed, the inter-chain interactions between particle-particle become stronger and thus compete with their interaction engendered by the external field. As a result, the chains tend to merge together to form a lattice structure, due to a greater impact caused by interactions between particles because of their smaller distances. In other words, moderate concentration of the embedded phosphor particles is necessary for the fabrication of an effective EL device [310]. As a matter of fact, the ability to have ideal concentration might help to offer not only in cost, but

Thèse accessible à l'adresse : https://theses.insa-lyon.fr/publication/2023ISAL0114/these.pdf © [L. Diatezo], [2023], INSA Lyon, tous droits réservés

also in reducing the impact of functionalization on response and behavior of the underlying polymer matrix material [354,355]. Previous studies have shown that functionalization can impact a number of material properties ranging from mechanical strength and durability to thermal stability [356,357]. Other metal-doped ZnS devices previously reported in the literature, in which phosphor loadings greater than 50 wt.% have been generally used to achieve the desired optical response and behavior for electroluminescent and mechanoluminescent applications [355,358,359].

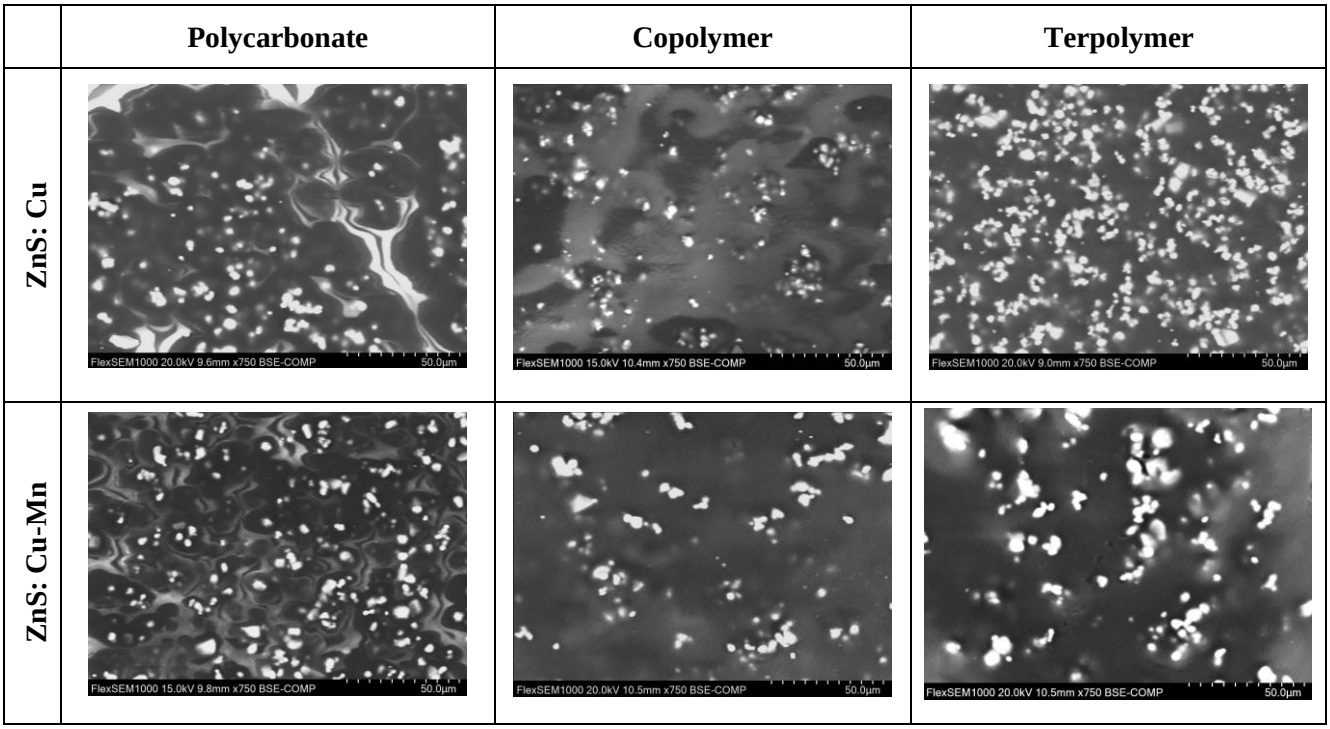

Figure 4.4. SEM images (× 750 magnification) of composites made of 20 vol.% content of phosphorus particles (i.e., ZnS:Cu and ZnS:Cu-Mn corresponding to samples at the first row and the second row) randomly dispersed in three different matrices (polycarbonate, copolymer, and terpolymer corresponding to samples from the left-side to the right-side column).

Il will be next demonstrated in Subsection 4.4.1 that the terpolymer/(ZnS:Cu) composites made with 20 vol.% of particles concentration leads to the best EL response among other tested samples. To a certain extent, this finding is confirmed by the SEM analyses based on the dispersion state of the microparticles within the matrix.

Thèse accessible à l'adresse : https://theses.insa-lyon.fr/publication/2023ISAL0114/these.pdf © [L. Diatezo], [2023], INSA Lyon, tous droits réservés

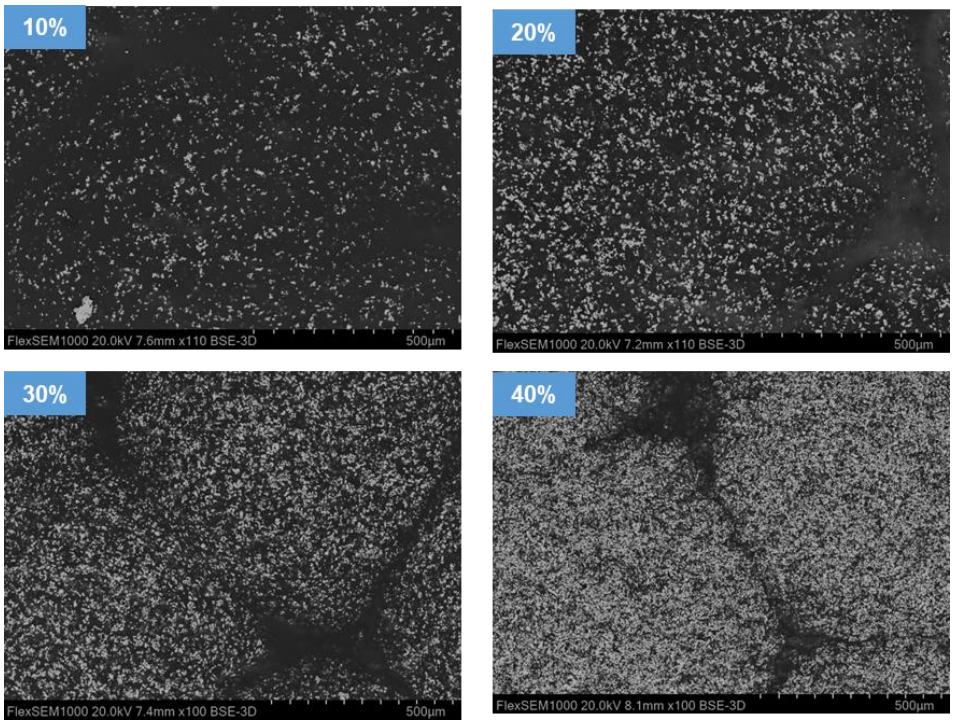

a)

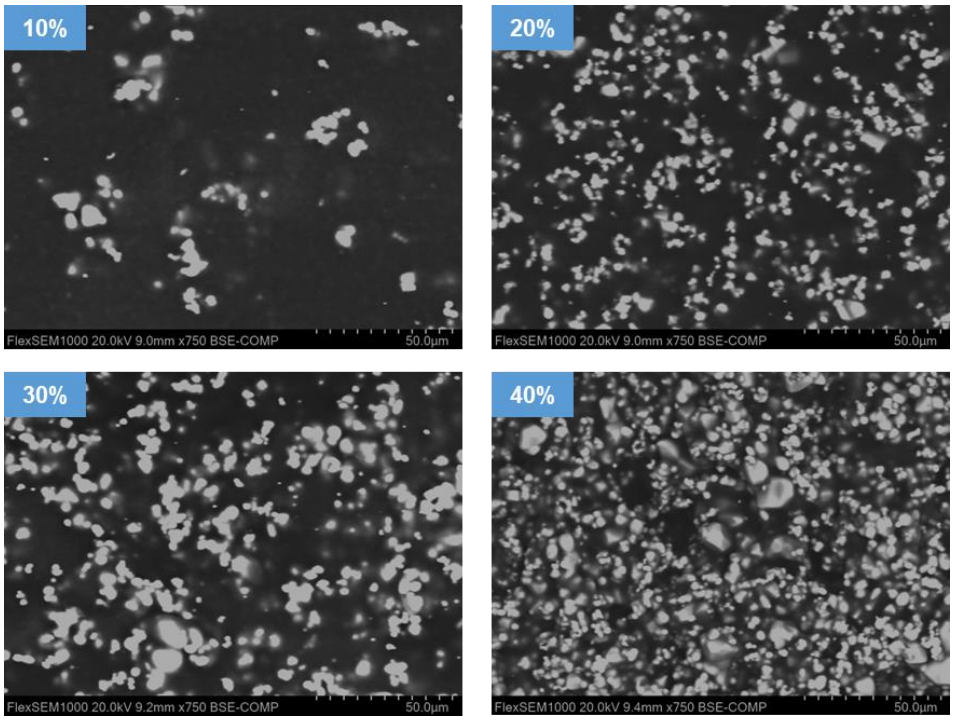

b)

Figure 4.5. SEM images of terpolymer/(ZnS:Cu) composite with different concentration from 10 vol.% to 40 vol.%. Observation waw performed under wo magnifications: a) × 100 ; and b) × 750

Thèse accessible à l'adresse : https://theses.insa-lyon.fr/publication/2023ISAL0114/these.pdf © [L. Diatezo], [2023], INSA Lyon, tous droits réservés

4.3 Electrical behavior of EL materials

4.3.1 Doped phosphor composites with different polymer matrices

The electrical behavior of the different materials (composite, particle, and matrix) was carried out based on the measurement of the input electric filed (denoted E) and the resulting current density (denote J). Figure 4.6 (a) and (b) respectively show the J-E hysteresis loops of the three pure matrices (terpolymer, copolymer, the polycarbonate) as well as their corresponding composite developed with the same volume fraction (i.e., 20 vol.%) of the ZnS:Cu particles. All samples were excited under an input electric field of 10 V/µm amplitude and 500 Hz frequency. Under such an applied field, the composites and the matrices exhibit principally capacitive behavior, which is confirmed by a spherical-shaped J-E plot. It has been suggested that the capacitive current density (J_{capa}) exhibits a circular (or ellipse) relationship with the electric field while the conduction current density (J_{cond}) shows a linear response in relation to the Ohm's law [310,310,360]. Graphically, one can predict that the terpolymer materials (pure or composite) have higher J_{capa} (represented by the area of the ellipse) and J_{cond} (represented by the slope of the ellipse) than the corresponding polycarbonate and copolymer. Therefore, the dielectric permittivity as well as the electrical conductivity of the terpolymer are revealed to be the maximum among the other. Those of the polycarbonate, however, are clearly demonstrated as the minimum.

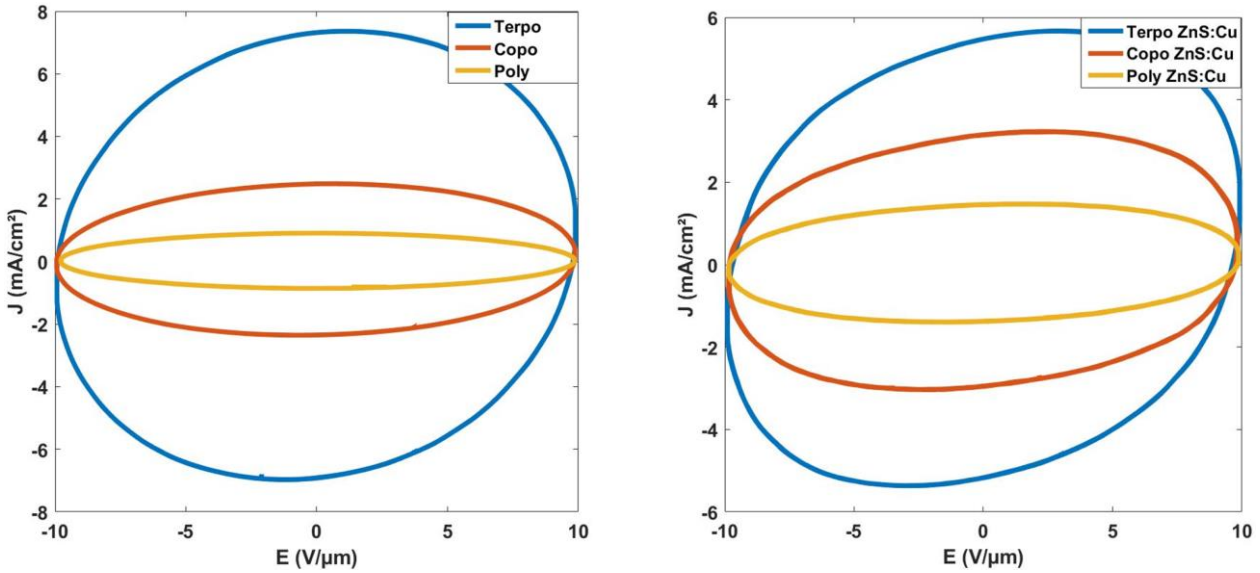

a) b)

Figure 4.6. Current-density-versus-electric-field (J-E) hysteresis curve of: (a) pure matrices; and (b) composites made of three different matrices filled with 20 vol.% ZnS:Cu phosphor particles. All samples were excited under an input electric field of 10 V/µm amplitude and 500 Hz frequency.

To further explore the electrical characteristics of the above materials in a more quantitative manner, a simple method for estimating their dielectric constant (capacitive behavior) and electrical conductivity (conduction behavior) is introduced. An example of data treatment together with several steps of calculation were performed on the case of the terpolymer/(ZnS:Cu) composite. Figure 4.7 (a) represents its J-E characteristics, under an input electric field of ~ 10 V/µm. The total current signal (J_{tot}) is considered as the sum of the conduction current (J_{cond}) and the capacitive current (J_{capa}), the result of the analysis described in Figure 4.7 consists of several steps [310]:

$$J_{total} = J_{cond} + J_{capa} \tag{4.6}$$

Thèse accessible à l'adresse : https://theses.insa-lyon.fr/publication/2023ISAL0114/these.pdf © [L. Diatezo], [2023], INSA Lyon, tous droits réservés

First, as shown in Figure 4.7 (a), the conduction current density (J_{cond}) is extracted and assumed, must be linear with respect to the electric field (E) according to Ohm's law. The electrical conductivity (σ) can be deduced from:

$$J_{cond} = \sigma E \tag{4.7}$$

The capacitive current is therefore:

$$J_{capa} = \frac{dE}{dt}\varepsilon_0.\varepsilon_r(E) \tag{4.8}$$

where t the is time, (ε_0) is the vacuum permittivity, and (ε_r) is the relative permittivity as a function of E. Subsequently, the charge density (D) can be determined by integrating the capacitive current density over time. The polarization consists solely of the dielectric properties and can be expressed as follows:

$$D = \int (J_{capa})dt = \varepsilon_0.\varepsilon_r E \tag{4.9}$$

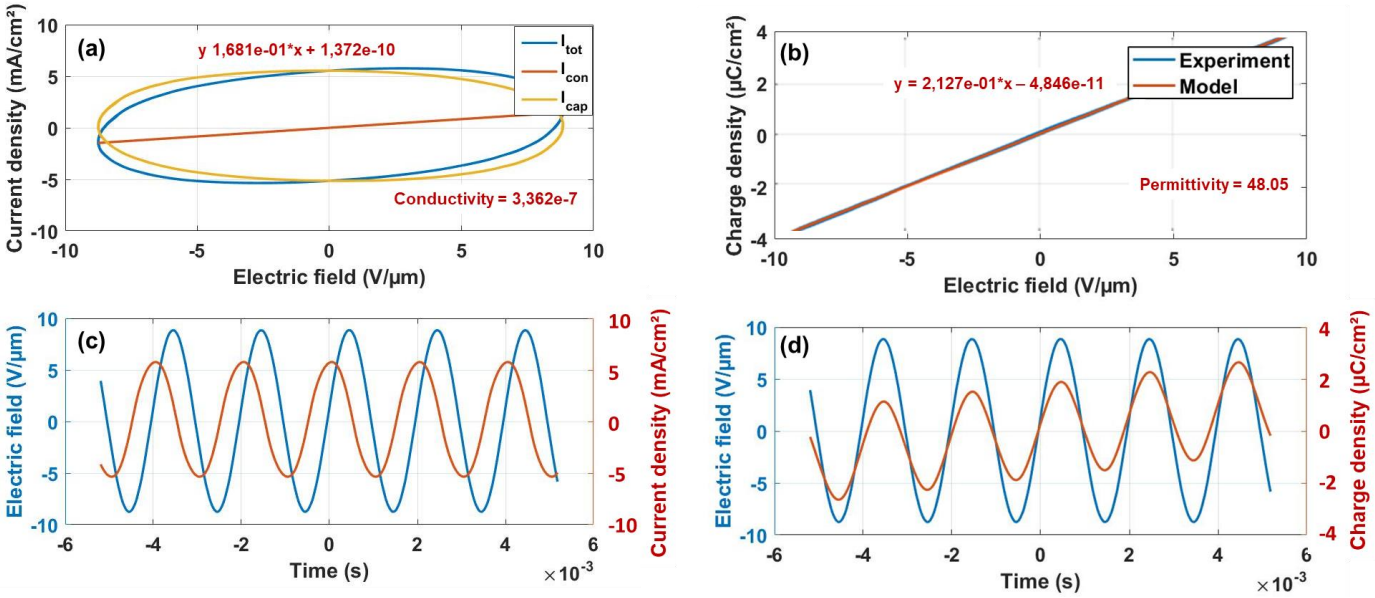

Figure 4.7. Electrical characterization of the terpolymer/ZnS:Cu composite at 20 vol.%, under an input electric field of 10 V/µm: (a) Decomposition of the total measured current densities into two components (J_{capa} and J_{cond}, [276]), allowing to determine the electrical conductivity; (b) Polarization loop of the charge density versus electric field to determine the dielectric permittivity; (c) Time evolution of the electric field, and the current density; (d) the resulting charge density that is in phase with the electric field.

Figure 4.7(b) describes the charge density as a linear function of electric field, allowing to determine the relative permittivity (ε_r) that is supposed to be constant over a low input voltage range. It has been found that ε_r = 48 for the 20 vol.% terpolymer/(ZnS:Cu) composite, which perfectly agrees with measurement obtained via Solartron (see Figure 4.11 (b)). Figure 4.7 (c)-(d) displays the temporal behavior of the electric field, the resulting current density, and charge density. On a one hand, the electric field lags behind the current density, reflecting the dominant capacitive property represented by the circular-shaped J-E curve. On the other hand, the electric field and the charge density are in phase, confirming the linear relationship between D and E. Table 4.1 summarized the estimations of the dielectric constant as well as the electrical conductivity of the pure matrix and their corresponding composites doped with 20 vol.% ZnS:Cu particles. Among the three matrices, the terpolymers lead to the highest values of the dielectric constant ε_r, which was demonstrated via FEM simulation as a key element that boosts the electroluminescent activity. On the other hand, greater electrical conductivity (σ) would induce more conduction leakage for the terpolymer with respect to the others, which in turn provoke higher dielectric losses, especially under low frequency or

Thèse accessible à l'adresse : https://theses.insa-lyon.fr/publication/2023ISAL0114/these.pdf © [L. Diatezo], [2023], INSA Lyon, tous droits réservés

quasi-static regime. In this study, the operating frequency chosen equals 500 Hz that is supposed to be sufficiently high to counterbalance the loss issue of the terpolymer and its composites.

The limited electric field (denoted E_l), beyond which the J-E curve is no longer linear, is also provided in Table 4.1. In practice, the samples is broken as soon as the input filed exceeds E_l, which significantly depends on the type of matrix and particle, as well as the filler's concentration. Indeed, the terpolymer composite exhibits the highest value of E_l (~ 35 V/µm) among the other counterparts, indicating that this matrix could be operated within a larger input range of the electric field. For all tested composites, the input filed is kept moderate, i.e., much lower than E_l when performing electroluminescence.

Table 4.1. Electrical parameters of the polymer matrices that are deduced from the J-E curve

Type of matrix	Pure matrix		Composite-based 20 vol.% (ZnS:Cu) particles		
	Dielectric constant ε_r (at 1 kHz)	Electrical conductivity σ (S/m)	Electrical conductivity σ (S/m)	Dielectric constant ε_r (at 1 kHz)	Limited electric field E_l (V/µm)
Polycarbonate	3	1.47 E–8	1.92 E–8	5	22
Copolymer	10	7.54 E–8	5.26 E–8	15	24
Terpolymer	35	9.29 E–7	3.36 E–7	48	35

4.3.2 Compact blocks of doped-phosphor particles

Besides the electrical characteristics of the matrices and the composites, this subsection aims to complete this study by identify the one of the three phosphor particles including (Zn:Cu), (Zn:Cu-Al), and (Zn:Cu-Mn). Figure 4.8 (a) shows the J-E hysteresis loops of those particles subjected a low electric field of 10 V/µm amplitude and 500 Hz frequency. This data allows for the identification of dielectric constant (ε_r) and the electrical conductivity (σ), together with the limited electric field (E_l) determined in practice These results are summarized in Table 4.2, leading to the following comments:

- All the particles are in the same order of magnitude of the electrical conductivity, which is sufficiently low to be considered as a dielectric material with negligible conduction losses.
- The Zn:Cu particles has the smallest value of the dielectric constant (ε_r) as opposed to the others. Therefore, those particles lead to the minimum discrepancy of ε_r with respect to the matrices presented in Table 4.1.
- Such a minimum discrepancy makes the local filed driven to the Zn:Cu particles within the polymer matrix much higher with respect to the case of the (Zn:Cu-Al), and (Zn:Cu-Mn) particles.
- The limited electric field (E_l) is found greater in the case of the Zn:Cu particles compared to the other counterparts.
- The above characteristics makes the Zn:Cu particles as the most appropriate choice for the development of electroluminescent (EL) device. This fact will be definitively confirmed by experimental tests investigated in the next Subsection 4.4.

When increasing the values of the input electric field ($E = 50$ V/µm in amplitude) beyond the limited value, a transition from the capacitive to the conductive behavior of the phosphor particles was observed (cf. Figure 4.8 (b)). In other words, with sufficient electrical power, the electrons of the valence band pass to the conduction band [361–363]. The J-E hysteresis curve of all particles are thus not linear any longer. Indeed, beyond the limited field, the resulting current density considerably increases, reflecting the nature semiconductor property of the phosphor. In such a configuration, the composites made of these particles are certainly broken, as the conduction pathways created within their polymer matrix might destroy them. Consequently, the input voltage should be controlled far below the limited value so as to avoid any breakdown of the samples.

Thèse accessible à l'adresse : https://theses.insa-lyon.fr/publication/2023ISAL0114/these.pdf © [L. Diatezo], [2023], INSA Lyon, tous droits réservés

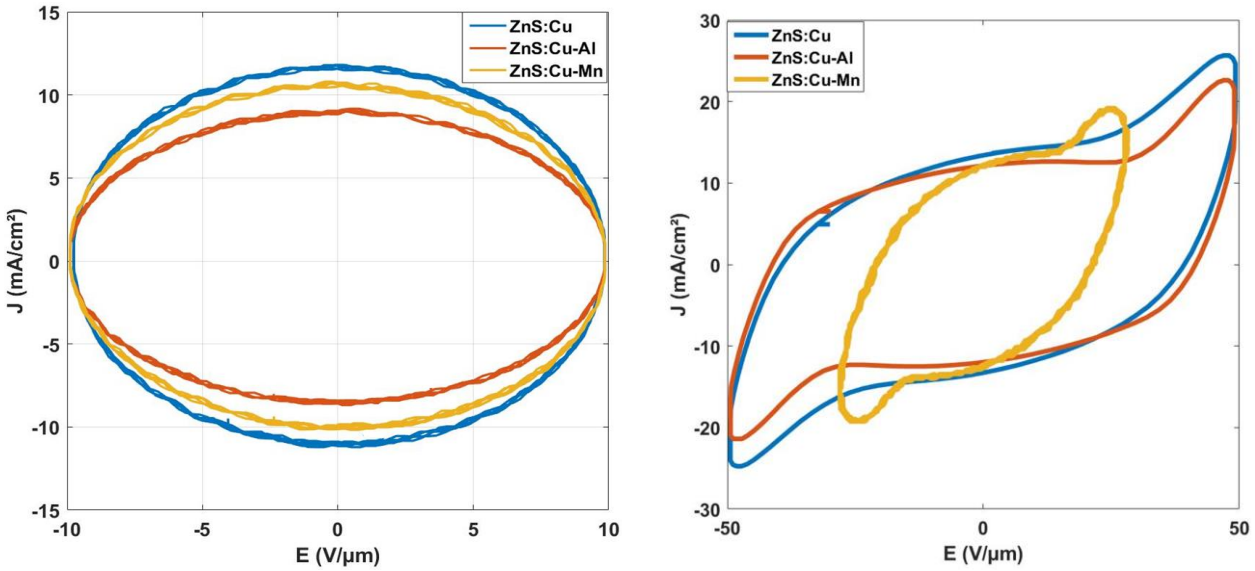

Figure 4.8. Current density as a function of electric field of (a) at low electric field with purely capacitive behavior (i.e., linear J-E characteristics); and (b) at high electric filed where the phosphor is transited as semi-conductor behavior (i.e., nonlinear J-E characteristics).

Table 4.2. Electrical parameters of the phosphorus particles that are deduced from the J-E curve

Type of particles	Electrical conductivity σ (S/m)	Dielectric constant ε_r (at 1 kHz)	Limited electric field E_l (V/µm)
ZnS: Cu	4.92 E–8	93	40
ZnS: Cu-Al	7.79 E–8	133	30
ZnS: Cu-Mn	2.55 E–8	253	25

4.4 Optimization of EL based on adequate combinations of particle and matrix

The electroluminescence (EL) of a composite depends on three main factors including the type of particles, the particle concentration, and the type of polymer matrix. In the following, each factor is going to be thoroughly analyzed by keeping the two other unchanged. The key objective here is to understand how these factors have an impact on the composite characteristics, which is of primary significance to find out the best material formulation for an optimization of electroluminescent (EL) response.

4.4.1 Influence of EL particles

To assess the influence of the type of particles, experimental tests were carried out on the ZnS phosphorus powders included with different dopants (Cu, Cu-Al, and Cu-Mn as indicated in Subsection 2.1). All the materials, made of the same terpolymer matrix and 20 vol.% of doped phosphorus particles, were subjected to an electric field (denoted E) of variable amplitude (from 2 to 10 V/µm) at a fixed frequency of 500 Hz. It is clearly seen from Figure 4.9(a) that under a given value of E, the (ZnS:Cu) composite leads to a much better brightness with respect to the two others. Furthermore, its luminance response (denoted L) is linearly increasing within the full range of the electric field. This behavior is contrary to the one of the (ZnS:Cu-Al) composite that reaches the maximum brightness of 2500 Cd/m² at $E = 8$ V/µm, then saturates and tends to decrease with higher value of E. On the other hand, the (ZnS:Cu-Mn) composite exhibits very weak luminosity in such a way that whatever the applied electric field, the luminance is revealed to be stable at an extremely low level of 12 Cd/m². Practical test demonstrates that the emitted light is not activated with

Thèse accessible à l'adresse : https://theses.insa-lyon.fr/publication/2023ISAL0114/these.pdf © [L. Diatezo], [2023], INSA Lyon, tous droits réservés

the (Cu-Mn) dopant under the field excitation, confirming that such a material is not appropriate for applications in ACEL.

Figure 4.9 (b) compares different properties of the three composites in terms of the brightness and the dielectric constant, as well as the ratio between the local field seen by the particles (computed from the FEM) and the external field (fixed at $5.5\ \mathrm{V/\mu m}$ in experiment). The results obviously shows an ultimate link between the light intensity and the dielectric property of the composite, which in turn significantly affects the field level internally distributed to the phosphorus particles. Concretely, the (ZnS:Cu)/terpolymer sample has the maximum brightness of 3700 Cd/m² compared to the other, which is 2.6 times higher than the one of the ZnS:Cu-Al composite. As a matter of fact, the internal field applied to the ZnS:Cu particles was revealed (from FEM simulation) to be the highest value with a ratio of 0.69 with respect to the field subjects to the own composite (i.e., $5.5\ \mathrm{V/\mu m}$). This observation can be explained due to the fact that the discrepancy in the dielectric constant between the terpolymer matrix ($\varepsilon_r = 40$) and the copper doped phosphor ($\varepsilon_r = 93$) are less than the other counterparts. Indeed, ZnS:Cu particles possesses superior value of ε_r to ZnS:Cu-Al (with $\varepsilon_r = 133$) and ZnS:Cu-Mn (with $\varepsilon_r = 253$). Logically, similar trend was obtained with their corresponding composites (Figure 4.9 (b)), in which the ZnS:Cu-Mn sample with its highest permittivity ($\varepsilon_r = 58$) leads to the lowest light intensity. In this composite, the electric field is more concentrated in the matrix, so the field seen by the particles is much weaker. Indeed, the luminosity is more significant when the permittivity of the phosphor particles is closer than that of the polymer matrix. Figure 4.9 (c) shows the emitted light driven by those composites. Among the three tested sample, the one elaborated with the zinc sulfide doped with copper (ZnS: Cu) is demonstrated as the best EL property with the most brightness intensity. This type of particle is thus chosen to be tested with different concentration in the composite.

Figure 4.10(a) displays the variation of the dielectric constant ε_r, which increases as a function of the filler rates (or volume fraction) in the (ZnS:Cu)/terpolymer. The dielectric property is performed under a dynamic of 1 kHz, around which the variation of the permittivity is relatively moderate as composed to the low frequency range. It can be seen that the mixed models developed by Pauer and Maxwell-Garnett are in perfect agreement with the experimental results. The simplified models relied on the serial and parallel configurations, however, lead to discrepancy in the prediction of the dielectric constant. The serial model tends to underestimate the value of ε_r, which is inversely to the parallel model. Interestingly, the error estimation is found to be much smaller with the serial configuration where the black curve is clearly closer to the real data as opposed to the blue one. Consequently, the capacitor C'_m in one of the parallel branches could be, to some extent, ignored in the equivalent electrical scheme (cf. Figure 4.2 (c)). As seen in Figure 4.10(b), the 20 vol.% (ZnS:Cu)/terpolymer leads to the best luminance with respect to those elaborated with other volume fraction. A decrease in the brightness at 30% and 40% is possibly due to irregularities related to the dispersion of phosphorus particles, the percolation, and the fact that agglomerates have probably formed during mixing. On a one hand, the permittivity of the composite increases with the increasing volume fraction of the phosphorus particles, as the permittivity of the phosphorus particles is higher than that of the polymer matrix. On the other hand, the local field seen by the particle slightly decreases as a function of the particles' content. In conclusion, the luminance depends on several factors including the dielectric permittivity, the local field applied to the particles, the composite concentration that have an impact on the dispersion of the particles. The evolution of the permittivity versus the concentration is somehow opposed to the one of the local distributed field. Based on the best compromise among these factors, it was demonstrated that the sample with 20 vol.% of (ZnS:Cu) powder can be considered as the most appropriate choice.

Thèse accessible à l'adresse : https://theses.insa-lyon.fr/publication/2023ISAL0114/these.pdf © [L. Diatezo], [2023], INSA Lyon, tous droits réservés

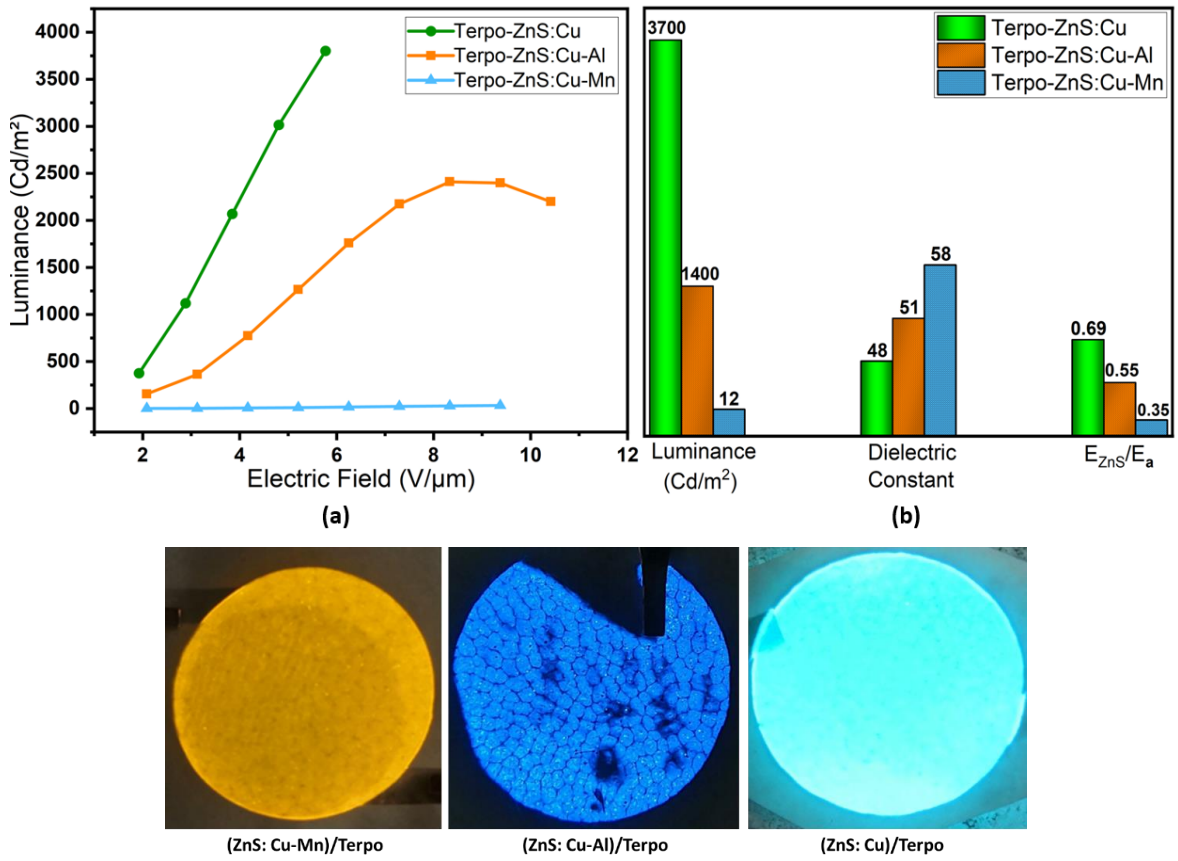

Figure 4.9. Influence of the type of particles on the EL property of composite: (a) Evolution of the luminance as a function of the electric field; (b) the ratio of the local field seen by the particles as well as the EL and the dielectric behaviors of the composites subjected to an input field of 5.5 V/µm at 500 Hz ; (c) Images demonstrating how light intensity varies with different types of ZnS phosphorus dopant. Tests were conducted on the composites-based terpolymer matrix made with different types of doped ZnS particles with the same content of 20 vol.%

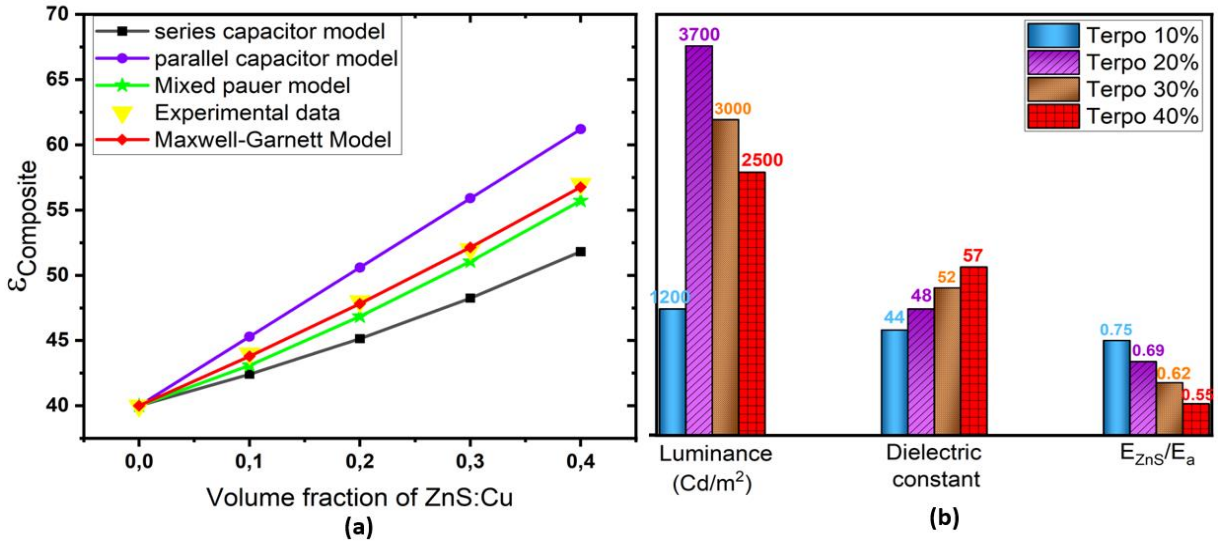

Thèse accessible à l'adresse : https://theses.insa-lyon.fr/publication/2023ISAL0114/these.pdf © [L. Diatezo], [2023], INSA Lyon, tous droits réservés

Figure 4.10. Influence of the particles' content on the composite characteristics: (a) Comparison between the numerical model and the empirical data (measured at 1 kHz) of the dielectric constant; (b) the ratio of the local field seen by the particles as well as the EL and the dielectric behaviors of the composites subjected to an input field of 5.5 V/µm at 500 Hz. Tests were conducted on the composites elaborated with different volume fraction of (ZnS:Cu) phosphorus particles dispersed into terpolymer matrix.

4.4.2 Influence of polymer matrix

The purpose of this study is to identify the influence of the polymer matrices on the light emission of the EL composite. To do this, we opted for three types of matrix consisting of polycarbonate ($\varepsilon_r = 3$), terpolymer ($\varepsilon_r = 40$), and copolymer ($\varepsilon_r = 10$). All of them were made of copper-doped zinc sulfide (ZnS:Cu) particles with a volume fraction of 20 vol.%. Moreover, they were subjected to an input electric field of 500-Hz frequency and variable moderate amplitude ($< 10V/\mu m$) so as to keep the composites in a linear electrical characteristics (see Figure 4.8).

Figure 4.11(a) illustrates the evolution of the light brightness as a function of the electric field of those three different matrices with the (ZnS:Cu) phosphor particles. As expected, the brightness of these composites increases in a linear trend with respect to an increase in the applied field. Interestingly, under the same amplitude of 5.5 V/µm as shown in Figure 4.11 (b), the terpolymer composite gives rise to the best luminosity as opposed to the others, with a luminance of 3700 Cd/m² against 1700 Cd/m² and 250 Cd/m² as in the cases of the copolymer and the polycarbonate, respectively. It can be therefore revealed that the EL coupling depends not only on the active element as phosphorus particles, but also on the polymer matrix with which electricity cannot convert to light. However, the dielectric property of the matrix itself does have significant impact on the internal field distributed to the active particles. As mentioned previously, this field is more considerable when discrepancy in the permittivity (ε_r) between the matrix and the particles are minimized. This result is again confirmed based on the ratio between the local field seen by the (ZnS:Cu) particles and the field applied to the composite, as displayed in Figure 4.11 (b). Among the three tested matrices, terpolymer possesses the highest permittivity value ($\varepsilon_r = 40$), which is revealed to be closer to the one of the (ZnS:Cu) phosphor particles ($\varepsilon_r = 93$). Consequently, a combination of those particles with the terpolymer induces a substantial enhancement in the electroluminescent response. On contrary, the copolymer and polycarbonate have a much lower dielectric constant. The electric field is thus concentrated more on them rather than on the phosphorus particles, which, to some extent, weakens the EL effect of the composite. Figure 4.11 (c) again demonstrates the highest intensity of light obtained with the terpolymer composite. Accordingly, selecting an adequate couple of matrix and particle is of key importance to achieve satisfactory electroluminescence.

Figure 4.12 shows the efficiency ($\mathrm{Cd/W}$) of the three composites as a function of the electric field, another indicator measuring the light power of the electroluminescence. It is expecting that the composite-based polycarbonate has very low EL efficiency (< 25 % at $\sim 8V/\mu\mathrm{m}$), as a consequence of its extremely weak brightness. Both copolymer and terpolymer samples shows a parabolic curve with a negative concavity (or concave down), where a maximum peak of 75 % and 50 % respectively occurs at $4.5\ \mathrm{V/\mu m}$ and $3.8\ \mathrm{V/\mu m}$. Whatever the applied electric field (E), the composite-based copolymer exhibits superior efficiency to the terpolymer counterpart. As indicated in Figure 4.6, the resulting current density of the copolymer composite is clearly smaller than that of the terpolymer, which in turns leads to smaller power consumption. Actually, the current density is ultimately related to the charge displacement D that is supposed to be proportional to the dielectric constant ε_r ($i.e., D = \varepsilon_r\ \varepsilon_0\ E$). Since ε_r of the terpolymer composite is much higher than the one of the copolymer (cf. Figure 4.11 (b)), its displacement *D*, as a result, is also higher. Therefore, even though the luminance generated by the terpolymer is more significant, its efficiency is somehow less than the one of the terpolymer. In other words, polymer matrix with a higher dielectric constant gives raise to enhanced light intensity but more energy consumption. A compromise would be made to get satisfactory efficiency. For a better utilization of electroluminescent devices, operating under low electric fields would lead to longer materials' life, lower power consumption, and more stable

Thèse accessible à l'adresse : https://theses.insa-lyon.fr/publication/2023ISAL0114/these.pdf © [L. Diatezo], [2023], INSA Lyon, tous droits réservés

brightness. For our target application, the choice between the copolymer or the terpolymer depends on the specifications imposed by Tesca.

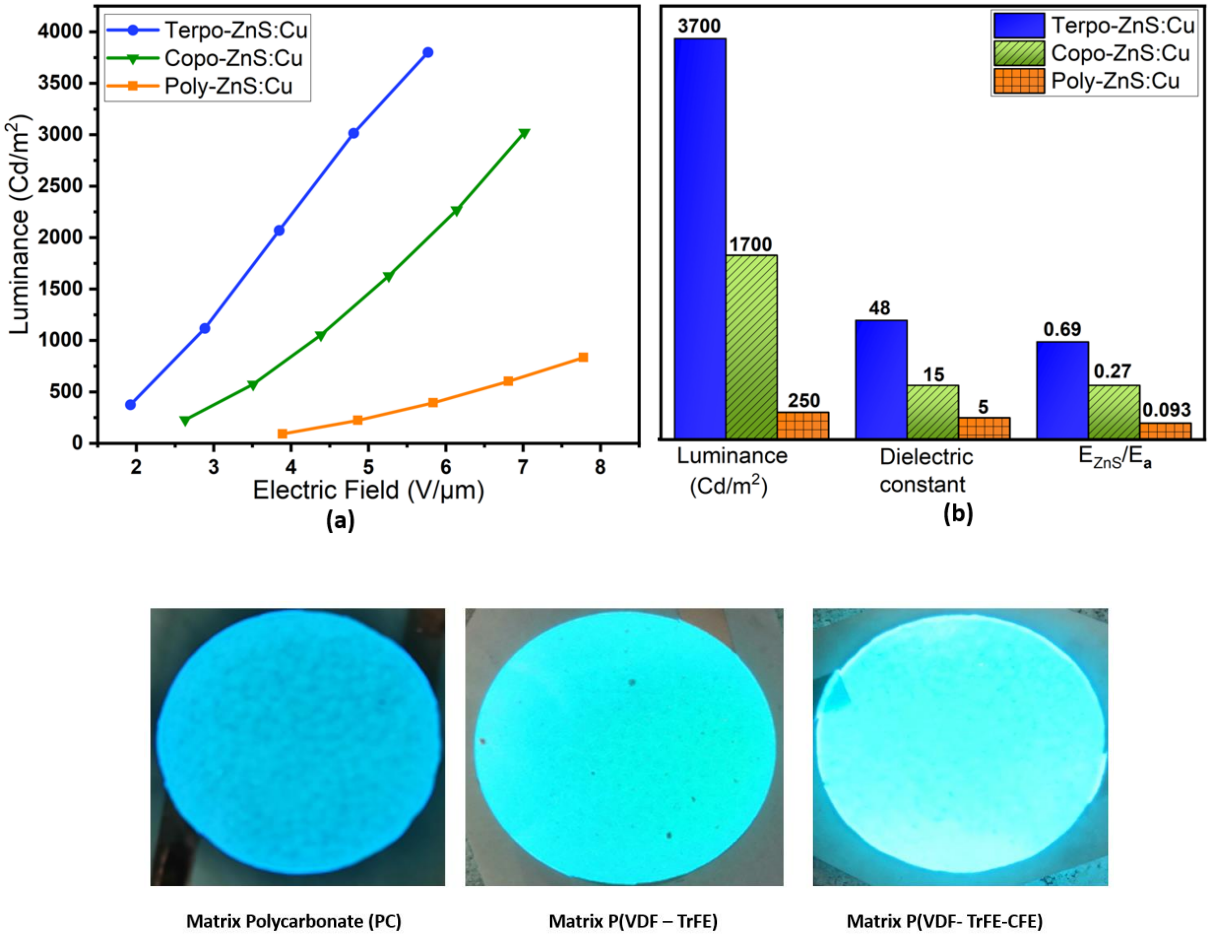

c)

Figure 4.11. Influence of the type of polymer matrices on the EL property of composites: (a) Evolution of the luminance as a function of the electric field; (b) the ratio of the local field seen by the particles as well as the EL and the dielectric behaviors of the composites subjected to an input field of 5.5 V/µm at 500 Hz; (c) Images demonstrating how light intensity varies with different types of polymer matrices. Tests were conducted on the composites elaborated with the same particles (20 vol. % (ZnS:Cu) phosphorus) dispersed into the three polymer matrices comprising terpolymer, copolymer, and polycarbonate.

Thèse accessible à l'adresse : https://theses.insa-lyon.fr/publication/2023ISAL0114/these.pdf © [L. Diatezo], [2023], INSA Lyon, tous droits réservés

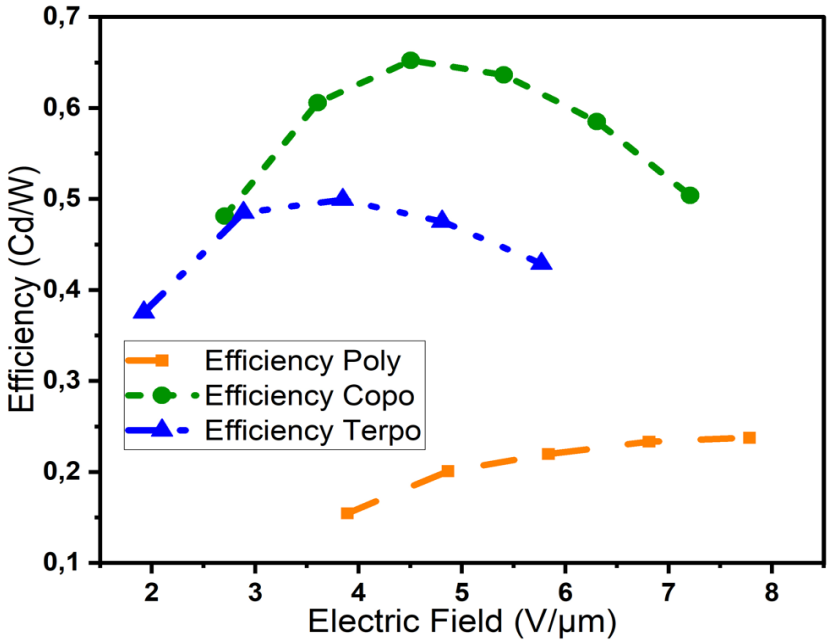

Figure 4.12. Light efficiency as a function of the electric field at a frequency of 500 Hz. . Tests were conducted on the composites elaborated with the same particles (20 vol. % (ZnS:Cu) phosphorus) dispersed into the three polymer matrices comprising terpolymer, copolymer, and polycarbonate.

4.4.3 Comparison with simulation-based FEM

The numerical simulation-based finite element method (FEM) investigated in this subsection allows to illustrate the electric field distribution among different phases consisting of phosphorus particles and polymer matrix. Also, it is possible to estimate the local field driven to the particle that is needed to determine the ratio between it and the input field used to power the composites (with an amplitude of 5.5 V/µm). This ratio were shown in the bar graphs of Figure 4.9–Figure 4.11 (b).

Figure 4.13 represents the electric field distribution of the three samples elaborated with the same terpolymer matrix but with different types of phosphorus particles. The color scale set for the three cases are identical, for easier visualization and comparison. As seen in Figure 4.13 (a), the (ZnS:Cu)/terpolymer composite exhibits the less gradient between the particles and the matrix, where the local field seen by the particles (~ 3.9 V/µm) is relatively near to the input field (5.5V/µm). Actually, when the matrix has a dielectric permittivity close to that of the particles, the field is somehow as concentrated on the particles as on the matrix. In our case, the permittivity of the (ZnS:Cu) filler approximately doubles the terpolymer's one, its local field is thus around half of that of the terpolymer (~ 7.6 V/µm). Regarding the phosphorus (ZnS:Cu-Al)/terpolymer composite shown in Figure 4.13 (b)**,** higher gradient between the particles (~ 3.1 V/µm) and the matrix (~ 8.5 V/µm) was observed. As previously shown in Table 4.2, the permittivity of the ZnS:Cu-Al particles is threefold superior to that of the matrix, which engenders threefold inferior for the local field. Compared to the last phosphorus (ZnS:Cu-Mn)/terpolymer composite displayed in Figure 4.13 (c)**,** the local field seen by the particles is extremely weak (~ 1.6 V/µm) as opposed to the input field. This fact is evidently due to a huge difference in the permittivity between the particles and the matrix. As a consequence, the electroluminescent (EL) is not well activated by the phosphorus particles under such a level of the input field. However, the electric field driven within the matrix, particularly surrounding the (ZnS:Cu-Mn) particles, could be very high, provoking increase probability of the sample breakdown. Moreover, under such a high electric field, a conductive path could be created among the particle-particle interaction, leading to an activation of the semiconductor nature of the phosphorus materials. Consequently, their electrical feature represented by the J-E curve is not linear any longer. As confirmed by Figure 4.8(b), the (ZnS:Cu)/terpolymer sample has the switching field (limit between linear and nonlinear behavior) higher

Thèse accessible à l'adresse : https://theses.insa-lyon.fr/publication/2023ISAL0114/these.pdf © [L. Diatezo], [2023], INSA Lyon, tous droits réservés

than the other counterparts, as the local field attributed to the (ZnS:Cu)/particles and the terpolymer is more homogenous. Accordingly, the field surrounding the particles is moderate, to some extents, which prevents from the electric breakdown and a creation of the conducive paths.

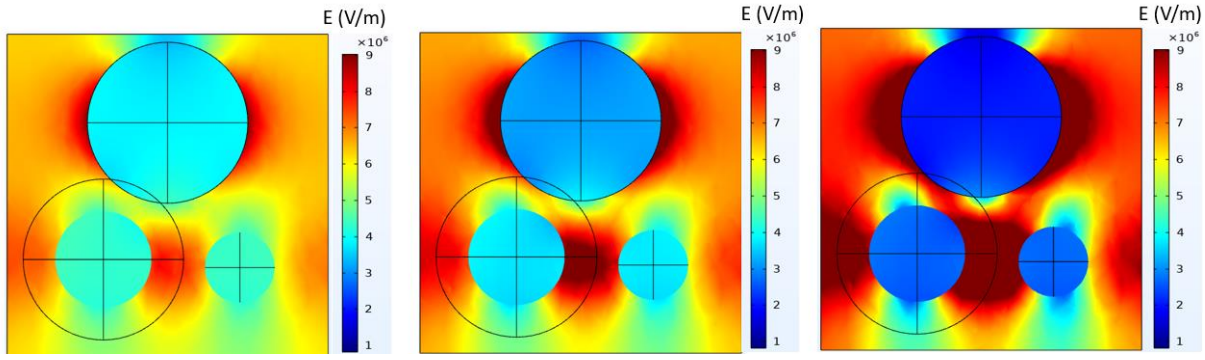

(a) (b) (c)

Figure 4.13. Electric field distribution using 3D finite element for modeling composites made of terpolymer matrix included with different doped phosphorus particles (20 vol.%) such as (a) ZnS: Cu; (b) ZnS: Cu-Al; and (c) ZnS: Cu-Mn.

Alternatively, Figure 4.14 represents the electric field distribution of the three samples elaborated with the same phosphorus particles (ZnS:Cu) but with different types of polymer matrices. Because of high discrepancy in the permittivity between the filler ($\varepsilon_r = 93$) and the matrix as the polycarbonate ($\varepsilon_r = 15$) and the copolymer ($\varepsilon_r = 5$), the local field seen by the (ZnS:Cu) particle is extremely low. The result shown in Figure 4.14 (a)–(b) gives out an estimation for such a local field of ~ 0.5 V/µm and ~ 1.5 V/µm, respectively in the case of the polycarbonate and the copolymer sample. These values are clearly very small compared to the one used to apply to the samples (5.5 V/µm). On the other hand, the field driven within the matrix is drastically considerable, which is contrary to the terpolymer sample displayed in Figure 4.14 (c). Accordingly, the combination between the copper-doped phosphorus (ZnS:Cu) and the terpolymer matrix leads to the best performance in terms of low breakdown probability, and homogenous field distribution. These features are demonstrated as of key significance to successfully activate electroluminescence with satisfactory brightness intensity. The simulation analyses are in good correlation with the experimental characterizations, confirming the reliability of our developed device. Also, this study allows for a better understanding in the EL mechanism, which is strongly impacted by the materials' properties.

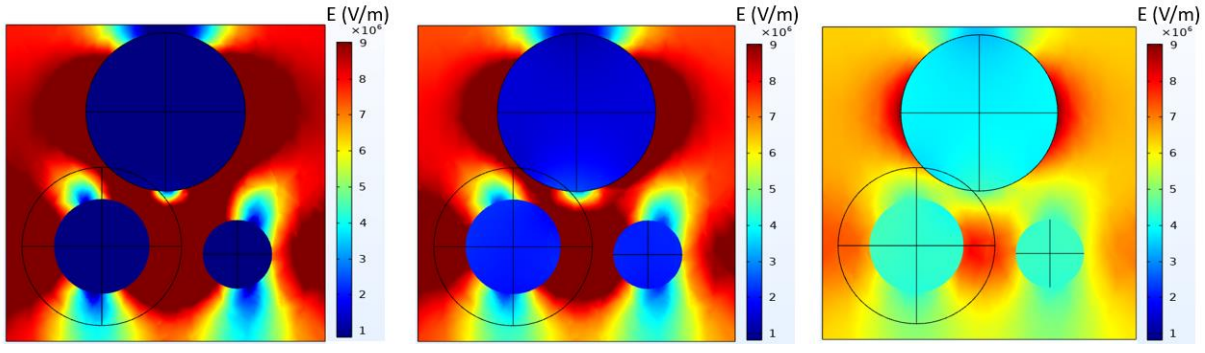

(a) (b) (c)

Figure 4.14. Electric field distribution using 3D finite elements for modeling composites made of 20 vol.% (ZnS: Cu) phosphorus particles incorporated within different matrices such as (a) polycarbonate; (b) copolymer; and (c) terpolymer.

Thèse accessible à l'adresse : https://theses.insa-lyon.fr/publication/2023ISAL0114/these.pdf © [L. Diatezo], [2023], INSA Lyon, tous droits réservés

Figure 4.14.(B) shows the influence of three matrices which have the permittivity of $\varepsilon_r = 3$ for polycarbonate, $\varepsilon_r = 10$ for copolymer and terpolymer of $\varepsilon_r = 35$ with the fixed phosphorus particles with permittivity $\varepsilon_r = 93$ respectively. An electric field Etotal = 5.5V/µm was applied to the samples made with the three matrices.

We note that with phosphorus (ZnS:Cu) by modeling, the gradient of permittivity between the phosphorus particles and the matrices, polycarbonate and copolymer are more important. The local field seen by the particle in practice, by applying a total field of Etotal =5.5V/µm by modeling, gives us a field of 0.51V/µm for the polycarbonate and 1.47V/µm for the copolymer which is very low compared to the field applied on the samples. In other words, the field concentrates more in the matrix than in the particle, because the interactions of the phosphorus particles are somewhat less important in the copolymer, and more important in the polycarbonate, this increases the breakdown field path, which is much faster in the samples. However, with the terpolymer by modeling, we see that there is less gradient between the particle and the matrix. The local field seen by the particle is stronger by 3.84 V/µm, and closer to the electric field applied on the sample of 5.5V/µm. This allows to have a more important light emission. We also note that, the results of dielectric permittivity by modeling of the three composites are respectively $\varepsilon_r = 5$ for polycarbonate, $\varepsilon_r = 15$ for copolymer and $\varepsilon_r = 48$ terpolymer. Well respect that the mixing law, is in perfect agreement with the experimental results (see section 4.4.1 of Figure 4.9 (b)). So we can say that terpolymer is our best matrix for electroluminescent device fabrication. In the next section, we plan to use TESCA-Group's screen-printing technique to manufacture electroluminescent devices.

4.5 Integration of EL devices on a textile substrate

Previous analyses highlighted that the terpolymer matrix, with its very high dielectric constant, leads to the best EL response with respect to the other polymer. However, the terpolymer is very expensive, which limits its wide use in industrial scale for automotive area. Therefore, to print a real EL composite on a textile substrate, we opted for three classical polymer binders including Archroma polyurethane (PU-AR), Archroma acrylic (AC-AR), and Rudolf acrylic (AC-RUD). These commercial products, i.e., provided by Tesca company, have been proven to be compatible with additive manufacturing (AM) based on 3D screen-printing industrial process. This study aims to compare the permittivity and the dielectric losses of the three binders in order to select the most appropriate candidate that meets the Tesca's requirements. Criteria such as cost and ease of processing are also considered.

4.5.1 Dielectric property of polymer binders

This study aims to determine the dielectric properties of the three printed polymer binders by using two different configurations:

- the binder is sandwiched between two thin gold electrodes and there is no substrate. This simple architecture is illustrated in Figure 4.15(a).
- the above electrode/binder/electrode architecture is coated on the textile substrate as depicted in Figure 4.15(b), allowing to confirm whether or not the substrate could influence on the dielectric property of the polymer matrix.

Thèse accessible à l'adresse : https://theses.insa-lyon.fr/publication/2023ISAL0114/these.pdf © [L. Diatezo], [2023], INSA Lyon, tous droits réservés

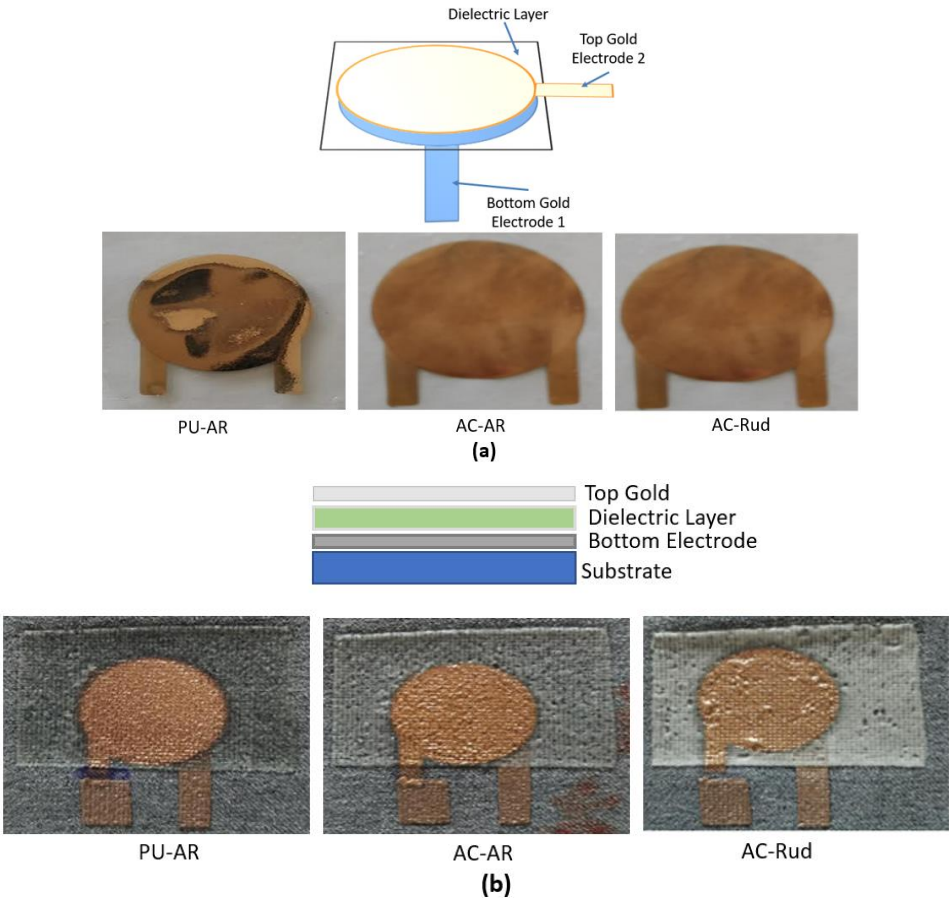

Figure 4.15. Photograph of three polymer-binder film sandwiched between two electrodes: (a) a substrate-free dielectric film; and (b) a device structure deposited on a textile substrate.

Table 4.3 presents the dielectric measurements (at 1 kHz) of the three polymer matrices tested with two configurations. It should be noted that the dielectric constant (ε_r) of the PU-AR polymer binder exhibits very small difference between these configurations. This is due to the high viscosity of the polyurethane ink, which limits its penetration into the porous substrate during the printing process. Such a behavior is contrary to that of the AC-AR and AC-RUD whose ε_r is drastically reduced (more than half) when coated on the textile substrate. Indeed, these polymer matrices have a lower viscosity that favors its penetration into the textile. This also impacts the drying temperature that results in the appearance of a few tiny holes on the film interface as well as a lack of homogeneity. These factors definitively contribute to dielectric losses and a decrease in the dielectric permittivity. As indicated in Table 4.3, all samples lead to important losses when deposited on the textile, which in turns introduces parasites to the polymer coating. Eventually, PU-AR will be chosen for the manufacture of the EL device, regarding its stable value of ε_r.

Table 4.3. Characterization of the dielectric constants of three polymer binders.

	Frequency (f) = 1000 (Hz)			
Binders	Devices without substrate		devices with substrate	
	Dielectric constant	Dielectric losses	Dielectric constant	Dielectric losses
PU-AR	3.25	0.088	2.91	0.42
AC-AR	4.36	0.071	1.83	0.67
AC-Rud	4.07	0.052	1.87	0.53

Thèse accessible à l'adresse : https://theses.insa-lyon.fr/publication/2023ISAL0114/these.pdf © [L. Diatezo], [2023], INSA Lyon, tous droits réservés

4.5.2 Morphological analyses of polymer binders

Figure 4.16 (a-c) and (d-f) respectively illustrated the top-view and the cross-section images of the three polymer matrices (PU-AR, AC-AR, and AC-RUD) via SEM. The aim of this study is to evaluate the print quality of the three polymer binders, with a particular emphasis on the surface uniformity and penetration depth of the polymer binder into the textile substrate.

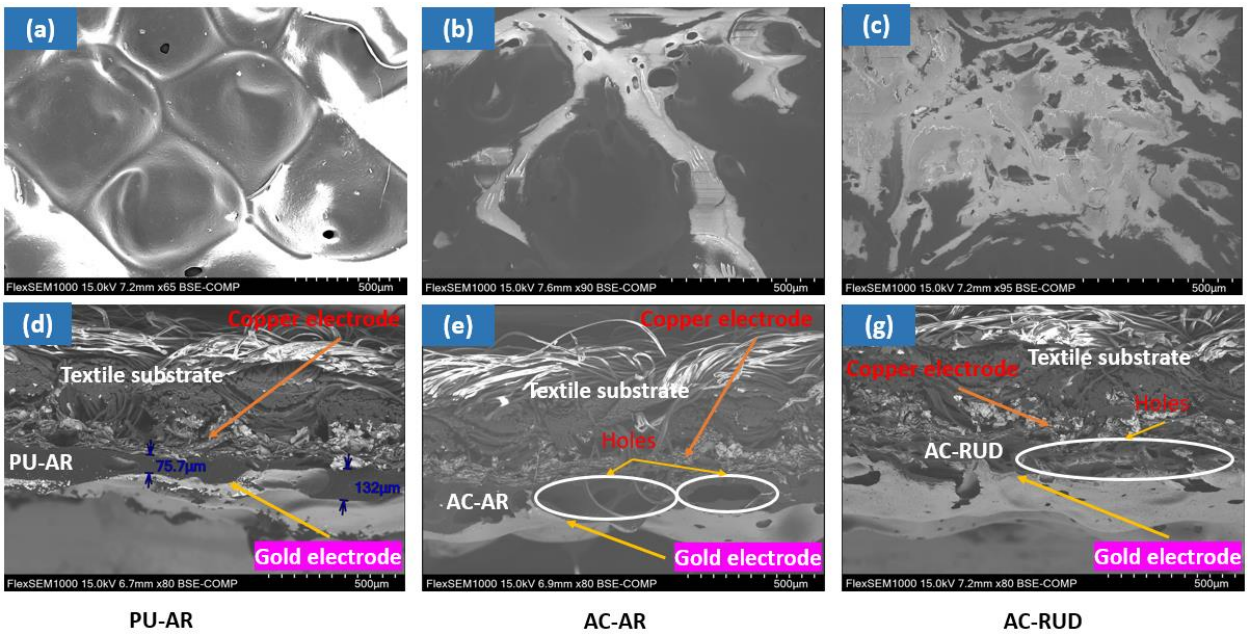

Figure 4.16. Micrographs of the three polymer matrices consisting of PU-AR, AC-AR, and AC-RUD (from the left-to the right-hand side, respectively) printed on a textile substrate. a-b-c) the top view (performed on the upper surface); and d-e-f) the edge view (performed on the cross-section).

According to the observation of Figure 4.16 (a), the polymer binder film generates somehow a uniform printed surface, in spite of some a few tiny holes visible on the coating surface. The entire area appears dark, indicating good adhesion of the film to the fabric surface. Contrarily to the AC-AR, and AC-RUD binders, significant defects can be seen on the film surfaces as displayed in Figure 4.16 (b)–(c). These defects appear in clear areas, indicating poor adhesion between the ink and the textile. Cross-sectional micrographs provide detailed information relating to morphological features. As shown in Figure 4.16 (d), the PU-AR coating, thanks to its adequate adhesion and high viscosity, is well maintained beyond the fabric surface. From a macroscopic point of view, it sems that a presence of unavoidable minor imperfections such as zigzag burrs and small snags might not have a significant impact on the dielectric behavior of the PU-AR coating. In contrast, the AC-AR and AC-RUD matrices shown in Figure 4.16 (e)–(f) exhibit excessive and irregular spreading along the edges of the textile substrate, resulting in zigzagging burrs and a presence of big holes. These undesirable effects can be attributed in part to the viscosity of the polymer binders, the drying temperature of the device, the porous substrates, as well as the print quality of the film. In addition, the textile substrate has a complex porous structure with a rough surface, resulting in regular variations in its surface energy. Consequently, the penetration of polymeric binders strongly depends on their viscosity and the quality of the drying process.

Accordingly, morphological feature-based SEM analysis confirm that the print quality of the PU-AR ink is satisfactory, which is of crucial importance for guaranteeing optimum luminous performance.

Thèse accessible à l'adresse : https://theses.insa-lyon.fr/publication/2023ISAL0114/these.pdf © [L. Diatezo], [2023], INSA Lyon, tous droits réservés

4.5.3 Preliminary prototype of EL device coated on textile substrate

For the fabrication of a real EL device implemented on the fabric substrate, PU-AR binder was mixed with 20 vol.% copper-doped zinc sulfide (ZnS:Cu) phosphor particles. With the aim of evaluating influence of the electrode on the dielectric property as well as the EL response of the composite, two types of conductive material were involved in the elaboration of the electrodes, which consist of:

- gold: excellent electrical conductivity but not transparent and high cost. This material was deposited, with a very thin layer of 25 nm, on the top of the composite film based on the sputtering method.
- (PEDOT: PSS) : transparent (esthetic issue), low cost but weak electrical conductivity. Being compatible with additive manufacturing (AM), this material was screen-printed on the composite surface with a thickness of ~ 30 µm.

It has been revealed that the dielectric losses of the sample made of (PEDOT: PSS) electrode is significantly higher ($D\sim 0.7$ at 1 kHz) than that of the gold-electrode sample ($D\sim 0.15$). This is probably due to the poor electrical conduction of the transparent electrode as well as its important thickness that might not be neglected as in the case of the gold electrode. Figure 4.17 illustrates the light emission of those devices subjected to an electric field of 5.5 V/µm and a frequency of 500 Hz. The gold composite, as displayed in Figure 4.17 (a), exhibits satisfactory light intensity with a luminance of around 330 Cd/m². Contrarily to the PEDOT sample (cf. Figure 4.17 (b)-(d)), its brightness is drastically lower (between 10 and 30 Cd/m²) in which light is not emitted homogenously on the whole surface of the device. Such a degradation can be explained by the poor characteristics of the transparent PEDOT: PSS electrode, as well as by some irregularities in the composite surface and lack of homogeneity.

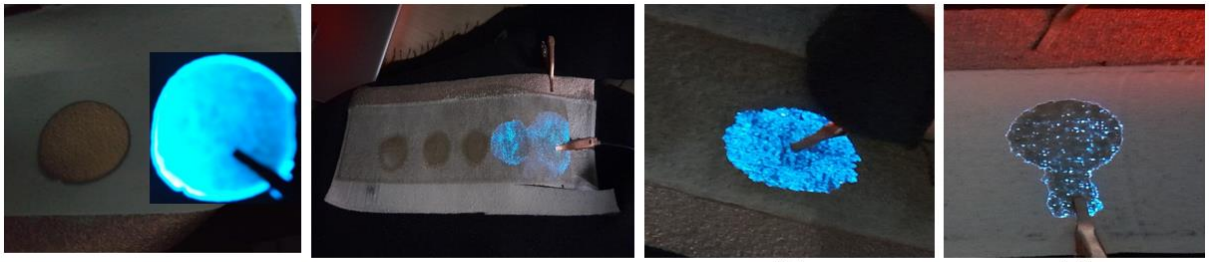

Figure 4.17. Implementation of EL samples on a fabric substrate using: (a) a gold top electrode; (b)-(d) a transparent PEDOT: PSS electrode.

As demonstrated, not only the composite's parameters (including those of the matrix and the particles, as well as their concentration) have strong impact on the light emission, but also the electrodes. As EL device is a combination of both composite and electrode, a deep analyses on the electrodes' parameters should be also thoroughly explored. This matter, however, is usually neglected by the research community, who tends to extensively investigate on new process and materials of composites only. Therefore, our future work aims to optimize electrodes to solve the problems of homogeneity of brightness. The new electrode should be flexible, transparent, good electrical conductivity, cost effective, as thin as possible, adaptable to 3D printing AM. It worth noting that the initial results achieved in this study are encouraging and satisfactory, confirming the reliability of the developed EL, even with the use of classical polyurethane polymer matrix. For the upcoming research, it is envisaged to enhance the dielectric property of this polymer by injecting high-permittivity particles like barium titanate, which is low cost and commercially available.

4.6 Summary

This chapter focuses on the development of an alternating current electroluminescence (ACEL) device based on a combination of zinc sulfide phosphor particles (ZnS) embedded into polymer matrix. To find out the best couple matrix/phosphorus to achieve satisfactory EL response, the ZnS particles doped with three

Thèse accessible à l'adresse : https://theses.insa-lyon.fr/publication/2023ISAL0114/these.pdf © [L. Diatezo], [2023], INSA Lyon, tous droits réservés

different metals were selected including Cu, Cu-Al, and Cu-Mn; also three different matrices were chosen comprising polycarbonate, copolymer, and terpolymer. The ACEL samples were fabricated using the solution casting method, where a layer of composite (matrix/phosphorus) was directly deposited on a conductive ITO glass slide. When an external voltage is applied, the ACEL devices emit light whose color and intensity can be modulated by tuning the amplitude and frequency of the input electric field. For instance, the (ZnS: Cu) composite changed from green the blue emitted light as the excitation frequency was increased, while the luminescent intensity linearly increased with an increase in the excitation amplitude. A comprehensive characterization of the EL composites was explored to evaluate the influence of their electrical and dielectric properties on the luminescent emission. The hysteresis loop based on current-density versus electric-field (J-E) curve allows for the determination of the dielectric constant as well as the electrical conductivity of the composites. Theses parameters definitively play an important role in the activation of the EL effect and performance, based on the results obtained with FEM via COMSOL Multiphysics software. Among several tested particles and matrices, (ZnS:Cu) phosphor combined with terpolymer allows for the formation of EL composite that exhibits the most luminous light. Thanks to the small discrepancy in their dielectric constant, the electric field repartition between the particle and polymer phases is more homogenous than the other combinations. In other words, the local field subjected to the particles is sufficiently enough to successfully trigger the EL response. On contrary to other combinations, especially those elaborated with (ZnS:Cu-Mn) phosphor or/and polycarbonate matrix, the local field is concentrated more on the matrix rather than on the particles, which in turn degrades the brightness or even impedes the EL activation.

The luminescent response of the solution-casted composites were also evaluated at different filler content from 10 to 40 vol.%. A volume fraction of 20 vol.% was found to be the most optimal concentration to achieve the best luminance. For higher concentrations of 30 and 40 vol.%, the EL response somewhat decreased due to an increase in the particle-particle interactions, which provokes a slight diminution in the local electric field seen by the particles themselves. Moreover, agglomerates have formed on the composite surface caused by heterogeneous distribution of the phosphor particles. To sum up, the investigation explored in this work allows for a better comprehension the EL mechanism that strongly depends on several parameters of materials. Understanding the ultimate role of each parameter is of crucial importance to achieve reliable ACEL device, which is expected to be conducted in a real-world operation for the automobile field. In this area, economy is also a crucial aspect that should be considered. Therefore, instead of using high-dielectric matrix (but very expensive) as the terpolymer, our first prototype has been carried out with low-cost materials like PU-AR, AC-AR, and AC-RUD whose dielectric constant is much smaller. Experimental results confirm that such polymers, even less performance than the terpolymer, are cable of activating the electroluminescence with acceptable light intensity. To boost the EL activity, an improvement in the formulation of the polymer matrix could envisaged in future work. For instance, injecting high-dielectric particles like barium titanate, which is low cost and commercially available, into the matrix so as to reduce the permittivity gradient between it and the EL particles. The new matrix will be developed in such a way that it must be adaptable to 3D printing AM, good adhesion with substrate, flexible enough to keep the textile stretchable and foldable. Another critical issue regarding the electrical conductivity of the electrode, which directly affects the ability of light emission, would be also considered in our research direction.

Thèse accessible à l'adresse : https://theses.insa-lyon.fr/publication/2023ISAL0114/these.pdf © [L. Diatezo], [2023], INSA Lyon, tous droits réservés

Chapter 5 Aging tests of conductive coating: Towards a development of high-performance flexible electrodes

Usually, copper is well-known to be cost effective, easy process, excellent electrical conductivity, making it as one of the most appropriate candidates for application in flexible printed electronics. Unfortunately, compared to other precious metals like gold and silver, copper is easily oxidized especially under humid and hot milieus. The aim of this chapter is to investigate a new formulation of the copper composite inks that are expected to be stable with respect to environmental changes. Different polymer binders are explored to enhance the electrical conductivity of the copper composite and to counterbalance the aging effect. The design of the printed electronics coated on the heating tablecloth is also optimized for preventing it from oxidation and corrosion, consequences of moisture penetration. Two protection coatings are implemented into a real prototype of the heating tablecloth, one on the fabric substrate while the other on the top of the copper electrodes. For an easier comparison, both optimized and non-optimized copper composite inks are subjected to several accelerated aging processes including:

- 24-hour and 48-hour thermal cycles at 100°C,
- 12-day hygrothermal cycles at 85°C and a humidity of 85% RH/–40°C,
- mechanical endurance test in accordance with the European SAE standard.

Scanning electron microscopy (SEM) together X-ray diffraction and energy dispersive analysis (EDS) are carried out to perform morphological analysis and to determine the chemical composition of the cooper composite under different condition of the surrounding environment. To justify the performance of the new ink, the electrical conductivity of all samples are measured and compared before and after the above aging tests. Experimental results reveal that optimizations of material and design architecture of the printed electrodes are of primary importance to prevent its electrical performance from degradation with respect to severe conditions.

Thèse accessible à l'adresse : https://theses.insa-lyon.fr/publication/2023ISAL0114/these.pdf © [L. Diatezo], [2023], INSA Lyon, tous droits réservés

5.1 Aging effect with non-optimized configurations

5.1.1 Stability tests on heating tablecloth

This study focusses on the electrical stability of non-optimized conductive coatings printed on porous textiles from foam lining fabrics supplied by Tesca. Following the successful design, development and integration of the heating tablecloth device (see Chapter 3) and the electroluminescent system (see Chapter 4), further studies regarding the accelerated ageing effect of the conductive coatings under environment changes By optimizing the design structure and material properties, together with improving the quality of printed electrodes, we are undoubtedly promoting the future development of heated textiles and electroluminescent devices. To verify the durability and stability of the coatings, three aging tests were carried out: (1) a temperature test, (2) a mechanical test, and (3) a moisture test .

5.1.1.1 Thermal cycle

Figure 5.1 shows the temperature variations of the printed heating tablecloth following a thermal cycle. To assess the effects of accelerated aging, the tablecloth was subjected to specific conditions imposed by Tesca. Test was carried out for 48 hours in a convection oven, with cooling periods of 30 minutes. After this stage, the webs were scanned by a thermal camera and their electrical resistance can be measured and assessed .

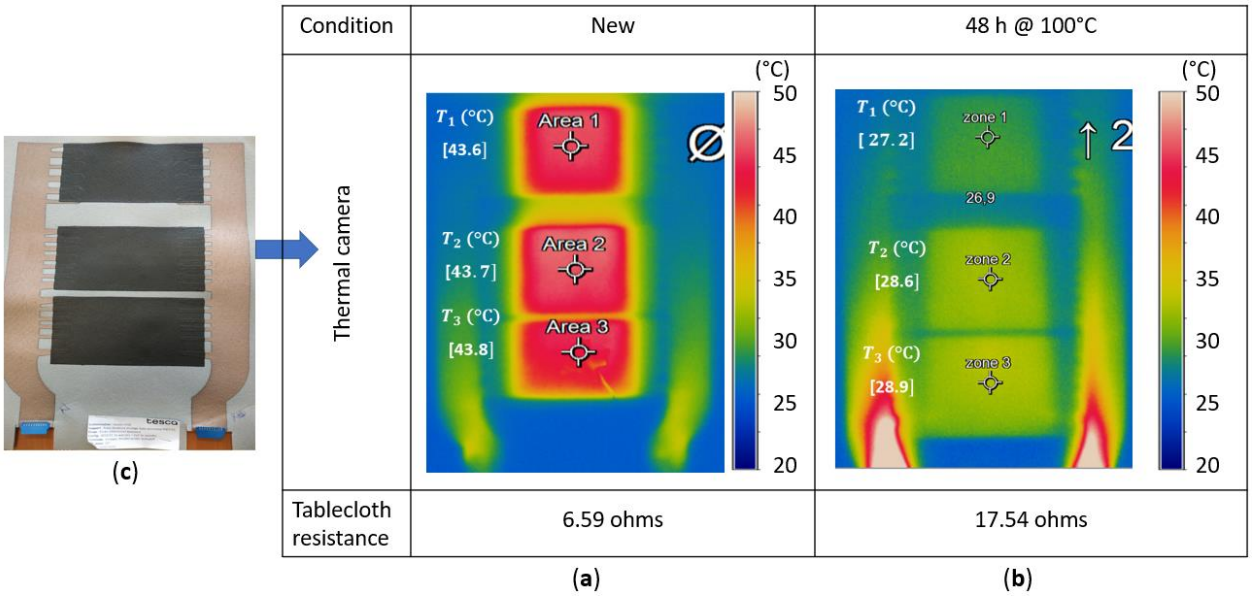

Figure 5.1. The evolution of resistance and temperature as a function of heating duration at 100°C for 48h, (a) before the thermal aging cycle, (b) after the thermal aging cycle, and (c) the screen-printed tablecloth .

Figure 5.1 (a) shows a heating tablecloth with a homogeneous temperature of around 43 ±0.5 °C for all zones, and a resistance of ~ 6.6 Ω when subjected to a 12 V power supply. It is revealed in Figure 5.1(b) that, after the thermal cycle, the electrical resistance of the mat significantly increases up to ~ 17.5 Ω. In general, the electrical conductivity of many materials tends to decrease with increasing temperature. This may be due to thermal vibrations of the material's crystalline structure, which disrupts the movement of charge carriers (electrons or holes). This results in a reduction in the electrical power injected into the tablecloth, and a significant drop in temperature of at least 15°C for all carbon zones. In the next Subsection, a further study of mechanical endurance ageing will be carried out in order to understand the such a behavior .

Thèse accessible à l'adresse : https://theses.insa-lyon.fr/publication/2023ISAL0114/these.pdf © [L. Diatezo], [2023], INSA Lyon, tous droits réservés

5.1.1.2 Mechanical endurance

The mechanical test involved applying a load of 890 N, equivalent to the average weight of an adult male at the 10th, 50th and 95th percentiles, over a period of 200,000 cycles at a speed of 100 cycles per minute [307]. Two approaches were used in this study. The first is to exert the same loads by kneeing on different areas of the carbon surface to analyze the mechanical responses of both stitched and unstitched fabrics. The second method involved using the weight and dimensions of an adult male to determine seat locations in vehicles, as shown in Figure 5.2(a). To carry out this test, J826 H-point dummies [227,364] (ETD Technical Trading, based on D-21218 Sevea, Germany) were used in accordance with the SAE European standard. Temperature measurements were carried out on all the three areas of the carbon surfaces using a thermal imaging camera for both sewn and unsewn samples. Experimental results of Figure 5.2(a) revealed that after the mechanical loading, all areas of the unstitched fabric reached the desired temperature of around 43 ± 0.5°C, confirming good mechanical behavior of the unstitched fabric, and the printed coating as well. Interestingly, this test did not significantly affect the thermal behavior of the center-sewn coated fabric. However, sewing could lead to a slight temperature increase (~ 50°C) due to the higher electrical current in the restricted section of the conductive coating [227].

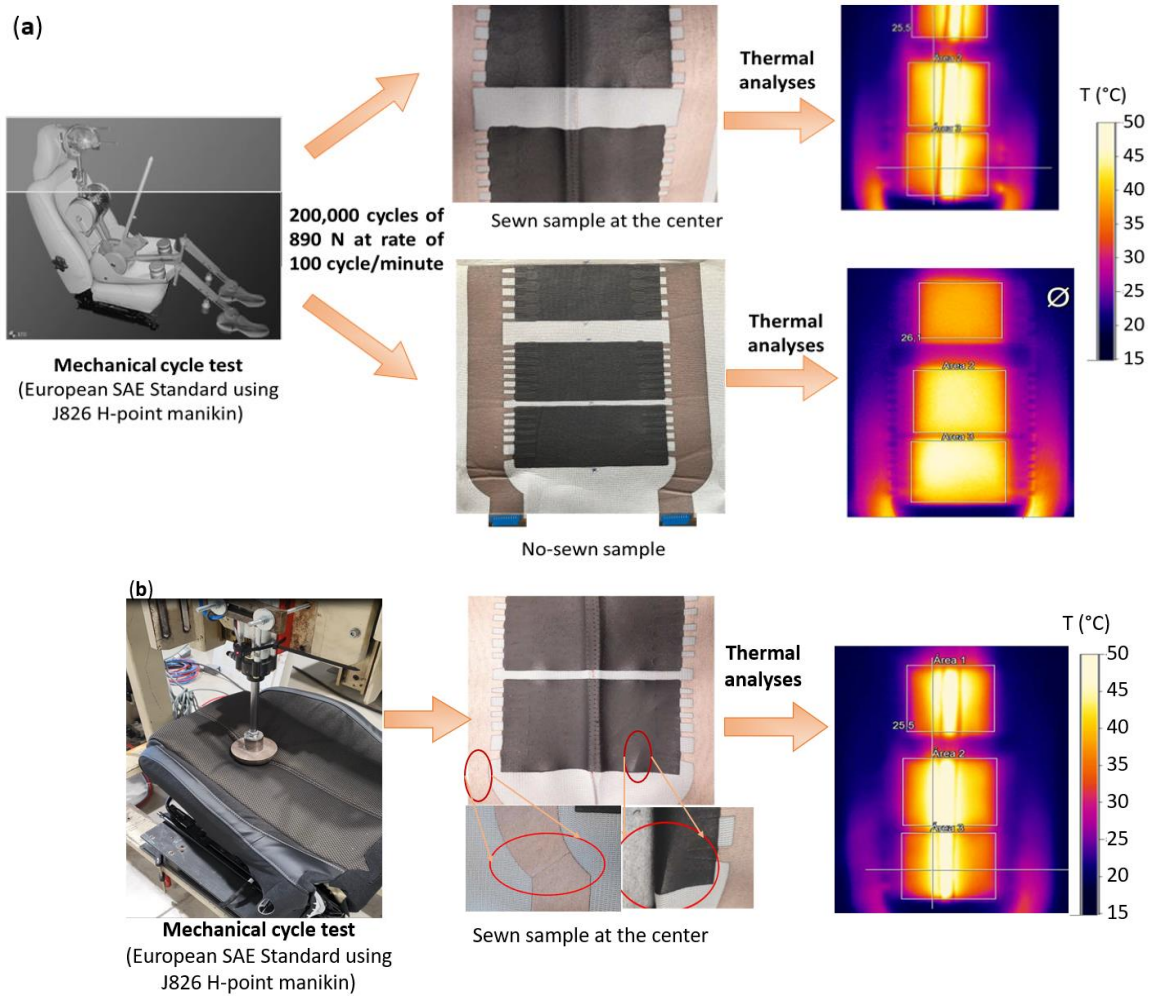

Figure 5.2. Thermal analysis of sewn and unsewn coated fabrics after several aging tests using mechanical cycles: (a) This dummy represents the weight and contour of an adult man, and (b) mechanical endurance of knee cuts.

Figure 5.2(b) shows the mechanical knee blow test, where a load of 890 N is applied to each carbon zone to analyze the mechanical response of the heating tablecloth. Temperature measurements were taken

Thèse accessible à l'adresse : https://theses.insa-lyon.fr/publication/2023ISAL0114/these.pdf © [L. Diatezo], [2023], INSA Lyon, tous droits réservés

using an infrared camera on the three carbon zones of the center-stitched samples. Experimental results indicate that all the carbon zones of the sewn fabric reached a temperature of 50°C ± 0.5°C, thus exceeding the reference value of 43°C established in the specifications. It is interesting to note that the mechanical stress did not have any significant impact on the thermal aging behavior of the center-sewn coated fabric. However, the presence of seams did cause a slight increase in temperature, which could eventually lead to the appearance of hot spots that could burn the heating tablecloth, resulting in malfunctions and breakdowns. Design and process improvements will be further investigated to determine the origin of this critical problem.

5.1.1.3 Moisture cycle

Figure 5.3(a) illustrates the profile of a PSA cycle with an indication carried in D47 1309 (4AF+6BF: 85°C85%RH/- 40°C [301]) according to the specifications (i.e., the equivalent of a 12 h period) concerning the temperature and moisture content applied to conductive coatings made of a copper or carbon composite. The humidity test, on the other hand, lasted much longer (12 days, i.e., 24 cycles). The thermal cycle consists of five stages, as described below.

For each stage, the temperature is :

- Increased from 20 °C to 8 5°C for 1h at a rate of 1 °C/min;
- Stable at 85 °C for 4h;
- Lowered to – 40 °C at a rate of 1 °C/min for 2h.
- Held constant at – 40 °C for 4h.
- Increased to 20 °C at a rate of 1 °C/min for 1h.

In addition, the moisture cycle consists of four stages, as described below. For each stage, the moisture content is:

- Increased from 30% to 95% at a rate of 0.98%/min for 1 h ;
- Maintained at 95% for 4 hours;
- Decreased to 30% at a rate of 0.98%/min for 1 h ;
- Maintained at 30% for 6 hours.

Figure 5.3 (b) clearly shows the heated tablecloth before the climatic chamber test (humidity/thermal stability). A homogeneous temperature distribution can be seen in all carbon zones. After subjecting the tablecloth to a humidity/temperature cycle of 85°C/85%RH and – 40°C for 12 days, an increase in the strength was observed. The average temperature of each zone, measured after 5 minutes of heating, decreased by 7°C in zone 1, 4°C in zone 2 and 2°C in the last zone .

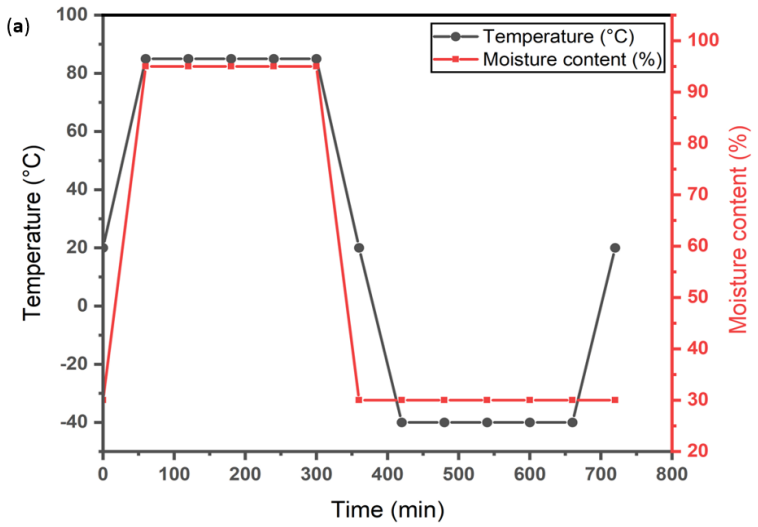

Thèse accessible à l'adresse : https://theses.insa-lyon.fr/publication/2023ISAL0114/these.pdf © [L. Diatezo], [2023], INSA Lyon, tous droits réservés

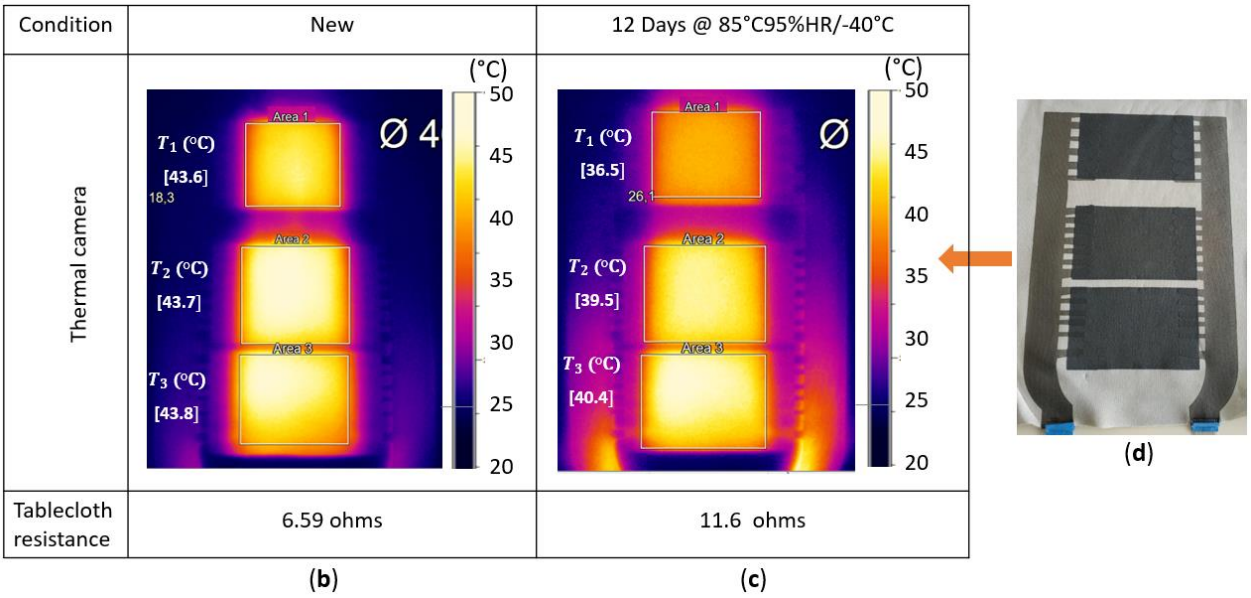

Figure 5.3. Ageing test of the copper electrode coating: (a) temperature and humidity profile over one cycle, (b) the coating before hygrothermal ageing, (c) the coating after hygrothermal ageing, and (d) the coating printed after the humidity cycle.

As far as the power consumption is concerned, before the humidity and thermal cycle, the tablecloth consumed a current of 2.26 A. After the cycle, consumption fell to 1.47 A. This drop can be explained by the intrinsic ageing of the materials. The combined effects of humidity and temperature might reduce the conductivity of the electrodes, leading to the formation of oxide films, as illustrated in Figure 5.3(d), and altering the electrical properties of the conductive particles . These materials can be susceptible to corrosion in the presence of moisture, which promotes the formation of corrosive deposits, damages conductive traces, shortens their life, and leads to circuit failures.

5.1.2 Morphology characterization

Scanning electron microscope (SEM) analysis was also carried out on each part of the heating tablecloth before and after accelerated ageing tests of the tablecloth. Figure 5.4 (a, b and c) display the surface structure of the carbon, confirming that there is no significant difference in surface topology after and before the three aging procedures. However, when subjected to temperature/humidity aging, the presence of moisture makes the carbon black and polyurethane deteriorated. Pores were observed in the carbon ink and the trace of the river line is clearly visible as in Figure 5.4 (b). With regard to the copper composite ink, after thermal and mechanical cycles (see Figure 5.4 (d and f)), it is difficult to determine whether or not it has undergone the aging tests. However, exposure in the climatic chamber revealed the presence of copper oxides. The next steps will involve further measurements, such as X-ray diffraction and energy dispersive X-ray analysis (EDS), to better understand the overall behavior of both carbon and copper composite inks.

Thèse accessible à l'adresse : https://theses.insa-lyon.fr/publication/2023ISAL0114/these.pdf © [L. Diatezo], [2023], INSA Lyon, tous droits réservés

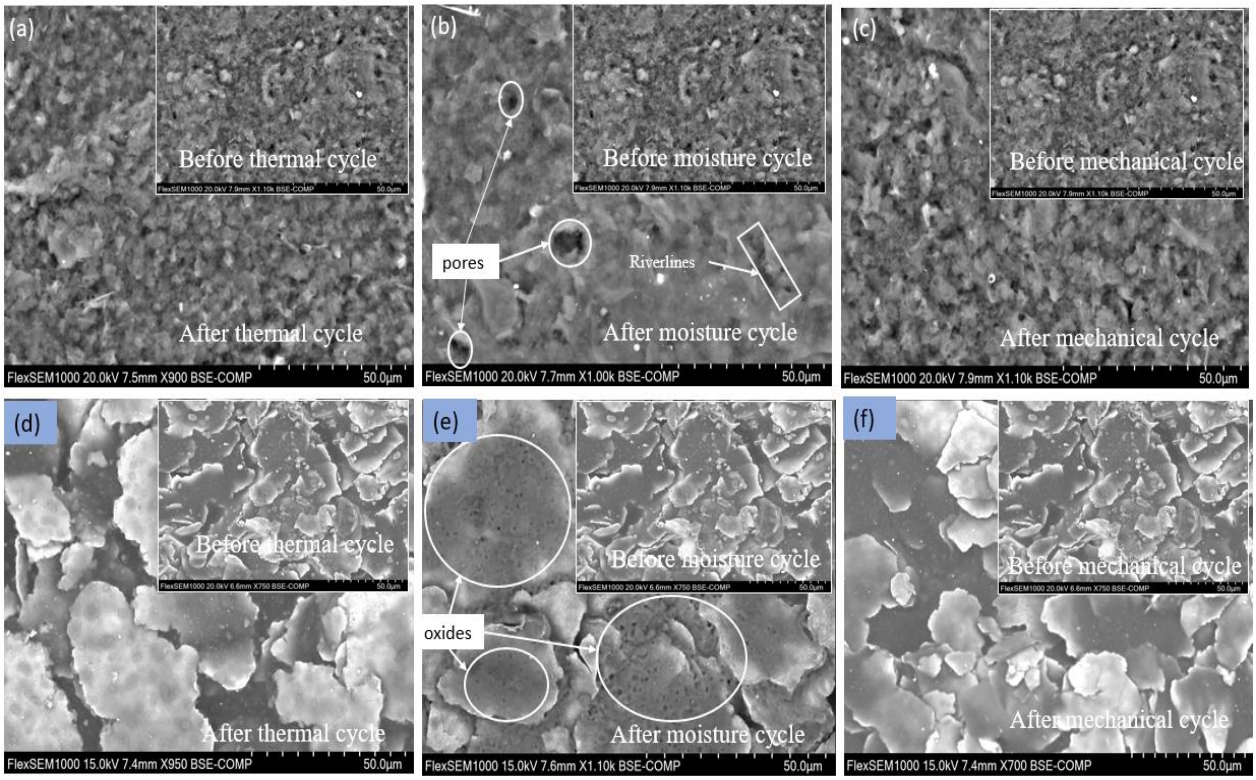

Figure 5.4. Morphologies of carbon- and copper-based composite ink before and after aging tests. Panels (a), (b) and (c) show the carbon-based conductive ink, while panels (d), (e) and (f) represent the copper-based conductive ink. These tests include thermal, humidity and mechanical cycles.

5.1.3 Material's aging after stability tests

Here, we focus on the three relevant parameters that can influence the material ageing. The electrical resistances (R) of the samples were measured after and before the stability tests, to highlight their impact on the performance of the printed coating. As illustrated in Figure 5.5, all the heating tablecloths had a similar resistance of around $6.6 \pm 0.5\ \Omega$ initially before the tests. After 12 days of moisture treatment, the electrical resistance of the tablecloth clearly increased by around $77 \pm 2\%$. Similarly, following exposure to the thermal procedures, a notable increase of around $167 \pm 3\%$ was observed. In contrast, a relatively smaller increase of around $34 \pm 1.4\%$ was observed after the mechanical solicitations. The results of these three ageing tests clearly demonstrated that the copper-carbon composites used in this study were not stable with respect to the environmental variations, particularly under extreme conditions such as excessively low or high temperatures, combined with high moisture content and high mechanical stress, either in static or dynamic regime. Figure 5.5 illustrates the relative evolution of the resistance (in %) to its initial value prior to aging trials.

As mentioned above, aging of the heating tablecloth is a problem due to the three constraints, resulting in deteriorated electrical properties of the conductive coatings. How to minimize the aging effect Actually, it is vital that the materials could withstand environmental variations, while preserving their strength properties as far as possible. To solve such issues, our approach is first to set up a prototype for analysis and testing these effects. This enables to evaluate and improve the performance, operation and characteristics of the tablecloth, while minimizing risks and guaranteeing end-user satisfaction. Next, a specific thermal is applied to the tablecloth in order to find out, between the copper electrodes and the carbon patches, which elements might be deteriorated first. Empirical tests were conducted by coating these two materials on the

Thèse accessible à l'adresse : https://theses.insa-lyon.fr/publication/2023ISAL0114/these.pdf © [L. Diatezo], [2023], INSA Lyon, tous droits réservés

same textile substrate, on which were printed the tracks with 150 mm long and 15 mm wide. The thickness of a single layer of the copper and carbon ink is respectively around 192 µm and 170 µm. Based on the best compromise between the fabric's mechanical flexibility and the print quality, the number of the coating layers for both two inks were chosen to equal 3, which is supposed to be the most optimized configuration.

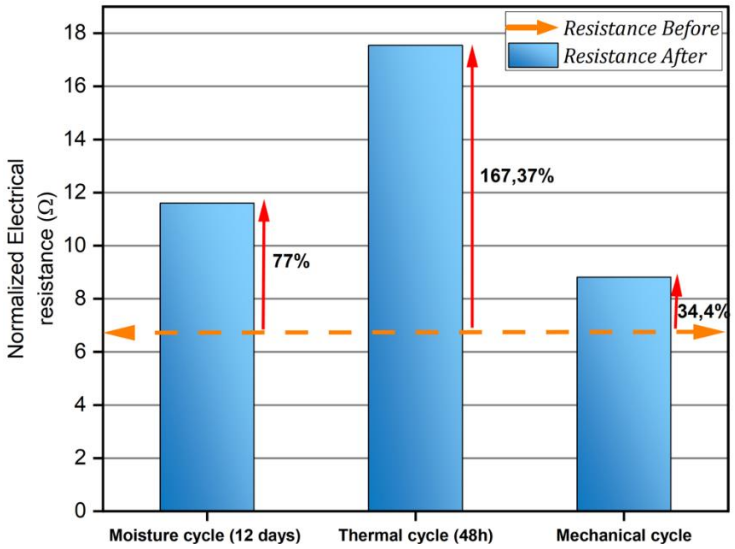

Figure 5.5. Ageing test of the heating tablecloth coating: profile of temperature and humidity over one cycle of mechanical endurance, as well as the evolution of electrical resistance before and after the stability tests.

By collecting data conducted on the set samples shown on Figure 5.6 (a), it is possible to identify the principal cause that is essentially responsible for the material aging. The thermal cycles of 24h and 48h under 100°C were carried out throughout the process whose measurements of the electrical conductivity (denoted σ) of the carbon and copper coatings were correspondingly displayed in Figure 5.6(c, d). σ was measured before and after the thermal aging tests so as to assess the influence of temperature on the performance of the printed coatings. The results show a very small variation ($\Delta\sigma < 1\%$) for the carbon coating, indicating its excellent thermal stability. This, to some extent, is in contrast to the copper electrode, whose electrical conductivity drastically drops of around 24 % and 48 % after a 1-day and a 2-day thermal treatment, respectively. These results highlight the aging effect of the copper composite vis-à-vis the environmental changes, particularly extreme temperatures and high humidity. In order to solve this problem, an envisaged solution is to develop a new ink with polymer matrix featuring adequate glass transition temperature. This crucial issue will be further explored in detail in the following paragraphs, as it is of great importance for improving the coating's ageing performance.



Thèse accessible à l'adresse : https://theses.insa-lyon.fr/publication/2023ISAL0114/these.pdf © [L. Diatezo], [2023], INSA Lyon, tous droits réservés

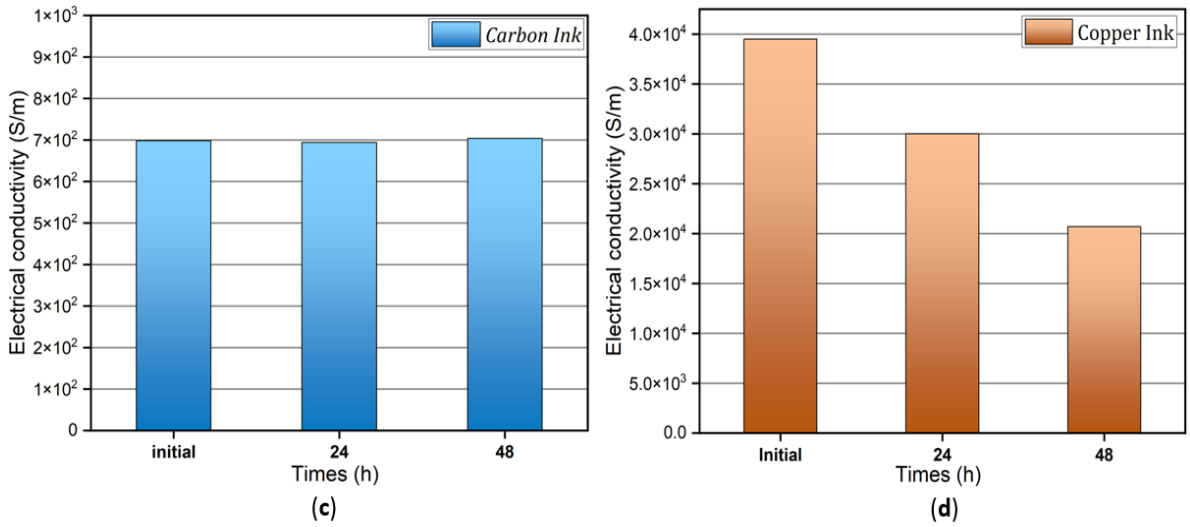

Figure 5.6. The influence of temperature on the electrical properties of (a) carbon ink, (b) copper ink, (c) copper ink and (d) carbon ink samples as a function of heating time.

5.2 Aging effect with optimized materials

5.2.1 Material selection

To improve the thermal stability of the copper electrodes, different formulation of the composite ink is developed based on the use of polymer binders such as Archroma acrylic (AC-AR), Archroma polyurethane (PU-AR), and Rudolf acrylic (AC-RUD). They were all offered by *Rodolf Group Better Chemistry and Archroma Life Enhanced*, and their properties are summarized in Table 5.1 (according to supplier's data sheet). These three polymer binders were chosen primarily for their glass transition temperatures (T_g), in order to solve the aging problems and to predict material behavior under different environmental and mechanical conditions. Binders based-Acrylic (AC-AR and AC-RUD) have positive values of T_g (respectively 10 °C and 26 °C, below which they become more rigid and brittle). On the other hand, polyurethane has a negative T_g of – 47°C, meaning that it remains elastic (rubbery properties) even at very cold temperatures. This approach enables to assess the durability of the new composite ink and optimize its performance in terms of electrical conductivity for the heating tablecloth. For all the three composites, the conductive copper has a fraction content of 30 wt.% so as to achieve good viscosity of ink.

Table 5.1. General properties of new commercially available polymer binders.

Supplier	**ARCHROMA**	**ARCHROMA**	**RUDOLF**
Polymer binders	Acrylic Archroma (AC-AR)	Polyurethane Archroma (PU-AR)	Acrylic Rudolf (AC-RUD)
Glass transition temperature (T_G)	+ 10 °C	– 47 °C	+ 26 °C
Conductive powder (%)	30	30	30
Viscosity ($mPa.s$)	100	$10-100$	<1000
Curing at temperature (°C)	$150-160$	$120-160$	$90-120$
Solid content (wt. %)	50	40	45
Mass density (g/cm^3) at 20 °C	1.05	1.042	1.06

Thèse accessible à l'adresse : https://theses.insa-lyon.fr/publication/2023ISAL0114/these.pdf © [L. Diatezo], [2023], INSA Lyon, tous droits réservés

5.2.2 Stability tests on a sample unit

In this study, the three new composites based on different polymer binders are evaluated and compared in aging performance through the stability procedures (thermal cycle, temperature/humidity cycle, and mechanical cycle). For an easier comparison, a threshold was set for the electrical conductivity (denoted σ_{th}) of the three copper inks, which must be $\geq 5.5\text{E}4\ S/m$ to fulfil the exigence of the Tesca's specifications.

5.2.2.1 Thermal cycle

Figure 5.7 shows the evolution of electrical conductivity (denoted σ) as a function of the heating time with the three optimized inks and the non-optimized one (used in Chapter 3), together with the deduced numerical values summarized in Table 5.2. Some pertinent remarks are provided as followings:

- Whatever the thermal condition, the value of σ is significantly improved thanks to the implementation of the binder on the copper ink;
- The electrical property of the non-optimized composite is too poor to meet the requirements of Tesca, even before the aging procedure;
- For all the optimized composites, σ drastically drops after a 24h thermal treatment, but its value is still higher than the threshold value. Regarding the 48h procedure, no change has been occurred for the AC-AR and AC-RUD samples as in the case of the 24h procedure. The PU-AR sample, however, is decreased in the electrical conductivity and its value is somewhat lower than the target value.
- Polymer binders-based Acrylic (AC-AR and AC-RUD) leads to composites with better thermal stability while those elaborated with Polyurethane (PU and PU-AR) makes composites deteriorated in the electrical performance.
- Accordingly, the cooper inks include with AC-AR and AC-RUD polymer binders successfully match the specifications where their σ value is beyond the threshold after a 24h and 48h thermal procedures.

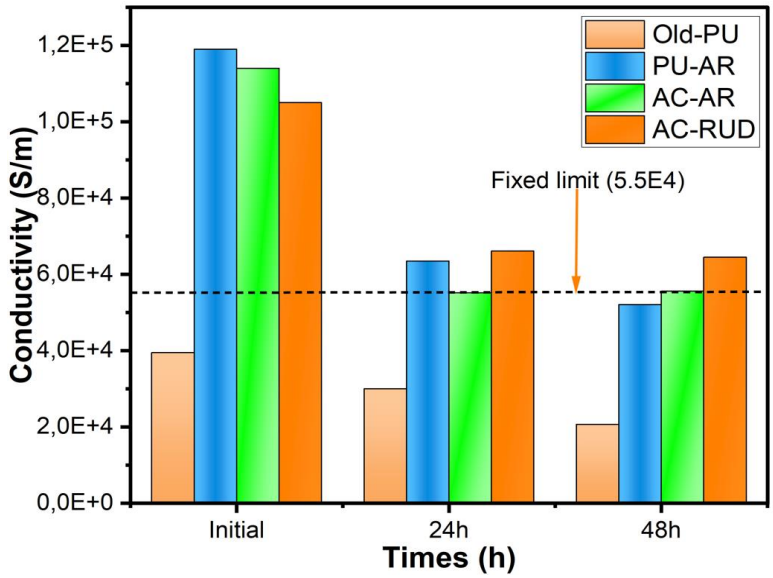

Figure 5.7. Evolution of electrical conductivity of copper ink as a function of heating time with optimized and non-optimized new ink.

Thèse accessible à l'adresse : https://theses.insa-lyon.fr/publication/2023ISAL0114/these.pdf © [L. Diatezo], [2023], INSA Lyon, tous droits réservés

Table 5.2. Electrical conductivities before and after the thermal cycles at 100°C for 24h and 48h.

Copper-formulated ink with binder:	Initial conductivity (S/m)	24-hour thermal-cycle conductivity (S/m)	48-hour thermal-cycle conductivity (S/m)	24-hour relative deviation (%)	48-hour relative deviation (%)
Old PU binder	3.9E4	3.00 E4	2.07E4	24.0	47.5
AC -Archroma	11.4E4	5.52 E4	5.56E4	46.6	56.2
PU- Archroma	11.9E4	6.35E4	5.21E4	51.6	51.3
AC- Rudolf	10.5E4	6.61E4	6.45E4	37.0	38.6

5.2.2.2 Thermal/humidity cycle

The electrical conductivity (σ) of the three optimized cooper inks undergone the thermal/humidity aging for 12 days at 85°C and 85% RH/–40°C are displayed in Figure 5.8 and Table 5.3. It has been pointed out that σ significantly decreases after the procedures and their value is revealed to be somewhat inferior to the set threshold. These observations suggest that the electrical behavior of the new copper formulation is strongly affected by the change in the materials' structure and surface [365,366]. It is supposed that corrosion might appear on the contact interface caused by moisture surrounding the sample, provoking failure of the device's connection. Interestingly, the AC-RUD sample, which initially has the lowest σ among the others, exhibits the maximum value after the aging procedure. This result confirms that the copper powders formulated with the AC-RUD polymer seems to be the most appropriate candidate to achieve ink somehow more stable in the wet and hot environments.

Table 5.3. Conductivity evolution of the new inks formulated before and after humidity test.

Polymer binder	**Initial conductivity (S/m)**	**After Humidity cycle (S/m)**	**12-day relative variation (%)**
AC-AR	1.14E5	4.97E4	56
PU-AR	1.19E5	3.24E4	73
AC-RUD	1.05E5	5.39E4	49

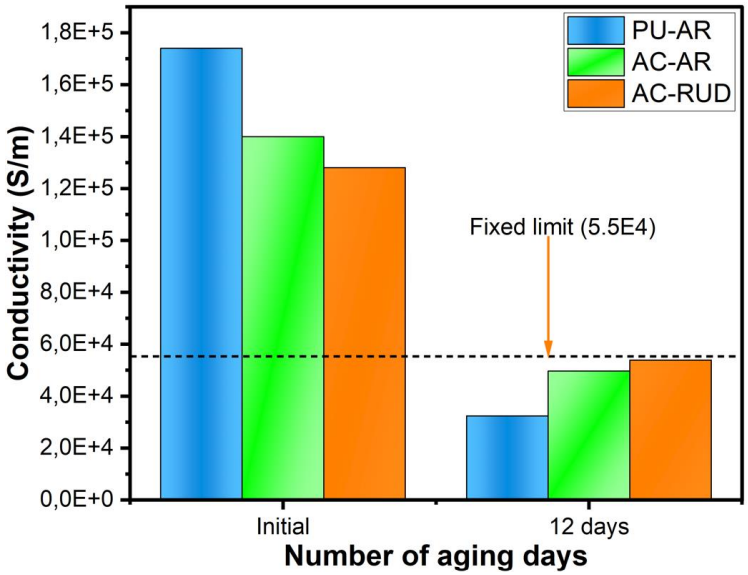

Figure 5.8. The conductivity of the new copper composite conductive ink formulated between room temperature and hygrothermal ageing for 12 days at 85°C/85%RH/–40°C.

Thèse accessible à l'adresse : https://theses.insa-lyon.fr/publication/2023ISAL0114/these.pdf © [L. Diatezo], [2023], INSA Lyon, tous droits réservés

5.2.2.3 Mechanical endurance

Based on a monotonic tensile test, the stress-strain response of the conductive track samples, elaborated with the new copper composites-based polymer binders, consists of 3 phases: 1) linearity in the elastic deformation zone, 2) non-linear behavior in the plastic regime, and 3) final fracture [367]. The average tensile Young modulus of these materials can be obtained based on a linear adjustment of the initial elastic stress region near the origin (Figure 5.9). As resumed in Table 5.4, the AC-RUD composite leads to the highest Young's modulus (~ 38.8 MPa) as opposed to the PU-AR (~ 10.5 MPa) and the AC-AR (~16.8 MPa). These values are found to be consistent with other materials made of the same PU or commercial PDMS [368–370], confirming the accuracy of the experiments. It is worth noting that the copper composite ink formulated with the PU binder is more flexible compared to the other counterparts. In the area of printed electronics for textiles, flexibility of inks is of primary importance so as not to drastically change the mechanical properties of the fabric substrate. In other words, the fabrics, which are usually expected to be bendable and/or stretchable for facilitating integration, should not be harden with an addition the printed coatings. Adapting the mechanical properties could be obtained by decreasing the copper filler content. This solution, however, might drastically affect the electrical conductivity of the coating, which in turn makes the heating efficiency deteriorated. Another alternative is to combine several polymer binders together to achieve desired mechanical properties. This issue is considered out of scope of the thesis as further investigations in fabrication process and chemical formulation should be involved, which may be very time and cost consuming.

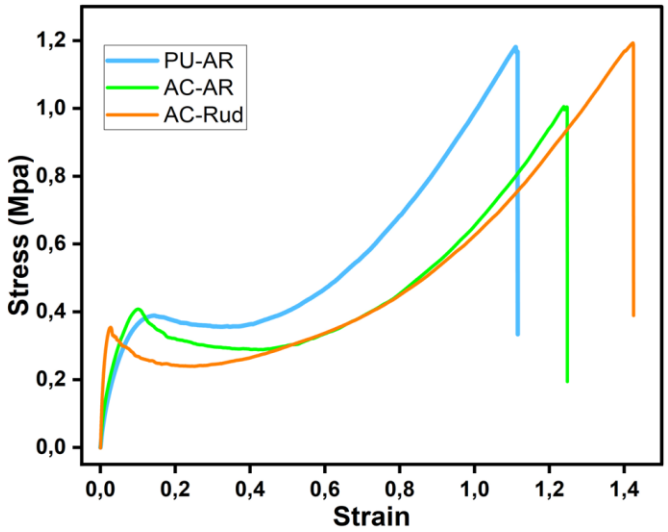

Figure 5.9. Tensile stress-versus-strain response of copper composite inks with different polymer binders.

As shown in Figure 5.10(a)-(b), the compressive stress-strain loops of the three composite inks are obtained based on 50 aging test cycles. The copper composite ink is subjected to a stepped loading profile in which a series of fixed strains in the range [0.1 - 0.7] is exerted. After reaching the maximum, the unloading processes were conducted to make the sample completely relaxed (i.e., zero strain after a duration called “relaxation time”). All the composite inks are revealed to be fully recovered at their own initial state (i.e., origin of the curve) for a large strain range, demonstrating high flexibility of the printed coating on the textile substrate. Interestingly, the PU-AR and AC-AR composites show a slightly larger hysteresis area, reflecting their greater mechanical losses. As observed in Figure 5.10(b), for all samples, the electrical conductivity (σ) exponentially decreases with the increasing strain. To the macroscopic point of view, when the conductive ink is deformed, its length increases and so is its electrical resistance. To the microscopic point of view, higher deformation of the ink can cause modification in the conduction pathways of the copper particles, which in turn dramatically affects the electrical conductivity of the coating. Particularly

Thèse accessible à l'adresse : https://theses.insa-lyon.fr/publication/2023ISAL0114/these.pdf © [L. Diatezo], [2023], INSA Lyon, tous droits réservés

when the applied strain becomes important (≥ 0.5), these pathways could be interrupted, and the copper coating may lose its conductivity behavior. To meet the specifications where σ is beyond the limited threshold, a deformation applied to the sample should not be greater than 10 % for the AC-RUD sample and 20 % for the two others. It was noted that the deformation of the AC-RUD composite ink is limited to 0.4 (instead of 0.7), because beyond 0.4 we have a contact break caused by the rigidity of the rudolf acrylic binder, and therefore we don't get conductivity measurements.

Table 5.4 summarizes the electrical and mechanical properties of the three copper composite inks conducted under three stability tests. To sum up, the AC-RUD sample has excellent electrical conductivity, which is demonstrated to be stable after both thermal and moisture tests. This is the only sample that satisfies the requirement in terms of electrical performance. However, its mechanical property is mediocre compared to the others because of its high rigidity. On the contrary, the AC-PU sample is much more flexible but electrically instable vis-à-vis the aging tests. The AC-AR seems to be the best compromise between the electrical and mechanical characteristics, but still do not match the automobile's exigence. At this stage, no configuration is revealed to be adequate in a long-term textile application. In the next study, we take a closer look on the origin of the aging effect, i.e., the corrosion of the copper electrode that might help to find out a corrosion protection preventing from high variation of temperature and humidity.

Table 5.4. Electrical and mechanical properties of different copper composite inks.

Foam liner without protection						
Binders' formulations copper		**Electrical conductivity σ(S/m)**				**Mechanical study**
inks		**Thermal cycle**			**Humidity cycles 85°C85%HR/-40°C**	**Elasticity modulus**
Measured data		Initial	24h	48h	4AF+6BF	E (MPa)
Archroma	PU	1.19E5	6.35E4	5.21E4	1.47E4	**10.49**
Archroma	Acrylique	1.14E5	5.52E4	5.56E4	5.12E4	**16.79**
Rudolf	Acrylique	1.05E5	6.61E4	6.45E4	6.47E4	**38.83**

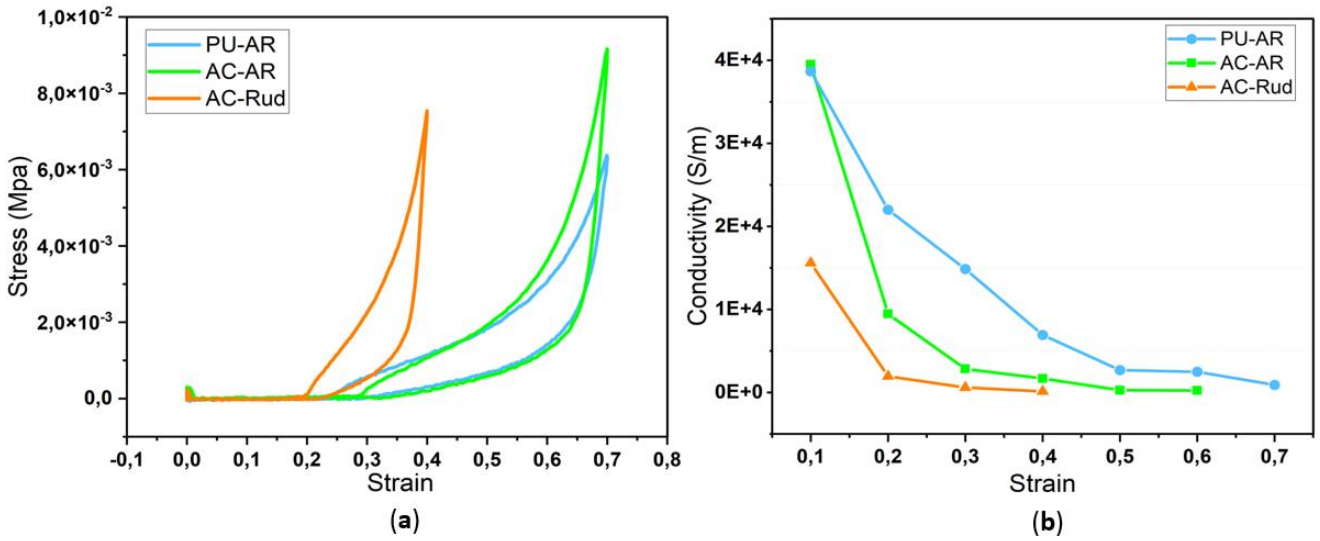

Figure 5.10. Compressive stress-strain loop of the copper composite formulated with different binders: (a) AC-AR binder, PU-AR binder, and (c) AR-RUD binder; (c) evolution of electrical conductivity as a function of strain.

Thèse accessible à l'adresse : https://theses.insa-lyon.fr/publication/2023ISAL0114/these.pdf © [L. Diatezo], [2023], INSA Lyon, tous droits réservés

5.2.3 Corrosion effect-based morphology characterization

When the copper (Cu) is subjected to the humidity and thermal test conditions, two types of corrosion products are formed: oxides and sulfides [371–373]. However, when the textile substrate coated with the copper composite ink is exposed to room temperature, the thickness of the copper (II) oxide (cupric oxide, CuO) is negligible compared with that of the copper (I) oxide (cuprous oxide, Cu_2O). In this case, the formation of the Cu_2O layer is the dominant slow reaction, which does not affect the electrical properties of the material. On the other hand, if the exposure temperature of the coated substrate exceeds the room temperature, as is the case of our study with an extreme environment (85°C, 85%HR/-40°C) for 12 days, the Cu_2O thickness of Cu_2O becomes negligible compared to that of CuO. In this situation, overall oxidation depends on the pressure of the medium, which, to some extent, could provoke corrosion situation. In addition, hygrothermal diffusion behavior can be altered by the nature and hydrogen bonding of the network, due to the increased polarity of the composite and water absorption, which can lead to chemical degradation. It is therefore essential to understand the effect of hygrothermal aging on the degradation of the material before using it for technical applications [371,374–376]. In the next paragraph, we present a complete study on X-ray diffraction, scanning electron microscope (SEM) observations and energy dispersive X-ray (EDS), as well as measurements of volume and surface electrical properties. The aim is to determine the origin of the aging issue and propose a suitable anti-corrosion solution.

5.2.3.1 X-Ray diffraction

The main objective of this study is to carry out the X-ray diffraction analysis on the copper composite inks, both before and after aging procedure through aggressive media of [– 40 °C, 85 °C] and 85% humidity. As the diffraction spectra of the three conductive inks were found to be similar in the practice, only one sample was chosen to be shown in Figure 5.11. It can be seen that both unoxidized and oxidized copper composites exhibited perfectly superimposable diffraction peaks, with the same variations in the peak position ($2\theta = 36°, 42.5°, 49°, 58.3°, 66°, 68.2°$) . However, these variations attest to the spatial modification of the crystal lattice, meaning that the humidity and temperature treatments altered the conformation of the crystalline phase. This confirms the presence of corrosion in the copper composite ink after exposure to an extreme ageing environment. Furthermore, the XRD diffraction peaks reveal variations in the crystal size distribution for both samples, with similar peak widths.

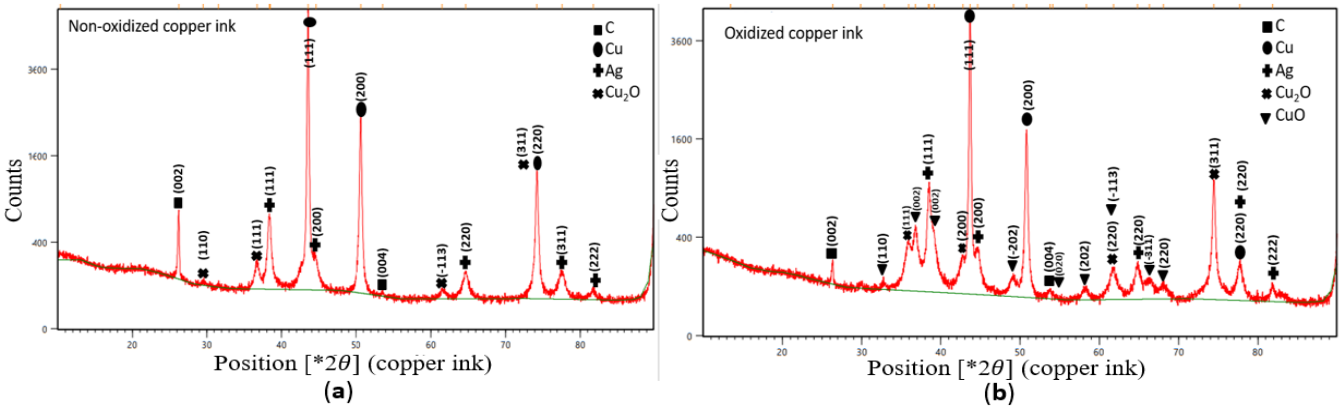

Figure 5.11. X-ray spectra for the two copper composite ink samples: (a) unoxidized and (b) oxidized electrodes.

5.2.3.2 Energy dispersive X-rays (EDS) and SEM

Figure 5.12 shows the results of energy dispersive X-ray (EDS) analysis of the oxidized copper composite after an ageing study under humidity and temperature. As indicated in the SEM image of Figure 5.12 (a), the brightest areas, located around and interconnect the copper particles, are rich in CuO that lead to electrical failure caused by important reduction of the bonds among particles. In contrast, the darker areas are rich in Cu_2O and slowly forms with a negligible thickness. This characteristic confers good electrical

Thèse accessible à l'adresse : https://theses.insa-lyon.fr/publication/2023ISAL0114/these.pdf © [L. Diatezo], [2023], INSA Lyon, tous droits réservés

properties, as indicated in previous research [377]. Subsequently, the same sample was subjected to energy dispersive X-ray (EDS) analysis, and a significant presence of four main elements was noted: silver, copper, oxygen, and carbon. These elements are particularly prominent at the surface of the material, as shown in Figure 5.12 (b, c), with atomic percentages specified in Table 5.5 (a).

The significant presence of oxygen on the sample surface (cf. Table 5.5 (b)) leads to electrochemical corrosion at the contact interface. This corrosion is caused by various factors, such as water penetration into polymer matrices, internal hydrolysis of colloids, stresses induced by surrounding changes and delamination between devices. Such phenomena contribute to increasing electrical resistance and reducing bond strength, potentially leading to failures in printed electronic devices [209,378,379]. These observations definitively confirm a presence of corrosion for the copper composite, which should be protected to prevent aging effect, especially in severe environments (i.e., high variation of temperature and humidity).

In the following paragraph, we take measurements of the electrical properties of the copper composite to determine whether the corrosion is of a volumetric or surface nature.

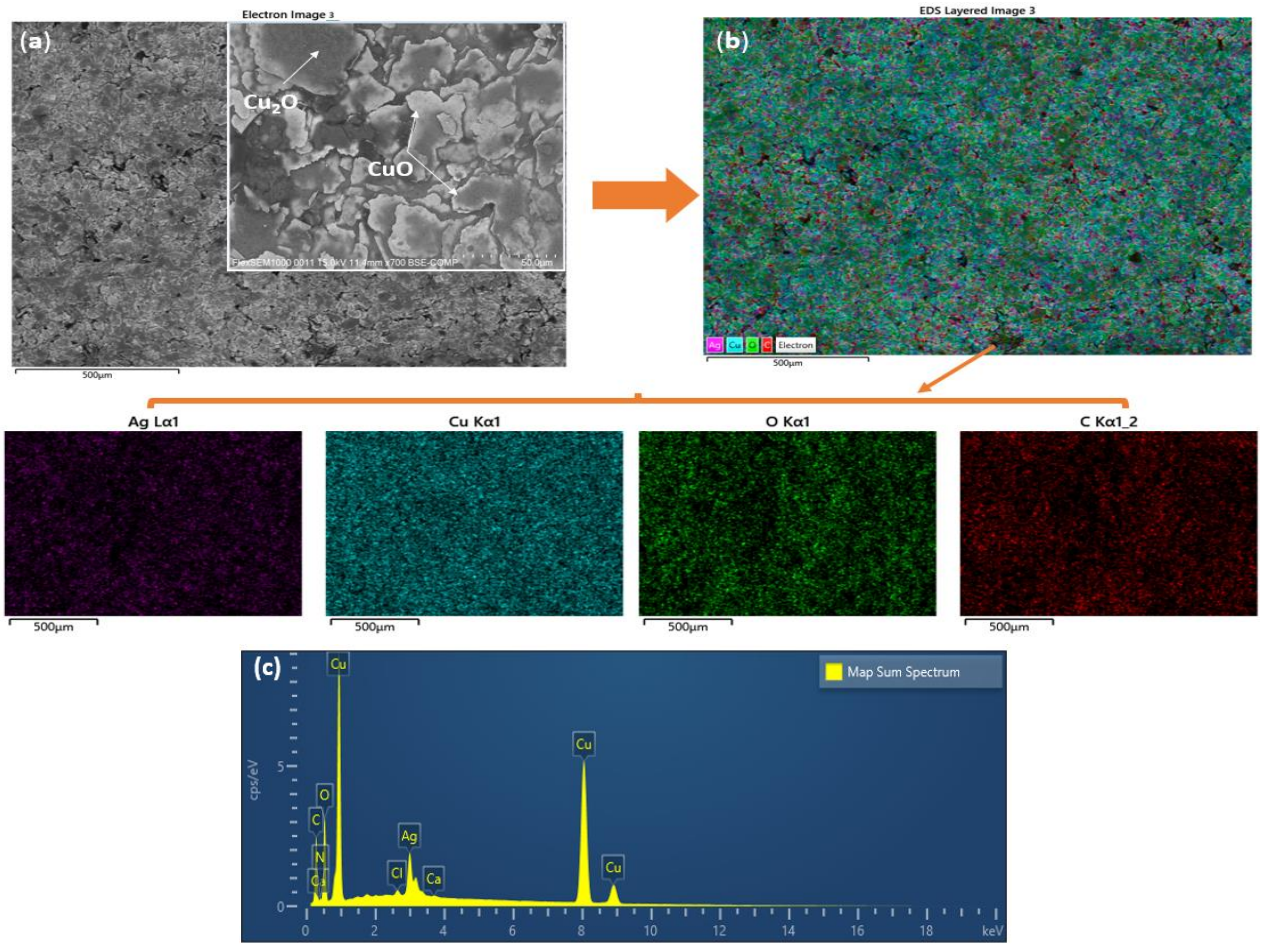

Figure 5.12. Energy dispersive X-ray (EDS) analysis: (a) SEM image of oxidized copper ink; (b, c) EDS image of oxidized copper ink, silver and copper conductors.

Thèse accessible à l'adresse : https://theses.insa-lyon.fr/publication/2023ISAL0114/these.pdf © [L. Diatezo], [2023], INSA Lyon, tous droits réservés

Table 5.5. (a) Energy dispersive X-ray map sum spectrum values of oxidized copper composite; and (b) Summary of compounds by means of XRD, EDS and SEM characterizations.

(a)

Map Sum Spectrum				
Element	Line Type	Weight %	Weight % Sigma	Atomic %
C	K series	31.82	0.55	57.94
O	K series	16.39	0.25	22.40
Cu	K series	43.88	0.46	15.10
Ag	L series	5.55	0.11	1.13
N	K series	2.10	0.58	3.28
Cl	K series	0.18	0.02	0.11
Ca	K series	0.08	0.03	0.04
Total		100.00		100.00

(b)

Analysis technique	Conductive ink	Compose
MEB/EDS	Non- oxidized copper ink	C, Cu, O, Ag, Cl, Ca, Si, N
	Oxidized copper ink	C, Cu, O, Ag, Cl, Ca, N
DRX	Non- oxidized copper ink	C, Ag, Cu, Cu_2O
	Oxidized copper ink	C, Ag, Cu, Cu_2O, CuO

5.2.3.3 Corrosion source

In this study, measures of the electrical resistance are conducted on the non-oxidized and oxidized specimens with the same area unit of 4 cm² as shown in Figure 5.13. On a one hand, the volume resistance were found to be similar (~ 2.3 Ω) for both samples. On the other hand, their surface resistance are totally different, ~ 0.62 Ω before the test (Figure 5.13(a)) and raises up to 7.2 Ω after 12-day test (Figure 5.13(b)). Obviously, the conductivity of the copper electrode drastically declined with high variation of the humidity (85%) and the thermal enclosure (– 40°C to 80°). It is interesting to note that this media provokes significant change in the surface color of the sample unit. Thus, the corrosion of the copper coating essentially originates from the surface rather than the volume. The following study explores a new design based on anti-corrosion protective layer(s) coated on the copper surface.

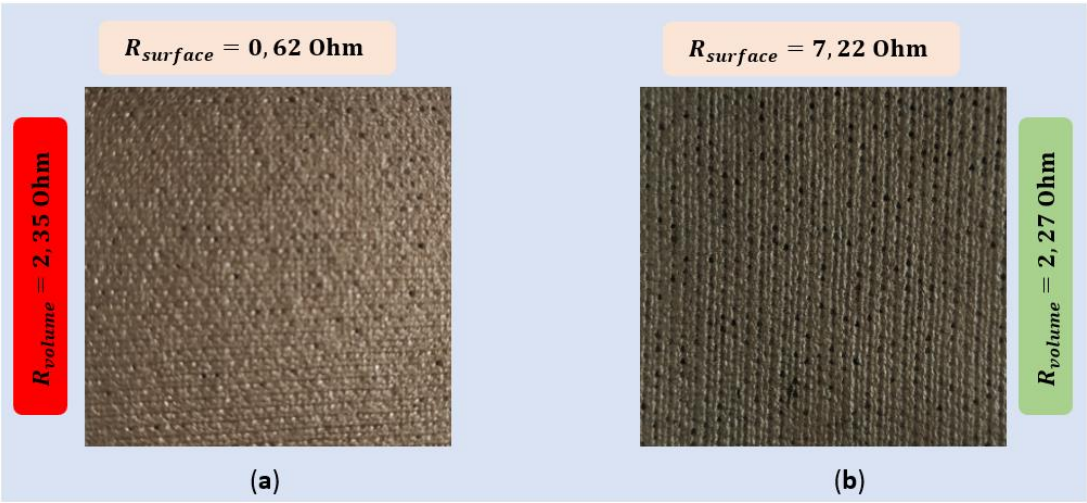

Figure 5.13. Two sample units used to measure the electrical resistance: (a) non-oxidized copper ink (before the aging test), and (b) oxidized copper ink (after the aging test).

5.3 Aging effect with optimized designs

5.3.1 Solution based on protective coatings

Copper-based conductive inks are frequently used to print flexible electronic circuits and other applications requiring electrical conductivity. However, copper is vulnerable to corrosion when exposed to

Thèse accessible à l'adresse : https://theses.insa-lyon.fr/publication/2023ISAL0114/these.pdf © [L. Diatezo], [2023], INSA Lyon, tous droits réservés

aggressive environmental conditions, which can compromise the performance and durability of printed circuit boards (PCB). To prevent corrosion, various protection methods exist for copper-based conductive inks. Among these, coating is the preferred method, involving the use of special materials and a suitable chemical environment. With this approach, an additional material is deposited on the surface of a textile substrate to impart special properties to the part, while retaining its structural properties prior to treatment. These coatings can take the form of varnishes or special resins, creating a physical barrier between the copper and the external environment, preventing moisture, oxygen and other corrosive agents from coming into direct contact with the copper. Figure 5.14 shows the two new designs of the corrosion protection from the copper oxidation after exposure to a 12-day humidity and temperature procedure as described previously. The main objective of this study is to analyze the impact of different anti-corrosion protections for the textile substrate, with the aim of reducing its porosity and protect it from heat and moisture. To achieve this, the textile substrate is protected with a polymer binder (such as PU-AR, AC-AR, or AC-RUD) coated on its surface as shown in Figure 5.14(a). The impact of each binder on the electrical properties of the copper composite ink is analyzed. The copper coating should be protected as well from any change in the environment so as to ensure its electrical performance. As illustrated in Figure 5.14(b), another anti-corrosion protection is deposited on the top of the copper composite layer. This protection also has an aesthetic function, giving the surface an appropriate gloss and color. It plays an essential role in preserving the metal contact interface against oxidation and ambient corrosion. For an easier process, both the protection layers (one above the fabric and the other above the copper coating) are made of the same polymer binder, which could be different to the one used in the synthesis of the copper ink formulation.

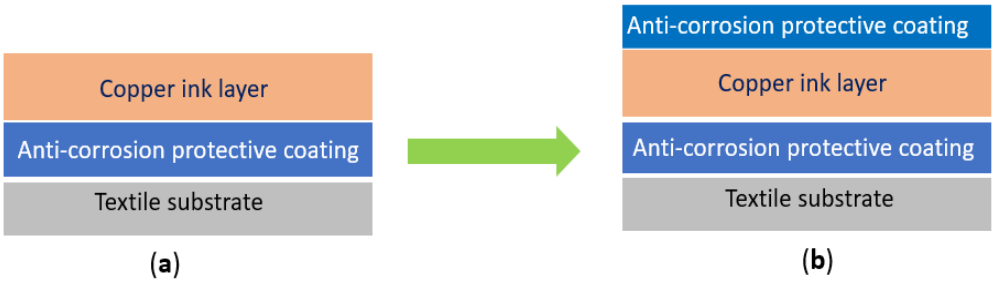

Figure 5.14. Two new designs of corrosion protection from the copper oxidation: (a) binder protection layer for the substrate; and (b) binder protection layer for the substrate and the copper composite ink.

5.3.2 Stability tests on a sample unit

5.3.2.1 Thermal cycle

The electrical conductivity of the textile substrates are measured before and after the thermal aging cycles at a temperature of 100 °C for 24 h and 48 h. Experimental tests were conducted on 9 sample units, a combination of 3 copper composites inks and 3 anti-corrosion protection. The results were graphically and numerically presented in Figure 5.15 and Table 5.6, showing how the electrical conductivity evolves as a function of thermal-cycles time. Several pertinent observations can be cited as following:

- In any materials' configuration, the electrical conductivity (σ) drastically decreases after the thermal procedure, which is strongly impacted by the exposure time (i.e., 24h and 48h).
- All materials used for the cooper composites and the anti-corrosion protections lead to satisfaction after a 24-h thermal procedure, in which the σ value is beyond the limited threshold ($\sigma_{th} = 5.4E4$ S/m).
- After 48 h, the result is more critical. For instance, all the three coated fabrics protected with anti-corrosion-based AC-RUD polymer (Figure 5.15 (c)) do not match the specifications ($\sigma_{48h} < \sigma_{th}$), whatever the binder used in the formulation of the cooper composite ink.
- The result shown in Figure 5.15 (a-b) reveals 4 combinations possible of the polymer binders used in the copper ink and the protection layers that meet the electrical performance ($\sigma_{48h} > \sigma_{th}$). As resumed

Thèse accessible à l'adresse : https://theses.insa-lyon.fr/publication/2023ISAL0114/these.pdf © [L. Diatezo], [2023], INSA Lyon, tous droits réservés

in Table 5.6, these combinations are highlighted in the orange color. Another solution indicated with the green color could be taken into consideration (subject to other criteria) as σ_{48h} is very close to σ_{th}.

Table 5.6. Electrical conductivity measured at the initial state (ambient condition) and after thermal cycles over 24 h and 48 h. Tests were performed on 9 samples with different combinations of the copper composite coating and the anti-corrosion protections.

		Electrical conductivity σ(S/m)								
Binder's formulations copper inks		Substrate protected by 3 layers AC- AR			Substrate protected by 3-layer PU-AR			Substrate protected by 3-layer AC-RUD		
		Thermal cycle			Thermal cycle			Thermal cycle		
Measured data		Initial	24h	48h	Initial	24h	48h	Initial	24h	48h
PU	Archroma	1.7E5	8.8E4	6.91E4	1.60E5	8.84E4	4.85E4	1.53E5	9.65E4	5.24E4
Acrylique	Archroma	1.93E5	1.04E5	6.29E4	1.52E5	8.78E4	6.33E4	1.33E5	7.90E4	4.99E4
Acrylique	Rudolf	7.88E4	5.5E4	4.3E4	1.17E5	9.47E4	7.12E4	7.24E4	5.74E4	3.99E4

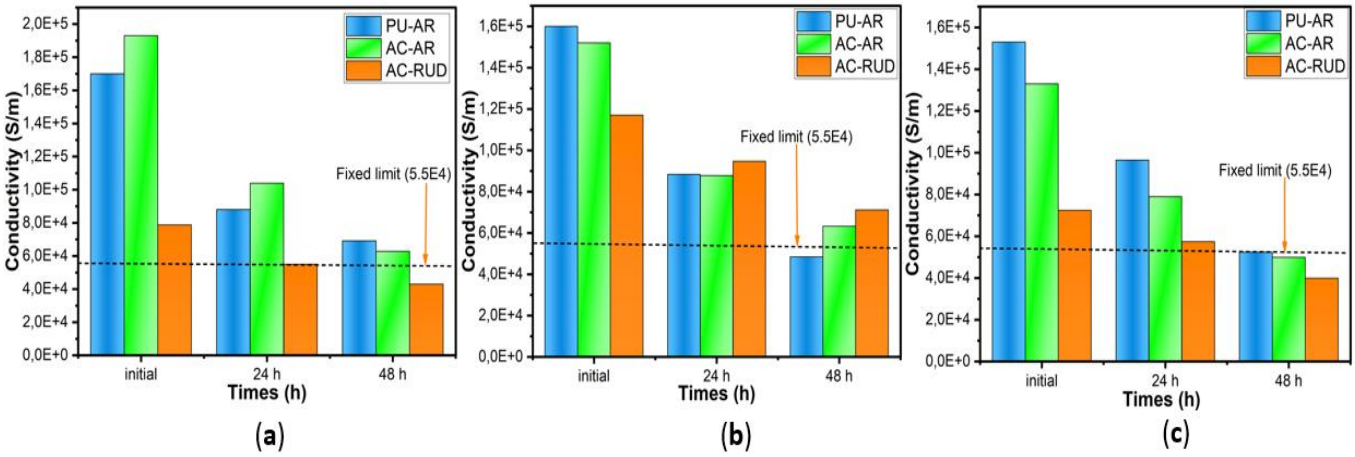

Figure 5.15. Electrical conductivity measured at room temperature (initial state) and hygrothermal aging (for 24 h and 48 h) of the copper composite inks formulated with the three different binders (shown in the legend) and different protection's materials like: (a) AC-AR; (b) PU-AR, and (c) AC-RUD.

5.3.2.2 Moisture cycle

In this study, we investigate the electrical performance of copper composite ink by analyzing the electrical conductivity of the nine printed samples before and after 12 days of hygrothermal aging at a temperature of 85°C and a humidity of 85% RH. This ageing simulates the conditions to which the material might be subjected as an interconnect material for applications such as heating mats or electroluminescent devices, where it would be exposed to humid environments and temperature variations. The results are shown in Figure 5.16 and Table 5.7, which lead to the following remarks:

- After undergoing 12 days of thermal/humidity environment, the electrical conductivity (σ) radically drops underneath the limited threshold ($\sigma_{th} = 5.4E4$ S/m) for several materials' configuration.
- The protection layers made of AC-AR is not adapted to the humidity aging as all the samples coated with this protection has a conductivity inferior to σ_{th} (cf. Figure 5.16 (a)).
- The protection layers made of PU-AR results in acceptable results where all samples possess the conductivity more or less close the threshold value, regardless of which binder has been chosen for the copper ink (cf. Figure 5.16 (b)).

Thèse accessible à l'adresse : https://theses.insa-lyon.fr/publication/2023ISAL0114/these.pdf © [L. Diatezo], [2023], INSA Lyon, tous droits réservés

- The protection layers made of AC-RUD when combined with the cooper composite elaborated with PU-AR (cf. Figure 5.16 (c)) leads to the satisfactory electrical conductivity that attains the maximum value as opposed to the other ($\sim 6.1E4$ S/m).
- The result shown in Table 5.7 reveals 3 combinations possible (highlighted in the orange color) of the polymer binders used in the copper ink and the protection layers that meet the electrical performance ($\sigma_{12h} > \sigma_{th}$). Two other solutions indicated with the green color could be taken into consideration their electrical conductivity is very close to σ_{th}.

Table 5.7. Electrical conductivity measured at the initial state and after a 12-day moisture cycles. Tests were performed on 9 samples with different combinations of the copper composite coating and the anti-corrosion protections.

Binder's formulations for copper inks		**Electrical conductivity σ(S/m)**					
		Substrate protected by 3-layers AC- AR		Substrate protected by 3-layer PU-AR		Substrate protected by 3-layer AC-RUD	
		Humidity cycles 85°C85%HR/-40°C		Humidity cycles 85°C85%HR/-40°C		Humidity cycles 85°C85%HR/-40°C	
Measured data		Initial	12 Days	Initial	12 Days	Initial	12 Days
PU	Archroma	1.70E5	2.69E4	1.60E5	5.39E4	1.53E5	6.08E4
Acrylique	Archroma	1.93E5	3.51E4	1.52E5	5.52E4	1.33E5	3.96E4
Acrylique	Rudolf	7.88E4	5.29E4	1.17E5	5.60E4	7.24E4	4.41E4

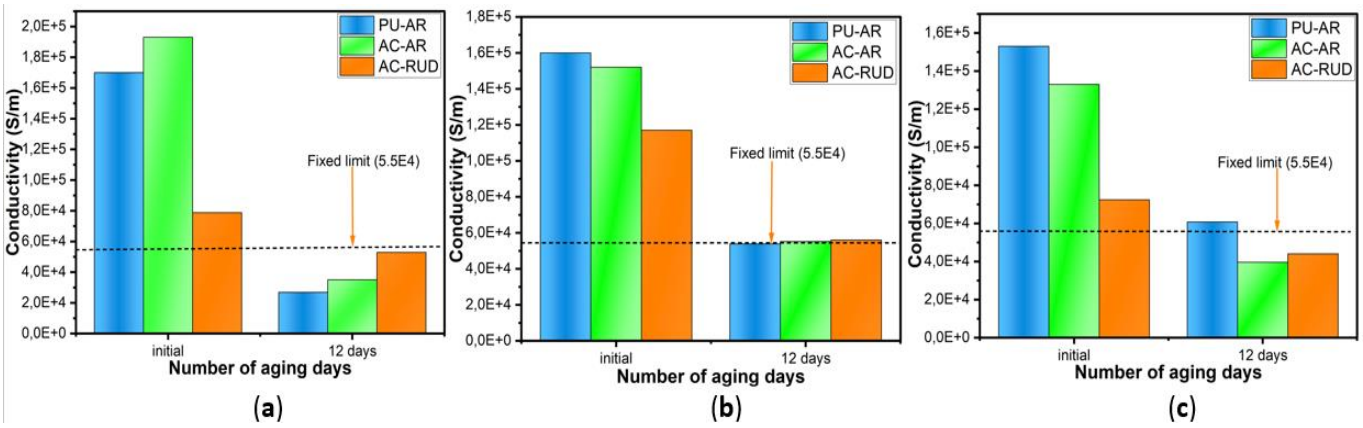

Figure 5.16. Electrical conductivity measured at ambient condition (initial state) and thermal/moisture aging (for 12 days) of the copper composite inks formulated with the three different binders (shown in the legend) and different protection's materials like: (a) AC-AR; (b) PU-AR, and (c) AC-RUD.

For an easier visualization, all results of Table 5.6 and Table 5.7 were gathered into Table 5.8 in which the highlighted colors have the same signification. By considering the solution figured out the two aging tests (orange color in the last two columns), it can be concluded that only one combination of materials (i.e., PU-AR used for the anti-corrosion protection and AC-AR for the copper) matches the Tesca's specifications. Two other combinations (highlighted in green) might be also retained since their results are very close the desired target after the temperature and moisture procedures. To a certain extent, the addition of anti-corrosion layers did not completely eliminate the aging effect, but it protected the copper electrodes as well as the textile substrate whose characteristics entirely satisfied the exigence of the automobile partner.

Thèse accessible à l'adresse : https://theses.insa-lyon.fr/publication/2023ISAL0114/these.pdf © [L. Diatezo], [2023], INSA Lyon, tous droits réservés

Table 5.8. Electrical properties of the two accelerated aging tests performed on the 9 sample units.

Anticorrosion coating	Composition conductive ink	Conductivity σ (S/m) Initial state	Conductivity σ (S/m) thermal cycling at 100°C for 24 h	Conductivity σ (S/m) thermal cycling at 100°C for 48 h	σ (S/m) Humidity 85°C85%RH/-40°C for (12 days))
Archroma polyurethane	PU-AR + copper	1.6E5	0.884E5	0.485E5	0.541E5
	AC-AR + copper	1.52E5	0.878E5	0.633E5	0.552E5
	AC-Rud + copper	1.17E5	0.947E5	0.712E5	0.510E5
Archroma acrylic	PU-AR + copper	1.7E5	0.880E5	0.691E5	0.269E5
	AC-AR + copper	1.93E5	1.04E5	0.629E5	0.351E5
	AC-Rud + copper	0.78E5	0.550E5	0,430E5	0.529E5
Acrylic Rudolf	PU-AR + copper	1.53E5	0.965E5	0.524E5	0.608E5
	AC-AR + copper	1.33E5	0.790E5	0.499E5	0.396E5
	AC-Rud + copper	0.724E5	0.574E5	0.399E5	0.441E5

5.3.2.3 Mechanical endurance

To assess the mechanical properties of the 9 printed samples, a monotonic tensile test is carried out. The corresponding stress-strain curves presented in Figure 5.17(a–c) consists of four typical phases: 1) linearity in the elastic deformation zone, 2) nonlinearity in the plastic regime, and 3) nonlinear behavior in the elastic deformation zone and the plastic regime, and 4) final failure [380]. Table 5.9 shows the numerical value of the Young modulus of all samples, which lead to the following comments:

- Similar to the trend observed in Figure 5.9, the samples made of AC-RUD copper composite are much more rigid than those made of PU-AR.
- In any materials' configuration, adding anti-corrosion protections clearly stiffens the sample, with an increase in the Young modulus (*Y*) especially for the protections made of PU-AR binder. On the other hand, the two other protections give rise to a moderate increase in *Y*, which do not drastically change the mechanical property of the textile substrate.
- Under the moderate deformation within the elastic regime (< 10 %), the electric property of the coated samples is assumed to be stable.

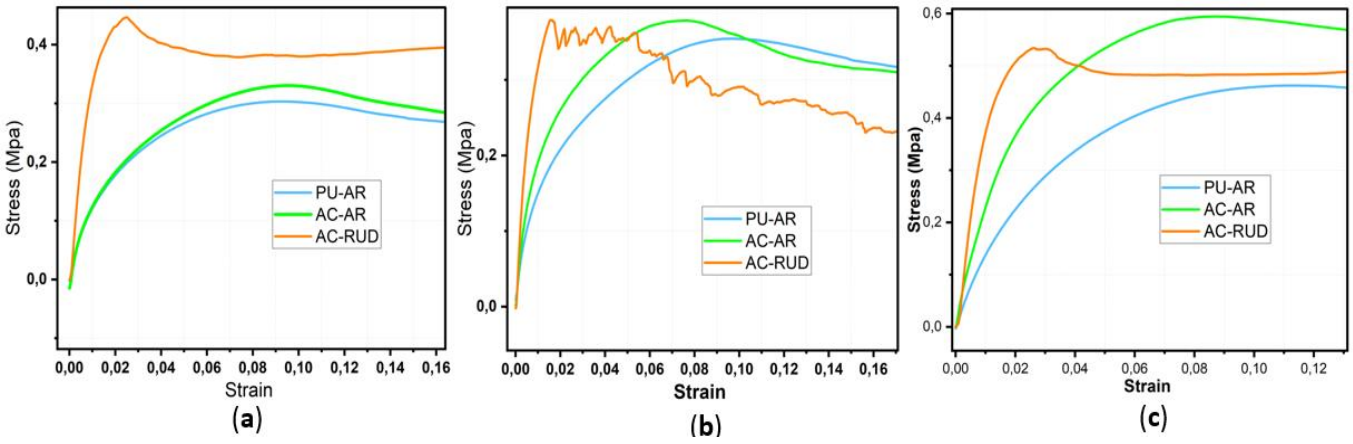

Figure 5.17. Stress-strain curves of the copper composite inks formulated with the three different binders (shown in the legend) and different protection's materials like: (a) AC-AR; (b) PU-AR, and (c) AC-RUD.

Table 5.9. Young modulus of different copper composite inks estimated based on tensile stress.

Thèse accessible à l'adresse : https://theses.insa-lyon.fr/publication/2023ISAL0114/these.pdf © [L. Diatezo], [2023], INSA Lyon, tous droits réservés

		Mechanical study			
Binder's formulations copper inks		Substrate protected by 3 layers AC- AR	Substrate protected by 3-layer PU-AR	Substrate protected by 3-layer AC-RUD	Ink without protection
		Elasticity modulus	Elasticity modulus	Elasticity modulus	Elasticity modulus
Measured data		E(MPa)	E(MPa)	E(MPa)	E(MPa)
PU	Archroma	15,6	21,03	14,2	10.49
Acrylique	Archroma	14,13	31,72	23,13	16.79
Acrylique	Rudolf	40,19	47,63	41,33	38.83

The two previous aging tests (temperature and moisture cycles) highlighted that the materials combination leading to the most appropriate electrical performance was PU-AR used for the anti-corrosion protection and AC-AR for the copper. Such a combination created a multilayered structure with a Young modulus of ~ 32 MPa, which is supposed to be acceptable for our target application. Thanks to these analyses, adequate materials have been identified and would be integrated into a real prototype of heating tablecloth. Several characterizations based on the aging trials are carried out to confirm the reliability of the proposed approach.

5.3.3 Stability tests on heating mats

In this study, the aging tests were conducted on a real heating tablecloth coated with a material couple PU-AR (used for the anti-corrosion protection of the textile substrate) and AC-AR (used for copper composite ink). Such materials were chosen based on the findings previously revealed in the experimental results.

5.3.3.1 Thermal cycle

Figure 5.18(a) shows an infrared thermography image of the heating tablecloth before the thermal cycles. The average temperatures of the three heating zones are around 50.8°C, with a slight difference of 2°C in zone 1 and 3°C in zone 2 (with respect to zone 3). This difference is attributed to the presence of the hot spots. After 48h thermal cycles (see Figure 5.18(b)), the temperature measured at all three zones are around 48°C, with a slight difference of 2.5 °C observed in zone 2. Table 5.10 summarizes the electrical resistance before and after the thermal cycles of the two copper electrodes, three carbon zones, and the total electrode of the tablecloth ($R_{tablecloth}$). Logically, the carbon ink was not affected by the thermal treatment, which is contrary to the case of copper electrodes whose electrical resistance increases almost double after a 48h aging test. However, this value is still reasonable (~ 1 Ω), which only involves in a slight increase of $R_{tablecloth}$ (from 3.8 to 4.5 Ω). Noted that the initial prototype presented in Figure 5.1 (subsection 5.1.1.1) without optimization of material and design has a very high value of $R_{tablecloth}$ (~ 17.5 Ω) after the test. Even before the test, the value of $R_{tablecloth}$ is also much smaller in the case of optimized device (3.8 Ω versus 7 Ω) It can be concluded that using the new copper-composite ink formulation as well as the anti-corrosion protections leads to significantly improved electrical conductivity of the heating tablecloth.

Table 5.10. Electrical resistance before and after thermal cycles conducted on different areas of the heating tablecloth.

		Electrode 1	**Electrode 2**	**Zone 1**	**Zone 2**	**Zone 3**	**$R_{tablecloth}$ (Ohm)**
Before	R_0(Ω)	0.6	0.58	15.61	15.43	15.85	**3.83**
After	R_{48h}(Ω)	**1.11**	**1.17**	17.39	15.62	14.57	**4.54**

Thèse accessible à l'adresse : https://theses.insa-lyon.fr/publication/2023ISAL0114/these.pdf © [L. Diatezo], [2023], INSA Lyon, tous droits réservés

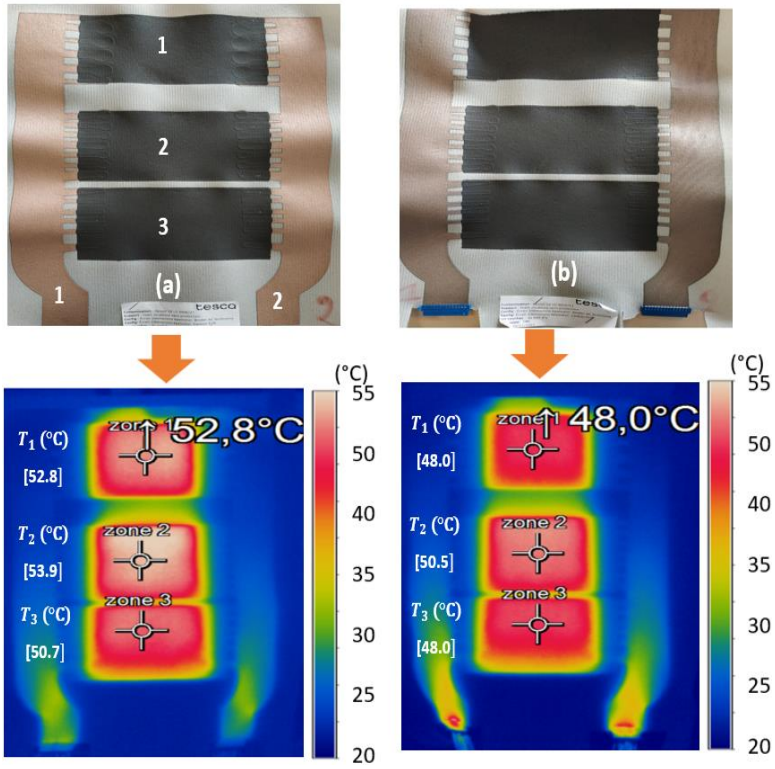

Figure 5.18. Images of the heating tablecloth elaborated with the protection-based AR-PU and the copper composite-based AC-AR polymer: (a) before and (b) after a 48-hour thermal cycles.

5.3.3.2 Moisture cycle

Figure 5.19(a)-(b) shows the infrared thermography image of the heating tablecloth before and after the 12-day hygrothermal cycles. Noted that there is no protection coated above the copper layer. The average temperature of the three carbon heating zones reaches around 45°C after the treatment, with discrepancy of 3°C due to the hot spots. Compared to the non-optimized prototype shown in Subsection 5.1.1.3, the new one developed in this study clearly demonstrates significant enhancement in the heating performance vis-à-vis the aging effect. The results shown in Table 5.11 are similar to those obtained in Table 5.10, again confirming the importance of the material's and design's optimization to achieve reliable device that is resistant to environmental changes.

Table 5.11. Electrical resistance before and after thermal/humidity cycles conducted on different areas of the heating tablecloth. Only one protection layer coated on the textile substrate.

		Electrode 1	**Electrode 2**	**Zone 1**	**Zone 2**	**Zone 3**	**$R_{tablecloth}$ (Ohm)**
Before	$R_0(\Omega)$	0.6	0.58	15.61	15.43	15.85	**3.83**
After	$R_{12\ days}(\Omega)$	**1.22**	**1.23**	18.13	15.52	16.44	**4.62**

As visualized in Figure 5.19 (b), the copper electrodes, with no protection layer, exhibits textural changes due to the humidity and pressure of the climatic chamber environment. In Figure 5.20, the device is full protected with two anti-corrosion protections: one coated on the textile and the other on the cooper composite. In that case, the electrodes, totally prevented from penetration of the moisture, does not change anymore in the texture. As observed in Table 5.12, the electrical property of the heating tablecloth is almost unchanged ($R_{tablecloth}$ ~ 4.22 Ω) with an addition of the top protection on the copper coating. However, the resistance of the electrode's double increases, but still small to be able to neglect the Joule-loss effect.

Thèse accessible à l'adresse : https://theses.insa-lyon.fr/publication/2023ISAL0114/these.pdf © [L. Diatezo], [2023], INSA Lyon, tous droits réservés

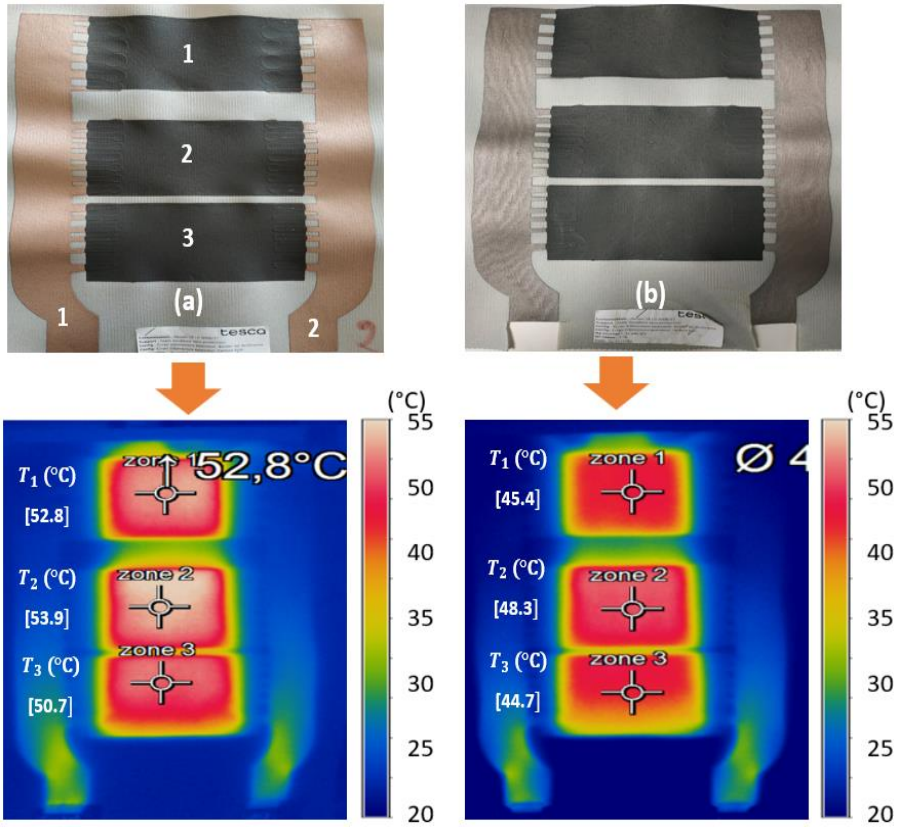

Figure 5.19. Images of the heating tablecloth protected by PU-AR binder (on the textile) and AC-AR-formulated composite ink, (a) before and (b) after the thermal and humidity cycles.

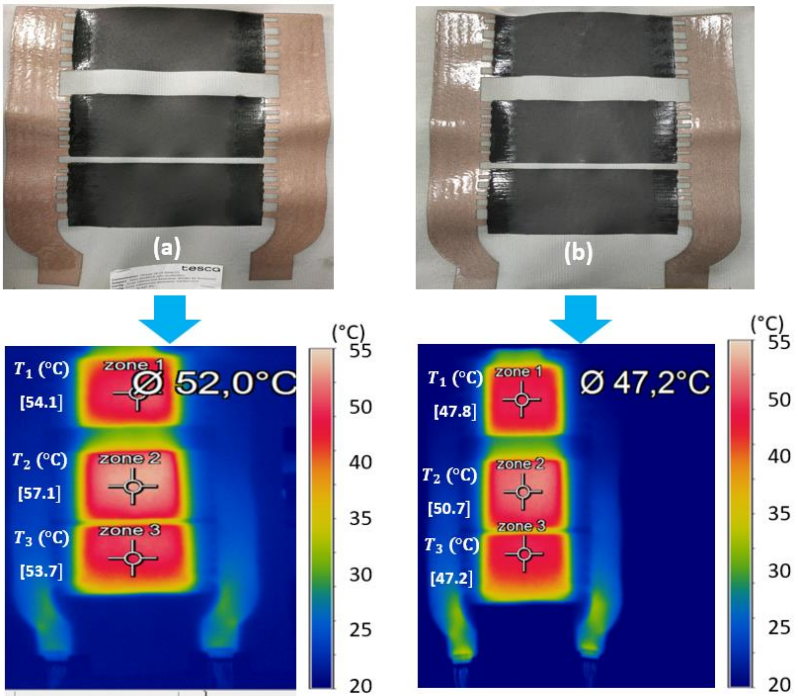

Figure 5.20. Heating images of the full protected device, (a) before and (b) after thermal cycles.

Thèse accessible à l'adresse : https://theses.insa-lyon.fr/publication/2023ISAL0114/these.pdf © [L. Diatezo], [2023], INSA Lyon, tous droits réservés

Table 5.12. Electrical resistance before and after the thermal aging conducted on different areas of the heating tablecloth. Two protection layers are used: one is coated on the textile substrate and the other is on the copper composite ink.

		Electrode 1	**Electrode 1**	**Zone 1**	**Zone 2**	**Zone 3**	**$R_{tablecloth}$ (Ohm)**
Before	$R_0(\Omega)$	0.72	0.87	16.27	13.51	13.13	**3.51**
After	$R_{48h}(\Omega)$	**2.13**	**2.3**	15.89	13.51	14.23	**4.22**

5.3.3.3 Mechanical endurance

The mechanical trials are directly performed on the sewn (cf. Figure 5.21(a)) and unsewn tablecloths, both being subjected to a load of 890 N for 200,000 cycles at a speed of 100 cycles/minute. After the tests, the unsewn device achieves a temperature of ~ 50 °C while 43°C for the sewn device. This temperature perfectly meets the requirements of Tesca's specifications. To some extent, the suture threads could have an impact on the electrical-to-thermal conversion, which lowers the efficiency and the final temperature as well. Furthermore, it appears additional hot spots, particularly at zones 2 and 3 around the suture threads (cf. Figure 5.21(b)). In that location, the section of the coating drastically reduced that impedes the circulation of the electrons and/or the heat flux. Consequently, an accumulation of these elements occurs, creating a peak in the temperature. Regarding the electrical property, the resistance of the sewn tablecloth increases from 3.9 Ω (before) to 5.8 Ω after the mechanical cycles, which is acceptable as the input mechanical stress is relatively low.

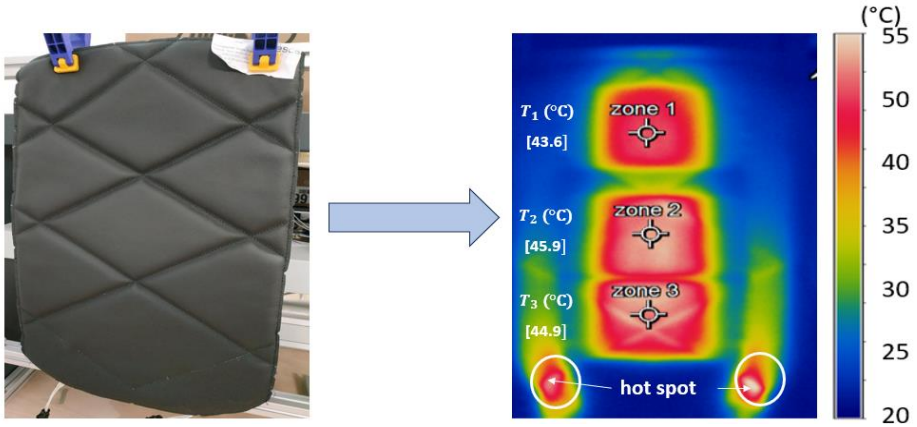

Figure 5.21. A real heating tablecloth sewn into car-seat system and its thermal image using an infrared camera.

5.4 Summary

Printed electronics on a flexible substrate often have to survive significant and repeated deformation, together with aggressive or extreme environment like high temperature and humidity, making their fatigue resistance and the stability of it during long-term storage and use a potential concern. The question of stability is obvious in the case of screen-printed traces where the polymer matrix remains a critical part of the structure. This study investigated on a new formulation of the copper composite inks that are combined with different types of polymer binder in order to create conductive materials more resistant to the aging effect in the long run. The ultimate reliability of the cooper electrodes is assumed to be limited by the electrical property and assessed by accelerated thermal cycling, mechanical solicitation, and moisture procedure.

Experimental results demonstrated a drastic decrease in the electrical conductivity of the cooper layer after both thermal and humidity cycles. This may be due to thermal vibrations in the material's crystalline structure, which disrupt the movement of the charge carriers. Also, an increase in the water absorption during the hygrothermal process containing high humidity could favor the oxidation of copper or even

Thèse accessible à l'adresse : https://theses.insa-lyon.fr/publication/2023ISAL0114/these.pdf © [L. Diatezo], [2023], INSA Lyon, tous droits réservés

corrosion/failure effect. Scanning electron microscopy (SEM), Energy dispersive X-rays (EDS) and X-ray diffraction revealed that the presence of water molecules led to an interruption in the conductive path of the charge. Moreover, the significant presence of oxygen on the electrode surface provoked electrochemical corrosion at the contact interface. To combat the corrosion, two protective layers are considered. The first one deposited on the textile substrate to reduce its porosity and improve the homogeneity of the conductive ink on the fabric, enhancing the electrical properties and limiting the ageing effect under humidity. The second one is applied to the metal surface to protect it from damage caused by rust, oxidation or corrosion. This protective layer are also expected to be an aesthetic function, capable of offering different surface aspects such as gloss, satin or matte, as well as color options. In conclusion, we have succeeded in improving the electrical properties of conductive inks, making them more resistant during application. The final prototype integrated with optimized printed coatings has fulfilled the exigence of our industrial partner Tesca.

Thèse accessible à l'adresse : https://theses.insa-lyon.fr/publication/2023ISAL0114/these.pdf © [L. Diatezo], [2023], INSA Lyon, tous droits réservés

General Conclusion

This thesis focuses on the development and improvement of multifunctional materials for printed electronics. It highlights the trade-offs between material properties and the specific requirements of the company (Tesca Group), in the context of applications linked to Joule-heating effect and electroluminescence functions for car seats. The originality of the work lies on a coupled approach between multifunctional materials and textile integration.

The study initially involves the exploration of multilayer coatings for a heating mat, using additive manufacturing (AM) based 3D screen-printing technology. This approach is based on the innovative concepts of design optimization as well as the integration of flexible electronics in fabric substrates. To create the heating tablecloth model, copper composite was used to print the conductive tracks and the electrodes, while carbon composite was used to make the heating resistors. These two commercial inks were selected regarding their excellent thermal and electrical properties, reasonable cost, good adhesion with textiles, and suitable viscosity that facilitated the AM procedure. They are designed in such a way that the resulting temperature of the fabric's surface is homogeneous within the interval 40–43 °C, with a temperature variation less than 0.5°C among the three carbon zones. Moreover, the duration of the transient regime must not be longer than 2 minutes, and no risk of overheating (> 45 °C) for the whole procedure. In addition, the printed coatings (copper and carbon) need to be flexible and as thin as possible so as not to alter the properties of the fabric substrate. To assess the print quality and the compatibility of composite inks with AM, characterization via scanning electron microscopy (SEM) was carried out. In addition, the thickness of the printed coating was determined through a laser profilometer, allowing for the determination of the optimum number of the conductive layers needed to be deposited on the porous fabric substrate. Finally, electrical and thermal characterizations were carried out using experimental testbenches combined with analytical methods, with the aim of identifying relevant material parameters for subsequent use in numerical models. The implementation of finite element method (FEM) via COMSOL software, based on identification of those parameters, is of key importance to conduct the design strategy. The results of the most optimized heat map design obtained from the numerical model were compared to a real screen-printed tablecloth. FEM simulation together with experimental measurements confirms that our new device definitively soleved the critical issues (significant hotspots and inhomogeneity heating) of the current protocol previously developed by Tesca.

Following the successful development and integration of the heating device in the intended configuration, further studies are investigated, focusing mainly on the aging effect of the conductive coatings under various external conditions, including temperature, humidity and mechanical load (dynamic and static regimes). This raises essential questions about fatigue resistance and long-term stability of materials in storage and in use where their electrical conductivity could be severely degraded in aggressive environments. This study therefore reported on the development of a new formulation of copper composite inks, combined with various types of polymer binders, with the aim of creating conductive materials more resistant to the effect of long-term aging. Experimental results showed a significant reduction in the electrical conductivity of the copper layer as a result of thermal cycling and humidity. Analytical techniques such as scanning electron microscopy (SEM), energy dispersive spectrometry (EDS), and X-ray diffraction showed that the presence of water molecules hindered electrical conductivity. In addition, a significant concentration of oxygen on the electrode surface led to electrochemical corrosion at the contact interface. To overcome such matters, a protective layer was coated on the whole surface of the textile substrate, and similarly for the copper electrodes. It is believed that optimizing design structure and material properties, as well as improving print quality, certainly promote sustainable development of high-performance heated textiles in the future.

Thèse accessible à l'adresse : https://theses.insa-lyon.fr/publication/2023ISAL0114/these.pdf © [L. Diatezo], [2023], INSA Lyon, tous droits réservés

Another aspect of this work involves the develop of electroluminescent (EL) devices that are integrated into ITO-coated textiles or glass substrates via screen-printing process. SEM has been chosen to analyze the morphological structure and the dispersion of phosphor microparticles within the matrix, somehow confirming the quality of the printing. A complete characterization of the EL composite has been explored to study the electrical, dielectric, and light emission properties, as well as the characterization of the phosphorescent materials. It has been pointed out that discrepancy in the dielectric constant between the polymer matrix and the phosphor particles has high impact on the luminance behavior, i.e., ultimately related to the brightness of the emitted light driven from the EL composites. The simulation results confirm that the P(VDF-TrFE-CFE) terpolymer matrix with its high dielectric constant, when combined with the copper-doped zinc sulfide (ZnS:Cu) microparticles, leads to improved concentration of the electric field applied on the phosphorus particles. As a matter of fact, these materials allow for the formation of a composite with the most appropriate EL response as opposed to the other tested samples. The EL performance and response of solution-coated matrix/phosphorus composite samples were also evaluated at different concentrations. A loading of 20 vol.% was found to be the most appropriate to achieve satisfactory luminescent response. The results are very encouraging, demonstrating that the metal doped ZnS composite offers undeniable advantages such as low power consumption, while outperforming the luminescent performance of conventional alternatives like $BaTiO_3$.

For the future, there are several directions for improvement of EL systems, including:

- Enhancing the electrical contacts of transparent electrodes to achieve optimum homogeneous brightness of EL devices for industrial use;
- Optimizing formulation parameters for EL composites to ensure greater reproducibility of results in an industrial context;
- Refining the flexible structure based on optimization strategies derived from screen-printing manufacturing. This could include exploring thinner EL composite films for improved brightness;
- Enriching the dielectric layer of the EL composite located between the conductive and transparent electrode, with the aim of minimizing the semiconducting impact (nonlinear hysteresis behavior) of phosphor particles;
- Performing advanced characterization to comprehensively assess the aging performance of EL devices. In particular, this would involve studying parameters related to luminescent excitation, such as frequency and electric field over a 5000-hour period, as well as the influence of the external environment, especially in a car seat context.

Thèse accessible à l'adresse : https://theses.insa-lyon.fr/publication/2023ISAL0114/these.pdf © [L. Diatezo], [2023], INSA Lyon, tous droits réservés

References

[1] K. Cherenack, L. van Pieterson, Smart textiles: Challenges and opportunities, Journal of Applied Physics 112 (2012) 091301. https://doi.org/10.1063/1.4742728.

[2] C. Marvin, When Old Technologies Were New: Thinking About Communication in the Late Nineteenth Century (pp. 9-32). York: Oxford University Press (1988).

[3] M.S. Sarif Ullah Patwary, Smart Textiles and Nano-Technology: A General Overview, J Textile Sci Eng 05 (2015). https://doi.org/10.4172/2165-8064.1000181.

[4] C. Gere, J. Rudoe, Jewellery in the Age of Queen Victoria: A Mirror to the World, pp 55 London. British Museum, 2010, 87-89 cloth.

[5] P. Smith, C. Lubell, A. Weatherson, Body Covering, Museum of Contemporary Crafts, the American Craft Council, New York (1968).

[6] K. Weisenstein, E. Renstrom, Artists Show Us How to Make Outrageous Costumes for $100, Vice (2017). https://www.vice.com/en/article/kz3zme/artists-show-us-how-to-make-outrageous-costumes-for-dollar100 (accessed September 19, 2023).

[7] R. Torres, ProyectosLA Opens Borders for Latin American Art in Los Angeles, Vice (2017). https://www.vice.com/en/article/3kkwb8/proyectosla-opens-borders-for-latin-american-art-in-los-angeles (accessed September 19, 2023).

[8] V. Staff, An Experience at the Heart of Nuclear Annihilation, Vice (2017). https://www.vice.com/en/article/3kvwaw/an-experience-at-the-heart-of-nuclear-annihilation (accessed September 19, 2023).

[9] D. Shi, The Art of "Shoe-Shi," Shoe-Shaped Sushi, Vice (2018). https://www.vice.com/en/article/a34pjj/the-art-of-shoe-shi-shoe-shaped-sushi (accessed September 19, 2023).

[10] E. Rosenthal, These Machines Will Teach You to Draw Whether You Like It Or Not, Vice (2018). https://www.vice.com/en/article/d34k4x/these-machines-will-teach-you-to-draw-whether-you-like-it-or-not (accessed September 19, 2023).

[11] D.J. Pangburn, These Glitched-Out Photos Look Like Paintings Made by a PC, Vice (2017). https://www.vice.com/en/article/zmmwk4/polina-efremova-glitched-out-photos-vintage-pc (accessed September 19, 2023).

[12] L. Lawson, How Plants Warn Each Other When They're Under Attack, Vice (2017). https://www.vice.com/en/article/8x5nzz/how-plants-warn-each-other-when-theyre-under-attack (accessed September 19, 2023).

[13] P.B. Kleck, Hundreds of Vintage Posters Are Now Available to Download and Print 100% Free, Vice (2018). https://www.vice.com/en/article/a343ba/hundreds-of-vintage-posters-are-now-available-to-download-and-print-100-free (accessed September 19, 2023).

[14] E. Jones, It's Time to Get a Fanny Pack, Vice (2017). https://www.vice.com/en/article/43ayam/why-its-time-to-get-a-fanny-pack-v24n7 (accessed September 19, 2023).

[15] S. Cole, Creators Are Concerned About Patreon's Service Fee Change, Vice (2017). https://www.vice.com/en/article/qvzb7v/creators-are-concerned-about-patreon-service-fee-change (accessed September 19, 2023).

Thèse accessible à l'adresse : https://theses.insa-lyon.fr/publication/2023ISAL0114/these.pdf © [L. Diatezo], [2023], INSA Lyon, tous droits réservés

[16] J. Buckley, “It’s Extremely Hard”: Inside Australia’s TikTok Economy, Vice (2022). https://www.vice.com/en/article/akvn9z/its-extremely-hard-inside-australias-tiktok-economy (accessed September 19, 2023).

[17] D. Axe, Weapon Manufacturers Are Making Robots That Deploy Other Robots, Vice (2018). https://www.vice.com/en/article/598edn/weapon-manufacturers-are-making-robots-that-deploy-other-robots (accessed September 19, 2023).

[18] E.R. Post, M. Orth, P.R. Russo, N. Gershenfeld, E-broidery: Design and fabrication of textile-based computing, IBM Syst. J. 39 (2000) 840–860. https://doi.org/10.1147/sj.393.0840.

[19] K. Cherenack, L. van Pieterson, Smart textiles: Challenges and opportunities, Journal of Applied Physics 112 (2012) 091301. https://doi.org/10.1063/1.4742728.

[20] T. Dang, M. Zhao, The application of smart fibers and smart textiles, J. Phys.: Conf. Ser. 1790 (2021) 012084. https://doi.org/10.1088/1742-6596/1790/1/012084.

[21] M. Mohamed, M. Abd El-AAty, S. Moawaed, A. Hashad, E. Abdel-Aziz, H. Othman, A. Hassabo, SMART Textiles via Photochromic and Thermochromic Colorant, J.Text.Color. Pol. Sci. 0 (2022) 0–0. https://doi.org/10.21608/jtcps.2022.143466.1125.

[22] X.X. Zhang, X. Tao, Smart textiles (2): Active smart, Textile Asia 32 (2001) 49–52.

[23] P.F. Gobin, M. Salvia, M. Morin, Matériaux intelligents structuraux et biomimétisme, Mater. Tech. 97 (2009) 19–28. https://doi.org/10.1051/mattech/2009009.

[24] Georges Akhras. http://www.journal.forces.gc.ca/vo1/no3/doc/7-14-fra.pdf, Automne (2000).

[25] X.X. Zhang, X. Tao, Smart textiles (3): Very smart, (2001).

[26] K. Cherenack, L. van Pieterson, Smart textiles: Challenges and opportunities, Journal of Applied Physics 112 (2012) 091301. https://doi.org/10.1063/1.4742728.

[27] A.R. Horrocks, Textile Institute, eds., Handbook of technical textiles, Repr, CRC Press [u.a.], Boca Raton, 2009.

[28] V. J, P. R, An Overview of Recent Developments in the Field of Wearable smart textiles, J Textile Sci Eng 08 (2018). https://doi.org/10.4172/2165-8064.1000368.

[29] V. Mecnika, M. Hoerr, I. Krievins, S. Jockenhoevel, T. Gries, Technical Embroidery for Smart Textiles: Review, Materials Science. Textile and Clothing Technology 9 (2015) 56. https://doi.org/10.7250/mstct.2014.009.

[30] H. Jin, N. Matsuhisa, S. Lee, M. Abbas, T. Yokota, T. Someya, Enhancing the Performance of Stretchable Conductors for E-Textiles by Controlled Ink Permeation, Advanced Materials 29 (2017) 1605848. https://doi.org/10.1002/adma.201605848.

[31] H.D. Henock, Literature over view of Smart textiles, (2010).

[32] M.S. Sarif Ullah Patwary, Smart Textiles and Nano-Technology: A General Overview, J Textile Sci Eng 05 (2015). https://doi.org/10.4172/2165-8064.1000181.

[33] G. Némoz, Chapitre 11 : Le textile, un matériau multifonctionnel, in: La Chimie et l’habitat, EDP Sciences, 2020: pp. 207–224. https://doi.org/10.1051/978-2-7598-1221-9.c016.

[34] X. Tao, Smart technology for textiles and clothing-introduction and review, in: Smart Fibres, Fabrics and Clothing, Woodhead Pub., 2001: pp. 1–6.

[35] V. Koncar, Introduction to smart textiles and their applications, in: Smart Textiles and Their Applications, Elsevier, 2016: pp. 1–8. https://doi.org/10.1016/B978-0-08-100574-3.00001-1.

Thèse accessible à l'adresse : https://theses.insa-lyon.fr/publication/2023ISAL0114/these.pdf © [L. Diatezo], [2023], INSA Lyon, tous droits réservés

[36] S. Park, S. Jayaraman, Smart Textiles: Wearable Electronic Systems, MRS Bull. 28 (2003) 585–591. https://doi.org/10.1557/mrs2003.170.

[37] N. Barnes, Smart Textiles for Designers – Inventing the Future of Fabrics, Journal of Textile Design Research and Practice 4 (2016) 191–194. https://doi.org/10.1080/20511787.2016.1247525.

[38] V. J, P. R, An Overview of Recent Developments in the Field of Wearable smart textiles, J Textile Sci Eng 08 (2018). https://doi.org/10.4172/2165-8064.1000368.

[39] Antistatic ESD home - Vetiwork, (n.d.). https://e-vetiwork.com/en/49-ESD-anti-static (accessed September 19, 2023).

[40] D.T.D. Edit, Passive Vs. Active Smart Textiles, OTEX Specialty Narrow Fabrics (2021). https://osnf.com/passive-vs-active-smart-textiles/ (accessed September 19, 2023).

[41] textileblog, Active Smart Textile Materials: Properties and Uses, Textile Blog (2021). https://www.textileblog.com/active-smart-textile-materials/ (accessed September 19, 2023).

[42] J.L. Hu, Introduction to active coatings for smart textiles, in: Active Coatings for Smart Textiles, Elsevier, 2016: pp. 1–7. https://doi.org/10.1016/B978-0-08-100263-6.00001-0.

[43] M. Stoppa, A. Chiolerio, Wearable Electronics and Smart Textiles: A Critical Review, Sensors 14 (2014) 11957–11992. https://doi.org/10.3390/s140711957.

[44] State of the art in Smart Textiles and Interactive Fabrics. https://studylib.net/doc/15335838/675 (accessed September 19, 2023).

[45] K. Priya, Smart Textiles and Intelligent Textiles - Page 2 of 6, Textile School (2022). https://www.textileschool.com/8307/smart-textiles-and-intelligent-textiles/ (accessed September 19, 2023).

[46] L.M. Castano, A.B. Flatau, Smart fabric sensors and e-textile technologies: a review, Smart Mater. Struct. 23 (2014) 053001. https://doi.org/10.1088/0964-1726/23/5/053001.

[47] K. Cherenack, L. van Pieterson, Smart textiles: Challenges and opportunities, Journal of Applied Physics 112 (2012) 091301. https://doi.org/10.1063/1.4742728.

[48] J. Zhang, S. He, L. Liu, G. Guan, X. Lu, X. Sun, H. Peng, The continuous fabrication of mechanochromic fibers, J. Mater. Chem. C 4 (2016) 2127–2133. https://doi.org/10.1039/C5TC04073F.

[49] G. Chen, Y. Li, M. Bick, J. Chen, Smart Textiles for Electricity Generation, Chem. Rev. 120 (2020) 3668–3720. https://doi.org/10.1021/acs.chemrev.9b00821.

[50] C. Moretti, X. Tao, L. Koehl, V. Koncar, Electrochromic textile displays for personal communication, in: Smart Textiles and Their Applications, Elsevier, 2016: pp. 539–568. https://doi.org/10.1016/B978-0-08-100574-3.00024-2.

[51] M.O. Gök, M.Z. Bilir, B.H. Gürcüm, Shape-Memory Applications in Textile Design, Procedia - Social and Behavioral Sciences 195 (2015) 2160–2169. https://doi.org/10.1016/j.sbspro.2015.06.283.

[52] S. Thakur, Shape Memory Polymers for Smart Textile Applications, in: B. Kumar, S. Thakur (Eds.), Textiles for Advanced Applications, InTech, 2017. https://doi.org/10.5772/intechopen.69742.

[53] H.L.O. Júnior, R.M. Neves, F.M. Monticeli, L. Dall Agnol, Smart Fabric Textiles: Recent Advances and Challenges, Textiles 2 (2022) 582–605. https://doi.org/10.3390/textiles2040034.

[54] T. Dang, M. Zhao, The application of smart fibers and smart textiles, J. Phys.: Conf. Ser. 1790 (2021) 012084. https://doi.org/10.1088/1742-6596/1790/1/012084.

Thèse accessible à l'adresse : https://theses.insa-lyon.fr/publication/2023ISAL0114/these.pdf © [L. Diatezo], [2023], INSA Lyon, tous droits réservés

[55] H.L.O. Júnior, R.M. Neves, F.M. Monticeli, L. Dall Agnol, Smart Fabric Textiles: Recent Advances and Challenges, Textiles 2 (2022) 582–605. https://doi.org/10.3390/textiles2040034.

[56] 3 Questions: The rapidly unfolding future of smart fabrics, MIT News | Massachusetts Institute of Technology (2020). https://news.mit.edu/2020/smart-fabrics-future-0508 (accessed September 19, 2023).

[57] Scientists create temperature-regulating fabric, Dezeen (2019). https://www.dezeen.com/2019/02/26/temperature-regulating-fabric-university-of-maryland/ (accessed September 19, 2023).

[58] Polyester Memory Fabric, (n.d.). https://www.leantex.com/memory-fabric/ (accessed September 19, 2023).

[59] Page not found, Nerdist (n.d.). https://nerdist.com/article/scientistsdevelop-electronic-textiles-interactive-gear-smart-clothes/ (accessed September 19, 2023).

[60] M.I. Kiron, Waterproof Breathable Fabrics: Product Modification and Recent Developments, Textile Learner (2021). https://textilelearner.net/waterproof-breathable-fabrics/ (accessed September 19, 2023).

[61] P.-C. Hsu, A.Y. Song, P.B. Catrysse, C. Liu, Y. Peng, J. Xie, S. Fan, Y. Cui, Radiative human body cooling by nanoporous polyethylene textile, Science 353 (2016) 1019–1023. https://doi.org/10.1126/science.aaf5471.

[62] S. Zeng, S. Pian, M. Su, Z. Wang, M. Wu, X. Liu, M. Chen, Y. Xiang, J. Wu, M. Zhang, Q. Cen, Y. Tang, X. Zhou, Z. Huang, R. Wang, A. Tunuhe, X. Sun, Z. Xia, M. Tian, M. Chen, X. Ma, L. Yang, J. Zhou, H. Zhou, Q. Yang, X. Li, Y. Ma, G. Tao, Hierarchical-morphology metafabric for scalable passive daytime radiative cooling, Science 373 (2021) 692–696. https://doi.org/10.1126/science.abi5484.

[63] Y. Peng, Y. Cui, Advanced Textiles for Personal Thermal Management and Energy, Joule 4 (2020) 724–742. https://doi.org/10.1016/j.joule.2020.02.011.

[64] testextextile, Classification et application des textiles textiles intelligents, Testex (2020). https://www.testextextile.com/fr/classification-et-application-de-textiles-textiles-intelligents/ (accessed September 19, 2023).

[65] Y. Peng, Y. Cui, Advanced Textiles for Personal Thermal Management and Energy, Joule 4 (2020) 724–742. https://doi.org/10.1016/j.joule.2020.02.011.

[66] H. Chen, X. Yu, X. Wang, Y. He, C. Zhang, G. Xue, Z. Liu, H. Lao, H. Song, W. Chen, Y. Qian, A. Zhang, X. Li, Dyeing and finishing wastewater treatment in China: State of the art and perspective, Journal of Cleaner Production 326 (2021) 129353. https://doi.org/10.1016/j.jclepro.2021.129353.

[67] Y. Peng, Y. Cui, Advanced textiles for personal thermal management and energy, Joule 4 (2020) 724–742.

[68] Y. Lu, X. Xiao, Y. Liu, J. Wang, S. Qi, C. Huan, H. Liu, Y. Zhu, G. Xu, Achieving multifunctional smart textile with long afterglow and thermo-regulation via coaxial electrospinning, Journal of Alloys and Compounds 812 (2020) 152144. https://doi.org/10.1016/j.jallcom.2019.152144.

[69] N. Notman, K.T. March 2020, Temperature-controlling textiles, RSC Education (n.d.). https://edu.rsc.org/feature/temperature-controlling-textiles/4011183.article (accessed September 19, 2023).

[70] S. Qian, M. Liu, Y. Dou, Y. Fink, W. Yan, A ‘Moore’s law’ for fibers enables intelligent fabrics, National Science Review 10 (2023) nwac202. https://doi.org/10.1093/nsr/nwac202.

Thèse accessible à l'adresse : https://theses.insa-lyon.fr/publication/2023ISAL0114/these.pdf © [L. Diatezo], [2023], INSA Lyon, tous droits réservés

[71] E. Mbise, T. Dias, W. Hurley, 6 - Design and manufacture of heated textiles, in: T. Dias (Ed.), Electronic Textiles, Woodhead Publishing, Oxford, 2015: pp. 117–132. https://doi.org/10.1016/B978-0-08-100201-8.00007-2.

[72] Chevy Avalanche Power & Heated Seat Parts | Kits, Motors — CARiD.com, (n.d.). https://www.carid.com/chevy-avalanche-power-heated-seats/ (accessed September 29, 2023).

[73] S.K. Bahadir, U.K. Sahin, S.K. Bahadir, U.K. Sahin, A Wearable Heating System with a Controllable e-Textile- Based Thermal Panel, in: Wearable Technologies, IntechOpen, 2018. https://doi.org/10.5772/intechopen.76192.

[74] 1 Pair 12V Universal Car Heated Seat Cushion Heated Seat Covers 30W-38W 45-65 Degree Adjustable Auto Heating Hot Pad Cushion, Quality Products for Sale l Kenya l South Africa (n.d.). https://imports.juakaliproducts.co.ke/shop/cheap-car-vehicle-replacement-spare-parts-sale-kenya-south-africa/1-pair-12v-universal-car-heated-seat-cushion-heated-seat-covers-30w-38w-45-65-degree-adjustable-auto-heating-hot-pad-cushion/ (accessed September 29, 2023).

[75] L.M. Degenstein, D. Sameoto, J.D. Hogan, A. Asad, P.I. Dolez, Smart Textiles for Visible and IR Camouflage Application: State-of-the-Art and Microfabrication Path Forward, Micromachines 12 (2021) 773. https://doi.org/10.3390/mi12070773.

[76] S. Zeng, S. Pian, M. Su, Z. Wang, M. Wu, X. Liu, M. Chen, Y. Xiang, J. Wu, M. Zhang, Q. Cen, Y. Tang, X. Zhou, Z. Huang, R. Wang, A. Tunuhe, X. Sun, Z. Xia, M. Tian, M. Chen, X. Ma, L. Yang, J. Zhou, H. Zhou, Q. Yang, X. Li, Y. Ma, G. Tao, Hierarchical-morphology metafabric for scalable passive daytime radiative cooling, Science 373 (2021) 692–696. https://doi.org/10.1126/science.abi5484.

[77] Y. Peng, Y. Cui, Advanced textiles for personal thermal management and energy, Joule 4 (2020) 724–742.

[78] L. Cai, Y. Peng, J. Xu, C. Zhou, C. Zhou, P. Wu, D. Lin, S. Fan, Y. Cui, Temperature Regulation in Colored Infrared-Transparent Polyethylene Textiles, Joule 3 (2019) 1478–1486. https://doi.org/10.1016/j.joule.2019.03.015.

[79] F. Lorussi, E.P. Scilingo, M. Tesconi, A. Tognetti, D. De Rossi, Strain sensing fabric for hand posture and gesture monitoring, IEEE Transactions on Information Technology in Biomedicine 9 (2005) 372–381. https://doi.org/10.1109/TITB.2005.854510.

[80] S.K. Bahadir, U.K. Sahin, A wearable heating system with a controllable e-textile-based thermal panel, Wearable Technologies 175 (2018).

[81] Y. Li, H. Zhu, Y. Wang, U. Ray, S. Zhu, J. Dai, C. Chen, K. Fu, S.-H. Jang, D. Henderson, T. Li, L. Hu, Cellulose-Nanofiber-Enabled 3D Printing of a Carbon-Nanotube Microfiber Network, Small Methods 1 (2017) 1700222. https://doi.org/10.1002/smtd.201700222.

[82] Y. Guo, C. Dun, J. Xu, J. Mu, P. Li, L. Gu, C. Hou, C.A. Hewitt, Q. Zhang, Y. Li, D.L. Carroll, H. Wang, Ultrathin, Washable, and Large-Area Graphene Papers for Personal Thermal Management, Small 13 (2017) 1702645. https://doi.org/10.1002/smll.201702645.

[83] Z. Yu, Y. Gao, X. Di, H. Luo, Cotton modified with silver-nanowires/polydopamine for a wearable thermal management device, RSC Adv. 6 (2016) 67771–67777. https://doi.org/10.1039/C6RA13104B.

[84] J. Huang, Y. Li, Z. Xu, W. Li, B. Xu, H. Meng, X. Liu, W. Guo, An integrated smart heating control system based on sandwich-structural textiles, Nanotechnology 30 (2019) 325203. https://doi.org/10.1088/1361-6528/ab15e8.

Thèse accessible à l'adresse : https://theses.insa-lyon.fr/publication/2023ISAL0114/these.pdf © [L. Diatezo], [2023], INSA Lyon, tous droits réservés

[85] P. Won, J.J. Park, T. Lee, I. Ha, S. Han, M. Choi, J. Lee, S. Hong, K.-J. Cho, S.H. Ko, Stretchable and Transparent Kirigami Conductor of Nanowire Percolation Network for Electronic Skin Applications, Nano Lett. 19 (2019) 6087–6096. https://doi.org/10.1021/acs.nanolett.9b02014.

[86] H. Dawit, Q. Zhang, Y. Li, S.R. Islam, J. Mao, L. Wang, Design of Electro-Thermal Glove with Sensor Function for Raynaud's Phenomenon Patients, Materials (Basel) 14 (2021) 377. https://doi.org/10.3390/ma14020377.

[87] P.-C. Hsu, X. Liu, C. Liu, X. Xie, H.R. Lee, A.J. Welch, T. Zhao, Y. Cui, Personal Thermal Management by Metallic Nanowire-Coated Textile, Nano Letters (2014). dx.doi.org/10.1021/nl5036572.

[88] A. Hazarika, B.K. Deka, D. Kim, H.E. Jeong, Y.-B. Park, H.W. Park, Woven Kevlar Fiber/Polydimethylsiloxane/Reduced Graphene Oxide Composite-Based Personal Thermal Management with Freestanding Cu–Ni Core–Shell Nanowires, Nano Lett. 18 (2018) 6731–6739. https://doi.org/10.1021/acs.nanolett.8b02408.

[89] A. Hazarika, B.K. Deka, C. Jeong, Y.-B. Park, H.W. Park, Biomechanical Energy-Harvesting Wearable Textile-Based Personal Thermal Management Device Containing Epitaxially Grown Aligned Ag-Tipped-NixCo1−xSe Nanowires/Reduced Graphene Oxide, Advanced Functional Materials 29 (2019) 1903144. https://doi.org/10.1002/adfm.201903144.

[90] J.H. Ortiz, Wearable Technologies, BoD – Books on Demand, 2018.

[91] T. Dang, M. Zhao, The application of smart fibers and smart textiles, J. Phys.: Conf. Ser. 1790 (2021) 012084. https://doi.org/10.1088/1742-6596/1790/1/012084.

[92] R. Soukup, A. Hamacek, L. Mracek, J. Reboun, Textile based temperature and humidity sensor elements for healthcare applications, in: Proceedings of the 2014 37th International Spring Seminar on Electronics Technology, IEEE, Dresden, Germany, 2014: pp. 407–411. https://doi.org/10.1109/ISSE.2014.6887634.

[93] K. Li, T. Chang, Z. Li, H. Yang, F. Fu, T. Li, J.S. Ho, P. Chen, Biomimetic MXene Textures with Enhanced Light-to-Heat Conversion for Solar Steam Generation and Wearable Thermal Management, Advanced Energy Materials 9 (2019) 1901687. https://doi.org/10.1002/aenm.201901687.

[94] M. Zulqarnain, S. Stanzione, G. Rathinavel, S. Smout, M. Willegems, K. Myny, E. Cantatore, A flexible ECG patch compatible with NFC RF communication, Npj Flex Electron 4 (2020) 13. https://doi.org/10.1038/s41528-020-0077-x.

[95] EurecatEG, DEPHOTEX, Eurecat (n.d.). https://eurecat.org/en/portfolio-items/dephotex/ (accessed September 19, 2023).

[96] M. Kuypers, New technologies for innovative sportswear • Stitch & Print, Stitch & Print (2013). https://stitchprint.eu/news/new-technologies-for-innovative-sportswear/ (accessed September 19, 2023).

[97] V. Mečņika, M. Hoerr, I. Krieviņš, A. Schwarz, Smart textiles for healthcare: applications and technologies, Rural Environment, Education, Personality 7 (2014) 150–161.

[98] D. Steffen, Smart Clothes. Product Semantics of Smart Clothes, (n.d.). https://www.academia.edu/212575/Smart_Clothes_Product_Semantics_of_Smart_Clothes (accessed September 19, 2023).

[99] V. Mečņika, Smart textiles for healthcare: applications and technologies, 7-8. 02 (2014).

[100] M. Catrysse, F. Pirotte, R. Puers, The use of electronics in medical textiles, Smart Textiles for Medicine and Healthcare: Materials, Systems and Applications (2007) 88–105. https://doi.org/10.1533/9781845692933.1.88.

Thèse accessible à l'adresse : https://theses.insa-lyon.fr/publication/2023ISAL0114/these.pdf © [L. Diatezo], [2023], INSA Lyon, tous droits réservés

[101] CEN/TR 16298:2011 - Textiles and textile products - Smart textiles - Definitions, categorisation, applications and standardization needs, ITeh Standards (n.d.). https://standards.iteh.ai/catalog/standards/cen/bc5e8f0a-eae5-4d47-98e9-420a25ca22f3/cen-tr-16298-2011 (accessed September 19, 2023).

[102] R. Dijcker, M. Van Der Wijk, O. Artières, G. Dortland, J. Lostumbo, Geotextile enabled smart monitoring solutions for safe and effective management of tailings and waste sites : two case studies : Volgermeerpolder (The Netherlands) and Suncor (Canada), (2011). https://doi.org/10.14288/1.0107729.

[103] M. Rothmaier, B. Selm, S. Spichtig, D. Haensse, M. Wolf, Photonic textiles for pulse oximetry, Opt. Express 16 (2008) 12973. https://doi.org/10.1364/OE.16.012973.

[104] L. Oscarsson, E.J. Heimdal, T. Lundell, J. Peterson, FLAT KNITTING OF A LIGHT EMITTING TEXTILE WITH OPTICAL FIBRES, AUTEX Research Journal 9 (2009).

[105] J. Peterson, J. Carlsson, M. Bratt, Smart textiles for knitted products-Prototype factory, (2009).

[106] Lusanda, Lessons from the Smartest Textiles I've met in Borås, Study in Sweden (2020). https://studyinsweden.se/blogs/2020/02/29/lessons-from-the-smartest-textiles-ive-met-in-boras/ (accessed September 19, 2023).

[107] A. Schwarz, L. Van Langenhove, P. Guermonprez, D. Deguillemont, A roadmap on smart textiles, Textile Progress 42 (2010) 99–180. https://doi.org/10.1080/00405160903465220.

[108] L.V. Langenhove, Smart Textiles for Medicine and Healthcare: Materials, Systems and Applications, Elsevier, 2007.

[109] Cette voiture est phosphorescente comme une luciole pendant la nuit - Le Temps, (2015). https://www.letemps.ch/societe/cette-voiture-phosphorescente-une-luciole-pendant-nuit (accessed September 19, 2023).

[110] Ford invente un siège auto avec capteurs de rythme cardiaque, La Tribune (2011). https://www.latribune.fr/entreprises-finance/industrie/automobile/20110610trib000628713/ford-invente-un-siege-auto-avec-capteurs-de-rythme-cardiaque.html (accessed September 19, 2023).

[111] NEUFU Housse de Double Siège Chauffante Voiture un, CDiscount (n.d.). https://www.cdiscount.com/auto/housses-couvres-sieges/neufu-housse-de-double-siege-chauffante-voiture-un/f-13341-neu6472063485461.html?cm_mmc=inf_facebook_like&cid=inf (accessed September 19, 2023).

[112] J. Wiklund, A. Karakoç, T. Palko, H. Yiğitler, K. Ruttik, R. Jäntti, J. Paltakari, A Review on Printed Electronics: Fabrication Methods, Inks, Substrates, Applications and Environmental Impacts, JMMP 5 (2021) 89. https://doi.org/10.3390/jmmp5030089.

[113] R. Bollström, Paper for printed electronics and functionality, (2013). https://www.doria.fi/handle/10024/92181 (accessed September 19, 2023).

[114] E. Dimitriou, N. Michailidis, Printable conductive inks used for the fabrication of electronics: an overview, Nanotechnology 32 (2021) 502009. https://doi.org/10.1088/1361-6528/abefff.

[115] Z. Cui, Printed Electronics: Materials, Technologies and Applications, John Wiley & Sons, 2016.

[116] S. Magdassi, The chemistry of inkjet inks, World scientific, 2009.

[117] A. Kamyshny, S. Magdassi, Conductive Nanomaterials for Printed Electronics, Small 10 (2014) 3515–3535. https://doi.org/10.1002/smll.201303000.

Thèse accessible à l'adresse : https://theses.insa-lyon.fr/publication/2023ISAL0114/these.pdf © [L. Diatezo], [2023], INSA Lyon, tous droits réservés

[118] J. Atkinson, T. Joyce, M. Joyce, Printed Electronics: A Landfill Simulation Study to Assess Environmental Impacts, J Solid Waste Technol Mngmnt 43 (2017) 145–150. https://doi.org/10.5276/JSWTM.2017.145.

[119] G. Baldini, A. Albini, P. Maiolino, G. Cannata, An Atlas for the Inkjet Printing of Large-Area Tactile Sensors, Sensors 22 (2022) 2332. https://doi.org/10.3390/s22062332.

[120] S. Chandrasekaran, A. Jayakumar, R. Velu, A Comprehensive Review on Printed Electronics: A Technology Drift towards a Sustainable Future, Nanomaterials 12 (2022) 4251. https://doi.org/10.3390/nano12234251.

[121] S. Mekhmouken, N. Battaglini, G. Mattana, A. Maurin, S. Zrig, B. Piro, D. Capitao, V. Noel, Gold nanoparticle-based eco-friendly ink for electrode patterning on flexible substrates, Electrochemistry Communications 123 (2021) 106918. https://doi.org/10.1016/j.elecom.2021.106918.

[122] I.J. Fernandes, A.F. Aroche, A. Schuck, P. Lamberty, C.R. Peter, W. Hasenkamp, T.L.A.C. Rocha, Silver nanoparticle conductive inks: synthesis, characterization, and fabrication of inkjet-printed flexible electrodes, Sci Rep 10 (2020) 8878. https://doi.org/10.1038/s41598-020-65698-3.

[123] J. Niittynen, E. Sowade, H. Kang, R.R. Baumann, M. Mäntysalo, Comparison of laser and intense pulsed light sintering (IPL) for inkjet-printed copper nanoparticle layers, Sci Rep 5 (2015) 8832. https://doi.org/10.1038/srep08832.

[124] Y.J. Lee, C. Lee, H.M. Lee, Synthesis of oxide-free aluminum nanoparticles for application to conductive film, Nanotechnology 29 (2018) 055602. https://doi.org/10.1088/1361-6528/aa9c1b.

[125] M. Nelo, S. Myllymäki, J. Juuti, A. Uusimäki, H. Jantunen, Cobalt Nanoparticle Inks for Printed High Frequency Applications on Polycarbonate, Journal of Elec Materi 44 (2015) 4884–4890. https://doi.org/10.1007/s11664-015-4072-2.

[126] S.-H. Park, H.-S. Kim, Flash light sintering of nickel nanoparticles for printed electronics, Thin Solid Films 550 (2014) 575–581. https://doi.org/10.1016/j.tsf.2013.11.075.

[127] P.V. Arsenov, A.A. Efimov, V.V. Ivanov, Optimizing Aerosol Jet Printing Process of Platinum Ink for High-Resolution Conductive Microstructures on Ceramic and Polymer Substrates, Polymers 13 (2021) 918. https://doi.org/10.3390/polym13060918.

[128] S. Majee, M.C.F. Karlsson, P.J. Wojcik, A. Sawatdee, M.Y. Mulla, N. ul H. Alvi, P. Dyreklev, V. Beni, D. Nilsson, Low temperature chemical sintering of inkjet-printed Zn nanoparticles for highly conductive flexible electronic components, Npj Flex Electron 5 (2021) 14. https://doi.org/10.1038/s41528-021-00111-1.

[129] C.-C. Tseng, C.-P. Chang, Y. Sung, Y.-C. Chen, M.-D. Ger, A novel method to produce Pd nanoparticle ink for ink-jet printing technology, Colloids and Surfaces A: Physicochemical and Engineering Aspects 339 (2009) 206–210. https://doi.org/10.1016/j.colsurfa.2009.02.026.

[130] Y.H. Jo, I. Jung, C.S. Choi, I. Kim, H.M. Lee, Synthesis and characterization of low temperature Sn nanoparticles for the fabrication of highly conductive ink, Nanotechnology 22 (2011) 225701. https://doi.org/10.1088/0957-4484/22/22/225701.

[131] A. Albrecht, A. Rivadeneyra, A. Abdellah, P. Lugli, J.F. Salmerón, Inkjet printing and photonic sintering of silver and copper oxide nanoparticles for ultra-low-cost conductive patterns, J. Mater. Chem. C 4 (2016) 3546–3554. https://doi.org/10.1039/C6TC00628K.

[132] A. Mazzotta, A. Gabbani, M. Carlotti, M. Ruggeri, E. Fantechi, A. Ottomaniello, F. Pineider, A. Pucci, V. Mattoli, Invisible Thermoplasmonic Indium Tin Oxide Nanoparticle Ink for Anti-counterfeiting Applications, ACS Appl. Mater. Interfaces 14 (2022) 35276–35286. https://doi.org/10.1021/acsami.2c10864.

Thèse accessible à l'adresse : https://theses.insa-lyon.fr/publication/2023ISAL0114/these.pdf © [L. Diatezo], [2023], INSA Lyon, tous droits réservés

[133] S.Y. Cho, Y.H. Kang, J.-Y. Jung, S.Y. Nam, J. Lim, S.C. Yoon, D.H. Choi, C. Lee, Novel Zinc Oxide Inks with Zinc Oxide Nanoparticles for Low-Temperature, Solution-Processed Thin-Film Transistors, Chem. Mater. 24 (2012) 3517–3524. https://doi.org/10.1021/cm2036234.

[134] W. Wang, Q. Li, A. Zheng, X. Li, Z. Pan, J. Jiang, L. Zhang, R. Hong, L. Zhuang, Superparamagnetic iron oxide nanoparticles for full-color photonic materials with tunable properties, Results in Physics 14 (2019) 102366. https://doi.org/10.1016/j.rinp.2019.102366.

[135] H.W. Tan, J. An, C.K. Chua, T. Tran, Metallic Nanoparticle Inks for 3D Printing of Electronics, Adv Elect Materials 5 (2019) 1800831. https://doi.org/10.1002/aelm.201800831.

[136] L. Kela, Metallic nanoparticles for conductive inks Author (s) Kela, Laura; Auvinen, Ari; Tapper, Unto; Hokkinen, Jouni Citation Int, (2014).

[137] Y.-H. Choi, D.-H. Kim, H.S. Han, S. Shin, S.-H. Hong, K.S. Hong, Direct Printing Synthesis of Self-Organized Copper Oxide Hollow Spheres on a Substrate Using Copper(II) Complex Ink: Gas Sensing and Photoelectrochemical Properties, Langmuir 30 (2014) 700–709. https://doi.org/10.1021/la404098s.

[138] D. Ito, K. Masuko, B.A. Weintraub, L.C. McKenzie, J.E. Hutchison, Convenient preparation of ITO nanoparticles inks for transparent conductive thin films, J Nanopart Res 14 (2012) 1274. https://doi.org/10.1007/s11051-012-1274-x.

[139] K.S. Suganthi, K. Harish, N.M. Nair, P. Swaminathan, Formulation and optimization of a zinc oxide nanoparticle ink for printed electronics applications, Flex. Print. Electron. 3 (2018) 015001. https://doi.org/10.1088/2058-8585/aaa166.

[140] G. Arrabito, Y. Aleeva, R. Pezzilli, V. Ferrara, P.G. Medaglia, B. Pignataro, G. Prestopino, Printing ZnO Inks: From Principles to Devices, Crystals 10 (2020) 449. https://doi.org/10.3390/cryst10060449.

[141] H.J. Kim, J. Jung, H.J. Kim, Enhancement of electrical characteristics and stability of self-patterned In–Zn–O thin-film transistors based on photosensitive precursors, Sci Rep 10 (2020) 18853. https://doi.org/10.1038/s41598-020-76080-8.

[142] M. Vaseem, F.A. Ghaffar, M.F. Farooqui, A. Shamim, Iron Oxide Nanoparticle-Based Magnetic Ink Development for Fully Printed Tunable Radio-Frequency Devices, Adv Materials Technologies 3 (2018) 1700242. https://doi.org/10.1002/admt.201700242.

[143] B. Deore, C. Paquet, A.J. Kell, T. Lacelle, X. Liu, O. Mozenson, G. Lopinski, G. Brzezina, C. Guo, S. Lafrenière, P.R.L. Malenfant, Formulation of Screen-Printable Cu Molecular Ink for Conductive/Flexible/Solderable Cu Traces, ACS Appl. Mater. Interfaces 11 (2019) 38880–38894. https://doi.org/10.1021/acsami.9b08854.

[144] A.J. Kell, C. Paquet, O. Mozenson, I. Djavani-Tabrizi, B. Deore, X. Liu, G.P. Lopinski, R. James, K. Hettak, J. Shaker, A. Momciu, J. Ferrigno, O. Ferrand, J.X. Hu, S. Lafrenière, P.R.L. Malenfant, Versatile Molecular Silver Ink Platform for Printed Flexible Electronics, ACS Appl. Mater. Interfaces 9 (2017) 17226–17237. https://doi.org/10.1021/acsami.7b02573.

[145] H. Hong, J. Hu, X. Yan, UV Curable Conductive Ink for the Fabrication of Textile-Based Conductive Circuits and Wearable UHF RFID Tags, ACS Appl. Mater. Interfaces 11 (2019) 27318–27326. https://doi.org/10.1021/acsami.9b06432.

[146] X. Guo, J. Yao, F. Ji, R. Wang, L. Hao, UV curable PUA ink with polymerizable surfactant-enhanced Ag@PPy for fabricating flexible and durable conductive coating on the surface of cotton fabric, Progress in Organic Coatings 174 (2023) 107239. https://doi.org/10.1016/j.porgcoat.2022.107239.

Thèse accessible à l'adresse : https://theses.insa-lyon.fr/publication/2023ISAL0114/these.pdf © [L. Diatezo], [2023], INSA Lyon, tous droits réservés

[147] H. Hong, L. Jiang, H. Tu, J. Hu, X. Yan, Formulation of UV curable nano-silver conductive ink for direct screen-printing on common fabric substrates for wearable electronic applications, Smart Mater. Struct. 30 (2021) 045001. https://doi.org/10.1088/1361-665X/abe4b3.

[148] H. Kipphan, Printing Technologies with Permanent Printing Master, in: H. Kipphan (Ed.), Handbook of Print Media, Springer Berlin Heidelberg, Berlin, Heidelberg, 2001: pp. 203–448. https://doi.org/10.1007/978-3-540-29900-4_2.

[149] H. Kipphan, Printing Technologies without a Printing Plate (NIP Technologies), in: H. Kipphan (Ed.), Handbook of Print Media, Springer Berlin Heidelberg, Berlin, Heidelberg, 2001: pp. 675–758. https://doi.org/10.1007/978-3-540-29900-4_5.

[150] W. d'Heureuse, H. Kipphan, H.D. Ag, Print Technologies and Design Concepts for Hybrid Printing Systems, IS T/DPP 1 (2001) 33–38.

[151] B.H. Kim, M.S. Onses, J.B. Lim, S. Nam, N. Oh, H. Kim, K.J. Yu, J.W. Lee, J.-H. Kim, S.-K. Kang, C.H. Lee, J. Lee, J.H. Shin, N.H. Kim, C. Leal, M. Shim, J.A. Rogers, High-Resolution Patterns of Quantum Dots Formed by Electrohydrodynamic Jet Printing for Light-Emitting Diodes, Nano Lett. 15 (2015) 969–973. https://doi.org/10.1021/nl503779e.

[152] M.S. Onses, E. Sutanto, P.M. Ferreira, A.G. Alleyne, J.A. Rogers, Mechanisms, Capabilities, and Applications of High-Resolution Electrohydrodynamic Jet Printing, Small 11 (2015) 4237–4266. https://doi.org/10.1002/smll.201500593.

[153] N. Saengchairat, T. Tran, C.-K. Chua, A review: additive manufacturing for active electronic components, Virtual and Physical Prototyping 12 (2017) 31–46. https://doi.org/10.1080/17452759.2016.1253181.

[154] J. Stringer, T.M. Althagathi, C.C.W. Tse, V.D. Ta, J.D. Shephard, E. Esenturk, C. Connaughton, T.J. Wasley, J. Li, R.W. Kay, P.J. Smith, Integration of additive manufacturing and inkjet printed electronics: a potential route to parts with embedded multifunctionality, Manufacturing Rev. 3 (2016) 12. https://doi.org/10.1051/mfreview/2016011.

[155] Y.-J. Kwon, Y. Park, W. Lee, Inkjet-Printed Organic Transistors Based on Organic Semiconductor/Insulating Polymer Blends, Materials 9 (2016) 650. https://doi.org/10.3390/ma9080650.

[156] F. Torrisi, T. Hasan, W. Wu, Z. Sun, A. Lombardo, T.S. Kulmala, G.-W. Hsieh, S. Jung, F. Bonaccorso, P.J. Paul, D. Chu, A.C. Ferrari, Inkjet-Printed Graphene Electronics, ACS Nano 6 (2012) 2992–3006. https://doi.org/10.1021/nn2044609.

[157] C. Aliaga, B. Ferreira, M. Hortal, M.Á. Pancorbo, J.M. López, F.J. Navas, Influence of RFID tags on recyclability of plastic packaging, Waste Management 31 (2011) 1133–1138. https://doi.org/10.1016/j.wasman.2010.12.015.

[158] M.Â.P.R. Cerqueira, J.M. Lagaron, L.M.P. Castro, A.A.M. de O.S. Vicente, eds., Nanomaterials for food packaging: materials, processing technologies, and safety issues, Elsevier, Cambridge, MA, 2018. https://search.ebscohost.com/login.aspx?direct=true&scope=site&db=nlebk&db=nlabk&AN=1627737 (accessed September 20, 2023).

[159] A. Blayo, B. Pineaux, Printing processes and their potential for RFID printing, in: Proceedings of the 2005 Joint Conference on Smart Objects and Ambient Intelligence: Innovative Context-Aware Services: Usages and Technologies, ACM, Grenoble France, 2005: pp. 27–30. https://doi.org/10.1145/1107548.1107559.

[160] M. Känsäkoski, A. Maaninen, Printed Intelligence and Applications in Sensing, Measurement and Control 40 (2007) 84–87. https://doi.org/10.1177/002029400704000306.

Thèse accessible à l'adresse : https://theses.insa-lyon.fr/publication/2023ISAL0114/these.pdf © [L. Diatezo], [2023], INSA Lyon, tous droits réservés

[161] S. Khan, L. Lorenzelli, R.S. Dahiya, Technologies for Printing Sensors and Electronics Over Large Flexible Substrates: A Review, IEEE Sensors J. 15 (2015) 3164–3185. https://doi.org/10.1109/JSEN.2014.2375203.

[162] X. Liu, J.T. Guthrie, A review of flexographic printing plate development, Surface Coatings International Part B: Coatings Transactions 86 (2003) 91–99. https://doi.org/10.1007/BF02699619.

[163] P. Brumm, H. Sauer, E. Dörsam, Scaling Behavior of Pattern Formation in the Flexographic Ink Splitting Process, Colloids and Interfaces 3 (2019) 37. https://doi.org/10.3390/colloids3010037.

[164] B. Kang, W.H. Lee, K. Cho, Recent Advances in Organic Transistor Printing Processes, ACS Appl. Mater. Interfaces 5 (2013) 2302–2315. https://doi.org/10.1021/am302796z.

[165] H.-B. Lee, H.J. Yang, J.H. We, K. Kim, K.C. Choi, B.J. Cho, Thin-Film Thermoelectric Module for Power Generator Applications Using a Screen-Printing Method, Journal of Elec Materi 40 (2011) 615–619. https://doi.org/10.1007/s11664-010-1481-0.

[166] J. Sakai, E. Fujinaka, T. Nishimori, N. lto, J. Adachi, S. Nagano, K. Murakami, High efficiency organic solar cells by screen printing method, in: Conference Record of the Thirty-First IEEE Photovoltaic Specialists Conference, 2005., IEEE, Lake buena Vista, FL, USA, 2005: pp. 125–128. https://doi.org/10.1109/PVSC.2005.1488085.

[167] M. Kujala, T. Kololuoma, J. Keskinen, D. Lupo, M. Mantysalo, T.M. Kraft, Screen Printed Vias for a Flexible Energy Harvesting and Storage Module, in: 2018 International Flexible Electronics Technology Conference (IFETC), IEEE, Ottawa, ON, 2018: pp. 1–6. https://doi.org/10.1109/IFETC.2018.8583967.

[168] A. Moya, G. Gabriel, R. Villa, F. Javier del Campo, Inkjet-printed electrochemical sensors, Current Opinion in Electrochemistry. 3 (2017) 29–39. https://doi.org/10.1016/j.coelec.2017.05.003.

[169] E. Feilden, E.G.-T. Blanca, F. Giuliani, E. Saiz, L. Vandeperre, Robocasting of structural ceramic parts with hydrogel inks, Journal of the European Ceramic Society 36 (2016) 2525–2533. https://doi.org/10.1016/j.jeurceramsoc.2016.03.001.

[170] T.A. Campbell, O.S. Ivanova, 3D printing of multifunctional nanocomposites, Nano Today 8 (2013) 119–120. https://doi.org/10.1016/j.nantod.2012.12.002.

[171] V. Mazzanti, L. Malagutti, F. Mollica, FDM 3D Printing of Polymers Containing Natural Fillers: A Review of their Mechanical Properties, Polymers 11 (2019) 1094. https://doi.org/10.3390/polym11071094.

[172] A. Zocca, G. Franchin, H. Elsayed, E. Gioffredi, E. Bernardo, P. Colombo, Direct Ink Writing of a Preceramic Polymer and Fillers to Produce Hardystonite (Ca 2 ZnSi 2 O 7) Bioceramic Scaffolds, J. Am. Ceram. Soc. 99 (2016) 1960–1967. https://doi.org/10.1111/jace.14213.

[173] L. Rueschhoff, W. Costakis, M. Michie, J. Youngblood, R. Trice, Additive Manufacturing of Dense Ceramic Parts via Direct Ink Writing of Aqueous Alumina Suspensions, Int J Applied Ceramic Tech 13 (2016) 821–830. https://doi.org/10.1111/ijac.12557.

[174] T. An, K.-T. Hwang, J.-H. Kim, J. Kim, Extrusion-based 3D direct ink writing of NiZn-ferrite structures with viscoelastic ceramic suspension, Ceramics International 46 (2020) 6469–6476. https://doi.org/10.1016/j.ceramint.2019.11.127.

[175] F. Cai, Y. Chang, K. Wang, W.T. Khan, S. Pavlidis, J. Papapolymerou, High resolution aerosol jet printing of D- band printed transmission lines on flexible LCP substrate, in: 2014 IEEE MTT-S International Microwave Symposium (IMS2014), IEEE, Tampa, FL, USA, 2014: pp. 1–3. https://doi.org/10.1109/MWSYM.2014.6848597.

Thèse accessible à l'adresse : https://theses.insa-lyon.fr/publication/2023ISAL0114/these.pdf © [L. Diatezo], [2023], INSA Lyon, tous droits réservés

[176] E. Dimitriou, N. Michailidis, Printable conductive inks used for the fabrication of electronics: an overview, Nanotechnology 32 (2021) 502009. https://doi.org/10.1088/1361-6528/abefff.

[177] T. Reitberger, J. Franke, G.-A. Hoffmann, L. Overmeyer, L. Lorenz, K.-J. Wolter, Integration of polymer optical waveguides by using flexographic and aerosol jet printing, in: 2016 12th International Congress Molded Interconnect Devices (MID), IEEE, Wuerzburg, Germany, 2016: pp. 1–6. https://doi.org/10.1109/ICMID.2016.7738933.

[178] Y.-D. Chen, V. Nagarajan, D.W. Rosen, W. Yu, S.Y. Huang, Aerosol jet printing on paper substrate with conductive silver nano material, Journal of Manufacturing Processes 58 (2020) 55–66. https://doi.org/10.1016/j.jmapro.2020.07.064.

[179] M. Landgraf, S. Reitelshofer, J. Franke, M. Hedges, Aerosol jet printing and lightweight power electronics for dielectric elastomer actuators, in: 2013 3rd International Electric Drives Production Conference (EDPC), IEEE, Nuremberg, Germany, 2013: pp. 1–7. https://doi.org/10.1109/EDPC.2013.6689733.

[180] N.J. Wilkinson, M.A.A. Smith, R.W. Kay, R.A. Harris, A review of aerosol jet printing—a non-traditional hybrid process for micro-manufacturing, Int J Adv Manuf Technol 105 (2019) 4599–4619. https://doi.org/10.1007/s00170-019-03438-2.

[181] S. Zhen, R.M. Bilal, A. Shamim, 3D printed System-on-Package (SoP) for environmental sensing and localization applications, in: 2017 International Symposium on Antennas and Propagation (ISAP), IEEE, Phuket, 2017: pp. 1–2. https://doi.org/10.1109/ISANP.2017.8228793.

[182] Q. Li, S. Luo, Q.-M. Wang, Piezoresistive thin film pressure sensor based on carbon nanotube-polyimide nanocomposites, Sensors and Actuators A: Physical 295 (2019) 336–342. https://doi.org/10.1016/j.sna.2019.06.017.

[183] G. Ponraj, S.K. Kirthika, C.M. Lim, H. Ren, Soft Tactile Sensors With Inkjet-Printing Conductivity and Hydrogel Biocompatibility for Retractors in Cadaveric Surgical Trials, IEEE Sensors J. 18 (2018) 9840–9847. https://doi.org/10.1109/JSEN.2018.2871242.

[184] L. Lo, H. Shi, H. Wan, Z. Xu, X. Tan, C. Wang, Inkjet-Printed Soft Resistive Pressure Sensor Patch for Wearable Electronics Applications, Adv Materials Technologies 5 (2020) 1900717. https://doi.org/10.1002/admt.201900717.

[185] Y.-M. Fu, M.-C. Chou, Y.-T. Cheng, E.B. Secor, M.C. Hersam, An inkjet printed piezoresistive back-to-back graphene tactile sensor for endosurgical palpation applications, in: 2017 IEEE 30th International Conference on Micro Electro Mechanical Systems (MEMS), IEEE, Las Vegas, NV, USA, 2017: pp. 612–615. https://doi.org/10.1109/MEMSYS.2017.7863482.

[186] H. Ervasti, T. Järvinen, O. Pitkänen, É. Bozó, J. Hiitola-Keinänen, O.-H. Huttunen, J. Hiltunen, K. Kordas, Inkjet-Deposited Single-Wall Carbon Nanotube Micropatterns on Stretchable PDMS-Ag Substrate–Electrode Structures for Piezoresistive Strain Sensing, ACS Appl. Mater. Interfaces 13 (2021) 27284–27294. https://doi.org/10.1021/acsami.1c04397.

[187] A. Salim, S. Lim, Review of Recent Inkjet-Printed Capacitive Tactile Sensors, Sensors 17 (2017) 2593. https://doi.org/10.3390/s17112593.

[188] S. Ma, F. Ribeiro, K. Powell, J. Lutian, C. Møller, T. Large, J. Holbery, Fabrication of Novel Transparent Touch Sensing Device via Drop-on-Demand Inkjet Printing Technique, ACS Appl. Mater. Interfaces 7 (2015) 21628–21633. https://doi.org/10.1021/acsami.5b04717.

[189] B. Ando, S. Baglio, V. Marletta, A. Pistorio, A contactless inkjet printed passive touch sensor, in: 2014 IEEE International Instrumentation and Measurement Technology Conference (I2MTC) Proceedings, IEEE, Montevideo, Uruguay, 2014: pp. 1638–1642. https://doi.org/10.1109/I2MTC.2014.6861023.

Thèse accessible à l'adresse : https://theses.insa-lyon.fr/publication/2023ISAL0114/these.pdf © [L. Diatezo], [2023], INSA Lyon, tous droits réservés

[190] A. Albrecht, M. Trautmann, M. Becherer, P. Lugli, A. Rivadeneyra, Shear-Force Sensors on Flexible Substrates Using Inkjet Printing, Journal of Sensors 2019 (2019) 1–11. https://doi.org/10.1155/2019/1864239.

[191] Y. Peng, S. Xiao, J. Yang, J. Lin, W. Yuan, W. Gu, X. Wu, Z. Cui, The elastic microstructures of inkjet printed polydimethylsiloxane as the patterned dielectric layer for pressure sensors, Applied Physics Letters 110 (2017) 261904. https://doi.org/10.1063/1.4990528.

[192] H. Ling, R. Chen, Q. Huang, F. Shen, Y. Wang, X. Wang, Transparent, flexible and recyclable nanopaper-based touch sensors fabricated via inkjet-printing, Green Chem. 22 (2020) 3208–3215. https://doi.org/10.1039/D0GC00658K.

[193] S. Choi, S. Eom, M.M. Tentzeris, S. Lim, Inkjet-Printed Electromagnet-Based Touchpad Using Spiral Resonators, J. Microelectromech. Syst. 25 (2016) 947–953. https://doi.org/10.1109/JMEMS.2016.2593956.

[194] T. Yun, S. Eom, S. Lim, Paper-Based Capacitive Touchpad Using Home Inkjet Printer, J. Display Technol., JDT 12 (2016) 1411–1416.

[195] L. Yang, A. Rida, R. Vyas, M.M. Tentzeris, RFID Tag and RF Structures on a Paper Substrate Using Inkjet-Printing Technology, IEEE Trans. Microwave Theory Techn. 55 (2007) 2894–2901. https://doi.org/10.1109/TMTT.2007.909886.

[196] S.M.Z. Hossain, R.E. Luckham, A.M. Smith, J.M. Lebert, L.M. Davies, R.H. Pelton, C.D.M. Filipe, J.D. Brennan, Development of a Bioactive Paper Sensor for Detection of Neurotoxins Using Piezoelectric Inkjet Printing of Sol−Gel-Derived Bioinks, Anal. Chem. 81 (2009) 5474–5483. https://doi.org/10.1021/ac900660p.

[197] K.-H. Choi, J. Yoo, C.K. Lee, S.-Y. Lee, All-inkjet-printed, solid-state flexible supercapacitors on paper, Energy Environ. Sci. 9 (2016) 2812–2821. https://doi.org/10.1039/C6EE00966B.

[198] J.-L. Zhuang, D. Ar, X.-J. Yu, J.-X. Liu, A. Terfort, Patterned Deposition of Metal-Organic Frameworks onto Plastic, Paper, and Textile Substrates by Inkjet Printing of a Precursor Solution, Adv. Mater. 25 (2013) 4631–4635. https://doi.org/10.1002/adma.201301626.

[199] R. Mikkonen, A. Koivikko, T. Vuorinen, V. Sariola, M. Mantysalo, Inkjet-Printed, Nanofiber-Based Soft Capacitive Pressure Sensors for Tactile Sensing, IEEE Sensors J. 21 (2021) 26286–26293. https://doi.org/10.1109/JSEN.2021.3085128.

[200] I. Basak, G. Nowicki, B. Ruttens, D. Desta, J. Prooth, M. Jose, S. Nagels, H.-G. Boyen, J. D'Haen, M. Buntinx, W. Deferme, Inkjet Printing of PEDOT:PSS Based Conductive Patterns for 3D Forming Applications, Polymers 12 (2020) 2915. https://doi.org/10.3390/polym12122915.

[201] X. Wang, Z. Liu, T. Zhang, Flexible Sensing Electronics for Wearable/Attachable Health Monitoring, Small 13 (2017) 1602790. https://doi.org/10.1002/smll.201602790.

[202] T. Sekine, R. Sugano, T. Tashiro, J. Sato, Y. Takeda, H. Matsui, D. Kumaki, F. Domingues Dos Santos, A. Miyabo, S. Tokito, Fully Printed Wearable Vital Sensor for Human Pulse Rate Monitoring using Ferroelectric Polymer, Sci Rep 8 (2018) 4442. https://doi.org/10.1038/s41598-018-22746-3.

[203] S. Pal, Y.-Z. Su, Y.-W. Chen, C.-H. Yu, C.-W. Kung, S.-S. Yu, 3D Printing of Metal-Organic Framework-Based Ionogels: Wearable Sensors with Colorimetric and Mechanical Responses, ACS Appl Mater Interfaces 14 (2022) 28247–28257. https://doi.org/10.1021/acsami.2c02690.

[204] K.L. Montero, M.-M. Laurila, M. Mantysalo, All Printed Flexible Piezoelectric Pressure Sensor with Interdigitated Electrodes, in: 2020 IEEE 8th Electronics System-Integration Technology Conference (ESTC), IEEE, Tønsberg, Vestfold, Norway, 2020: pp. 1–6. https://doi.org/10.1109/ESTC48849.2020.9229777.

Thèse accessible à l'adresse : https://theses.insa-lyon.fr/publication/2023ISAL0114/these.pdf © [L. Diatezo], [2023], INSA Lyon, tous droits réservés

[205] D. Thuau, K. Kallitsis, F.D. Dos Santos, G. Hadziioannou, All inkjet-printed piezoelectric electronic devices: energy generators, sensors and actuators, J. Mater. Chem. C 5 (2017) 9963–9966. https://doi.org/10.1039/C7TC02558K.

[206] C. Graßmann, T. Grethe, L. van Langenhove, A. Schwarz-Pfeiffer, Digital printing of electroluminescent devices on textile substrates, Journal of Engineered Fibers and Fabrics 14 (2019) 155892501986162. https://doi.org/10.1177/1558925019861624.

[207] M. de Vos, R. Torah, S. Beeby, J. Tudor, Functional Electronic Screen-printing – Electroluminescent Lamps on Fabric, Procedia Engineering 87 (2014) 1513–1516. https://doi.org/10.1016/j.proeng.2014.11.586.

[208] X. Tao, Smart fibres, fabrics and clothing: fundamentals and applications, Elsevier, 2001. https://books.google.com/books?hl=fr&lr=&id=plWkAgAAQBAJ&oi=fnd&pg=PP1&dq=X.+Tao,+Smart+Fibres,+Fabrics+and+Clothing:+Fundamentals+and+Applications,+Woodhead+Publishing,+2001&ots=uV_AEUgnYs&sig=HwWBbuvFz80x1-WcaozVwtr_ULs (accessed October 4, 2023).

[209] J.C. Jagt, Reliability of electrically conductive adhesive joints for surface mount applications: a summary of the state of the art, IEEE Trans. Comp., Packag., Manufact. Technol. A 21 (1998) 215–225. https://doi.org/10.1109/95.705467.

[210] K. Yang, R. Torah, Y. Wei, S. Beeby, J. Tudor, Waterproof and durable screen printed silver conductive tracks on textiles, Textile Research Journal 83 (2013) 2023–2031. https://doi.org/10.1177/0040517513490063.

[211] H. Hong, J. Hu, X. Yan, Effect of the basic surface properties of woven lining fabric on printing precision and electrical performance of screen-printed conductive lines, Textile Research Journal 90 (2020) 1212–1223. https://doi.org/10.1177/0040517519888251.

[212] M. Gajadhur, M. Regulska, Mechanical and light resistance of flexographic conductive ink films intended for printed electronics, Dyes and Pigments 178 (2020) 108381. https://doi.org/10.1016/j.dyepig.2020.108381.

[213] S. Merilampi, T. Laine-Ma, P. Ruuskanen, The characterization of electrically conductive silver ink patterns on flexible substrates, Microelectronics Reliability 49 (2009) 782–790. https://doi.org/10.1016/j.microrel.2009.04.004.

[214] M. Petru, A. Ali, A.S. Khan, P. Srb, L. Kucera, J. Militky, Flexible Coated Conductive Textiles as Ohmic Heaters in Car Seats, Applied Sciences 13 (2023) 6874. https://doi.org/10.3390/app13126874.

[215] A. Claypole, J. Claypole, J. Leeder, G. Stevens, F. Johnson, N. Bezodis, M. Parker, T. Claypole, D. Gethin, L. Kilduff, Large area, stretchable, wearable, screen-printed carbon heaters for use in elite sport, J Coat Technol Res 20 (2023) 261–273. https://doi.org/10.1007/s11998-022-00666-2.

[216] P.S. Pillai, B.S. Athira, H. Varghese, S. Agarwal, B. Kumar, R. Alagirusamy, A. Das, K.P. Surendran, A. Chandran, A resistive ink based all-printed fabric heater integrated wearable thermotherapy device, J Mater Sci: Mater Electron 34 (2023) 1261. https://doi.org/10.1007/s10854-023-10665-7.

[217] H. Nakashima, M.J. Higgins, C. O'Connell, K. Torimitsu, G.G. Wallace, Liquid Deposition Patterning of Conducting Polymer Ink onto Hard and Soft Flexible Substrates via Dip-Pen Nanolithography, Langmuir 28 (2012) 804–811. https://doi.org/10.1021/la203356s.

[218] S. Glatzel, Z. Schnepp, C. Giordano, From Paper to Structured Carbon Electrodes by Inkjet Printing, Angew. Chem. Int. Ed. 52 (2013) 2355–2358. https://doi.org/10.1002/anie.201207693.

[219] W.R. Small, M. in het Panhuis, Inkjet Printing of Transparent, Electrically Conducting Single-Walled Carbon-Nanotube Composites, Small 3 (2007) 1500–1503. https://doi.org/10.1002/smll.200700110.

Thèse accessible à l'adresse : https://theses.insa-lyon.fr/publication/2023ISAL0114/these.pdf © [L. Diatezo], [2023], INSA Lyon, tous droits réservés

[220] S.B. Walker, J.A. Lewis, Reactive Silver Inks for Patterning High-Conductivity Features at Mild Temperatures, J. Am. Chem. Soc. 134 (2012) 1419–1421. https://doi.org/10.1021/ja209267c.

[221] M. Zenou, L. Grainger, Additive manufacturing of metallic materials, in: Additive Manufacturing, Elsevier, 2018: pp. 53–103. https://doi.org/10.1016/B978-0-12-812155-9.00003-7.

[222] W. Barthel, F. Markwardt, Aggregation of blood platelets by adrenaline and its uptake, Biochem Pharmacol 24 (1975) 1903–1904. https://doi.org/10.1016/0006-2952(75)90415-3.

[223] E. Mbise, T. Dias, W. Hurley, Design and manufacture of heated textiles, in: Electronic Textiles, Elsevier, 2015: pp. 117–132. https://doi.org/10.1016/B978-0-08-100201-8.00007-2.

[224] V.-C. Nguyen, M.-Q. Le, A. Fimbel, S. Bernadet, Y. Hebrard, J.-F. Mogniotte, J.-F. Capsal, P.-J. Cottinet, Printing smart coating of piezoelectric composite for application in condition monitoring of bearings, Materials & Design 215 (2022) 110529. https://doi.org/10.1016/j.matdes.2022.110529.

[225] C. Carbone, M. Benwadih, G. D'Ambrogio, M.-Q. Le, J.-F. Capsal, P.-J. Cottinet, Influence of Matrix and Surfactant on Piezoelectric and Dielectric Properties of Screen-Printed BaTiO3/PVDF Composites, Polymers 13 (2021) 2166. https://doi.org/10.3390/polym13132166.

[226] Z. Xiang, V. Nguyen, B. Ducharne, N. Della Schiava, J. Capsal, P. Cottinet, M. Le, 3D Printing of Flexible Composites via Magnetophoresis: Toward Medical Application Based on Low-Frequency Induction Heating Effect, Macromol. Mater. Eng. 306 (2021) 2100211. https://doi.org/10.1002/mame.202100211.

[227] L. Diatezo, M.-Q. Le, C. Tonellato, L. Puig, J.-F. Capsal, P.-J. Cottinet, Development and Optimization of 3D-Printed Flexible Electronic Coatings: A New Generation of Smart Heating Fabrics for Automobile Applications, Micromachines 14 (2023) 762. https://doi.org/10.3390/mi14040762.

[228] O. Isaac, K. Thiemer, [Biochemical studies on camomile components/III. In vitro studies about the antipeptic activity of (--)-alpha-bisabolol (author's transl)], Arzneimittelforschung 25 (1975) 1352–1354.

[229] J.-H. Ahn, J.-H. Choi, C.-Y. Lee, Electrical evaluations of anisotropic conductive film manufactured by electrohydrodynamic ink jet printing technology, Organic Electronics 78 (2020) 105561. https://doi.org/10.1016/j.orgel.2019.105561.

[230] A. Pajor-Świerzy, Y. Farraj, A. Kamyshny, S. Magdassi, Air stable copper-silver core-shell submicron particles: Synthesis and conductive ink formulation, Colloids and Surfaces A: Physicochemical and Engineering Aspects 521 (2017) 272–280. https://doi.org/10.1016/j.colsurfa.2016.08.026.

[231] W. Li, Q. Sun, L. Li, J. Jiu, X.-Y. Liu, M. Kanehara, T. Minari, K. Suganuma, The rise of conductive copper inks: challenges and perspectives, Applied Materials Today 18 (2020) 100451. https://doi.org/10.1016/j.apmt.2019.100451.

[232] T. Araki, T. Sugahara, J. Jiu, S. Nagao, M. Nogi, H. Koga, H. Uchida, K. Shinozaki, K. Suganuma, Cu Salt Ink Formulation for Printed Electronics using Photonic Sintering, Langmuir 29 (2013) 11192–11197. https://doi.org/10.1021/la402026r.

[233] A. Pajor-Świerzy, Y. Farraj, A. Kamyshny, S. Magdassi, Effect of carboxylic acids on conductivity of metallic films formed by inks based on copper@silver core-shell particles, Colloids and Surfaces A: Physicochemical and Engineering Aspects 522 (2017) 320–327. https://doi.org/10.1016/j.colsurfa.2017.03.019.

[234] S.J. Kim, J. Lee, Y.-H. Choi, D.-H. Yeon, Y. Byun, Effect of copper concentration in printable copper inks on film fabrication, Thin Solid Films 520 (2012) 2731–2734. https://doi.org/10.1016/j.tsf.2011.11.056.

Thèse accessible à l'adresse : https://theses.insa-lyon.fr/publication/2023ISAL0114/these.pdf © [L. Diatezo], [2023], INSA Lyon, tous droits réservés

[235] R. Dharmadasa, M. Jha, D.A. Amos, T. Druffel, Room Temperature Synthesis of a Copper Ink for the Intense Pulsed Light Sintering of Conductive Copper Films, ACS Appl. Mater. Interfaces 5 (2013) 13227–13234. https://doi.org/10.1021/am404226e.

[236] Y. Aleeva, B. Pignataro, Recent advances in upscalable wet methods and ink formulations for printed electronics, J. Mater. Chem. C 2 (2014) 6436–6453. https://doi.org/10.1039/C4TC00618F.

[237] J.T. Bendler, Handbook of Polycarbonate Science and Technology, CRC Press, 1999.

[238] A. Davis, J.H. Golden, Stability of Polycarbonate, Journal of Macromolecular Science, Part C 3 (1969) 49–68. https://doi.org/10.1080/15583726908545896.

[239] A. Malik, R. Magisetty, V. Kumar, A. Shukla, B. Kandasubramanian, Dielectric and conductivity investigation of polycarbonate-copper phthalocyanine electrospun nonwoven fibres for electrical and electronic application, Polymer-Plastics Technology and Materials 59 (2020) 154–168. https://doi.org/10.1080/25740881.2019.1625390.

[240] W. Yu, E. Maynard, V. Chiaradia, M.C. Arno, A.P. Dove, Aliphatic Polycarbonates from Cyclic Carbonate Monomers and Their Application as Biomaterials, Chem. Rev. 121 (2021) 10865–10907. https://doi.org/10.1021/acs.chemrev.0c00883.

[241] J. Feng, R.-X. Zhuo, X.-Z. Zhang, Construction of functional aliphatic polycarbonates for biomedical applications, Progress in Polymer Science 37 (2012) 211–236. https://doi.org/10.1016/j.progpolymsci.2011.07.008.

[242] T. Hotaka, F. Kondo, R. Niimi, F. Togashi, Y. Morita, Industrialization of automotive glazing by polycarbonate and hard-coating, Polym J 51 (2019) 1249–1263. https://doi.org/10.1038/s41428-019-0240-1.

[243] M. Gohil, G. Joshi, Chapter 18 - Perspective of polycarbonate composites and blends properties, applications, and future development: A review, in: T. Altalhi, Inamuddin (Eds.), Green Sustainable Process for Chemical and Environmental Engineering and Science, Elsevier, 2022: pp. 393–424. https://doi.org/10.1016/B978-0-323-99643-3.00012-7.

[244] H. Kawai, The Piezoelectricity of Poly (vinylidene Fluoride), Jpn. J. Appl. Phys. 8 (1969) 975. https://doi.org/10.1143/JJAP.8.975.

[245] M. Oshiki, E. Fukada, Inverse piezoelectric effect and electrostrictive effect in polarized poly(vinylidene fluoride) films, J Mater Sci 10 (1975) 1–6. https://doi.org/10.1007/BF00541025.

[246] L. Ibos, A. Bernès, C. Lacabanne, Annealing or Storage Influence on Pyroelectricity of Ferroelectric PVDF and P(VDF-TrFE) Copolymer, Ferroelectrics 320 (2005) 15–21. https://doi.org/10.1080/00150190590966739.

[247] A.J. Lovinger, Ferroelectric Polymers, Science 220 (1983) 1115–1121. https://doi.org/10.1126/science.220.4602.1115.

[248] S.W. Or, H.L.W. Chan, C.L. Choy, P(VDF-TrFE) copolymer acoustic emission sensors, Sensors and Actuators A: Physical 80 (2000) 237–241. https://doi.org/10.1016/S0924-4247(99)00305-2.

[249] S.S. Guo, W.P. Li, K. Li, H.L.W. Chan, X.-Z. Zhao, C.L. Choy, Electron-irradiated electrostrictive P(VDF–TrFE) copolymer transducers, Sensors and Actuators A: Physical 112 (2004) 134–141. https://doi.org/10.1016/j.sna.2003.10.030.

[250] N. Snis, E. Edqvist, U. Simu, S. Johansson, Monolithic fabrication of multilayer P(VDF-TrFE) cantilevers, Sensors and Actuators A: Physical 144 (2008) 314–320. https://doi.org/10.1016/j.sna.2008.01.004.

Thèse accessible à l'adresse : https://theses.insa-lyon.fr/publication/2023ISAL0114/these.pdf © [L. Diatezo], [2023], INSA Lyon, tous droits réservés

[251] K.H. Lee, K. Lee, M.S. Oh, J.-M. Choi, S. Im, S. Jang, E. Kim, Flexible high mobility pentacene transistor with high-k/low-k double polymer dielectric layer operating at −5V, Organic Electronics 10 (2009) 194–198. https://doi.org/10.1016/j.orgel.2008.09.005.

[252] K. Müller, I. Paloumpa, K. Henkel, D. Schmeißer, Organic thin film transistors with polymer high-k dielectric insulator, Materials Science and Engineering: C 26 (2006) 1028–1031. https://doi.org/10.1016/j.msec.2005.09.057.

[253] H. Jiang, J. Yang, F. Xu, Q. Wang, W. Liu, Q. Chen, C. Wang, X. Zhang, G. Zhu, VDF-content-guided selection of piezoelectric P(VDF-TrFE) films in sensing and energy harvesting applications, Energy Conversion and Management 211 (2020) 112771. https://doi.org/10.1016/j.enconman.2020.112771.

[254] S. Majumdar, Ultrafast switching and linear conductance modulation in ferroelectric tunnel junctions via P(VDF-TrFE) morphology control, Nanoscale 13 (2021) 11270–11278. https://doi.org/10.1039/D1NR01722E.

[255] B. Li, C. Cai, Y. Liu, F. Wang, B. Yang, Q. Li, P. Zhang, B. Deng, P. Hou, W. Liu, Ultrasensitive mechanical/thermal response of a P(VDF-TrFE) sensor with a tailored network interconnection interface, Nat Commun 14 (2023) 4000. https://doi.org/10.1038/s41467-023-39476-4.

[256] Z. Dang, F. Guo, Z. Wu, K. Jin, J. Hao, Interface Engineering and Device Applications of 2D Ultrathin Film/Ferroelectric Copolymer P(VDF-TrFE), Advanced Physics Research 2 (2023) 2200038. https://doi.org/10.1002/apxr.202200038.

[257] J.-F. Capsal, E. Dantras, C. Lacabanne, Molecular mobility interpretation of the dielectric relaxor behavior in fluorinated copolymers and terpolymers, Journal of Non-Crystalline Solids 363 (2013) 20–25.

[258] T.C. Chung, A. Petchsuk, Synthesis and properties of ferroelectric fluoroterpolymers with curie transition at ambient temperature, Macromolecules 35 (2002) 7678–7684. https://doi.org/10.1021/ma020504c.

[259] R.J. Klein, F. Xia, Q.M. Zhang, F. Bauer, Influence of composition on relaxor ferroelectric and electromechanical properties of poly(vinylidene fluoride-trifluoroethylene- chlorofluoroethylene), Journal of Applied Physics 97 (2005) 094105. https://doi.org/10.1063/1.1882769.

[260] A. Fimbel, T. Abensur, M.-Q. Le, J.-F. Capsal, P.-J. Cottinet, Accurate Electroadhesion Force Measurements of Electrostrictive Polymers: The Case of High Performance Plasticized Terpolymers, Polymers 14 (2022) 24. https://doi.org/10.3390/polym14010024.

[261] N. Della Schiava, M.-Q. Le, J. Galineau, F. Domingues Dos Santos, P.-J. Cottinet, J.-F. Capsal, Influence of Plasticizers on the Electromechanical Behavior of a P(VDF-TrFE-CTFE) Terpolymer: Toward a High Performance of Electrostrictive Blends, J. Polym. Sci. Part B: Polym. Phys. 55 (2017) 355–369. https://doi.org/10.1002/polb.24280.

[262] J.-F. Capsal, J. Galineau, M.-Q. Le, F. Domingues Dos Santos, P.-J. Cottinet, Enhanced electrostriction based on plasticized relaxor ferroelectric P (VDF-TrFE-CFE/CTFE) blends, Journal of Polymer Science Part B: Polymer Physics 53 (2015) 1368–1379.

[263] N. Della Schiava, F. Pedroli, K. Thetpraphi, A. Flocchini, M.-Q. Le, P. Lermusiaux, J.-F. Capsal, P.-J. Cottinet, Effect of beta-based sterilization on P(VDF-TrFE-CFE) terpolymer for medical applications, Sci Rep 10 (2020) 8805. https://doi.org/10.1038/s41598-020-65893-2.

[264] K. Thetpraphi, W. Kanlayakan, S. Chaipo, G. Moretto, J. Kuhn, D. Audigier, M.Q. Le, P.-J. Cottinet, L. Petit, J.-F. Capsal, 3D-Printed Electroactive Polymer Force-Actuator for Large and High Precise Optical Mirror Applications, Additive Manufacturing (2021) 102199. https://doi.org/10.1016/j.addma.2021.102199.

Thèse accessible à l'adresse : https://theses.insa-lyon.fr/publication/2023ISAL0114/these.pdf © [L. Diatezo], [2023], INSA Lyon, tous droits réservés

[265] Q. Liu, M.Q. Le, C. Richard, R. Liang, P.-J. Cottinet, J.-F. Capsal, Enhanced pseudo-piezoelectric dynamic force sensors based on inkjet-printed electrostrictive terpolymer, Organic Electronics 67 (2019) 259–271. https://doi.org/10.1016/j.orgel.2019.01.028.

[266] N. Della Schiava, K. Thetpraphi, M.-Q. Le, P. Lermusiaux, A. Millon, J.-F. Capsal, P.-J. Cottinet, Enhanced Figures of Merit for a High-Performing Actuator in Electrostrictive Materials, Polymers 10 (2018) 263. https://doi.org/10.3390/polym10030263.

[267] K. Thetpraphi, M.Q. Le, A. Houachtia, P.-J. Cottinet, L. Petit, D. Audigier, J. Kuhn, G. Moretto, J.-F. Capsal, Surface Correction Control Based on Plasticized Multilayer P(VDF-TrFE-CFE) Actuator—Live Mirror, Advanced Optical Materials 7 (2019) 1900210. https://doi.org/10.1002/adom.201900210.

[268] F. Ganet, M.Q. Le, J.F. Capsal, P. Lermusiaux, L. Petit, A. Millon, P.J. Cottinet, Development of a smart guide wire using an electrostrictive polymer: option for steerable orientation and force feedback, Sci Rep 5 (2015). https://doi.org/10.1038/srep18593.

[269] X. Zhang, F. Wang, Recent advances in flexible alternating current electroluminescent devices, APL Materials 9 (2021) 030701. https://doi.org/10.1063/5.0040109.

[270] M. de Vos, R. Torah, S. Beeby, J. Tudor, Functional Electronic Screen-printing – Electroluminescent Lamps on Fabric, Procedia Engineering 87 (2014) 1513–1516. https://doi.org/10.1016/j.proeng.2014.11.586.

[271] C. Graßmann, T. Grethe, L. van Langenhove, A. Schwarz-Pfeiffer, Digital printing of electroluminescent devices on textile substrates, Journal of Engineered Fibers and Fabrics 14 (2019) 155892501986162. https://doi.org/10.1177/1558925019861624.

[272] B. Bonev, A. Stoynova, I. Zhivkov, Thermal Monitoring of Flexible ZnS-based Screen-Printed Electroluminescence Structures Subjected to Accelerated Ageing, in: 2020 43rd International Spring Seminar on Electronics Technology (ISSE), IEEE, Demanovska Valley, Slovakia, 2020: pp. 1–6. https://doi.org/10.1109/ISSE49702.2020.9121155.

[273] J. Wang, C. Yan, K.J. Chee, P.S. Lee, Highly Stretchable and Self-Deformable Alternating Current Electroluminescent Devices, Adv. Mater. 27 (2015) 2876–2882. https://doi.org/10.1002/adma.201405486.

[274] G. D'Ambrogio, O. Zahhaf, Y. Hebrard, M.Q. Le, P.-J. Cottinet, J.-F. Capsal, Micro-Structuration of Piezoelectric Composites Using Dielectrophoresis: Toward Application in Condition Monitoring of Bearings, Advanced Engineering Materials 23 (2021) 2000773. https://doi.org/10.1002/adem.202000773.

[275] X. Zhang, M.-Q. Le, O. Zahhaf, J.-F. Capsal, P.-J. Cottinet, L. Petit, Enhancing dielectric and piezoelectric properties of micro-ZnO/PDMS composite-based dielectrophoresis, Materials & Design 192 (2020) 108783. https://doi.org/10.1016/j.matdes.2020.108783.

[276] F. Pedroli, A. Marrani, M.-Q. Le, C. Froidefond, P.-J. Cottinet, J.-F. Capsal, Processing optimization: A way to improve the ionic conductivity and dielectric loss of electroactive polymers, J. Polym. Sci. Part B: Polym. Phys. 56 (2018) 1164–1173. https://doi.org/10.1002/polb.24636.

[277] R.D. Bland, T.L. Clarke, L.B. Harden, Rapid infusion of sodium bicarbonate and albumin into high-risk premature infants soon after birth: a controlled, prospective trial, Am J Obstet Gynecol 124 (1976) 263–267. https://doi.org/10.1016/0002-9378(76)90154-x.

[278] H.R. Mendez-Rossal, G.M. Wallner, Printability and Properties of Conductive Inks on Primer-Coated Surfaces, International Journal of Polymer Science 2019 (2019) 1–8. https://doi.org/10.1155/2019/3874181.

Thèse accessible à l'adresse : https://theses.insa-lyon.fr/publication/2023ISAL0114/these.pdf © [L. Diatezo], [2023], INSA Lyon, tous droits réservés

[279] T. Liimatta, E. Halonen, H. Sillanpaa, J. Niittynen, M. Mantysalo, Inkjet printing in manufacturing of stretchable interconnects, in: 2014 IEEE 64th Electronic Components and Technology Conference (ECTC), IEEE, Orlando, FL, USA, 2014: pp. 151–156. https://doi.org/10.1109/ECTC.2014.6897281.

[280] Y.Z.N. Htwe, W.S. Chow, G. Suriati, A.A. Thant, M. Mariatti, Properties enhancement of graphene and chemical reduction silver nanoparticles conductive inks printed on polyvinyl alcohol (PVA) substrate, Synthetic Metals 256 (2019) 116120. https://doi.org/10.1016/j.synthmet.2019.116120.

[281] N. Athanasopoulos, A. Baltopoulos, M. Matzakou, A. Vavouliotis, V. Kostopoulos, Electrical conductivity of polyurethane/MWCNT nanocomposite foams, Polym Compos 33 (2012) 1302–1312. https://doi.org/10.1002/pc.22256.

[282] P.-Y. Tsai, T.-E. Chen, Y.-L. Lee, Development and Characterization of Anticorrosion and Antifriction Properties for High Performance Polyurethane/Graphene Composite Coatings, Coatings 8 (2018) 250. https://doi.org/10.3390/coatings8070250.

[283] Y. Yang, Thermal conductivity, in: Physical Properties of Polymers Handbook, Springer, 2007: pp. 155–163.

[284] Overview of materials for Thermoset Polyurethane Foam, Unreinforced, (n.d.). https://www.matweb.com/search/DataSheet.aspx?MatGUID=91d44cae736e4b36bcba94720654eeae&ckck=1 (accessed June 14, 2022).

[285] Technical information BASF_E-CPI_1015e_Butylglycol_Acetate-3.pdf, (2020).

[286] N. Athanasopoulos, A. Baltopoulos, M. Matzakou, A. Vavouliotis, V. Kostopoulos, Electrical conductivity of polyurethane/MWCNT nanocomposite foams, Polymer Composites 33 (2012) 1302–1312. https://doi.org/10.1002/pc.22256.

[287] Carbon - Thermal Properties - Melting Point - Thermal Conductivity - Expansion, Material Properties (2020). https://material-properties.org/carbon-thermal-properties-melting-point-thermal-conductivity-expansion/ (accessed April 28, 2022).

[288] J. Carvill, 3 - Thermodynamics and heat transfer, in: Mechanical Engineer's Data Handbook, Butterworth-Heinemann, Oxford, 1993: pp. 102–145. https://doi.org/10.1016/B978-0-08-051135-1.50008-X.

[289] Heat Capacity, (n.d.). https://www2.chem.wisc.edu/deptfiles/genchem/netorial/modules/thermodynamics/enthalpy/enthalpy3.htm (accessed May 3, 2022).

[290] Specific Heat Capacity of Metals Table Chart, (n.d.). https://www.engineersedge.com/materials/specific_heat_capacity_of_metals_13259.htm (accessed May 3, 2022).

[291] What Makes Metals Conductive?, ThoughtCo (n.d.). https://www.thoughtco.com/electrical-conductivity-in-metals-2340117 (accessed May 2, 2022).

[292] J. Bardeen, Electrical Conductivity of Metals, Journal of Applied Physics 11 (1940) 88–111. https://doi.org/10.1063/1.1712751.

[293] D. Pantea, H. Darmstadt, S. Kaliaguine, L. Sümmchen, C. Roy, Electrical conductivity of thermal carbon blacks: Influence of surface chemistry, Carbon 39 (2001) 1147–1158. https://doi.org/10.1016/S0008-6223(00)00239-6.

[294] T.R. Anderson, T.A. Slotkin, Maturation of the adrenal medulla--IV. Effects of morphine, Biochem Pharmacol 24 (1975) 1469–1474. https://doi.org/10.1016/0006-2952(75)90020-9.

Thèse accessible à l'adresse : https://theses.insa-lyon.fr/publication/2023ISAL0114/these.pdf © [L. Diatezo], [2023], INSA Lyon, tous droits réservés

[295] N. Uvarov, Estimation of composites conductivity using a general mixing rule, Solid State Ionics 136–137 (2000) 1267–1272. https://doi.org/10.1016/S0167-2738(00)00585-3.

[296] T.R. Southwood, S. Khalaf, R.E. Sinden, The micro-organisms of tsetse flies, Acta Trop 32 (1975) 259–266.

[297] Z. Xiang, B. Ducharne, N. Della Schiava, J.-F. Capsal, P.-J. Cottinet, G. Coativy, P. Lermusiaux, M.Q. Le, Induction heating-based low-frequency alternating magnetic field: High potential of ferromagnetic composites for medical applications, Materials & Design 174 (2019) 107804. https://doi.org/10.1016/j.matdes.2019.107804.

[298] J. Wang, J.K. Carson, M.F. North, D.J. Cleland, A new structural model of effective thermal conductivity for heterogeneous materials with co-continuous phases, International Journal of Heat and Mass Transfer 51 (2008) 2389–2397. https://doi.org/10.1016/j.ijheatmasstransfer.2007.08.028.

[299] Editorial: Childhood poisoning: prevention and first-aid management, Br Med J 4 (1975) 483–484. https://doi.org/10.1136/bmj.4.5995.483.

[300] M. Jodal, D.A. Hallbäck, J. Svanvik, O. Lundgren, A method for the continuous study of net water transport in the feline small bowel, Acta Physiol Scand 95 (1975) 441–447. https://doi.org/10.1111/j.1748-1716.1975.tb10072.x.

[301] MATERIAUX ET PICES - VIEILLISSEMENT SUIVANT CYCLE CLIMATIQUE, D47 1309 G FR 12.07.(2013).

[302] K.J. Loh, D. Chang, Zinc oxide nanoparticle-polymeric thin films for dynamic strain sensing, J Mater Sci 46 (2011) 228–237. https://doi.org/10.1007/s10853-010-4940-3.

[303] H. Aglan, M. Calhoun, L. Allie, Effect of UV and hygrothermal aging on the mechanical performance of polyurethane elastomers, J. Appl. Polym. Sci. 108 (2008) 558–564. https://doi.org/10.1002/app.27049.

[304] A. Boubakri, K. Elleuch, N. Guermazi, H.F. Ayedi, Investigations on hygrothermal aging of thermoplastic polyurethane material, Materials & Design 30 (2009) 3958–3965. https://doi.org/10.1016/j.matdes.2009.05.038.

[305] A. Atalay, V. Sanchez, O. Atalay, D.M. Vogt, F. Haufe, R.J. Wood, C.J. Walsh, Batch Fabrication of Customizable Silicone-Textile Composite Capacitive Strain Sensors for Human Motion Tracking, Adv. Mater. Technol. 2 (2017) 1700136. https://doi.org/10.1002/admt.201700136.

[306] K. Moroi, T. Sato, Comparison between procaine and isocarboxazid metabolism in vitro by a liver microsomal amidase-esterase, Biochem Pharmacol 24 (1975) 1517–1521. https://doi.org/10.1016/0006-2952(75)90029-5.

[307] Product specifications Heating functions through the seat. 32-05-843 / --D, Renault (2015).

[308] X. Zhang, Characterization and structuration of piezoelectric ZnO-based composites : Toward medical applications, phdthesis, Université de Lyon, 2022. https://theses.hal.science/tel-03709331 (accessed September 29, 2023).

[309] M. Mokni, F. Pedroli, G. D'Ambrogio, M.-Q. Le, P.-J. Cottinet, J.-F. Capsal, High-Capacity, Fast-Response, and Photocapacitor-Based Terpolymer Phosphor Composite, Polymers 12 (2020) 349. https://doi.org/10.3390/polym12020349.

[310] X. Zhang, M.-Q. Le, V.-C. Nguyen, J.-F. Mogniotte, J.-F. Capsal, D. Grinberg, P.-J. Cottinet, L. Petit, Characterization of micro-ZnO/PDMS composite structured via dielectrophoresis – Toward medical application, Materials & Design 208 (2021) 109912. https://doi.org/10.1016/j.matdes.2021.109912.

Thèse accessible à l'adresse : https://theses.insa-lyon.fr/publication/2023ISAL0114/these.pdf © [L. Diatezo], [2023], INSA Lyon, tous droits réservés

[311] K. Pitchai, J. Chen, S. Birla, R. Gonzalez, D. Jones, J. Subbiah, A microwave heat transfer model for a rotating multi-component meal in a domestic oven: Development and validation, Journal of Food Engineering 128 (2014) 60–71. https://doi.org/10.1016/j.jfoodeng.2013.12.015.

[312] I.C. Ehrhart, P.E. Parker, W.J. Weidner, J.M. Dabney, J.B. Scott, F.J. Haddy, Coronary vascular and myocardial responses to carotid body stimulation in the dog, Am J Physiol 229 (1975) 754–760. https://doi.org/10.1152/ajplegacy.1975.229.3.754.

[313] A. Sihvola, [No title found], Subsurface Sensing Technologies and Applications 1 (2000) 393–415. https://doi.org/10.1023/A:1026511515005.

[314] H. Shahariar, I. Kim, H. Soewardiman, J.S. Jur, Inkjet Printing of Reactive Silver Ink on Textiles, ACS Appl. Mater. Interfaces 11 (2019) 6208–6216. https://doi.org/10.1021/acsami.8b18231.

[315] L. Xie, M. Mäntysalo, A.L. Cabezas, Y. Feng, F. Jonsson, L.-R. Zheng, Electrical performance and reliability evaluation of inkjet-printed Ag interconnections on paper substrates, Materials Letters 88 (2012) 68–72. https://doi.org/10.1016/j.matlet.2012.08.030.

[316] Z. Li, T. Le, Z. Wu, Y. Yao, L. Li, M. Tentzeris, K.-S. Moon, C.P. Wong, Rational Design of a Printable, Highly Conductive Silicone-based Electrically Conductive Adhesive for Stretchable Radio-Frequency Antennas, Adv. Funct. Mater. 25 (2015) 464–470. https://doi.org/10.1002/adfm.201403275.

[317] R. Faddoul, N. Reverdy-Bruas, A. Blayo, Formulation and screen printing of water based conductive flake silver pastes onto green ceramic tapes for electronic applications, Materials Science and Engineering: B 177 (2012) 1053–1066. https://doi.org/10.1016/j.mseb.2012.05.015.

[318] H. Hong, J. Hu, X. Yan, Effect of the basic surface properties of woven lining fabric on printing precision and electrical performance of screen-printed conductive lines, Textile Research Journal 90 (2020) 1212–1223. https://doi.org/10.1177/0040517519888251.

[319] T.-G. La, S. Qiu, D.K. Scott, R. Bakhtiari, J.W.P. Kuziek, K.E. Mathewson, J. Rieger, H.-J. Chung, Two-Layered and Stretchable e-Textile Patches for Wearable Healthcare Electronics, Adv. Healthcare Mater. 7 (2018) 1801033. https://doi.org/10.1002/adhm.201801033.

[320] R.T. Frankle, Nutrition education in the medical school curriculum: a proposal for action: a curriculum design, Am J Clin Nutr 29 (1976) 105–109. https://doi.org/10.1093/ajcn/29.1.105.

[321] L. Diatezo, M.-Q. Le, C. Tonellato, L. Puig, J.-F. Capsal, P.-J. Cottinet, Development and Optimization of 3D-Printed Flexible Electronic Coatings: A New Generation of Smart Heating Fabrics for Automobile Applications, Micromachines 14 (2023) 762. https://doi.org/10.3390/mi14040762.

[322] Y. Zhang, X. Chen, F. Liu, L. Li, J. Dai, T. Liu, Enhanced Coffee-Ring Effect via Substrate Roughness in Evaporation of Colloidal Droplets, Advances in Condensed Matter Physics 2018 (2018) 1–9. https://doi.org/10.1155/2018/9795654.

[323] Y. Li, Q. Yang, M. Li, Y. Song, Rate-dependent interface capture beyond the coffee-ring effect, Sci Rep 6 (2016) 24628. https://doi.org/10.1038/srep24628.

[324] L.D. Landau, J.S. Bell, M.J. Kearsley, L.P. Pitaevskii, E.M. Lifshitz, J.B. Sykes, Electrodynamics of Continuous Media, Elsevier, 2013.

[325] H. Looyenga, Dielectric constants of heterogeneous mixtures, Physica 31 (1965) 401–406. https://doi.org/10.1016/0031-8914(65)90045-5.

[326] A. Tommasi, M. Cocuzza, D. Perrone, C. Pirri, R. Mosca, M. Villani, N. Delmonte, A. Zappettini, D. Calestani, S. Marasso, Modeling, Fabrication and Testing of a Customizable Micromachined Hotplate for Sensor Applications, Sensors 17 (2016) 62. https://doi.org/10.3390/s17010062.

Thèse accessible à l'adresse : https://theses.insa-lyon.fr/publication/2023ISAL0114/these.pdf © [L. Diatezo], [2023], INSA Lyon, tous droits réservés

[327] P.G. Kosky, R.T. Balmer, W. Keat, G. Wise, eds., Exploring engineering: an introduction to engineering and design, Third edition, Elsevier/AP, Burlington, MA, 2013.

[328] Y. Yang, J. He, Q. Li, L. Gao, J. Hu, R. Zeng, J. Qin, S.X. Wang, Q. Wang, Self-healing of electrical damage in polymers using superparamagnetic nanoparticles, Nature Nanotech 14 (2019) 151–155. https://doi.org/10.1038/s41565-018-0327-4.

[329] N. Ida, Engineering electromagnetics, Springer, New York, 2014.

[330] F.P. Incropera, F.P. Incropera, eds., Fundamentals of heat and mass transfer, 6th ed, John Wiley, Hoboken, NJ, 2007.

[331] A. Gadeikytė, R. Barauskas, Investigation of influence of forced ventilation through 3D textile on heat exchange properties of the textile layer, J. Meas. Eng. 8 (2020) 72–78. https://doi.org/10.21595/jme.2020.21555.

[332] S. Zandi, P. Saxena, M. Razaghi, N.E. Gorji, Simulation of CZTSSe Thin-Film Solar Cells in COMSOL: Three-Dimensional Optical, Electrical, and Thermal Models, IEEE J. Photovoltaics 10 (2020) 1503–1507. https://doi.org/10.1109/JPHOTOV.2020.2999881.

[333] A.H. Ganie, A.A. Memon, M.A. Memon, A.M. Al-Bugami, K. Bhatti, I. Khan, Numerical analysis of laminar flow and heat transfer through a rectangular channel containing perforated plate at different angles, Energy Reports 8 (2022) 539–550. https://doi.org/10.1016/j.egyr.2021.11.232.

[334] Z. Xiang, M.Q. Le, P.-J. Cottinet, P. Griffiths, G.P. Baeza, J.-F. Capsal, P. Lermusiaux, N. Della Schiava, B. Ducharne, Development of anisotropic ferromagnetic composites for low-frequency induction heating technology in medical applications, Materials Today Chemistry 19 (2021) 100395. https://doi.org/10.1016/j.mtchem.2020.100395.

[335] M. Pope, H.P. Kallmann, P. Magnante, Electroluminescence in Organic Crystals, The Journal of Chemical Physics 38 (1963) 2042–2043. https://doi.org/10.1063/1.1733929.

[336] C.W. Tang, S.A. VanSlyke, Organic electroluminescent diodes, Applied Physics Letters 51 (1987) 913–915. https://doi.org/10.1063/1.98799.

[337] J.H. Burroughes, D.D.C. Bradley, A.R. Brown, R.N. Marks, K. Mackay, R.H. Friend, P.L. Burns, A.B. Holmes, Light-emitting diodes based on conjugated polymers, Nature 347 (1990) 539–541. https://doi.org/10.1038/347539a0.

[338] O. Pras, Utilisation de cellulose pour l'élaboration de matériaux photoluminescents ou conducteurs, phdthesis, Université de Grenoble, 2011. https://theses.hal.science/tel-00685846 (accessed October 11, 2023).

[339] P. Hu, Y. Shen, Y. Guan, X. Zhang, Y. Lin, Q. Zhang, C.W. Nan, Topological-structure modulated polymer nanocomposites exhibiting highly enhanced dielectric strength and energy density, Advanced Functional Materials 24 (2014) 3172–3178. https://doi.org/10.1002/adfm.201303684.

[340] Y. Wang, J. Chen, Y. Li, Y. Niu, Q. Wang, H. Wang, Multilayered hierarchical polymer composites for high energydensity capacitors, Journal of Materials Chemistry A 7 (2019) 2965–2980.

[341] F. Pedroli, A. Flocchini, A. Marrani, M.-Q. Le, O. Sanseau, P.-J. Cottinet, J.-F. Capsal, Boosted energy-storage efficiency by controlling conduction loss of multilayered polymeric capacitors, Materials & Design 192 (2020) 108712. https://doi.org/10.1016/j.matdes.2020.108712.

[342] F. Pedroli, A. Marrani, M.-Q. Le, O. Sanseau, P.-J. Cottinet, J.-F. Capsal, Reducing leakage current and dielectric losses of electroactive polymers through electro-annealing for high-voltage actuation, RSC Adv. 9 (2019) 12823–12835. https://doi.org/10.1039/C9RA01469A.

Thèse accessible à l'adresse : https://theses.insa-lyon.fr/publication/2023ISAL0114/these.pdf © [L. Diatezo], [2023], INSA Lyon, tous droits réservés

[343] T. Tunkasiri, G. Rujijanagul, U. Intatha, K. Pengpat, K. Sutjarittangtham, S. Eitssayeam, Model for the dielectric constant for 0-3 piezoelectric-polymer composites, Ferroelectrics 502 (2016) 101–106. https://doi.org/10.1080/00150193.2016.1234910.

[344] H. Shim, B. Allabergenov, J. Kim, H.Y. Noh, H.-K. Lyu, M.-J. Lee, B. Choi, Highly Bright Flexible Electroluminescent Devices with Retroreflective Electrodes, Adv. Mater. Technol. 2 (2017) 1700040. https://doi.org/10.1002/admt.201700040.

[345] W. Nhuapeng, T. Tunkasiri, Properties of 0-3 Lead Zirconate Titanate-Polymer Composites Prepared in a Centrifuge, Journal of the American Ceramic Society 85 (2004) 700–702. https://doi.org/10.1111/j.1151-2916.2002.tb00154.x.

[346] R. Mitkus, M. Sinapius, Piezoelectric Ceramic/Photopolymer Composites Curable with UV Light: Viscosity, Curing Depth, and Dielectric Properties, J. Compos. Sci. 6 (2022) 212. https://doi.org/10.3390/jcs6070212.

[347] V.G. Zvyagin, M.V. Turbin, The study of initial-boundary value problems for mathematical models of the motion of Kelvin–Voigt fluids, J Math Sci 168 (2010) 157–308. https://doi.org/10.1007/s10958-010-9981-2.

[348] R. Lewandowski, B. Chorążyczewski, Identification of the parameters of the Kelvin–Voigt and the Maxwell fractional models, used to modeling of viscoelastic dampers, Computers & Structures 88 (2010) 1–17. https://doi.org/10.1016/j.compstruc.2009.09.001.

[349] XII. Colours in metal glasses and in metallic films, Phil. Trans. R. Soc. Lond. A 203 (1904) 385–420. https://doi.org/10.1098/rsta.1904.0024.

[350] G. Liang, Z. Liu, F. Mo, Z. Tang, H. Li, Z. Wang, V. Sarangi, A. Pramanick, J. Fan, C. Zhi, Self-healable electroluminescent devices, Light Sci Appl 7 (2018) 102. https://doi.org/10.1038/s41377-018-0096-8.

[351] A.G. Fischer, Electroluminescent Lines in ZnS Powder Particles, J. Electrochem. Soc. 110 (1963) 733. https://doi.org/10.1149/1.2425863.

[352] M. Godlewski, E. Guziewicz, V. Yu Ivanov, Zinc selenide and zinc telluride, in: D. Vij (Ed.), Handbook of Electroluminescent Materials, Taylor & Francis, 2004. https://doi.org/10.1201/9781420033410.ch3.

[353] S. Song, H. Shim, S.K. Lim, S.M. Jeong, Patternable and Widely Colour-Tunable Elastomer-Based Electroluminescent Devices, Sci Rep 8 (2018) 3331. https://doi.org/10.1038/s41598-018-21726-x.

[354] C.D. Brubaker, K.N. Newcome, G.K. Jennings, D.E. Adams, 3D-Printed alternating current electroluminescent devices, J. Mater. Chem. C 7 (2019) 5573–5578. https://doi.org/10.1039/C9TC00619B.

[355] S.M. Jeong, S. Song, S. Lee, N.Y. Ha, Color Manipulation of Mechanoluminescence from Stress-Activated Composite Films, Adv. Mater. 25 (2013) 6194–6200. https://doi.org/10.1002/adma.201301679.

[356] C.D. Brubaker, T.M. Frecker, J.R. McBride, K.R. Reid, G.K. Jennings, S.J. Rosenthal, D.E. Adams, Incorporation of fluorescent quantum dots for 3D printing and additive manufacturing applications, J. Mater. Chem. C 6 (2018) 7584–7593. https://doi.org/10.1039/C8TC02024H.

[357] B.J. Ash, R.W. Siegel, L.S. Schadler, Mechanical Behavior of Alumina/Poly(methyl methacrylate) Nanocomposites, Macromolecules 37 (2004) 1358–1369. https://doi.org/10.1021/ma0354400.

[358] S.M. Jeong, S. Song, H. Kim, Simultaneous dual-channel blue/green emission from electro-mechanically powered elastomeric zinc sulphide composite, Nano Energy 21 (2016) 154–161. https://doi.org/10.1016/j.nanoen.2016.01.012.

Thèse accessible à l'adresse : https://theses.insa-lyon.fr/publication/2023ISAL0114/these.pdf © [L. Diatezo], [2023], INSA Lyon, tous droits réservés

[359] D.K. Patel, B.-E. Cohen, L. Etgar, S. Magdassi, Fully 2D and 3D printed anisotropic mechanoluminescent objects and their application for energy harvesting in the dark, Mater. Horiz. 5 (2018) 708–714. https://doi.org/10.1039/C8MH00296G.

[360] S. Zhang, C.S. Tan, T.K.S. Wong, H. Su, R.J.W. Teo, Opto-impedance spectroscopy and equivalent circuit analyses of AC powder electroluminescent devices, Opt. Express 25 (2017) A454. https://doi.org/10.1364/OE.25.00A454.

[361] S. Krishnan, H. Van der Walt, V. Venkatesh, V.B. Sundaresan, Dynamic characterization of elastico-mechanoluminescence towards structural health monitoring, Journal of Intelligent Material Systems and Structures 28 (2017) 2458–2464. https://doi.org/10.1177/1045389X17689939.

[362] S.M. Jeong, S. Song, K.-I. Joo, J. Kim, S.-H. Hwang, J. Jeong, H. Kim, Bright, wind-driven white mechanoluminescence from zinc sulphide microparticles embedded in a polydimethylsiloxane elastomer, Energy Environ. Sci. 7 (2014) 3338–3346. https://doi.org/10.1039/C4EE01776E.

[363] S. Moon Jeong, S. Song, S.-K. Lee, B. Choi, Mechanically driven light-generator with high durability, Appl. Phys. Lett. 102 (2013) 051110. https://doi.org/10.1063/1.4791689.

[364] K. Moroi, T. Sato, Comparison between procaine and isocarboxazid metabolism in vitro by a liver microsomal amidase-esterase, Biochem Pharmacol 24 (1975) 1517–1521. https://doi.org/10.1016/0006-2952(75)90029-5.

[365] Ungku Omar Polytechnic, Ipoh, Perak, M.Z. Zainal, N. Buyamin, Ungku Omar Polytechnic, Ipoh, Perak, S.H.S.M. Fadzulllah, Universiti Teknikal Malaysia Melaka, Melaka, R. Muhammad, Ungku Omar Polytechnic, Ipoh, Perak, Reliability Performance of Conductive Ink Subjected to Hygrothermal Aging, IJEAT 9 (2019) 4060–4065. https://doi.org/10.35940/ijeat.B4945.129219.

[366] J. Sánchez-González, A. Macías-García, M.F. Alexandre-Franco, V. Gómez-Serrano, Electrical conductivity of carbon blacks under compression, Carbon 43 (2005) 741–747. https://doi.org/10.1016/j.carbon.2004.10.045.

[367] C. Miehe, S. Göktepe, J. Méndez Diez, Finite viscoplasticity of amorphous glassy polymers in the logarithmic strain space, International Journal of Solids and Structures 46 (2009) 181–202. https://doi.org/10.1016/j.ijsolstr.2008.08.029.

[368] A. del Bosque, X.F. Sánchez-Romate, D. Calvo, M. Sánchez, A. Ureña, Mechanical and sensing performance under hydrothermal ageing of wearable sensors made of polydimethylsiloxane with graphitic nanofillers, Polymer Degradation and Stability 209 (2023) 110278. https://doi.org/10.1016/j.polymdegradstab.2023.110278.

[369] V.-T. Nguyen, Q.-D. Nguyen, B.K. Min, Y. Yi, C.-G. Choi, Ti3C2Tx MXene/carbon nanotubes/waterborne polyurethane based composite ink for electromagnetic interference shielding and sheet heater applications, Chemical Engineering Journal 430 (2022) 133171. https://doi.org/10.1016/j.cej.2021.133171.

[370] A.M. Mäntysalo, JARI SUIKKOLA PRINTED STRETCHABLE INTERCONNECTS FOR WEARABLE HEALTH AND WELLBEING APPLICATIONS, Tampere University of Technology. pp 59. (2015).

[371] P. Vassiliou, V. Gouda, Ancient silver artefacts: corrosion processes and preservation strategies, in: Corrosion and Conservation of Cultural Heritage Metallic Artefacts, Elsevier, 2013: pp. 213–235. https://doi.org/10.1533/9781782421573.3.213.

[372] B. Valdez Salas, M. Schorr Wiener, R. Zlatev Koytchev, G. López Badilla, R. Ramos Irigoyen, M. Carrillo Beltrán, N. Radnev Nedev, M. Curiel Alvarez, N. Rosas Gonzalez, J.M. Bastidas Rull, Copper Corrosion by Atmospheric Pollutants in the Electronics Industry, ISRN Corrosion 2013 (2013) 1–7. https://doi.org/10.1155/2013/846405.

Thèse accessible à l'adresse : https://theses.insa-lyon.fr/publication/2023ISAL0114/these.pdf © [L. Diatezo], [2023], INSA Lyon, tous droits réservés

[373] G. Lopez, H. Tiznado, G. Soto Herrera, W. De la Cruz, B. Valdez, M. Schorr, Z. Roumen, Use of AES in corrosion of copper connectors of electronic devices and equipments in arid and marine environments, Anti-Corrosion Methods and Materials 58 (2011) 331–336. https://doi.org/10.1108/00035591111178909.

[374] A. Boubakri, N. Haddar, K. Elleuch, Y. Bienvenu, Impact of aging conditions on mechanical properties of thermoplastic polyurethane, Materials & Design 31 (2010) 4194–4201. https://doi.org/10.1016/j.matdes.2010.04.023.

[375] A. Boubakri, K. Elleuch, N. Guermazi, H.F. Ayedi, Investigations on hygrothermal aging of thermoplastic polyurethane material, Materials & Design 30 (2009) 3958–3965. https://doi.org/10.1016/j.matdes.2009.05.038.

[376] P. Jojibabu, G.D.J. Ram, A.P. Deshpande, S.R. Bakshi, Effect of carbon nano-filler addition on the degradation of epoxy adhesive joints subjected to hygrothermal aging, Polymer Degradation and Stability 140 (2017) 84–94. https://doi.org/10.1016/j.polymdegradstab.2017.04.017.

[377] K. Gilleo, Assembly with Conductive Adhesives, Soldering & Surface Mount Technology 7 (1995) 12–17. https://doi.org/10.1108/eb037885.

[378] B.-S. Yim, Y. Kwon, S.H. Oh, J. Kim, Y.-E. Shin, S.H. Lee, J.-M. Kim, Characteristics of solderable electrically conductive adhesives (ECAs) for electronic packaging, Microelectronics Reliability 52 (2012) 1165–1173. https://doi.org/10.1016/j.microrel.2011.12.004.

[379] H.-W. Cui, D.-S. Li, Q. Fan, H.-X. Lai, Electrical and mechanical properties of electrically conductive adhesives from epoxy, micro-silver flakes, and nano-hexagonal boron nitride particles after humid and thermal aging, International Journal of Adhesion and Adhesives 44 (2013) 232–236. https://doi.org/10.1016/j.ijadhadh.2013.03.007.

[380] K.J. Loh, D. Chang, Zinc oxide nanoparticle-polymeric thin films for dynamic strain sensing, J Mater Sci 46 (2011) 228–237. https://doi.org/10.1007/s10853-010-4940-3.

Thèse accessible à l'adresse : https://theses.insa-lyon.fr/publication/2023ISAL0114/these.pdf © [L. Diatezo], [2023], INSA Lyon, tous droits réservés

List of Figures

Figure 1.1. Passive smart textile :(a) Protective gloves, Antistatic ESD, (b) Smock Anti-static ESD White, and (c) Shoe safety UVEX S1P black-red-ESD antistatic [39]. 20

Figure 1.2. Active smart textile materials [41]. 20

Figure 1.3. Several applications associated with smart textiles [53,56–60]. 22

Figure 1.4. Temperature-controlling textiles: Textile-based car seat heaters (a) [72], (b) [73] and (c) [74]. 23

Figure 1.5 Proposed structure and simulated properties of the meta-fabric [80] : (a) Schematic of a meta fabric for daytime radiative cooling (scale bar: 400 nm); (b) Scattering and absorption efficiencies calculated for particles of different sizes encapsulated in the meta-fabric, (c) Top: scattering coefficients of PTFE and TiO_2 nanoparticles with optimized size distributions and 15% volume fractions. Bottom: solar radiation band reflectivity curves measured for meta-fabrics, meta-textiles and PTFE clothing films [62]. 23

Figure 1.6. Flexible polymer-based heated back support (a) by EXO2 [79], (b) Storm Walker jacket by EXO2 [90], and (c) 5-zone heated jacket by DelphyneWomens [90]. 24

Figure 1.7. Heated gloves, socks and slippers based on flexible polymers [79]. 25

Figure 1.8. Active heating textiles based on Joule heat and light-to-heat conversion [76,84,93]. 26

Figure 1.9. Optical fiber applications in smart textiles for environmental engineering [102] : (a) medicine [103], (b) design [104–106], and (c) decorative purposes [105]. 27

Figure 1.10. Design rules [109–111]. 27

Figure 1.11. Classification of printing techniques to manufacture electronic components and circuits. 30

Figure 1.12. Schematics of gravure printing [153]. 31

Figure 1.13. Schematic drawing of flexographic printing technique [112,163]. 32

Figure 1.14. Schematic drawing of flatbed screen-printing [164]. 32

Figure 1.15. Principal schema of inkjet printing [168]. 33

Figure 1.16. Schematic diagram of a representative fused deposition modeling (FDM) installation. FDM consists of an extruder (A), which directs the ink to the nozzle (B) for fluid ejection to form the printed object (C). The process involves forming the printed object on a heating plate (D) to control the temperature and fluidity of the resulting ink. The ink is usually a highly viscous fluid obtained by heating a thermoplastic material, and is deposited through the extruder/nozzle system in the form of a continuous filament of well-defined dimensions (E) [140,171]. 34

Figure 1.17. Schematic of the aerosol jet printing process [179]. 35

Figure 1.18. Printed electronics applications: sensors, biomedical devices, energy devices and other electronic communication devices such as antennas [120]. 35

Figure 1.19. Illustrations of printed piezoresistive sensor: (a) [184] and (b) [182]. 36

Figure 1.20. Layout of an inkjet-printed capacitive sensor on (a) PET substrate [189]. (b) Photo paper [193] and (c) TPU substrate [200]. 37

Figure 1.21. Illustration of printed piezoelectric sensor coatings : (a) [204] and (b) [205]. 37

Figure 1.22. Screen-printed EL samples on fabrics (a) Light blue powered, (b) Dark blue powered, (c) Orange powered, (d) Dark blue unpowered, and (e) Light blue EL lamp on flexibility fabric [207]. 38

Figure 1.23. Six individually printed layers built up to produce EL display [207]. 38

Figure 1.24. (a) Photograph of the printed carbon heater (b) thermal image of the heater at 15 V at 0% nominal strain clamped in the Hounsfield tensile tester (c) the effect of the applied voltage on the heating response of the printed carbon heaters [215]. 39

Thèse accessible à l'adresse : https://theses.insa-lyon.fr/publication/2023ISAL0114/these.pdf © [L. Diatezo], [2023], INSA Lyon, tous droits réservés

Figure 2.1. Formulation process with copper conductive ink. 44

Figure 2.2. Elaboration of phosphorus composites based using a casting and screen-printing method, consisting of several stages: (a) mixing the metal-doped ZnS microparticles with a polymer solution at a specific ratio; (b) dispersing the ZnS particles by ultrasound to obtain homogeneous suspensions; (c) implementing the composite mixture onto ITO coated glass substrate and textile, and (d) thermal treating the film thank to annealing process; (e) depositing gold electrodes by sputtering technique, and (f) illustrating the whole electroluminescent sample with electrode deposition. 46

Figure 2.3. 50 µm-thick ZnS:Cu/matrix composite films with volume fractions of 20%: (a) EL device deposited on a textile substrate with a transparent silver electrode by screen printing technique and (b) EL device deposited on ITO-coated glass substrates with a gold electrode deposited by sputtering technique. 47

Figure 2.4. Silk-screen printing process used by Tesca. 48

Figure 2.5. Screen-printing process for electroluminescent composites 49

Figure 2.6. Principle of thickness measurement by laser profilometer. 51

Figure 2.7. Experimental setup used for measurement of the electrical resistance. 52

Figure 2.8. Thermal characterization of fabrics with and without printed coatings: a) Thermal resistance measurement using a Jeulin device; b) Equivalent scheme of a simple thermal model. 53

Figure 2.9. Schematic illustration of the measuring bench used for the thermal characterization of heated tablecloth. 54

Figure 2.10. Thermal/climatic stability enclosures. 55

Figure 2.11. Load frames for (a) tensile test as a function of sample size; (b) mechanical compression endurance test of knee strike on heating tablecloth, (c) sitting endurance test European SAE Standard using J826 H-point manikin. 56

Figure 2.12. Experimental setup for dielectric characterization 57

Figure 2.13. Electrical characterization bench for the electroluminescent (EL) device. 58

Figure 2.14. Geometric design of the ZnS:Cu/ P(VDF-TrFE-CFE) composite. 60

Figure 2.15. Boundary conditions of the electrostatic modulus 60

Figure 3.1. Micrographs of carbon, copper, and silver coatings respectively for a-b-c) the top view 63

Figure 3.2. Thickness variation profiles observed on the textile substrates: (a) and (c) comparison between the raw and treated data for the copper and carbon inks respectively; (b) and (d) treated data with different layers of copper and carbon inks respectively; (e) evolution of the thickness variation versus the layers number of these two inks. 65

Figure 3.3. Evolution of the electrical property as a function of the length of different conductive inks: (a) electrical resistance; (b) electrical conductivity 68

Figure 3.4. Whisker-box plots calculated from 17 samples coated with (a) copper or (b) carbon composites 69

Figure 3.5. a) Heating system composed of copper tracks and carbon patches built on a fabric substrate; b) 2D dimension of the heater design; c) Equivalent electrical scheme 70

Figure 3.6. Mesh build in COMSOL Multiphysics for model geometry of the tablecloth. a) face of fabric substrate (back side), and b) coating face (front side) 72

Figure 3.7. Comparison of the three temperature zones of (a) the initial theoretical design (denoted D0) and (b) the practical model Tesca REF. 22 (denoted D). 73

Figure 3.8. Influence of the on the numerical heatmap of tablecloth set with different thermal conductivity of inks (λ): (a) $\lambda carbon$ and $\lambda copper$ are shown on Table 3.5; and (b) $\lambda carbon = \lambda copper = 10\ W.\mathrm{m} - 1.\mathrm{K} - 1$ 74

Figure 3.9. Influence of changing the size of the copper electrode in the design. 75

Thèse accessible à l'adresse : https://theses.insa-lyon.fr/publication/2023ISAL0114/these.pdf © [L. Diatezo], [2023], INSA Lyon, tous droits réservés

Figure 3.10. Optimization of the printed coatings: a) Initial design; b) Zoom-in on the connection between copper electrode and carbon patch; c) Optimizations performed in designs 1 and 2. 76

Figure 3.11. Design enhancement for reducing hot spots and reaching uniform heating surface. 77

Figure 3.12. Temperature evolution along the x axis: (a) lateral temperature, and (b) central temperature. 78

Figure 3.13. Time evolution of the measured and simulation temperatures performed on the tablecloth with optimized design. 79

Figure 3.14. Heat map of (a) a real prototype screen-printed with a thermal camera and (b) a digital model using COMSOL software. 80

Figure 3.15. Thermal behavior under different applied input voltages: (a) Time evolution of temperature behavior; (b) Temperature (blue curve) and electrical power (orange curve) versus the input voltage. Dotted lines represent the quadratic models. 81

Figure 4.1. Jablonski diagram, extracted from [338]. 84

Figure 4.2. (a) classic configuration and research axis [271], (b) Schematic principal and structure of the EL device and (c) Equivalent electrical circuit of a 0-3 particle-polymer composite based on the mixed model. 85

Figure 4.3. SEM images (magnification $\times$ 2000 with the scale bar of 200 µm) of phosphorus particles with different doppants : a) ZnS:Cu-Al; b) ZnS:Cu; and c) ZnS:Cu-Mn. 87

Figure 4.4. SEM images ($\times$ 750 magnification) of composites made of 20 vol.% content of phosphorus particles (i.e., ZnS:Cu and ZnS:Cu-Mn corresponding to samples at the first row and the second row) randomly dispersed in three different matrices (polycarbonate, copolymer, and terpolymer corresponding to samples from the left-side to the right-side column). 88

Figure 4.5. SEM images of terpolymer/(ZnS:Cu) composite with different concentration from 10 vol.% to 40 vol.%. Observation waw performed under wo magnifications: a) $\times$ 100 ; and b) $\times$ 750 89

Figure 4.6. Current-density-versus-electric-field (J-E) hysteresis curve of: (a) pure matrices; and (b) composites made of three different matrices filled with 20 vol.% ZnS:Cu phosphor particles. All samples were excited under an input electric field of 10 V/µm amplitude and 500 Hz frequency. 90

Figure 4.7. Electrical characterization of the terpolymer/ZnS:Cu composite at 20 vol.%, under an input electric field of 10 V/µm: (a) Decomposition of the total measured current densities into two components (J_{capa} and J_{cond}, [276]), allowing to determine the electrical conductivity; (b) Polarization loop of the charge density versus electric field to determine the dielectric permittivity; (c) Time evolution of the electric field, and the current density; (d) the resulting charge density that is in phase with the electric field. 91

Figure 4.8. Current density as a function of electric field of (a) at low electric field with purely capacitive behavior (i.e., linear J-E characteristics); and (b) at high electric filed where the phosphor is transited as semi-conductor behavior (i.e., nonlinear J-E characteristics). 93

Figure 4.9. Influence of the type of particles on the EL property of composite: (a) Evolution of the luminance as a function of the electric field; (b) the ratio of the local field seen by the particles as well as the EL and the dielectric behaviors of the composites subjected to an input field of 5.5 V/µm at 500 Hz ; (c) Images demonstrating how light intensity varies with different types of ZnS phosphorus dopant. Tests were conducted on the composites-based terpolymer matrix made with different types of doped ZnS particles with the same content of 20 vol.% 95

Figure 4.10. Influence of the particles' content on the composite characteristics: (a) Comparison between the numerical model and the empirical data (measured at 1 kHz) of the dielectric constant; (b) the ratio of the local field seen by the particles as well as the EL and the dielectric behaviors of the composites subjected to an input field of 5.5 V/µm at 500 Hz. Tests were conducted on the composites elaborated with different volume fraction of (ZnS:Cu) phosphorus particles dispersed into terpolymer matrix. 96

Figure 4.11. Influence of the type of polymer matrices on the EL property of composites: (a) Evolution of the luminance as a function of the electric field; (b) the ratio of the local field seen by the particles as well as the EL and the dielectric behaviors of the composites subjected to an input field of 5.5 V/µm at 500 Hz; (c) Images demonstrating how light intensity varies with different types of polymer matrices. Tests were conducted on the composites elaborated with the

Thèse accessible à l'adresse : https://theses.insa-lyon.fr/publication/2023ISAL0114/these.pdf © [L. Diatezo], [2023], INSA Lyon, tous droits réservés

same particles (20 vol. % (ZnS:Cu) phosphorus) dispersed into the three polymer matrices comprising terpolymer, copolymer, and polycarbonate. 97

Figure 4.12. Light efficiency as a function of the electric field at a frequency of 500 Hz. . Tests were conducted on the composites elaborated with the same particles (20 vol. % (ZnS:Cu) phosphorus) dispersed into the three polymer matrices comprising terpolymer, copolymer, and polycarbonate. 98

Figure 4.13. Electric field distribution using 3D finite element for modeling composites made of terpolymer matrix included with different doped phosphorus particles (20 vol.%) such as (a) ZnS: Cu; (b) ZnS: Cu-Al; and (c) ZnS: Cu-Mn. 99

Figure 4.14. Electric field distribution using 3D finite elements for modeling composites made of 20 vol.% (ZnS: Cu) phosphorus particles incorporated within different matrices such as (a) polycarbonate; (b) copolymer; and (c) terpolymer. 99

Figure 4.15. Photograph of three polymer-binder film sandwiched between two electrodes: (a) a substrate-free dielectric film; and (b) a device structure deposited on a textile substrate. 101

Figure 4.16. Micrographs of the three polymer matrices consisting of PU-AR, AC-AR, and AC-RUD (from the left- to the right-hand side, respectively) printed on a textile substrate. a-b-c) the top view (performed on the upper surface); and d-e-f) the edge view (performed on the cross-section). 102

Figure 4.17. Implementation of EL samples on a fabric substrate using: (a) a gold top electrode; (b)-(d) a transparent PEDOT: PSS electrode. 103

Figure 5.1. The evolution of resistance and temperature as a function of heating duration at 100°C for 48h, (a) before the thermal aging cycle, (b) after the thermal aging cycle, and (c) the screen-printed tablecloth 106

Figure 5.2. Thermal analysis of sewn and unsewn coated fabrics after several aging tests using mechanical cycles: (a) This dummy represents the weight and contour of an adult man, and (b) mechanical endurance of knee cuts. 107

Figure 5.3. Ageing test of the copper electrode coating: (a) temperature and humidity profile over one cycle, (b) the coating before hygrothermal ageing, (c) the coating after hygrothermal ageing, and (d) the coating printed after the humidity cycle. 109

Figure 5.4. Morphologies of carbon- and copper-based composite ink before and after aging tests. Panels (a), (b) and (c) show the carbon-based conductive ink, while panels (d), (e) and (f) represent the copper-based conductive ink. These tests include thermal, humidity and mechanical cycles. 110

Figure 5.5. Ageing test of the heating tablecloth coating: profile of temperature and humidity over one cycle of mechanical endurance, as well as the evolution of electrical resistance before and after the stability tests. 111

Figure 5.6. The influence of temperature on the electrical properties of (a) carbon ink, (b) copper ink, (c) copper ink and (d) carbon ink samples as a function of heating time. 112

Figure 5.7. Evolution of electrical conductivity of copper ink as a function of heating time with optimized and non-optimized new ink. 113

Figure 5.8. The conductivity of the new copper composite conductive ink formulated between room temperature and hygrothermal ageing for 12 days at 85°C/85%RH/–40°C. 114

Figure 5.9. Tensile stress-versus-strain response of copper composite inks with different polymer binders. 115

Figure 5.10. Compressive stress-strain loop of the copper composite formulated with different binders: (a) AC-AR binder, PU-AR binder, and (c) AR-RUD binder; (c) evolution of electrical conductivity as a function of strain. 116

Figure 5.11. X-ray spectra for the two copper composite ink samples: (a) unoxidized and (b) oxidized electrodes. 117

Figure 5.12. Energy dispersive X-ray (EDS) analysis: (a) SEM image of oxidized copper ink; (b, c) EDS image of oxidized copper ink, silver and copper conductors. 118

Figure 5.13. Two sample units used to measure the electrical resistance: (a) non-oxidized copper ink (before the aging test), and (b) oxidized copper ink (after the aging test). 119

Thèse accessible à l'adresse : https://theses.insa-lyon.fr/publication/2023ISAL0114/these.pdf © [L. Diatezo], [2023], INSA Lyon, tous droits réservés

Figure 5.14. Two new designs of corrosion protection from the copper oxidation: (a) binder protection layer for the substrate; and (b) binder protection layer for the substrate and the copper composite ink. 120

Figure 5.15. Electrical conductivity measured at room temperature (initial state) and hygrothermal aging (for 24 h and 48 h) of the copper composite inks formulated with the three different binders (shown in the legend) and different protection's materials like: (a) AC-AR; (b) PU-AR, and (c) AC-RUD. 121

Figure 5.16. Electrical conductivity measured at ambient condition (initial state) and thermal/moisture aging (for 12 days) of the copper composite inks formulated with the three different binders (shown in the legend) and different protection's materials like: (a) AC-AR; (b) PU-AR, and (c) AC-RUD. 122

Figure 5.17. Stress-strain curves of the copper composite inks formulated with the three different binders (shown in the legend) and different protection's materials like: (a) AC-AR; (b) PU-AR, and (c) AC-RUD. 123

Figure 5.18. Images of the heating tablecloth elaborated with the protection-based AR-PU and the copper composite-based AC-AR polymer: (a) before and (b) after a 48-hour thermal cycles. 125

Figure 5.19. Images of the heating tablecloth protected by PU-AR binder (on the textile) and AC-AR-formulated composite ink, (a) before and (b) after the thermal and humidity cycles. 126

Figure 5.20. Heating images of the full protected device, (a) before and (b) after thermal cycles. 126

Figure 5.21. A real heating tablecloth sewn into car-seat system and its thermal image using an infrared camera... 127

Thèse accessible à l'adresse : https://theses.insa-lyon.fr/publication/2023ISAL0114/these.pdf © [L. Diatezo], [2023], INSA Lyon, tous droits réservés

List of Tables

Table 1.1. Key properties and parameters of different printing methods [159,160] 30

Table 2.1. General properties of commercially available conductive inks. 42

Table 2.2. General properties of commercially available binders and percentage of copper particles used. 43

Table 2.3. General properties of commercially available electroluminescent phosphors. 44

Table 2.4. General properties of commercially available dielectric matrices 45

Table 2.5. General properties of matrix and particles used in the composite inks. 50

Table 2.6. Thermal properties the composite inks based on the mixing laws. 53

Table 3.1. Average thickness measured by laser profilometer. 64

Table 3.2. Measured thermal conductivity of coated and neat fabric samples. The resistance and the conductivity of the conductive coatings were deduced from Equations (2.8) and (2.9) of Chapter 2. 66

Table 3.3. Measured electrical conductivity (σ) and fitting factor (α). 68

Table 3.4. Statistical data relating to the electrical properties of conductive coatings. All parameters have the same unit of electrical conductivity $\sigma\ S.m-1$, with the exception of the two relative coefficients *VR* and *QCD* in % 69

Table 3.5. Measured thermal conductivity of coated and neat fabric samples. 71

Table 3.6. Measured thermal conductivity of coated and neat fabric samples. 73

Table 3.7. Comparison of the heating performance for the three designs. 77

Table 3.8. Comparison between measured and theoretical temperatures of three heating areas. 79

Table 3.9. Electrical power and temperature at steady state were obtained with different input voltage levels. The response time during which the system reaches 95% of the steady temperature were also provided. 81

Table 4.1. Electrical parameters of the polymer matrices that are deduced from the J-E curve 92

Table 4.2. Electrical parameters of the phosphorus particles that are deduced from the J-E curve 93

Table 4.3. Characterization of the dielectric constants of three polymer binders. 101

Table 5.1. General properties of new commercially available polymer binders. 112

Table 5.2. Electrical conductivities before and after the thermal cycles at 100°C for 24h and 48h. 114

Table 5.3. Conductivity evolution of the new inks formulated before and after humidity test. 114

Table 5.4. Electrical and mechanical properties of different copper composite inks. 116

Table 5.5. (a) Energy dispersive X-ray map sum spectrum values of oxidized copper composite; and (b) Summary of compounds by means of XRD, EDS and SEM characterizations. 119

Table 5.6. Electrical conductivity measured at the initial state (ambient condition) and after thermal cycles over 24 h and 48 h. Tests were performed on 9 samples with different combinations of the copper composite coating and the anti-corrosion protections 121

Table 5.7. Electrical conductivity measured at the initial state and after a 12-day moisture cycles. Tests were performed on 9 samples with different combinations of the copper composite coating and the anti-corrosion protections. 122

Table 5.8. Electrical properties of the two accelerated aging tests performed on the 9 sample units. 123

Table 5.9. Young modulus of different copper composite inks estimated based on tensile stress. 123

Table 5.10. Electrical resistance before and after thermal cycles conducted on different areas of the heating tablecloth. 124

Thèse accessible à l'adresse : https://theses.insa-lyon.fr/publication/2023ISAL0114/these.pdf © [L. Diatezo], [2023], INSA Lyon, tous droits réservés

Table 5.11. Electrical resistance before and after thermal/humidity cycles conducted on different areas of the heating tablecloth. Only one protection layer coated on the textile substrate. 125

Table 5.12. Electrical resistance before and after the thermal aging conducted on different areas of the heating tablecloth. Two protection layers are used: one is coated on the textile substrate and the other is on the copper composite ink. 127

Thèse accessible à l'adresse : https://theses.insa-lyon.fr/publication/2023ISAL0114/these.pdf © [L. Diatezo], [2023], INSA Lyon, tous droits réservés

List of publications

Peer-reviewed publications:

Léopold Diatezo, Minh-Quyen Le, Christine Tonellato, Lluis Puig, Jean-Fabien Capsal, Pierre-Jean Cottinet. Development and Optimization of 3D-Printed Flexible Electronic Coatings: A New Generation of Smart Heating Fabrics for Automobile Applications, Micromachines 2023, 14(4), 762; https://doi.org/10.3390/mi14040762.

Conference publications:

Léopold Diatezo, Minh-Quyen Le, Christine Tonellato, Lluis Puig, Jean-Fabien Capsal, Pierre-Jean Cottinet.Enhancement of a smart stretchable resistive heater textile using printed electronic coatings: towards application in automobile, Proceedings Volume 12483, Active and Passive Smart Structures and Integrated Systems XVII; 124830O (2023) https://doi.org/10.1117/12.2656929

Conferences participation:

- Prix Techtera au pôle de compétitivité dédié à la filière textile française, en partenariat avec UNITEX Auvergne Rhône Alpes, organisation professionnelle régionale, juillet 2021

- Remise des distinctions scientifiques de l'INSA-Lyon reçu le 22 juillet 2021 le Prix Techtera, pour son travail sur le développement des textiles chauffants (en partenariat avec TESCA Group) qui a permis de mettre en évidence la conversion d'énergie électrique en énergie thermique.

- SPIE Smart Structures + Nondestructive Evaluation, Online, March 22

Thèse accessible à l'adresse : https://theses.insa-lyon.fr/publication/2023ISAL0114/these.pdf © [L. Diatezo], [2023], INSA Lyon, tous droits réservés

FOLIO ADMINISTRATIF

THESE DE L'UNIVERSITE DE LYON OPEREE AU SEIN DE L'INSA LYON

NOM : DIATEZO DATE de SOUTENANCE : 18 /Décembre/ 2023

Prénom: Léopold

TITRE: Multifunctional materials for smart textiles: Towards automotive applications

NATURE : Doctorat Numéro d'ordre : 2023ISAL0114

Ecole doctorale : MEGA.

Spécialité : Electronique - Génie électrique

RESUME : Les matériaux multifonctionnels jouent un rôle crucial dans le développement des matériaux intelligents. En effet, le progrès des matériaux définis comme multifonctionnels, sera probablement le principal moteur de cette évolution technologique. Il s'agit de concevoir, optimiser, développer et d'intégrer des fonctions pour rendre les produits plus intelligents, ainsi que d'améliorer leurs processus de fabrication additive. Ces matériaux sont utilisés comme composants fonctionnels dans diverses applications, notamment dans le domaine de la santé, de la défense, de l'automobile et de la sécurité au travail.

Les travaux de thèse se sont focalisés sur deux applications principales. La première consiste en la création d'une application thermique en utilisant le chauffage par effet Joule de ces matériaux conducteurs. L'objectif était de concevoir une nouvelle génération de tissus intelligents destinés aux sièges de voitures, avec des applications spécifiques dans le domaine automobile. La seconde application concerne l'utilisation de matériaux composites phosphorescents, qui jouent un rôle central dans le fonctionnement des capteurs photo-capacitifs ou électroluminescents. Des études préliminaires ont été menées sur les caractéristiques électriques de ces matériaux afin d'optimiser leurs propriétés, de les rendre compatibles avec la technique d'impression par sérigraphie, et de mieux comprendre leurs limites et règles d'intégration.

Première application porte sur la création d'une nappe chauffante destinée aux sièges de véhicules. Ce dispositif de chauffage est composé de deux électrodes principales en cuivre, communément appelées "bus d'alimentation", ainsi que de trois résistances chauffantes identiques en composites de carbone. Les connexions entre les bus d'alimentation en cuivre et les résistances en carbone sont réalisées sous forme d'électrodes subdivisées, jouant un rôle essentiel dans l'assurance du couplage électrique-thermique. Des modèles basés sur la méthode des éléments finis (FEM) ont été développés pour prédire comment ces sous-ensembles se comportent en termes de conversion par effet joule, en tenant compte de différentes configurations de motifs. Il est souligné que la conception la plus optimisée permet de résoudre les problèmes inhérents à la conception initiale, notamment en ce qui concerne la régularité de la température et d'effet de surchauffe. Une analyse complète des propriétés électriques et thermiques, ainsi que des études morphologiques à l'aide d'images (SEM), a été réalisée sur différents échantillons revêtus d'encre conducteur. Cela a permis d'identifier les paramètres physiques pertinents des matériaux et de confirmer la qualité de l'impression par sérigraphie. Une combinaison de méthode des Éléments Finis (FEM) et d'évaluation expérimentale a révélé que les motifs de revêtement imprimés jouent un rôle crucial dans la conversion d'énergie et les performances de chauffage. Les architectures proposées et implémentées ont satisfait aux normes exigées par l'industrie automobile. Par conséquent, l'utilisation de matériaux multifonctionnels associés à la technologie d'impression pourrait offrir une méthode de chauffage très efficace pour les textiles intelligents, avec un niveau de confort nettement amélioré, tant pour les concepteurs et les utilisateurs.

Pour pousser plus loin la compréhension et limites technologiques des encres développées, une étude de vieillissement a été entreprise en lien avec les contraintes applicatives (cyclage mécanique, thermique en en humidité). Les travaux de corrélation structure propriétés ont permis de mettre en avant une limite technologique dans la formulation des encres. Pour répondre à ce point de blocage, des travaux de formulations sur de nouvelles matrices avec de meilleurs stabilités en raison de leurs propriétés physico-chimiques et aussi en modifiant les charges conductrices. Les travaux ont ainsi débouché sur la formulation d'une encre pouvant tenir les contraintes applicatives.

La deuxième application implique la création d'un dispositif électroluminescent en utilisant un matériau composite électroluminescent. L'objectif est d'identifier les paramètres clés à optimiser. Nous avons réalisé des simulations à l'aide de la méthode des éléments finis (FEM) pour déterminer le meilleur couplage entre les particules de phosphore et la matrice polymère. Nous avons également examiné l'impact des permittivités des particules, de la matrice du matériau et des dimensions du design. Pour mener à bien cette étude, nous avons sélectionné trois types de particules de phosphore en raison de leurs propriétés électriques, optiques distinctes, ainsi que différents types de matrices polymères aux caractéristiques variées. Une analyse a été effectuée sur l'influence des particules de phosphore et des matériaux diélectriques en termes de permittivité et de proportion idéales dans la fabrication de composite électroluminescence, ainsi que leur luminosité. Les résultats obtenus montrent l'importance d'ajuster les permittivités des particules de phosphore et de la matrice polymère. En conséquence, nous avons pu établir des proportions optimales de phosphore et de diélectrique pour obtenir une émission lumineuse améliorée.

Directeur de thèse: COTTINET Pierre-Jean
Co-directrice de thèse : CAPSAL Jean-Fabien
Président de jury :
Composition du jury : GUIFFARD Benoit (rapporteur de thèse), BELHORA Fouad (rapporteur de thèse), DEMOLY Frédéric (examinateur), CONSONNI Vincent (examinateur), KANDA Masae (examinatrice), Christine TONELLATO (Invitée), LE Minh Quyen (examinatrice, co-encadrante de thèse).

Thèse accessible à l'adresse : https://theses.insa-lyon.fr/publication/2023ISAL0114/these.pdf © [L. Diatezo], [2023], INSA Lyon, tous droits réservés